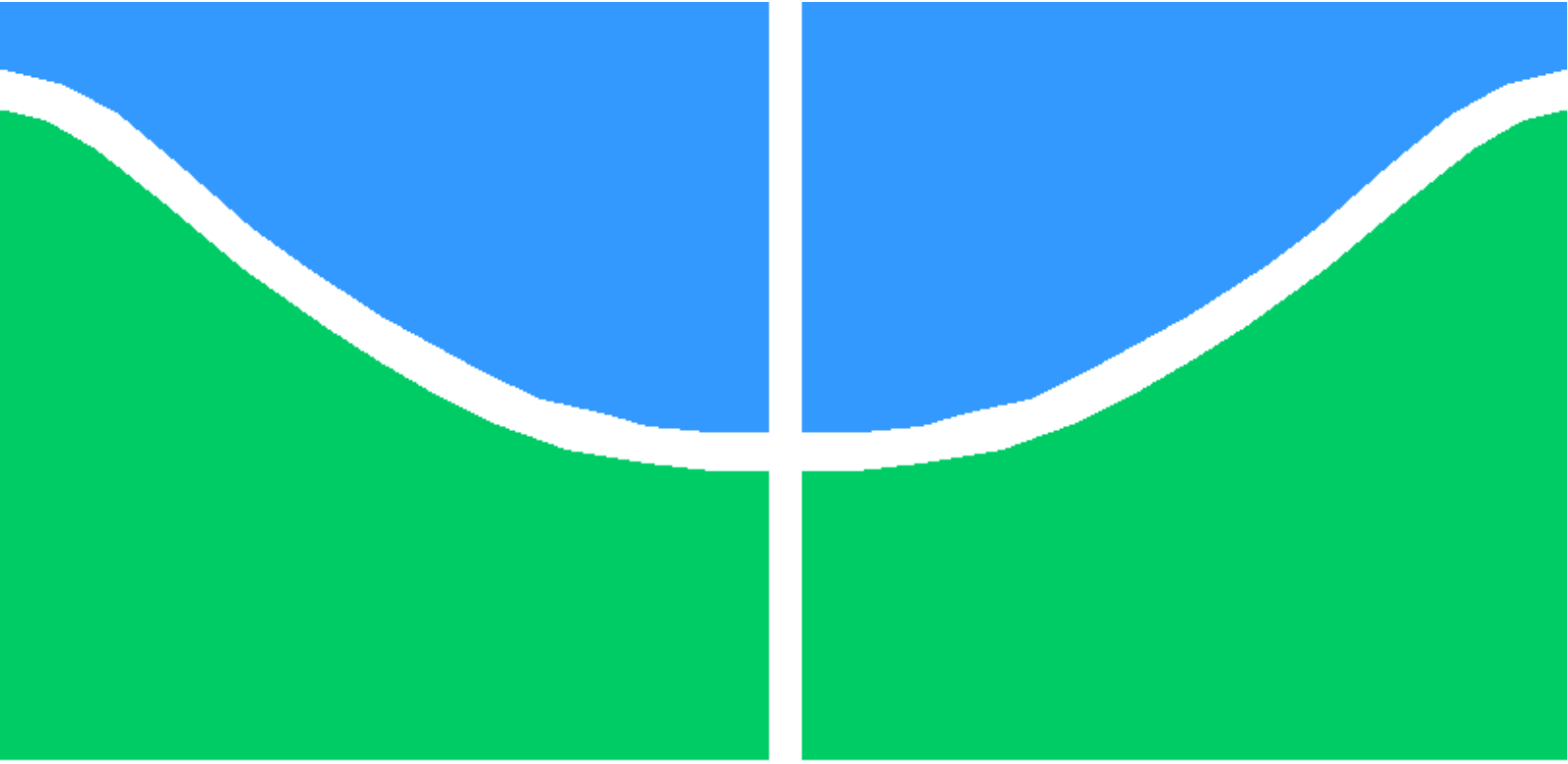

DISSERTAÇÃO DE MESTRADO

Bubble Dynamics in Magnetic Fluids: Theory and Applications

Sara Malvar

Brasília, julho de 2015

UNIVERSIDADE DE BRASÍLIA

FACULDADE DE TECNOLOGIA

UNIVERSIDADE DE BRASILIA
Faculdade de Tecnologia

MASTER'S DISSERTATION

Bubble Dynamics in Magnetic Fluids: Theory and Applications

Sara Malvar

Report submitted to the Mechanical Engineering Department
as a partial requirement to obtain the degree of
Master in Mechanical Sciences

EXAMINING COMMITTEE

Professor Francisco Ricardo da Cunha, PhD
Advisor (ENM-UnB)

Professor Jorge Carlos Lucero, PhD
External Member (CIC-UnB)

Professor Adriano Todorovic Fabro, PhD
Internal Member (ENM-UnB)

UNIVERSIDADE DE BRASÍLIA
FACULDADE DE TECNOLOGIA
DEPARTAMENTO DE ENGENHARIA MECÂNICA

Bubble Dynamics in Magnetic Fluids: Theory and Applications

SARA MALVAR

Dissertação de Mestrado submetida ao Departamento de Engenharia Mecânica da Faculdade de Tecnologia da Universidade de Brasília, como parte dos requisitos necessários para obtenção do grau de Mestre em Ciências Mecânicas.

APROVADA POR:

Professor Francisco Ricardo da Cunha, PhD (ENM-UnB)
(Orientador)

Professor Jorge Carlos Lucero, PhD (CIC-UnB)
(Examinador Externo)

Professor Adriano Todorovic Fabro, PhD (ENM-UnB)
(Examinador Interno)

BRASÍLIA/DF, JULHO DE 2015.

FICHA CATALOGRÁFICA

MALVAR, SARA
Bubble Dynamics in Magnetic Fluids: Theory and Applications
[Distrito Federal] 2015.
xxii, 216p., 297 mm (ENM/FT/UnB), Mestre, Ciências Mecânicas, 2015
Dissertação de Mestrado - Universidade de Brasília.
Faculdade de Tecnologia.
Departamento de Engenharia Mecânica.
1. Magnetic Fluids 2. Bubble Dynamics
3. Nonlinear Control 4. Maxwell Equations
I. ENM/FT/UnB II. DM 229

REFERÊNCIA BIBLIOGRÁFICA

MALVAR., S. (2015). Bubble Dynamics in Magnetic Fluids: Theory and Applications. Dissertação de Mestrado em Ciências Mecânicas, Publicação ENM.DM - 229, Departamento de Engenharia Mecânica, Universidade de Brasília, Brasília, DF, 216p.

CESSÃO DE DIREITOS

NOME DO AUTOR: Sara Malvar.

TÍTULO DA DISSERTAÇÃO DE MESTRADO: Bubble Dynamics in Magnetic Fluids: Theory and Applications.

GRAU / ANO: Mestra / 2015

Sara Malvar
SQN 311, Bloco A, Apto 602. Asa Norte.
70.757-010 Brasília - DF - Brasil.

Para meus pais, Helena e Roberto
e para meu marido, Rafael.

Sara Malvar

Agradecimentos

Marrie Curier disse uma vez que "Na ciência, nós devemos estar interessados nas coisas e não nas pessoas". Entretanto, eu acredito que só cheguei aqui porque outras pessoas pensaram o exato oposto. Enquanto eu me interessei pela ciência, elas estavam interessadas em mim. Hoje, eu posso dizer que eu descobri o que quero fazer pelo resto da minha vida. Eu nasci para descobrir, produzir e lutar todos os dias da mnha vida para produzir conhecimento, um legado que o mundo pode usar.

Neste sentido, eu gostaria de agradecer aos meus pais, Helena e Roberto, que sempre me deram tudo que eu poderia precisar e querer. Obrigada por acreditar em mim, por me ajudar e me desculpem pelas vezes que minha cabeça estava em outro lugar, aventurando-se pelo desconhecido. É bom saber que vocês estão sempre torcendo por mim e prontos para me ajudar quando eu preciso. Amo vocês com todo meu coração!

Obrigada ao meu marido, pela ajuda profissional dada pelo Professor Rafael e pela ajuda pessoal dada pelo Rafa. Eu agradeço pelas intermináveis discussões, pelo conhecimento compartilhado e por acreditar em mim. Obrigada pelo suporte quando eu decidi seguir este caminho. Eu acredito que juntos podemos ir mais longe! Conte comigo, meu amigo, parceiro e amor.

Professor e amigo Francisco Ricardo, obrigada. Agradeço por me receber de braços aberto quando eu decidi trabalhar contigo. Obrigada por toda ajuda e conhecimento. Você se tornou uma inspiração para mim. Agradeço por acreditar em minhas ideias e me dar a liberdade para pensar por mim, propor sugestões e tentar coisas novas sem medo de errar.

Meu tio, Henrique, que sempre foi uma inspiração para mim, obrigada por fazer parte deste momento especial. E muito obrigada por ser sempre tão bom! Você tem sido uma inspiração desde quando eu era criança e sempre me motivou a tentar ser melhor. Desde a infância, eu sempre quis que você e toda a família tivessem orgulho de mim. Espero que hoje, parte deste desejo esteja sendo realizado.

Rê, minha "prima-irmã", obrigada por estar aqui e obrigada por ser a irmã que eu nunca tive. Eu poderia escrever sobre várias de nossas histórias, mas nenhuma delas poderia mostrar o quanto eu sou grata de você existir! Obrigada, obrigada, obrigada!

Eu também gostaria de agradecer aos Professores Jorge Lucero e Adriano Todorovic, que nos ajudaram durante a avaliação deste trabalho e fizeram sugestões valiosas para melhorar sua qualidade. Também agradeço aos colegas de grupo Igor Dal Osto, Yuri Sinzato e Livia Araujo pela ajuda na obtenção dos resultados experimentais de caracterização dos fluidos base obtidos por meio do reômetro, tensiômetro e microscópio, respectivamente.

E eu não poderia esquecer de meus animais, que me deram muito apoio na forma de afeição, lambidas e arranhões. Flicka, Fumaça e Canela, que sempre estiveram prontas para se aninhar no meu colo quando eu estava cansada ou trabalhando e nunca reclamaram de nada, obrigada!

Sara Malvar

RESUMO

O presente trabalho tem por objetivo principal investigar o comportamento não-linear de uma bolha imersa em um fluido magnético, sujeita a um campo de pressão acústico e um campo magnético. Uma nova versão da equação de Rayleigh-Plesset é proposta com o tensor magnético. Esta equação para dinâmica de bolhas é resolvida computacionalmente pelo método Runge-Kutta de quinta ordem com passo de tempo adaptativo, visando diminuir o custo computacional. O código é validado por meio de uma teoria assintótica em função da amplitude de excitação e do número de Reynolds Magnético. A influência de parâmetros adimensionais é investigada, como o número de Reynolds e Weber e dos parâmetros magnéticos, como Reynolds Magnético e Susceptibilidade Magnética. A excitação magnética aplicada foi variada contando com campos oscilatórios e constantes. Uma solução assintótica para o raio mínimo de colapso é apresentada. Isto permite uma análise utilizando tanto as teorias de estabilidade linear hidrodinâmica quanto as teorias não-lineares - como as redes neurais e os expoentes de Lyapunov. Uma série de análises como diagrama de bifurcação dos padrões vibracionais e diagramas de colapso são construídos. Neste contexto, um novo método baseado nas ferramentas de diagrama de fase e DFT é proposto para analisar o comportamento da bolha oscilando em diferentes números de Reynolds Magnético e Suscetibilidade Magnética. Os novos padrões vibracionais apresentados devido ao acoplamento das escalas de tempo do problema são estudados e que leva a identificação de padrões caóticos. Neste sentido, a magnetização do ferrofluido é analizada tanto do ponto de vista das interações partícula-partícula, utilizando-se tanto das ferramentas já apresentadas quanto da equação fenomenológica da magnetização. Essa última permite a comparação deste modelo com o modelo superparamagnético proposto para a modelagem matemática. Visando verificar os conceitos utilizados e as hipóteses restritivas de movimento radial e não deformação uma bancada experimental é desenvolvida. Nesta bancada, estuda-se uma bolha ascendente em diversos fluidos magnéticos que foram sintetizados para este fim. Estes fluidos tem suas características analizadas por meio de um reômetro de discos rotativos e um tensiômetro. Por fim, adiciona-se um campo magnético estacionário por meio de um imã de neodímio e observa-se como a bolha responde.

Palavras-Chave: Equações de Maxwell, Fluidos magnéticos, Equação de Rayleigh-Plesset, Dinâmica de Bolhas, Análise não-Linear.

ABSTRACT

The main purpouse of the present work is to investigate the nonlinear behaviour of a bubble immersed in a magnetic fluid, subjected to an acoustic pressure forcing and a magnetic field. A new version of the Rayleigh-Plesset equation is proposed with the magnetic tensor. That equation is numerically solved using a fith order Runge-Kutta scheme with and adaptive time step, in order to lower the computacional cost. That code is validated with an asymptotic solution in terms of Magnetic Reynolds number and the pressure forcing amplitude. The influence of the main Newtonian dimentionless physical parameters, such as the Reynolds and Weber numbers and the non-Newtonian parameters, as Magnetic Reynolds and Magnetic Susceptibility are investigated. The applied magnetic excitation was varied between stationary and oscillatory fields. An asymptotic theory for the minimum radius before collapse is presented. This permits an analysis using both hydrodynamic linear stability theory and nonlinear theories, such as neural networks and Lyapunov exponents. A serie of analyzes using vibrational pattern bifurcation diagrams and collapse diagrams are built. In this context, a new method based in the phase plot and DFT is proposed in order to analyze the bubble behavior when oscillating. The identified vibrational patterns are studied in order to generate chaotic patterns due to time scales coupling. In this sense, the magnetization of the ferrofluid is analyzed from the particle-particle interactions point of view, using the tools already presented and the phenomenological equation of magnetization. This last allows the comparison of this model with the superparamagnetic model proposed for the mathematical modeling. In order to verify the concepts used, the restrictive assumption of radial movement and lack of deformation an experimental bench is developed. In this bench, a rising bubble immersed in synthesized magnetic fluid is observed. These fluids have their characteristics (such as viscosity and surface tension) analyzed using a rotating disc rheometer and a tensiometer. Finally, a stationary magnetic field is applied using a neodymium magnet and the bubble behavior is observed.

Key-Words: Maxwell Equations, Magnetic Fluids, Rayleigh-Plesset Equation, Bubble Dynamics, Nonlinear Control.

Contents

List of Figures

List of Tables

List of Symbols

Latin Symbols

a, b	Asymptotic solution constants
$\boldsymbol{B}$	Induced magnetic field
D	Deformation parameter
$\mathscr{D}$	Stokes-Einstein Brownian diffusion coefficient
$\boldsymbol{E}$	Electric field
$\boldsymbol{H}$	Applied magnetic field
H_0	Magnetic field reference
H	Column heigh (experimental setup)
H_c	Critical column heigh (experimental setup)
$\boldsymbol{J}$	Density of electrical current
$\boldsymbol{M}$	Magnetization vector
M_d	Particle magnetization
n	Polytropic coefficient
p	Pressure field
p_l	Outside liquid pressure
$p_\infty, \tilde{p}_\infty$	Ambient pressure and equilibrium ambient pressure
p_b	Bubble internal pressure
$\tilde{p}_b$	Bubble internal equilibrium pressure
p_g	Gas pressure
$\tilde{p}_g$	Gas equilibrium pressure
p_m	Mechanic pressure
p_v	Steam pressure
r	Distance from the bubble center to any point in the fluid
R	Bubble radius
$\dot{R}$	Temporal derivative of the bubble radius
$\ddot{R}$	Second order derivative of the bubble radius
$R_0, R(0)$	Bubble initial radius
$\dot{R}_0, G(0)$	Bubble initial velocity
R_{min}, R^*_{min}	Dimensional and non-dimensional minimum radius of the bubble
R_E	Equilibrium radius
V	Bubble volume
Y	Asymptotic solution constant

Time and Velocity Scales

t	Flow time
t_μ	Viscous diffusion time scale
t_σ	Surface tension relaxation time
t_ω	Excitation time
t_m	Magnetic effects time scale
t_c	Problem characteristic time scale
t_r	Bubble relaxation time scale
T_b	Bubble temperature
$\boldsymbol{u}$	Velocity vector
u_ϕ	Polar component of angular velocity
u_υ	Azimuthal component of velocity
u_r	Radial component of velocity
U_c	Characteristic velocity scale

Greek Symbols

α	Relation between magnetic field and Brownian energy
$\dot{\gamma}$	Shear rate
ε	Excitation amplitude
ε^*	Non-dimensional excitation amplitude
ρ	Density
ρ_b	Gas and steam mixture density
ρ_v	Saturated steam density
ϵ_0	Electric permittivity
ϕ	Particle volume fraction
μ	Dynamic viscosity
μ_r	Relative permeability relativa do meio
∇	Nabla operator
∇^s	Superficial nabla operator
σ_{rr}	Radial component of the stress tensor in spherical coordinates
$\sigma_{\kappa\kappa}, \sigma_{\phi\phi}$	Angular component of the stress tensor in spherical coordinates
σ^N	Newtonian contribution of the stress tensor
σ_{nn}	Normal component of the stress tensor
σ_s	Tension coefficient in the bubble interface
κ	Average curvature of the bubble surface
ω	Excitation frequency
ω_n	System natural frequency
ω_{mag}	Magnetic field frequency
ξ	System damping factor
ξ	System damping factor
τ_c	Time of collapse of the Rayleigh cavity
τ_s	Magnetic relaxation time
$\mathbf{\Sigma}$	Fluid stress tensor
$\Delta\tilde{p}$	Pressure difference ($\tilde{p}_\infty - p_v$)
Δt	Time interval for Runge-Kutta method
Δ_{err}	Error estimate for the adaptive time step control

Non-dimensional Groups

Re	Reynolds number
We	Weber number
Re_{mag}	Magnetic Reynolds number
χ	Magnetic susceptibility
Bo	Bond number
Eo	Eötvös number
St	Stokes number
Mo	Morton number
Pe	Péclet number
Ma	Marangoni number

Subscriptions and Superscripts

min	Referring to the minimum radius obtained by the asymptotic solution
nn	Regarding the tensions normal to the bubble surface
Ray	Referring to the time interval obtained by Rayleigh solution
$*$	Referring to the non-dimensional version of a term
mag	Referring to the magnetic case

Chapter 1

Introduction

In this chapter, we present an overview on bubble dynamics, cavitation and its practical applications and ferrofluids. The motivations, references and specific objectives are exposed.

Bubble dynamics is a research line that has been studied since the middle of the industrial revolution. However, the study of ferrohydrodynamics is fairly new. However, both themes have many different applications. Works involving bubbles immersed in magnetic fluids are still sparse and little depth. The study of a rising bubble in a ferrofluid was first made in order to clarify the effects of nonuniform magnetic field on the bubble behavior in a magnetic fluid. The behavior of vapor bubbles is visualized with ultrasonic wave echo under the nonuniform magnetic field [1]. The visual observation of the effect of magnetic fields in air and vapor bubbles immersed in magnetic fluids [2] was one of the first attempts to study this topic. However, the attention was more focused in magnetohydrodynamics (MHD) research lines. MHD is the study of the flow of electrically conducting liquids in electric and magnetic fields [3].

The study of bubbles immersed in magnetic fluids based on the ferrohydrodynamics (FHD) perspective was first conducted in Vortex research group at University of Brasília [4]. Indeed, other works regarding ferrofluid foams have been made aiming to order bubbles spiral arrangements in a tube [5]. However, both themes - bubble dynamics and FHD - have several practical applications when used in other contexts that will be explored in this chapter.

1.1 Cavitation

Cavitation is the term used to represent the formation, behavior and collapse of bubbles (or cavities) in a liquid. The dynamic behavior of bubbles under the effects of variable pressure fields in liquids has always been of great interest in many areas of scientific and technological importance.

Bubbles may be composed of both gases and steam and can be produced by several different ways. The diffusion of gases dissolved in liquids (degassing), for example, is one way of creating bubbles. Another possibility is the pressure reduction or temperature rise (gaseous cavitation)

within the liquid. For bubbles containing steam, the formation is somehow different. Indeed, it happens when there is a sufficient reduction of ambient pressure at constant temperature (vaporous cavitation) or a sudden temperature raise at constant pressure (boiling).

The dynamics of bubbles is a broad theme in our daily life since the human body uses cavitation. One example is the inlet and discharge of blood in the heart chambers. The sudden pressure differences facilitate the formation of cavitation in this region. Bubbles are also associated with the microfluidic transport in cells and blood, performing a pump function in micro-channels [6]. The use of micro-bubbles should produce a drag reduction, ie the flow resistance. This decrease is directly associated with the deformation of bubbles in the flow direction. This geometric anisotropy of the deformed bubble produces a stress in the flow lines direction, which inhibits the transverse fluctuations during blood circulation, especially in the larger arteries and veins. This effect is also seen in turbulent flows when macromolecules are added to the fluid [7].

Cavitation has become a problem during the Industrial Revolution. During this period, several fluid flow mechanisms have emerged. The hydrodynamic flow effects on those systems result in regions where the pressure assumes values lower than the vapor pressure. The turbines in ships provided a thorough study of this phenomenon, since a cloud of bubbles is formed when the water pressure decreases in the turbine boosters.

When the bubbles collapse occurs near solid boundaries, it is typically associated with a high jet velocity [8]. The formation of these jets has been demonstrated experimentally [9]. Some experts point out that there is a high probability that this damage on solid surfaces of materials is caused by the collapse of vapor bubbles; not only by the jet that can occur due to a non-spherical collapse, but also the shock wave itself generated after several collapses [10]. The effect of the collapse is shown in figure 1.1.

Figure 1.1: Photo of a propeller blade from the aircraft carrier Intrepid, taken in the Intrepid Sea, Air & Space Museum (Taken by the author - NY/2015). It is possible to notice small spherical erosions caused by the collapse of cavitating bubbles.

Some experiments and theories have been formulated in order to minimize those damages [11]. The inventor of the steam turbine [12] also stood out for the research about the amount of energy dissipated due to cavitation in turbines. In all these cases, all studies of bubbles were developed

based on radial movements, in which the bubbles oscillate spherically. Some subsequent studies [9] have been based on the collapse of near wall bubbles. In these situations, the bubble was attracted to the membrane surface at the time of collapse, deforming itself. This type of failure creates a shock wave that can have devasting effects on a surface. One example is the erosion of metals such as steel, reducing the useful life of materials.

From a theoretical point of view, some studies have been done aiming the description of the bubble radial motion. Rayleigh model is the oldest, as pointed before, and describes an empty space in the water, influenced by a constant external pressure. The effects of viscosity, surface tension and a non-constant external pressure have been included to the equation by Plesset [10], who proposed the famous Rayleigh-Plesset equation. The version proposed by Gilmore [13] accounted the compressibility of the liquid.

Large amplitudes of oscillation result when the acoustic frequency is at the bubble natural frequency, or certain rational multiples of it. In this case, Keller and Miksis [14] combine several modifications to derive a new equation for the bubble radius. It includes the effects of acoustic radiation, present when the bubble oscillation is large enough, viscosity, surface tension and an incident sound wave. Many other works have presented new versions of bubble dynamic equations, but all of them are based on a variation of the Rayleigh-Plesset equation.

1.2 Acoustic Cavitation

Different fields can be applied in order to excitate bubbles. The use of ultrasound applied to the study of bubbles promotes increased chemical reactions in a research field called sonochemistry [15]. Such use can reduce the use of catalysts, the reaction temperature and allow the generation of useful reactive species. The turbulent flow and shock waves produced by ultrasound may trigger - when used in high intensity - the shock of metallic particles at sufficiently high speed to allow the melting at the point of collision [16]. This process is also used in water purification [17].

The collapse of bubbles induced by ultrasound is also used for cleaning. These processes are used for cleaning jewelry, lenses, surgical instruments and industrial components [18]. The control of the frequency and intensity of ultrasound is essential for the control of the bubble collapse, as it will be shown later.

However, the latest application to control cavitation occurs in the branch of biomedicine. Ultrasound with contrast is an example of how cavitation can be used in the biomedical industry [19]. The microbubbles are injected into the body and take part in image contrast. The ultrasound pulses are applied with the approximate resonance frequency of the microbubbles. These microbubbles respond to pulses with increase and decrease of its diameter, generating echoes in its neighborhood. The difference between these echoes and echoes produced by the tissue generates a contrast. Furthermore, bubbles may be used to transport drugs [6]. The stability of microbubbles is ensured using gases and membranes of different materials that create a shell on the bubble [20]. Thus, they can be injected into the human body through intravenous injection.

Another new application is the use of cavitation to increase membrane permeability of tumor cells [21]. The increase of the cell permeability allows medicinal macromolecules to be injected into the tumor cell. One of the interesting factors of this technology is that the ultrasonic radiation can be focused on almost any part of the body, does not present hazards and is not expensive.

Some studies describe methods for the delivery of genes and drugs in the pancreas of diabetic patients [22]. The two main forms of diabetes involve the destruction or dysfunction in the beta cells. Type 1 diabetes, which affects about 1 million Americans is a condition of complete deficiency of insulin due to beta cell destruction. Type 2 diabetes afflicts over 20 million Americans and the hyperglycemia associated with this disease develops when the ability to secrete insulin can no longer compensate for the resistance thereof [23]. In this study, genes incorporated into microbubbles are injected intravenously. When the bubbles collapse near the pancreas, the gene for human insulin is thus embedded in the pancreas of rats, which in turn produce human insulin, lowering blood glucose. The technique involves incorporating plasmids - which are double circular DNA molecules capable of reproducing independently of cromossomic DNA - in the bubble membrane, which are inserted in rats and disposed near the pancreas with ultrasound.

The chemical effects of ultrasound [24, 25] are not directly linked to a sound field interacting with chemical agents. In fact, sonoluminescence and sonochemistry derive mainly from acoustic cavitation: the formation, and increasing collapse of bubbles in liquids, irradiated with high intensity ultrasound [26].

The collapse of bubbles during the process of cavitation means that all the diffusive sound energy is concentrated, causing the generation of heat due to the compression of the gas bubble. When this compression occurs during cavitation, heating is produced faster than its transported.

A few years ago, noninvasive and reversible disruption of the blood brain barrier was demonstrated using focused ultrasound bursts in conjunction with an ultrasound contrast agent [27]. Contrast agents that contain preformed microbubbles are now extensively investigated for many therapeutic applications. This method for blood brain barrier disruption with ultrasound utilizes preformed microbubbles injected into the blood stream before the ultrasound burst exposures. The working hypothesis for this research was that since the microbubbles act as energy concentrators and are contained in the blood, the induced biological effects would be confined to the blood vessel walls.

1.3 Sonoluminescence

Sonoluminescence is a unique phenomenon in fluid mechanics related to bubble dynamics [28]. Its dynamics is modeled with the classic equations and parameters, governed by hydrodynamic Navier Stokes equation [29] or in Cauchy equation on the more general case of bubbles immersed on complex fluids, evolving to a process of high energy density, which can be described by a very different set of equations.

Basically, sonoluminescence describes the transformation of sound energy into light, as seen in

figure 1.2. This energy transformation takes place in specific situations in a short period of time (order of nanoseconds). This transformation also generates a great heat dissipation and emits high frequency waves.

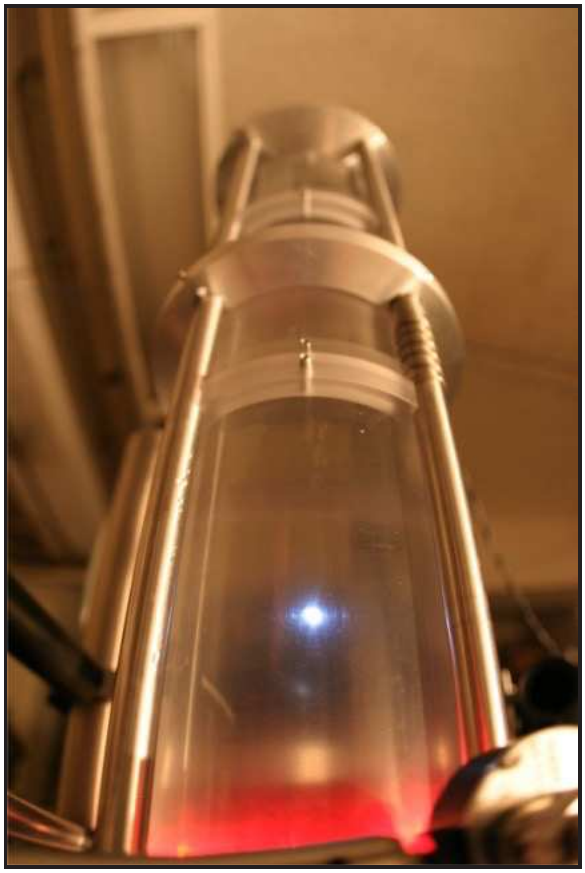

Figure 1.2: Drop tower Sonoluminescence yields 150 Watt flashes of light, one at a time, from a 1/5 atmosphere pressure pulse. Credit to Brian Kappus and Avik Chakravarty from Putterman Research Group (UCLA)

The process of sonoluminescence, which is directly connected to the bubble radius R as a function of time t for an oscilatting bubble due to an external acoustic field can be divided into two types: sonoluminescence caused by the collapse of several bubbles (*Multiple bubble sonoluminescence*, MBSL) or just one bubble (*Single bubble sonoluminescence*, SBSL).

Indeed, this sonoluminescence process is found in nature. The small snapping-shrimp (Alpheidae family), for example, competes with the beluga whale as the "loudest animals of the sea". The red creature pops its claw creating an acoustic wave that generates pressures up to $80kPa$ at a distance of 4 centimeters. Measurements indicate levels of up to $190dB$ at one meter distance. The click lasts less than a millisecond and is a form of defense against predators [30].

In experiments, when the local acoustic pressure applied to the fluid exceeds a cavitation threshold, an interesting area of bubbles is formed. If cavitation is severe enough, the sonoluminescence processes ocurs. In MBSL, a large number of bubbles grow and collapse at the higher sound pressure region. This process is in the temporal order of picoseconds and space of micrometers. Since

the time scales are out of the continuum scope, it is difficult to apply a physical theory to describe this phenomenon. Thus, a new mathematical framework is required, differing from the classical treatment used in the study of classical hydrodynamics equations.

The collapse of bubble in sonoluminescence condition can cause points of extreme conditions of temperature and pressure. In the case of the so called multibubble cavitation, the collapse produces hot spots with effective temperature of over $10,000K$ and pressures of $10,000atm$. In the process of single bubble cavitation, these conditions can be even more extreme [31, 32].

1.4 Ferrofluids

A magnetic fluid (or ferrofluid) is a colloidal suspension of magnetic particles, with typical dimensions of about $10nm$, dispersed in a liquid carrier [33]. The base fluids typically used in the manufacture of magnetic fluids are synthetic oils, ester or water. Ferrofluids are different from the usual magnetorheological fluids (MRF) used for dampers, brakes and clutches, formed by micron sized particles dispersed in oil. In MRF the application of a magnetic field causes an enormous increase of the viscosity. Indeed, for strong fields, the magnetorheological suspension behaves like a solid. Thus, magnetorheological suspensions do not undergo Brownian effect and are not stable, so the particles undergo sedimentation.

In order to avoid agglomeration, the magnetic particles have to be coated with a shell of an appropriate material. According to the coating, the FFs are classified into two main groups: surfacted (SFF), if the coating is a surfactant molecule, and ionic (IFF) if it is an electric shell.

The combination of magnetic fields and ferrofluids has attracted, more recently, professionals in the fields of physics, chemistry, engineering and biomedicine. This theme has been very endorsed lately, including in science museums, so that more people have access to this information as can be seen in figure 1.3.

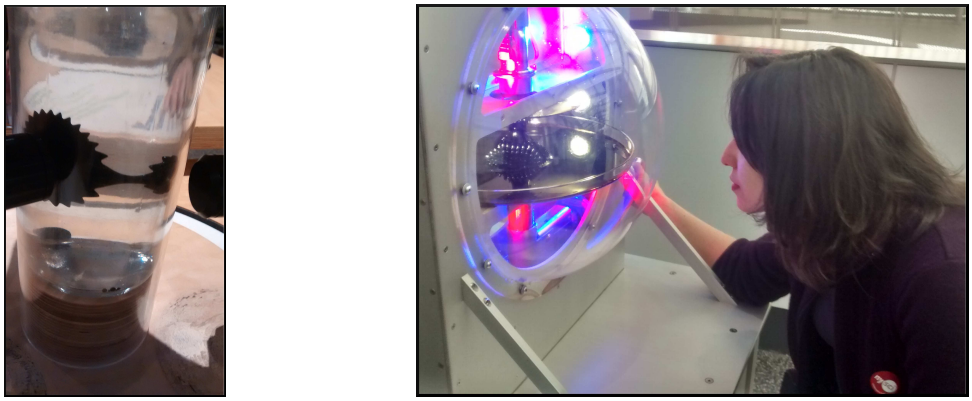

Figure 1.3: (a) A highly concentrated ferrofluid immersed in a water column allows the visitor from the Science Museum of Boston to create spikes and interact the magnetic drops. (b) A ferrofluid pool is subject to two permanent magnets. The New York Hall of Science visitor can approximate or remove the magnets, controlling the formation of spikes in the field lines directions.

At a high dipolar strength and low volume fraction the ferrofluid tends to aggregates in chains. Naturally, these microstructures may be formed only by rather large ferroparticles, intensively interacting magnetically which each other, as seen in figure 1.4. These instabilities show less prominence of viscous and surface tension effects in the ferrofluid. At low concentration the chain formation tends to increase the magnetization and induces a larger initial susceptibility. At high densities, the particle spatial distribution starts to homogenize again, and the significance of the chains goes down. This is due to the fact that in dense ferrofluids the interparticle interaction results in chain disintegration. To sum up, we may conclude that the chain aggregates are most conspicuous in diluted ferrofluids, while dense ferrofluids are characterized by a homogeneous fluid like structure [34].

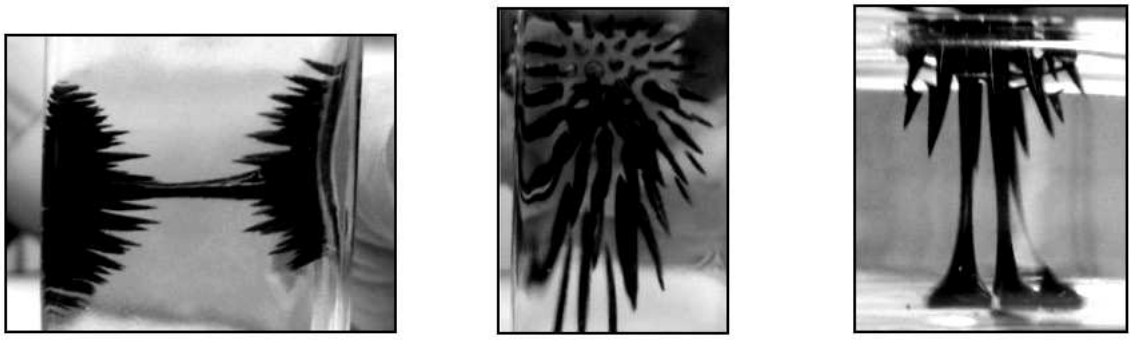

Figure 1.4: Instabilities formed due thee interaction of a ferrofluid (with volume fraction of particles equal to 13 %) with a magnetic field. These instabilities are a result of the balance between magnetic and gravitational forces. The magnetic force was generated by a neodymium magnet. The pictures are related to a video produced by Cunha and Abade [35, 36].

Besides the use in several practical applications, biocompatible ferrofluids are also used in cancer treatment, for example [37]. Magnetic particle hyperthermia improves the precision of heating by embedding the heating source (magnetic particles) into the tumour tissue and heating it using an external alternating magnetic field [38].

Magnetic drug targeting (MDT) is another technique that uses ferrofluids. Indeed, it is an active of drug targeting for the medical treatment of various diseases and cardiovascular episodes, such as stenosis and thrombosis. In MDT, magnetically guided droplets of biocompatible ferrofluid with specific chemotherapeutic agents bonded to nanoparticles are used to carry and release medicinal drugs at target sites in vivo. This enhances the efficacy of the drug while simultaneously minimizing its deleterious side effects.

1.5 Objectives

1.5.1 General Objectives

In the present study we investigate the non-linear oscillatory motion of a bubble immersed in a complex fluid, wherein the magnetic properties are considered. The bubble is subjected to a sinusoidal external acoustic field. Thus, this study aims to determine an extension of the Rayleigh-Plesset equation for a magnetic fluid, based on the work of Cunha [4].

The major contribution to the study concerns a bubble immersed in a colloidal suspension with permanently magnetized particles, suffering the influence of an external pressure field and a magnetic field determined by Rosensweig [39]. Secondarily, this study uses linear dynamic systems analysis approaches such as Fourier Transforms, phase diagrams and Lyapunov exponents. Finally, an experimental bench was developed, allowing observation of the behavior of a bubble rising in different Newtonian and non-Newtonian fluids, including magnetic fluids.

1.5.2 Specific Objectives

- Development of a dimensional analysis of the governing bubble dynamics equation (Rayleigh-Plesset), applying the magnetic stress tensor. We propose then the Magnetic Rayleigh-Plesset equation (MRP);
- Based on typical quantities and the use of known and proposed dimensionless parameters such as the Magnetic Reynolds number, we proposed the non-dimensional version of MRP equation;
- Determination of the asymptotic solution of the governing equation of bubble dynamics in magnetic fluids using the perturbation method for small values of stipulated parameters;
- Elaboration and validation of a computational code based on the fifth order Runge-Kutta scheme with adaptive time step;
- Study of an asymptotic theory for the collapse radius and its use as stop criteria;
- Analysis of vibrational patterns for the bubble immersed in a magnetic fluid through typical dynamical systems analysis approaches, such as Fourier transform, phase diagram and Lyapunov exponents considering variations of dimensionless parameters;
- Creation and trainning of a neural network with the *backpropagation* method in order to identify the determined vibrational patterns;
- Analysis of the collapse diagram, proposed as a function of the non-dimensional patterns in order to understand how they influence the bubble behavior;
- Comparison between the application of three different magnetic fields: static, oscillatory and a combiation of static and oscillatory;

- Chaos identification with Lyapunov exponents and correlation analysis using scatter diagrams;
- Application of the validated dynamical system approaches to the ferrofluid where the bubble is immersed aiming to study the particles magnetization. With that, we aim to identify the particle volume fraction and magnetization with neural networks;
- Comparison between the superparamagnetic model and a magnetization model using Langevin equilibrium magnetization in order to understand how this asymetry changes the magnetic contribution of MRP equation;
- Elaboration of an experimental bench to study a bubble rising in different sintetized ferrofluids;
- Characterization of the sintetized ferrofluids in the rotating disks rhemeter and the tensiometer;
- Analyse of the bubble rising in different fluids under the application of a static magnetic field provided by a neodymium magnet. Analysis of the magnet with two different gaussmeters and an analytical solution;

Chapter 2

Mathematical Formulation

This chapter aims to demonstrate the basic mathematical formulation, expressing the governing equations and modeling the bubble behavior from both Continuity and Cauchy equation. The theoretical foundation permeates the linearization of the system and stability analysis. For the magnetic model, Maxwell's equations are used, considering a superparamagnetic model, coupling magnetism and hydrodynamics.

2.1 Governing Equations

The study of the dynamic oscillatory movement of a bubble presented in this work is based on the analysis of its radial movement when immersed in a ferrofluid subjected to a pressure field excitation and a magnetic field. The mathematical modeling of this movement is based on the combination of apropriate restrictive hypothesis and classical hydrodynamic equations.

The main restrictive assumptions used in this work consist in assuming that the fluid in which the bubble is immersed is incompressible and isotropic, free of nonlinear effects associated with viscoelasticity, for example. The principal governing equations used for the mathematical modeling are based on the mass conservation principle (continuity equation) and Newton's second law of motion (Cauchy equation), besides a constitutive model apropriate to represent the jump of traction in the bubble interface and Maxwell equations.

The next sections describe in details the mathematical modeling of this problem, shown in figure (2.1), which leads to the development of a nonlinear differential equation, called Magnetic Rayleigh-Plesset equation (MRP). The Rayleigh-Plesset equation is a classical equation in this research field. Even though this equation is based on a radial motion model, it allows us to test physical concepts associated with the influence of different nonlinear mechanisms from the interaction between the bubble and the liquid that surrounds it.

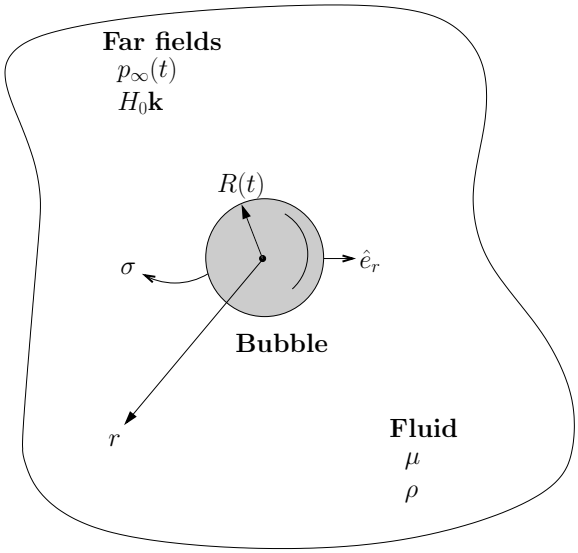

Figure 2.1: Problem schematic of a gas bubble immersed in a magnetic fluid of viscosity μ and density ρ with acoustic and magnetic applied fields.

2.1.1 Continuity Equation

The mass conservation equation is mathematically given by:

$$\frac{\partial \rho}{\partial t} + \nabla \cdot (\rho \boldsymbol{u}) = 0, \tag{2.1}$$

where ρ is the fluid density, t represents time and $\boldsymbol{u}$ is the flow Euleurian velocity field of the flow. However, for an incompressible fluid, we have:

$$\nabla . \boldsymbol{u} = 0. \tag{2.2}$$

The above equation shows that in an incompressible flow, the velocity field is solenoidal. Considering an analogy with electromagnetism, this is the same behavior expected for the magnetic induction field according to Gauss' law of magnetism. Physically, both laws propose that the flux of a certain quantity that crosses a closed surface boundary is zero. In the continuity equation case, the quantity is represented by mass, while in Gauss' law of magnetism we have the magnetic flux density. Considering that all perturbations on the flow are purelly radial, the components in the θ and ϕ direction are null. In that case, the continuity equation can be written in spherical coordinates as:

$$\frac{1}{r}\left[\frac{\partial}{\partial r}(r^2 u_r)\right] = 0 \rightarrow \int \frac{\partial}{\partial r}(r^2 u_r) dr = 0, \tag{2.3}$$

where r represents the physical distance from the spherical bubble center to any point in the surrounding fluid and u_r is the radial component of velocity. Therefore, integrating equation 2.3 over the medium, we have:

$$r^2 u_r(r,t) = F(t) \rightarrow u_r(r,t) = \frac{F(t)}{r^2}. \tag{2.4}$$

In this situation, the bubble radius, $R(t)$, will be perturbed. With that in mind, we idealize that there is no mass transport in the interface. To sum up, the impenetrability kinematic condition of the bubble interface is considered:

$$u_r(R,t) = \frac{dR}{dt}, \tag{2.5}$$

substituting equation 2.5 in 2.4 and considering $r = R(t)$ we have

$$F(t) = R^2 \frac{dR}{dt}. \tag{2.6}$$

If one considers the existence of evaporation in the interface between the bubble and the fluid, the volumetric production rate of vapour would be equal to the bubble growth rate. The rate of evaporation inside the bubble is given by:

$$\dot{m} = \rho_v 4\pi R^2 \frac{dR}{dt}, \tag{2.7}$$

where ρ_v is the saturated vapour density. Applying the mass conservation principle, we note that this rate must be equal to the liquid mass flow into the bubble. Therefore, the ratio between the internal speed of the liquid relative to the interface is given by the ratio between the densities of the vapor and fluid. Figure 2.1 ilustrates that principle.

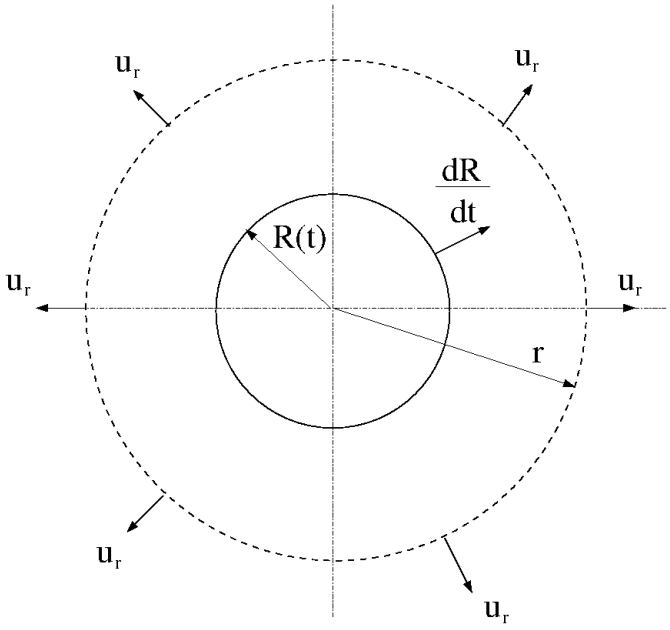

Figure 2.2: Schematic showing a bubble of radius $R(t)$, immersed in a fluid.

In this way, using the continuity equation:

$$\underbrace{4\pi R^2 \frac{dR}{dt}}_{1} - \underbrace{4\pi R^2 \frac{\rho_v}{\rho} \frac{dR}{dt}}_{2} = \underbrace{4\pi r^2 u_r}_{3}, \tag{2.8}$$

where 1 is the volumetric flow into the bubble, 2 the expansional volumetric vapour flow and 3 the mass flow in a control surface far from the bubble. Isolating $u_r(r,t)$ and considering $r = R$:

$$u_r(R,t) = \left(1 - \frac{\rho_v}{\rho}\right) \frac{dR}{dt} \tag{2.9}$$

substituting in 2.6, we have:

$$F(t) = \left(1 - \frac{\rho_v}{\rho}\right) R^2 \frac{dR}{dt}. \tag{2.10}$$

In many pratical applications, the bubbles are immersed in liquids. In that case, $\rho_v << \rho$. Otherwise, $\frac{\rho_v}{\rho} << 1$, such that the term in brackets in equation 2.10 can be approximated to 1. Therefore, equation 2.6 becomes valid for both steam and gas bubbles. In that case, combining equations 2.4 and 2.10, we have:

$$u(r,t) = \frac{R^2}{r^2} \frac{dR}{dt} = \frac{R^2}{r^2} \dot{R}. \tag{2.11}$$

Note that equation 2.11 will be essential in the calculations that follow and physically expresses the mass balance in the bubble-liquid interface.

2.1.2 Cauchy Equation

The balance of linear momentum, which comes from the postulate of Newton's second law applied to the description of the movement of a continuous medium in its differential formulation is known as Cauchy equation. This equation is the result of a balance of the rate change of linear momentum that cross an infinitesimal volume control in a continuum medium, the external forces acting on that same volume and temporal momentum variations and is given by:

$$\rho \left(\frac{\partial \boldsymbol{u}}{\partial t} + \boldsymbol{u} \cdot \nabla \boldsymbol{u} \right) = -\nabla p + \nabla . \boldsymbol{\sigma^N} + \nabla . \boldsymbol{\sigma}, \tag{2.12}$$

where $\boldsymbol{u}$ is the Euleurian velocity field, $\boldsymbol{\sigma^N}$ represents the Newtonian contribution of the stress tensor, $\boldsymbol{\sigma}$ denotes the non-Newtonian effects of the fluid and p is the pressure field.

2.1.2.1 Non-Newtonian Fluid Model

Considering the basic principle of Material Frame Indifference (or, in other words, considering that the description remain unchanged when observed under a variety of conditions), the stress tensor for magnetic fluids is given by:

$$\boldsymbol{\sigma} = \left(-\frac{\mu_0 H^2}{2}\right)\boldsymbol{I} + \boldsymbol{BH}, \tag{2.13}$$

where $\boldsymbol{B}$ represents the induced magnetic field, $\boldsymbol{H}$ the applied magnetic field and μ_0 is the magnetic permeability. For an imcompressible Newtonian fluid, the trace of the stress tensor, excluding the normal stresses since the effects of the pressure field are already incorporated in the radial gradient of pressure, is null. That means that $tr(\boldsymbol{\sigma^N}) = \nabla \cdot \boldsymbol{u} = 0$. This hypothesis must be carefully analysed if a non-Newtonian fluid is considered. In the case of a viscoelastic fluid, it is still valid [40]. On the other hand, considering a magnetic fluid, that hypothesis is not valid.

For the radial motion, the Cauchy equation in spherical coordinates considering only radial motion is given by:

$$\rho\left(\frac{\partial u}{\partial t} + u\frac{\partial u}{\partial r}\right) = -\frac{\partial p}{\partial r} + \frac{1}{r^2}\frac{\partial}{\partial r}(r^2\sigma_{rr}^N) + \frac{1}{r^2}\frac{\partial}{\partial r}\left(r^2\sigma_{rr}\right) - \frac{(\sigma_{\theta\theta^N} + \sigma_{\phi\phi^N})}{r} - \frac{(\sigma_{\theta\theta} + \sigma_{\phi\phi})}{r}. \tag{2.14}$$

Considering that $\sigma_{rr}^N + \sigma_{\phi\phi}^N + \sigma_{\theta\theta}^N = 0$, we may write equation 2.14 using $\sigma_{rr}^N = -\sigma_{\theta\theta}^N - \sigma_{\phi\phi}^N$:

$$\rho\left(\frac{\partial u}{\partial t} + u\frac{\partial u}{\partial r}\right) = -\frac{\partial p}{\partial r} + \left[\frac{\partial \sigma_{rr}^N}{\partial r} + \frac{3\sigma_{rr}^N}{r}\right] + \frac{\partial \sigma_{rr}}{\partial r} + \frac{2\sigma_{rr}}{r} - \frac{\sigma_{\theta\theta}}{r} - \frac{\sigma_{\phi\phi}}{r}. \tag{2.15}$$

On the next steps, only radial and tangential effects regarding θ will be considered. We may write the strain rate tensor, $\boldsymbol{D}$, or the deviatoric part of the incompressible Newtonian fluid ($\boldsymbol{\sigma^N} = 2\mu\boldsymbol{D}$) in radial components as:

$$\boldsymbol{D} = \left(\frac{\partial u_r}{\partial r}\right)\hat{e}_r\hat{e}_r. \tag{2.16}$$

Therefore, the terms associated with the Newtonian contribution of the stress tensor in the radial direction result in:

$$\frac{\partial \sigma_{rr}^N}{\partial r} + \frac{3\sigma_{rr}^N}{r} = 2\mu\left(\frac{\partial^2 u_r}{\partial r^2} + \frac{3}{r}\frac{\partial u_r}{\partial r}\right) = 0. \tag{2.17}$$

The velocity $u(R)$ is given by equation 2.11, which represents the continuity equation for the radial motion. Thus, some terms of equation 2.17 are canceled resulting in

$$\frac{\partial^2 u}{\partial r^2} = \frac{\partial}{\partial r}\left(-\frac{2R^2\dot{R}}{r^3}\right) = \frac{6R^2\dot{R}}{r^4}, \tag{2.18}$$

$$\frac{3}{r}\frac{\partial u}{\partial r} = \frac{3}{r}\frac{\partial}{\partial r}\left(-\frac{2R^2\dot{R}}{r^3}\right) = \frac{6R^2\dot{R}}{r^4}, \tag{2.19}$$

substituting equation 2.17 in 2.15 results:

$$\rho\left(\frac{\partial u_r}{\partial t}+u_r\frac{\partial u_r}{\partial r}\right)=\frac{-\partial p}{\partial r}+\frac{\partial \sigma_{rr}}{\partial r}+\frac{3\sigma_{rr}}{r}. \tag{2.20}$$

The inertial terms on the left side of equations refering to the velocity are

$$\frac{\partial u_r}{\partial t}=\frac{2R\dot{R}^2+R^2\ddot{R}}{r^2}, \tag{2.21}$$

and

$$u_r\frac{\partial u_r}{\partial r}=-\frac{2\dot{R}^2R^4}{r^5}, \tag{2.22}$$

substituting 2.21 and 2.22 in 2.20 and integration the resulting equation in the flow domain, i.e. the region between the bubble surface and infinite, $R\leq r<\infty$ we have:

$$\int_R^\infty\frac{2\dot{R}^2R+R^2\ddot{R}}{r^2}dr-\int_R^\infty\frac{2\dot{R}^2R^4}{r^5}dr=-\frac{1}{\rho}\int_R^\infty\frac{\partial p}{\partial r}dr+\frac{1}{\rho}\int_R^\infty\frac{\partial \sigma_{rr}}{\partial_r}dr+\frac{2}{\rho}\int_R^\infty\frac{\sigma_{rr}}{r}dr-\frac{1}{\rho}\int_R^\infty\frac{\sigma_{\theta\theta}}{r}dr. \tag{2.23}$$

After the integration, we obtain an equation relating p_∞, which denotes the ambient pressure field, and the liquid pressure avaliated at the buble's interface (i.e. in $r=R$).

$$\frac{2\dot{R}^2R+R^2\ddot{R}}{R}-\frac{2\dot{R}^2R^4}{4R^4}=\frac{p_l(R)-p_\infty}{\rho}-\frac{1}{\rho}\sigma_{rr}|_{r=R}+\frac{2}{\rho}\int_R^\infty\frac{\sigma_{rr}}{r}dr-\frac{1}{\rho}\int_R^\infty\frac{\sigma_{\theta\theta}}{r}dr. \tag{2.24}$$

Note that the integral term is null in the Newtonian regime. We may observe new terms related to the fluid anisotropy. In this condition, there is an extra contibuition of the σ_{rr} effect, given by the integral parcel in equation . In this case, that term sums to $-\frac{1}{\rho}\sigma_{rr}$. This is associated to the non-linearity of the fluid. Every non-Newtonian fluid has a non-linear contribution in the constitutive equation, such as elasticity [40] or the existence of magnetic tensions. A Lagrangian description of the bubble surface motion and the use of more sophisticated numerical algorithms is appropriate in these cases [41, 42, 40].

2.1.2.2 Ferrofluid Modelling

The Gauss' law of magnetism states that the magnetic induction flow passing through a closed surface is zero. The magnetic induction lines that pass through a Gaussian surface are closed, resulting in the absence of lines created or terminated within that surface:

$$\nabla.\boldsymbol{B}=0, \tag{2.25}$$

where $\boldsymbol{B}$ is a vector field defined by the sum of $\boldsymbol{H}$ and magnetization $\boldsymbol{M}$ multiplied by the free space permeability given by $\mu_0=4\pi\times10^{-7}H.m^{-1}$:

$$\boldsymbol{B} = \mu_0(\boldsymbol{H} + \boldsymbol{M}). \tag{2.26}$$

Considering that the fluid is composed of superparamagnetic nanoparticles, it is possible to state that $\boldsymbol{M} = \chi\boldsymbol{H}$, where χ is the magnetic susceptibility and:

$$\boldsymbol{B} = \mu_0(1 + \chi)\boldsymbol{H}. \tag{2.27}$$

Futhermore, Ampère-Maxwell's law stablishes that a magnetic field can be generated by an electric current or by the temporal variation of an applied electric field. In other words:

$$\nabla \times \boldsymbol{H} = \boldsymbol{J}\epsilon_0\frac{\partial \boldsymbol{E}}{\partial t}, \tag{2.28}$$

where $\boldsymbol{J}$ represents the current density measure in A/m^2, ϵ_0 is the permittivity of free space given by $8.8541878 \times 10^{-12}C^2/N.m^2$ and $\boldsymbol{E}$ is the electric field.

Considering the magnetostatic regime, the magnetic effects related to the electrical charges movement are neglected and so do the involved electric fields. In this case, we may consider

$$\frac{\partial \boldsymbol{E}}{\partial t} = 0, \tag{2.29}$$

Thus, using the conditions expressed in 2.29, the Maxwell equations can be reduced to:

$$\nabla.\boldsymbol{B} = 0; \tag{2.30}$$

$$\frac{\partial \boldsymbol{B}}{\partial t} = 0; \tag{2.31}$$

$$\nabla \times \boldsymbol{H} = 0; \tag{2.32}$$

For a magnetic fluid, that approach would be valid if the particles are surrounded of insulating material. In this case, there would be no electric current being conducted.

Furthermore, the components of the magnetic stress tensor are given by:

$$\sigma_{rr}^{mag} = \frac{-\mu_0}{2}(H_r^2 + H_\theta^2) + \mu(1 + \chi)H_r^2 \tag{2.33}$$

$$\sigma_{\theta\theta}^{mag} = \frac{-\mu_0}{2}(H_r^2 + H_\theta^2) + \mu(1 + \chi)H_{\theta\theta}^2 \tag{2.34}$$

2.1.2.3 Applied Field ($\boldsymbol{H}$) Determination

At this point, it is essential to determine the field $\boldsymbol{H}$. In spherical coordinates considering symmetry of axes, Laplace's equation for the magnetic potential has the form below:

$$\frac{\partial}{\partial r}\left(r^2\frac{\partial \Psi}{\partial r}\right) + \frac{1}{sen\theta}\frac{\partial}{\partial \theta}\left(\frac{\partial \Psi}{\partial \theta}\right) = 0, \tag{2.35}$$

where r is the radial distance from the origin, θ is the polar angle and Ψ is the associated potential.

A plausible solution attempt would be:

$$\Psi(r,\theta) = R(r)\Psi(\theta), \tag{2.36}$$

leading to solutions in terms of Legendre polynomials. Indeed, it was determined by Rosensweig [39] as:

$$\Psi = \begin{cases} Ar\cos\theta, \text{ para r} < \text{R} \\ -(C - \frac{2D}{r^3})\cos\theta, \text{ para r} > \text{R}, \end{cases} \tag{2.37}$$

where R is the sphere radius. The associated magnetic field is then expressed by:

$$\boldsymbol{H} = -\boldsymbol{\nabla}\Psi = -\frac{\partial \Psi}{\partial r}\hat{e}_r - \frac{1}{r}\frac{\partial \Psi}{\partial \theta}\hat{e}_\theta, \tag{2.38}$$

leading to:

$$\boldsymbol{H} = \begin{cases} -A(\cos\theta\hat{e}_r - \sin\theta\hat{e}_\theta), \text{ para r} < \text{R} \\ -(C - \frac{2D}{r^3})\cos\theta\hat{e}_r + (C + \frac{D}{r^3})\sin\theta\hat{e}_\theta, \text{ para r} > \text{R}. \end{cases} \tag{2.39}$$

The magnetic field far from the sphere should approximate the uniform applied field $H_0\boldsymbol{k}$, in which $\boldsymbol{k}$ is the unitary vector in z direction. In spherical coordinates, $\boldsymbol{k} = \hat{e}_r\cos\theta - \hat{e}_\theta\sin\theta$, so for $r \longrightarrow \infty$, we have:

$$C = -H_0. \tag{2.40}$$

Likewise, the form of the solution for $r < R$ presents $\boldsymbol{H} = A\boldsymbol{k}$. Since the tangential component of $\boldsymbol{H}$ and the normal component of $\boldsymbol{B}$ are both continuous between the sphere interface, two more relations for the constats can be obtained:

$$A = \frac{-3\mu_1 H_0}{\mu_r + 2\mu_1}, \tag{2.41}$$

$$D = \frac{\mu_2 - \mu_1}{\mu_2 + 2\mu_1}R^3 H_0, \tag{2.42}$$

where μ_1 is the permeability of the medium around the sphere and μ_2 is the permeability of the sphere. Considering that field $\boldsymbol{H}$, it is possible to demonstrate (see **Appendix I**) that the Raylegh-Plesset equation becomes:

$$\frac{2\dot{R}R + R^2\ddot{R}}{R} - \frac{2\dot{R}^2R^4}{4R^4} = \frac{p_l(R) - p_\infty}{\rho} - \frac{1}{\rho}\left[\mu_0\left(\frac{-3\mu_r^2H_0^2}{8}\right)\right] + \frac{1}{\rho}\mu_0)\chi\left[\frac{-\mu_r H_0^2}{3} - \frac{17\mu_r H_0^2}{12} + \frac{H_0^2}{2}\ln(R_\infty) - \frac{H_0^2}{2}\ln(R)\right]. \tag{2.43}$$

where μ_r represents $(\mu_2 - \mu_1)/(\mu_2 + 2\mu_1)$ and R_∞ is the distance from the bubble interface to a point where $\boldsymbol{H} = 0,99H_0$.

2.1.3 Interface Condition

The conservation equations introduced above can be applied within each phase and up to an interface. However, they are not valid across the interface, where sharp changes in several properties occur. That is the case of pressure. Any change in the bubble surface tension will create, for example, tangential forces also known as Marangoni forces [43]. These variations may occur by several factors such as temperature gradients or the addition of sulfactants in the fluid.

In other cases, the weight of the surface itself, as in the case of soap bubbles, is one of the reasons why the surface tension does not remain constant. While pressure jumps can sustain normal stress jumps across a fluid interface, they do not contribute to the tangential stress jump. Consequently, tangential surface stresses can only be balanced by viscous stresses associated with fluid motion. The influence of surfactants, for example, is greater on small bubbles. Knowing that the Marangoni effect is more pronounced in this cases, there will be no consideration of concentration or temperature gradients on the bubble surface in this work.

Considering a clean interface, there is a continuity in both velocity and tangential stresses:

$$(\sigma_{tt})_l = (\sigma_{tt})_b, \tag{2.44}$$

$$(u)_l = (u)_b, \tag{2.45}$$

where $(\sigma_{tt})_l$ represents the tangential component of stresses on the fluid side, while $(\sigma_{tt})_b$ represents the same component on the gas side. Likewise, $(u)_l$ and $(u)_b$ are both the radial components of velocity in the liquid and gas sides respectively.

In figure 2.3, we may observe that interface. Indeed, σ_s is the surface tension coefficient, in such a way that its tangent vector is given by $\sigma_{tt} = \boldsymbol{t} \cdot \boldsymbol{\Sigma} \cdot \boldsymbol{t}$. On the other hand there is a discontinuity in the interface regarding normal tractions. This discontinuity can be modelled based on the informations of both fluids surrounding the interface. Considering that the bubble is immersed in a fluid 1 and filled with a fluid 2. In this case, the balance of forces in the bubbles interface is given by:

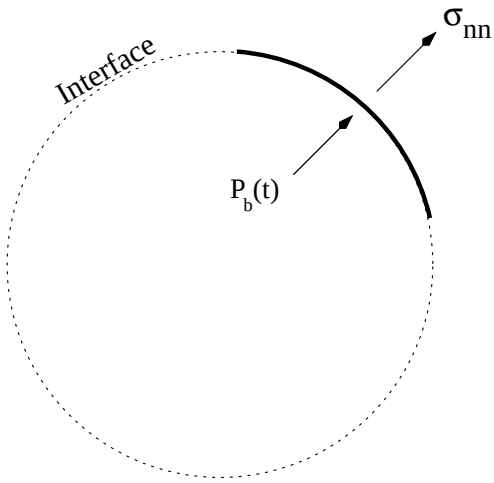

Figure 2.3: Bubble spherical interface to be analyzed.

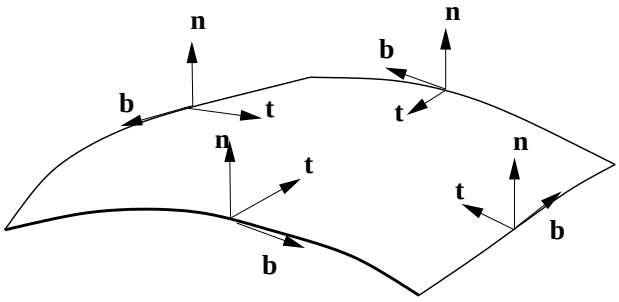

Figure 2.4: Interface condition showing the three main unitary vectors $\hat{t}$, $\hat{n}$ and $\hat{b}$.

$$\int_D \left[\boldsymbol{f^1}(\hat{\boldsymbol{n}}) - \boldsymbol{f^2}(\hat{\boldsymbol{n}})\right] dS + \boldsymbol{F_n} = \boldsymbol{0}, \tag{2.46}$$

where $\boldsymbol{F_n}$ is related with the forces acting on the interface (such as Marangoni forces, for example) and $\boldsymbol{f^1}(\hat{\boldsymbol{n}})$ and $\boldsymbol{f^2}(\hat{\boldsymbol{n}})$ are related with the tensors projected in the normal direction (traction) of both fluids 1 and 2. The forces on the interface can be written as:

$$\boldsymbol{F_n} = \int_C \sigma \boldsymbol{b} dl, \tag{2.47}$$

where σ is the surface tension, a force per length in a direction tangent to the surface and $\boldsymbol{b} = \hat{t} \times \hat{n}$, as seen in figure 2.4.

Using equation 2.47 in equation 2.46 we have:

$$\int_D [\boldsymbol{f^1}(\hat{\boldsymbol{n}}) - \boldsymbol{f^2}(\hat{\boldsymbol{n}})] dS + \int_C \sigma \boldsymbol{b} dl = \boldsymbol{0}, \tag{2.48}$$

or, in other words,

$$\int_D [\boldsymbol{\sigma^1} - \boldsymbol{\sigma^2}] \cdot \hat{n} dS + \int_C \sigma \boldsymbol{b} dl = \boldsymbol{0}. \tag{2.49}$$

Substituting $\boldsymbol{b}$ by $\hat{t} \times \hat{n}$ and $[\boldsymbol{\sigma^1} - \boldsymbol{\sigma^2}] \cdot \hat{n}$ as $\boldsymbol{\Delta f}$ and using the Stokes Theorem, we obtained:

$$\int_D \boldsymbol{\Delta f} dS = \int_D [\hat{n}\nabla \cdot (\sigma \hat{n}) - \nabla(\sigma \hat{n}) \cdot \hat{n}] dS. \tag{2.50}$$

After some algebric manipulation:

$$\boldsymbol{\Delta f} = (\sigma \nabla^s \cdot \hat{n})\hat{n} - (\boldsymbol{I} - \hat{n}\hat{n}) \cdot \nabla\sigma. \tag{2.51}$$

Writing $(\boldsymbol{I} - \hat{n}\hat{n}) \cdot \nabla = \nabla^s$, as the superficial gradient we have:

$$\boldsymbol{\Delta f} = (\sigma \nabla^s \cdot \hat{n})\hat{n} - \nabla^s\sigma. \tag{2.52}$$

Knowing that $\nabla^s \cdot \hat{n}$ is the curvature of the interface (or twice the mean curvature), we may rewrite equation 2.52 as:

$$\boldsymbol{\Delta f} = 2\sigma < \kappa > \hat{n} - \nabla^s\sigma. \tag{2.53}$$

When the Marangoni number tends to zero, which is our case of study, the forces are given only by the normal stresses. Considering the associated time scales, that the flow time scale dominates the surfactant time. This non-dimensional number is given by:

$$Ma = \frac{t_{surfactant}}{t_{flow}} = \frac{(\mu a)/(\beta \Delta C^*)}{(1/\dot{\gamma})} = \frac{\mu a \dot{\gamma}}{\beta \Delta C^*}, \tag{2.54}$$

where σ is the surface tension, L is a characteristic lenght, ΔC^* is the surfactant concentration difference, $\beta = (\partial\sigma/\partial C)$, η is the dynamic viscosity, α is the thermal diffusivity, a is a typical length and $\cdot\gamma$ is a shear rate. In this case:

$$(-p_1\boldsymbol{I} + p_2\boldsymbol{I}) \cdot \hat{n} = 2\sigma < \kappa > \hat{n}, \tag{2.55}$$

where κ is the surface curvature and the viscous effects were disconsidered due to the radial nature of the problem. This is know as Young [44] and Laplace [45] law. In the case of the bubble, we may rewrite this law as [46]:

$$\sigma_{nn} = (\boldsymbol{n} \cdot \boldsymbol{\Sigma} \cdot \boldsymbol{n})_l - (\boldsymbol{n} \cdot \boldsymbol{\Sigma} \cdot \boldsymbol{n})_b = \sigma_s \nabla^s \cdot \boldsymbol{n}, \tag{2.56}$$

where the term l determines the side of the liquid and b represents the the normal stresses on the gas/vapour side of the bubble.

- **Determining the Pressure Inside the Bubble**

Returning to equation 2.56, we may write:

$$\nabla^s \cdot \hat{n} = 2\kappa \rightarrow \kappa = \frac{1}{2}\left(\frac{1}{R_1} + \frac{1}{R_2}\right), \tag{2.57}$$

where R_1 and R_2 are the semi-axis along x and y retrospectively. Since the bubble is spherical, $R_1 = R_2$, then $\kappa = 1/R$. Thus, the interior of the bubble is defined as:

$$(\boldsymbol{n} \cdot \boldsymbol{\Sigma} \cdot \boldsymbol{n})_b = -p_b(t) = -[p_v(T_b) + p_g(t)], \tag{2.58}$$

where $p_v(T_b)$ the vapour pressure of the liquid inside the bubble at temperature T_b. This temperature does not vary in our context. Thus, $p_g(t)$ is the pressure of the gas assumed as perfect and subjected to the polytropic process: $p_g V^n = constant$.

The gas volume is given by $V = (\frac{4}{3})\pi R^3$. Using an equilibrium pressure that corresponds to the bubble condition when its radius is R_E (an equilibrium radius), we have assumed by the polytropic law:

$$p_g(t)\left(\frac{4}{3}\pi R^3\right)^n = \tilde{p_g}(t)\left(\frac{4}{3}\pi R_E^3\right)^n. \tag{2.59}$$

After some manipulation

$$p_g(t) = \tilde{p_g}(t)\left(\frac{R_E}{R}\right)^{3n}. \tag{2.60}$$

Now, substituting equation 2.60 in 2.58, the internal pressure results in

$$p_b(t) = p_v + \tilde{p_g}\left(\frac{R_E}{R}\right)^{3n}. \tag{2.61}$$

Assuming that in the initial instant of study $t = 0$ and the bubble radius is R_E the pressure discontinuity in the interface assumes the form given bellow, based on the Young-Laplace condition:

$$\tilde{p}_{b(t)} = \tilde{p}_\infty + \frac{2\tilde{\sigma}}{R_E}. \tag{2.62}$$

considering that:

$$\tilde{p_b}(t) = \tilde{p_g} + p_v \tag{2.63}$$

In this case, $\tilde{p}_\infty$ denotes the static pressure of equilibrium applied by the fluid in the initial time and $\tilde{p_b}$ represents the internal pressure of equilibrium. For $t = 0$, there is no deviatoric part of the stress tensor, since the viscous effect can be neglected. We can now use equation 2.58 for the internal pressure of equilibrium. In this case, substituting equation 2.62 in 2.63 one reaches:

$$\tilde{p_g} = (\tilde{p_\infty} - p_v) + \frac{2\tilde{\sigma}}{R_E}. \tag{2.64}$$

Thus, returning the term $\tilde{p}_g$ to its original form, we obtain:

$$p_b = p_v + \left[(\tilde{p}_\infty - p_v) + \left(\frac{2\tilde{\sigma}}{R_E}\right)\left(\frac{R_E}{R}\right)\right]^{3n}. \tag{2.65}$$

Defining $\tilde{p}_\infty - p_v$ as $\Delta\tilde{p}$, we have the contribution of normal traction in the interface on the gas side as:

$$\Sigma_{rr,l} + p_v + \left(\Delta\tilde{p} + \frac{2\tilde{\sigma}}{R_E}\right)\left(\frac{R_E}{R}\right)^{3n} = \frac{2\tilde{\sigma}}{R}. \tag{2.66}$$

- **Determining the Pressure in the Liquid**

For the liquid side, the component of normal stresses becomes:

$$\sigma_{nn} = (\boldsymbol{n}\cdot\boldsymbol{\Sigma}\cdot\boldsymbol{n})_l = -\boldsymbol{n}.p_l(R,t)\boldsymbol{I}\cdot\boldsymbol{n} + \boldsymbol{n}\cdot[2\mu\boldsymbol{D} + 2\boldsymbol{\Sigma}^f]\cdot\boldsymbol{n}, \tag{2.67}$$

where $\boldsymbol{\Sigma}^f$ represents the tensorial contribution of the effective stress tensor of the liquids due to non-Newtonian effects.

In this case, we must identify the stress component on the liquid side $\Sigma_{rr,l}$. According to the liquid stress tensor, different traction conditions are obtained. Said that, the discontinuity analysis assumes the form:

$$\boldsymbol{\Sigma} = -p\boldsymbol{I} + \boldsymbol{\sigma}^N + \boldsymbol{\sigma}, \tag{2.68}$$

with

$$\Sigma_{rr,l} = -\hat{e}_r\cdot p_l\boldsymbol{I}\cdot\hat{e}_r + \hat{e}_r\cdot\boldsymbol{\sigma}^N\cdot\hat{e}_r + \hat{e}_r\cdot\boldsymbol{\sigma}\cdot\hat{e}_r. \tag{2.69}$$

Equation 2.68 is the stress tensor that describes the liquid behavior. In the same way, when $\boldsymbol{\sigma}^N$ is known, we may rewrite the discontinuity as:

$$\Sigma_{rr,l} = -p_l + 2\mu\boldsymbol{D}_{rr}|_{r=R} + \sigma_{rr}|_{r=R}. \tag{2.70}$$

This discontinuity is given in $r = R$. In this case, $u_r = R^2\dot{R}/r^2$. At the same way, substituting the stress tensor in the radial direction, we have:

$$\Sigma_{rr,l} = -p_l + 4\mu\frac{\dot{R}}{R} + \sigma_{rr}|_{r=R}. \tag{2.71}$$

Finally, using equation 2.70 in 2.66 it is possible to determine the boundary condition where:

$$-p_l - 4\mu\frac{\dot{R}}{R} + \sigma_{rr}|_{r=R} + p_v + \left(\Delta\tilde{p} + \frac{1\tilde{\sigma}}{R_E}\right)\left(\frac{R_E}{R}\right)^{3n} = \frac{2\tilde{\sigma}}{R}. \tag{2.72}$$

Rewriting p_l as function of the internal pressure (p_b), the equation is simplified. It is possible to verify that this external pressure is written as a function of the non-Newtonian effects, the superficial tensor and the internal pressure of the bubble.

$$p_l = 4\mu\frac{\dot{R}}{R} - \frac{2\tilde{\sigma}}{R} + p_b + \sigma_{rr}|_{r=R}. \tag{2.73}$$

2.1.3.1 Interface Condition for a Ferrofluid

The jump of traction in the bubble's interface given by Young-Laplace condition (equation 2.56) maintains itself if the liquid is a magnetic fluid. However, the avaliation of the stress tensor is modified due the extra magnetic pressure. In this section, we intend to understand how the interface condition is modified if the bubble is immersed in a magnetic fluid.

In $t = 0$, we may consider or not the presence of an external applied magnetic field. If $\boldsymbol{H} \neq 0$, equation 2.62 becomes:

$$\tilde{p_b}(t) = \tilde{p}_\infty + \frac{2\tilde{\sigma}}{R_E} - \sigma_{rr}^{mag}|_{r=R}. \tag{2.74}$$

Thus, considering yet that the equilibrum pressure inside the bubble is

$$\tilde{p_b}(t) = \tilde{p_g} + p_v, \tag{2.75}$$

and substituting equation 2.74 in 2.75 we obtain a new version of 2.64, given by:

$$\tilde{p_g} = (\tilde{p}_\infty - p_v) + \frac{2\tilde{\sigma}}{R_E} - \sigma_{rr}^{mag}|_{r=R}. \tag{2.76}$$

Rewriting $\tilde{p_g}$ in its original format, we have:

$$p_b = p_v + \left[(\tilde{p}_\infty - p_v) + \left(\frac{2\tilde{\sigma}}{R_E} - \sigma_{rr}^{mag}|_{r=R}\right)\left(\frac{R_E}{R}\right)\right]^{3n}. \tag{2.77}$$

Since $(\tilde{p}_\infty - \tilde{p}_v) = \Delta\tilde{p}$ and $\sigma_{rr}|_b = -p_b$ then:

$$\sigma_{rr}|_b = -p_v - \left(\Delta\tilde{p} + \frac{2\tilde{\sigma}}{R_E} - \sigma_{rr}^{mag}|_{r=R}\right)\left(\frac{R_E}{R}\right)^{3n}. \tag{2.78}$$

In the same way, it is possible to determine the traction on the liquid side:

$$\sigma_{rr}|_l + p_v + \left(\Delta\tilde{p} + \frac{2\tilde{\sigma}}{R_E} - \sigma_{rr}^{mag}|_{r=R}\right)\left(\frac{R_E}{R}\right)^{3n} = \frac{2\tilde{\sigma}}{R}. \tag{2.79}$$

Substituting equation 2.79 in 2.71 we obtain:

$$-p_l - 4\mu\frac{\dot{R}}{R} + \sigma_{rr}^{mag}|_{r=R}\left[1 - \left(\frac{R_E}{R}\right)^{3n}\right] + p_v + \left(\Delta\tilde{p} + \frac{2\tilde{\sigma}}{R_E}\right)\left(\frac{R_E}{R}\right)^{3n} = \frac{2\tilde{\sigma}}{R}. \tag{2.80}$$

2.1.4 Generalized Governing Equation

Considering the above development, we may write the Magnetic version of Rayleigh-Plesset equation as:

$$\ddot{R}R + \frac{3}{2}\dot{R}^2 = -4\frac{\mu}{\rho}\frac{\dot{R}}{R} - \frac{2\tilde{\sigma}}{\rho R} + \frac{p_b - p_\infty}{\rho} + \frac{2}{\rho}\int_R^\infty \frac{\sigma_{rr}}{r}dr - \frac{1}{\rho}\int_R^\infty \frac{\sigma_{\theta\theta}}{r}dr + \frac{1}{\rho}\int_R^\infty \frac{\partial\sigma_{rr}}{\partial r}dr, \tag{2.81}$$

which represents the generalized governing equation for a unidimensional radial flow. Any extra pressure can be considered as an external field [47]. In this case, an harmonic pressure forcing expressed by:

$$p_\infty(t) = \tilde{p}_\infty[1 + \varepsilon\sin(\omega t)], \tag{2.82}$$

was used. In this case, ε represents the amplitude of pressure and ω defontes the frequency of excitation. We may observe that in this case, there is a magnetic pressure condition expressed by the magnetic stress tensor valued in the bubble interface. Moreover, the non-Newtonian intergral is considered for both components r and θ. Using the jump condition obtained, we have:

$$\begin{aligned}\ddot{R}R + \frac{3}{2}\dot{R}^2 = -\frac{\Delta\tilde{p}}{\rho} + \frac{1}{\rho}\left(\Delta\tilde{p} + \frac{2\tilde{\sigma}}{R_E} - \sigma_{rr}^{mag}|_{r=R}\right)\left(\frac{R_E}{R}\right)^{3n} \\ -\frac{4\mu}{\rho}\frac{\dot{R}}{R} - \frac{p_\infty}{\rho}\epsilon\sin(\omega t) - \frac{2\tilde{\sigma}}{\rho R} + \frac{2}{\rho}\int_R^\infty \frac{\sigma_{rr}}{r}dr - \frac{1}{\rho}\int_R^\infty \frac{\sigma_{\theta\theta}}{r}dr + \frac{1}{\rho}\int_R^\infty \frac{\partial\sigma_{rr}}{\partial r}dr.\end{aligned} \tag{2.83}$$

2.1.5 Dimensionless Version of the Governing Equation

In order to write the governing equation in a non-dimensional form, a scale analysis is needed. In this case, all dimensionless variables are written with an asterisks. Considering the typical scales of radius and time given by:

$$R^* = \frac{R}{R_E}, \qquad\qquad t^* = \frac{t}{t_c}, \tag{2.84}$$

where the typical scale of velocity is written $U_c = (|\Delta\tilde{p}|/\rho)^{1/2}$ and $t_c = R_E/U_c$. Thereby, velocity and acceleration in the bubble surface assume the following form:

$$\dot{R}^* = \frac{\dot{R}}{U_c}, \qquad\qquad \ddot{R}^* = \ddot{R}\frac{R_E}{U_c^2}. \tag{2.85}$$

The parameter ε must also be defined in non-dimensional terms:

$$\varepsilon^* = \varepsilon \left(\frac{\tilde{p}_\infty}{\Delta \tilde{p}} \right). \tag{2.86}$$

On the other hand, the non-dimensional form of the traction σ_{rr} might be written as:

$$\sigma^*_{rr} = \frac{\sigma_{rr}}{\rho U_c^2}. \tag{2.87}$$

Considering the new notation for the non-dimensional variables and using the typical scales, the governing equation assumes the form:

$$U_c^2 R^* \ddot{R}^* + \frac{3}{2} U_c^2 (\dot{R}^*)^2 = -U_c^2 + \frac{1}{\rho} \frac{2\tilde{\sigma}}{R_E} \left[\left(\frac{R_E}{R_E R^*} \right)^{3n} - \frac{1}{R^*} \right] \frac{U_c^2}{U_c^2} + \left(\frac{R_E}{R_E R^*} \right)^{3n} U_c^2 - U_c^2 \varepsilon(\omega^* t^*) - \frac{4\mu}{\rho} \frac{U_c^*}{R_E} \frac{U_c}{U_c} \frac{\dot{R}^*}{R^*} + 2U_c^2 \int_R^\infty \frac{\sigma^*_{rr}}{r} dr - U_c^2 \int_R^\infty \frac{\sigma^*_{\theta\theta}}{r} dr + U_c^2 \sigma^*_{rr}, \tag{2.88}$$

where the frequency can be written as $\omega^* = \omega t_c$. Dividing equation 2.88 for U_c^2 and using simple algebric manupulation one reaches:

$$R^* \ddot{R}^* + \frac{3}{2} (\dot{R}^*)^2 = -1 + \frac{1}{\rho} \frac{2\tilde{\sigma}}{R_E U_c^2} \left[\left(\frac{1}{R^*} \right)^{3n} - \frac{1}{R^*} \right] + \left(\frac{1}{R^*} \right)^{3n} - \varepsilon(\omega^* t^*) - \frac{4\mu}{\rho} \frac{1}{R_E U_c} \frac{U_c}{U_c} \frac{\dot{R}^*}{R^*}. + 2 \int_R^\infty \frac{\sigma^*_{rr}}{r} dr - \int_R^\infty \frac{\sigma^*_{\theta\theta}}{r} dr + \sigma^*_{rr}. \tag{2.89}$$

In equation 2.89 it is possible to identify both Reynolds and Weber numbers, defined as:

$$Re = \frac{\rho U_c R_E}{\mu}, \tag{2.90}$$

and

$$We = \frac{\rho U_c^2 R_E}{\sigma_s}. \tag{2.91}$$

The Reynolds number relates both inertial and viscous forces of the flow. The fundamental meaning of the Reynolds number is the same that allow us to carachterize the type of flow as turbulent or laminar, for example. Besides, it may also indicate bifurcation and instability levels of a flow during its transient until it reaches a turbulent regime.

The Weber number denotes a ratio between inertial forces and surface tension. The higher the Weber number, the lower the resistance of the surface tension regarding the bubble oscillations.

Considering these parameters, we may rewrite equation 2.89 as:

$$R^*\ddot{R}^* + \frac{3}{2}(\dot{R}^*)^2 = \frac{2}{We}\left[\frac{1}{(R^*)^{3n}} - \frac{1}{R^*}\right] - 1 - \varepsilon^* sen(\omega^* t^*) + \frac{1}{(R^*)^{3n}} - \frac{4}{Re}\frac{\dot{R}^*}{R^*} + 2\int_R^\infty \frac{\sigma_{rr}^*}{r}dr - \int_R^\infty \frac{\sigma_{\theta\theta}^*}{r}dr + \sigma_{rr}^*. \quad (2.92)$$

To sum up, it is emphasized that the vapor pressure inside the bubble is also written in a dimensionless form, such that:

$$p_b^* = p_v^* + \left(1 + \frac{2}{We}\right)\left(\frac{1}{R*}\right)^{3n} \rightarrow p_g^* = \left(1 + \frac{2}{We}\right)\left(\frac{1}{R^*}\right)^{3n}. \quad (2.93)$$

2.1.5.1 Non-Dimensional Formulation of the Magnetic Component

In order to write the magnetic component in a dimensionless form, the same variables are used:

$$R^* = \frac{R}{R_E}, \quad (2.94)$$

$$t^* = \frac{t}{t_c}, \quad (2.95)$$

where the velocity scales are given by $U_c = (|\Delta\tilde{p}|/\rho)^{1/2}$ and $t_c = R_E/U_c$, respectively. Using those variables, the Magnetic Version of Rayleigh-Plesset equation (Eq. 2.83) may be written in a dimensionless form as:

$$U_c^2 R_E \ddot{R}^* R^* + \frac{3}{2}U_c^2\dot{R}^{2*} = \frac{-4\mu}{\rho}\frac{U_c}{R_E}\frac{\dot{R}^*}{R^*} - \frac{2\tilde{\sigma}}{\rho R_E R^*} + \\ + U_c^2\left(U_c^2 + \frac{2\tilde{\sigma}}{\rho R_E} - \frac{\sigma_{rr}^{mag}\rho U_c^2}{\rho}\right)\left(\frac{R_E}{R^* R_E}\right)^{3n} - U_c^2\epsilon^*\sin(\omega^* t^*) + \sigma_{rr}^* U_c^2 + \\ U_c^2\int\frac{2\sigma_{rr}^*}{r}dr - \int\frac{2\sigma_{\theta\theta}^*}{r}dr - U_c^2\sigma_{rr}^{mag}|_{r=R}\left(\frac{R_E}{R_E R^*}\right)^{3n}, \quad (2.96)$$

where σ_{rr}^{mag} represents the magnetic stress tensor obtained in the jump of traction study. Thus, σ_{rr} represents the non-Newtonian stress tensor. Reorganizing all terms and writing the equation as a function of U_c, we have:

$$U_c^2 R_E \ddot{R}^* R^* + \frac{3}{2}U_c^2\dot{R}^{2*} = \frac{1}{\rho}\frac{2\tilde{\sigma}}{R_E}\left[-\frac{1}{R^*} + \left(\frac{1}{R^*}\right)^{3n}\right]\frac{U_c^2}{U_c^2} + \left(\frac{1}{R^*}\right)^{3n}U_c^2 + \\ -U_c^2\epsilon^*\sin(\omega^* t^*) - U_c^2 - \frac{-4\mu}{\rho}\frac{U_c}{R_E}\frac{\dot{R}^*}{R^*}\frac{U_c}{U_c} + \sigma_{rr}^* U_c^2 + U_c^2\int\frac{2\sigma_{rr}^*}{r}dr + \\ -U_c^2\int\frac{2\sigma_{\theta\theta}^*}{r}dr - U_c^2\sigma_{rr}^{mag}|_{r=R}\left(\frac{1}{R^*}\right)^{3n}. \quad (2.97)$$

Dividing the whole equation by U_c^2:

$$R_E\ddot{R}^*R^* + \frac{3}{2}\dot{R}^{2*} = \frac{1}{\rho}\frac{2\tilde{\sigma}}{R_E U_c}\left[-\frac{1}{R^*} + \left(\frac{1}{R^*}\right)^{3n}\right] + \left(\frac{1}{R^*}\right)^{3n} - \epsilon^*\sin(\omega^* t^*)$$
$$-1 - \frac{-4\mu}{\rho}\frac{U_c}{R_E}\frac{\dot{R}^*}{R^*} + \sigma_{rr}^* + \int\frac{2\sigma_{rr}^*}{r}dr - \int\frac{2\sigma_{\theta\theta}^*}{r}dr - \sigma_{rr}^{mag}|_{r=R}\left(\frac{1}{R^*}\right)^{3n}, \tag{2.98}$$

and using the non-dimensional numbers presented, it is possible to rewrite equation 2.98 as:

$$R_E\ddot{R}^*R^* + \frac{3}{2}\dot{R}^{2*} = \frac{1}{\rho}\frac{2}{We}\left[-\frac{1}{R^*} + \left(\frac{1}{R^*}\right)^{3n}\right] + \left(\frac{1}{R^*}\right)^{3n} - \epsilon^*\sin(\omega^* t^*)$$
$$-1 - \frac{-4}{Re}\frac{\dot{R}^*}{R^*} + \sigma_{rr}^* + \int\frac{2\sigma_{rr}^*}{r}dr - \int\frac{2\sigma_{\theta\theta}^*}{r}dr - \sigma_{rr}^{mag}|_{r=R}\left(\frac{1}{R^*}\right)^{3n}. \tag{2.99}$$

We note that the non-Newtonian integral, which determines the extra pressure on both directions r and θ is not written in a dimensionless form. Considering $\sigma_{rr}^* = \sigma_{rr}/(\rho U_c^2)$, these integrals are given by:

$$\int\frac{2\sigma_{rr}^*}{r}dr - \int\frac{\sigma_{\theta\theta}}{r}dr - \sigma_{rr}^{mag}|_{r=R}\left(\frac{1}{R^*}\right)^{3n} =$$
$$= \frac{1}{\rho U_c^2}\left[\mu_0\left(\frac{-3\mu_r^2 H_0^2}{8}\right) + \mu_0\chi\left(-\frac{\mu_r H_0^2}{3} - \frac{17\mu_r^2 H_0^2}{12} + \frac{H_0^2}{2}\ln(R_\infty) - \frac{H_0^2}{2}\ln(R)\right)\right]$$
$$-\frac{1}{\rho U_c^2}\left[\mu_0\left(-\frac{3\mu_r H_0^2}{2} - \frac{3\mu_r^2 H_0^2}{4}\right) + \mu_0\chi\left(-\frac{4\mu_r H_0^2}{2} - \frac{4\mu_r^2 H_0^2}{2}\right)\right]\left(\frac{R_E}{R}\right)^{3n}, \tag{2.100}$$

substituting $\mu_r = -1/2$ (considering that there is no magnetization inside the bubble or applied field) we have:

$$\int\frac{2\sigma_{rr}^*}{r}dr - \int\frac{\sigma_{\theta\theta}}{r}dr - \sigma_{rr}^{mag}|_{r=R}\left(\frac{1}{R^*}\right)^{3n} =$$
$$= \frac{1}{\rho U_c^2}\left[\mu_0\left(\frac{-3H_0^2}{32}\right) + \mu_0\chi\left(\frac{H_0^2}{6} - \frac{17H_0^2}{48} + \frac{H_0^2}{2}\ln(R_\infty) - \frac{H_0^2}{2}\ln(R)\right)\right]$$
$$-\frac{1}{\rho U_c^2}\left[\mu_0\left(\frac{3H_0^2}{4} - \frac{3H_0^2}{16}\right) + \mu_0\chi\left(\frac{4H_0^2}{4} - \frac{4H_0^2}{8}\right)\right]\left(\frac{R_E}{R}\right)^{3n}. \tag{2.101}$$

Using the conditions stated above and after some algebric manipulation, it results in

$$\int\frac{2\sigma_{rr}^*}{r}dr - \int\frac{\sigma_{\theta\theta}}{r}dr - \sigma_{rr}^{mag}|_{r=R}\left(\frac{1}{R^*}\right)^{3n} =$$
$$= \frac{1}{\rho U_c^2}\left\{\mu_0\left[\frac{-3H_0^2}{32}\right) + \mu_0\chi\left(-\frac{9H_0^2}{48} + \frac{H_0^2}{2}\ln(R_\infty^* R_E) - \frac{H_0^2}{2}\ln(R^* R_E)\right]\right\}$$
$$-\frac{1}{\rho U_c^2}\left[\mu_0\left(\frac{9H_0^2}{16}\right) + \mu_0\chi\left(\frac{H_0^2}{2}\right)\right]\left(\frac{R_E}{R}\right)^{3n}. \tag{2.102}$$

Finally, one reaches:

$$\frac{1}{Re^{mag}}\left\{\frac{\chi}{2}\left[\ln\left(\frac{R^*_\infty}{R^*}\right)-\frac{C_1}{2}\right]-\left[\frac{C_1}{8}+\frac{1}{(R^*)^{3n}}\left(C_1^2-\frac{\chi}{2}\right)\right]\right\}, \tag{2.103}$$

where

$$C_1=\frac{3}{4}, \tag{2.104}$$

$$Re^{mag}=\frac{\rho U_c^2}{\mu_0 H_0^2}. \tag{2.105}$$

Equation 2.105 represents what is defined as Magnetic Reynolds number. The hydrodynamic Reynolds number, by definition, compares both inertial and viscous forces. In this case, the relation between inertial and magnetic forces may be considerer as a Magnetic Reynolds number.

2.1.6 Final Version of Magnetic Rayleigh-Plesset Equation

Until now the formulation considered an applied magnetic field in $t = 0$ for the jump of traction. Even though this is a valid condition, this consideration does not imply that the applied field reaches it maximum value at R_∞ and decays as it approaches the bubble surface. Mathematically, using this formulation, the applied field on the bubble's surface is null. However, in order to maintain the most complete formulation, this condition was not used until now since it may not be guaranteed in a pratical application.

Considering now this simplification, equation 2.103 may be written as:

$$\frac{1}{Re^{mag}}\left\{\frac{\chi}{2}\left[\ln\left(\frac{R^*_\infty}{R^*}\right)-\frac{C_1}{2}\right]-\frac{C_1}{8}\right\}. \tag{2.106}$$

For now on, the form bellow will be considered the final version of Magnetic Rayleigh-Plesset equation (MRP). More information regarding the algebric manipulation can be found in Appendix 1. Therefore, the complete equation with the magnetic stress tensor is written as:

$$\begin{aligned} R^*\ddot{R}^*+\frac{3}{2}(\dot{R}^*)^2 &= \frac{2}{We}\left[\frac{1}{(R^*)^{3n}}-\frac{1}{R^*}\right]-1-\varepsilon^* sen(\omega^* t^*) \\ +\frac{1}{(R^*)^{3n}}-\frac{4}{Re}\frac{\dot{R}^*}{R^*}&+\frac{1}{Re^{mag}}\left\{\frac{\chi}{2}\left[\ln\left(\frac{R^*_\infty}{R^*}\right)-\frac{C_1}{2}\right]-\frac{C_1}{8}\right\}. \end{aligned} \tag{2.107}$$

In order to develop a numerical code to solve the Magnetic Rayleigh-Plesset equation we must define what will be considered R_∞. For that, the applied field described by Rosensweig [39] was plotted. In this case, we consider that at a sufficient distance from the bubble, the applied field would value $0.99H_0$.

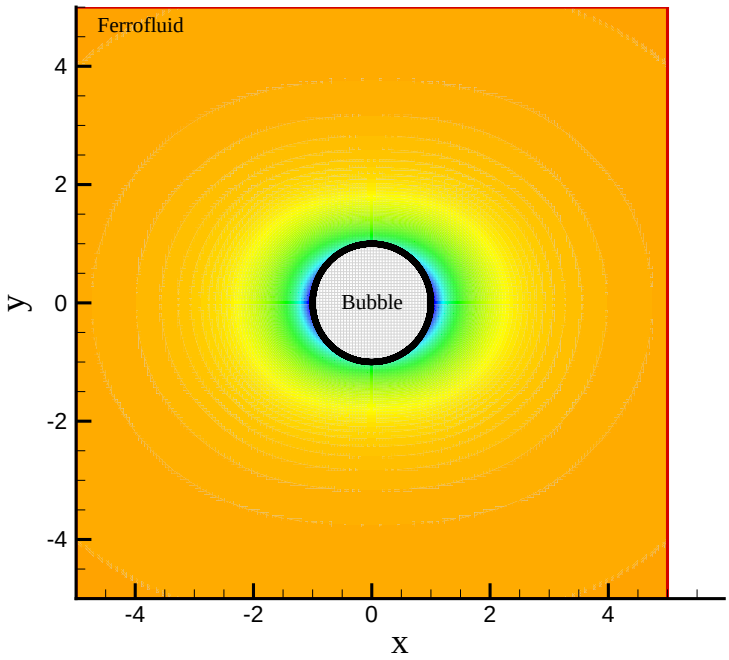

Figure 2.5: Magnetic applied field $\boldsymbol{H}$ as a function of the distance from the bubble.

We notice from figure 2.5 that the field decays as the observer approaches the bubble. This characteristic may be observed by the change in colors: orange being the higher values of $\boldsymbol{H}$ and blue the lower. Since this decay is substantially fast (scaling with r^2), R_∞ will not be high.

In figure 2.6, we observe that from $r \sim 2.3$ the field value starts to decay expressively. However, as seen in the insert, $H_0 = 0.99$ is obtained with $r = 4.658$. In this way, any value above that one can be consider as R_∞. With that said, $R_\infty = 5$ will be used for further investigations in respect of numerical formulation.

2.1.7 Associated Time Scales

The model presented in this work involves several time scales associated with different physical mechanisms present in the study of an oscillating bubble immersed in a magnetic field. The main physical parameters are associated with the viscous diffusion (denoted as t_μ); the surface tension relaxation (expressed as t_σ); the excitation time due to the oscillating pressure field applied (t_ω); and one associated with the magnetic effects (defined as t_m).

This last scale, t_m, represents the relaxation time of the fluid magnetization. In other words, it represents the fluid relaxation time. Indeed, it is the time the fluid takes to magnetize in the presence of an external field. In addition to represent the innovation in this work, the time scale can be interpreted as an interaction between the particles magnetic dipoles and the external field. The forces and torques in each magnetic nanoparticle interact with the applied field, generating

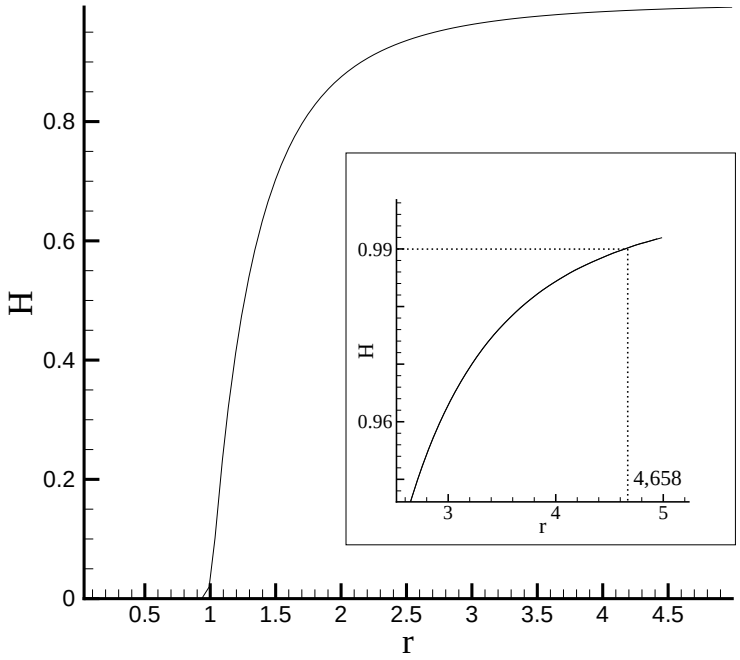

Figure 2.6: Magnetic applied field H as a function of the distance r from the bubble.

rotational and translational movements.

We can also define a typical macroscopic time scale of the problem, which will be called inertial scale (or convective) and denoted by t_i. This scale represents the time that an infinitesimal volume of fluid takes to cover a radial distance equivalent to the equilibrium radius R_E, at velocity U_c. In this case, $t_i = R_E/U_c$.

Using Bernoulli's principle, it is possible to write U_c as $\sqrt{|\Delta\tilde{p}|/\rho}$, where $\Delta\tilde{p} = \tilde{p}_\infty - p_v$. The static pressure of the liquid evaluated far from the bubble at the equilibrium instant ($t = 0$) is given by $\tilde{p}_\infty$ and p_v denotes the steam pressure inside the bubble.

The problem studied is governed by a nonlinear equation involving multiple time scales, the physical interpretation of the results necessarily requires an interpretation of the relationship between these scales. When the MRP equation was written in its non-dimensional form, several dimentionless parameters that are related with those time scales appeared spontaneously. So we may rewrite the time scales t_ω, t_μ, t_σ and t_m as:

$$t_\omega = \frac{1}{\omega},\ \ t_\mu = \frac{R_E^2}{\nu},\ \ t_\sigma = \sqrt{\frac{\rho R_E^3}{\sigma}},\ \ t_m = R_E \times \left(\frac{\mu_0 H_0^2}{\rho}\right)^{-1/2}, \tag{2.108}$$

where ν represents the cinematic viscosity of the fluid, given by μ/ρ, σ is the surface tension coefficient and ω is the frequency of excitation of the forcing pressure field. These time scales represented in (2.108) can be written in a dimensionless form regarding the inertial time scale (t_i),

such that:

$$t_\omega{}^* = \frac{t_\omega}{t_i} = \frac{1}{\omega \times (R_E/U_c)} = \frac{1}{\omega^*}, \tag{2.109}$$

$$t_\nu{}^* = \frac{t_\nu}{t_i} = \frac{R_E^2 U_c}{\nu R_E} = \frac{U_c R_E}{\nu} = Re, \tag{2.110}$$

$$t_\sigma{}^* = \frac{t_\sigma}{t_i} = \sqrt{\frac{\rho R_E^3}{\sigma}} \times \frac{U_c}{Re} = \sqrt{\frac{\rho U_c^2 R_E}{\sigma}} = \sqrt{We}, \tag{2.111}$$

$$t_m{}^* = \frac{t_m}{t_i} = R_E \times \left(\frac{\mu_0 H_0^2}{\rho}\right)^{-1/2} \times \frac{U_c}{Re} = \sqrt{\frac{\rho U_c^2}{\mu_0 H_0^2}} = \sqrt{Re_{mag}}, \tag{2.112}$$

where Reynolds, Weber and Magnetic Reynolds number have already been defined previously. In this case, the Magnetic Reynolds number, for example, represents the relation between two time scales besides been described as a quotient between inertial and magnetic forces. When the applied field grows, the Magnetic Reynolds decreases. In conclusion, when there is no applied field, $Re_{mag} \to \infty$. The decrease in Re_{mag} implies an increase in the applied field, so the magnetic time scale also decreases, as seen in (2.112). Typically, the magnetic time scales are very small and the system tends to react quickly. When there is an increase in the magnitude order of that time scale, such that it equates the continuous time scales (such as t_i), the bubble reacts more expressively.

On the other hand, if the magnetic scale is very small in relation to the inertial one ($Re_{mag} \ll 1$) during a typical time of the bubble oscillation (considering that $t_\omega{}^* \sim 1$) the nanoparticles will have a much larger number of microstructural changes that the bubble will not notice.

The same thing happens in the other asymptotic limit, where the magnetic time is too large, so that while the bubble oscillates one or more periods, the field has not yet been able to change the microstructure of the ferrofluid. In this sense, it is expected that the bubble reacts better to the magnetic effects when its magnetic time scales are in the same order of magnitude that the inertial and excitation ones.

This same interpretation applies to the other non-dimensional parameters of the problem. Whenever possible, the physical results obtained from the simulations in this work will be interpreted in terms of the typical time scales of the problem expressed in terms of non-dimensional parameters that will serve as input for processing data.

Chapter 3

Numerical Solution

The numerical solution used for calculating the nonlinear differential equation that governs the bubble dynamics developed in the previous section is modeled in this chapter. The application of the fourth order Runge-Kutta and later its evolution to the fifth order with adaptive time step is reproduced and validated.

3.1 Introduction

Due to the nonlinearity of the governing differential equation we do not have an analytic solution for arbitrary input parameters. In this sense we must reccur to the use of computer simulation techniques. There are several numerical methods for solving ordinary differential equations. In fact, each one has strengths and weaknesses, depending on the application. One widely used method within the class of differential equations described by Initial Value Problems (IVP), is the Runge-Kutta scheme, which is presented in different orders of accuracy. This method corresponds to the advanced predictor-corrector algorithm, which uses weighted averages of a function f calculated at the extremes and at intermediate points with start and end time, i.e. $[t_j, t_j + 1]$ [48].

3.2 Fourth Order Runge-Kutta

For the fourth order method, considering $y' = f(t, y)$ and $y(t_0) = y_0$, each time step is evaluated into four sub-steps. In this case, four integrations per time step are made. The standard expression that characterizes it is [49]:

$$y_{n+1} = y_n \left(+ \frac{k_1 + 2k_2 + 2k_3 + k_4}{6} \right), \tag{3.1}$$

where

$$k_1 = \Delta t f(x_n, y_n), \tag{3.2}$$

$$k_2 = \Delta t f\left(x_n + \frac{\Delta t}{2}k_1, y_n + \frac{\Delta t}{2}\right), \tag{3.3}$$

$$k_3 = \Delta t f\left(x_n + \frac{\Delta t}{2}k_2, y_n + \frac{\Delta t}{2}\right), \tag{3.4}$$

$$k_4 = \Delta t f\left(x_n + \Delta t k_3, y_n + \Delta t\right). \tag{3.5}$$

Note that this method will separate the ordinary differential equation, regardless of their order, into first-order equations and then solve this system. For an initial value problem using n time steps, it is necessary $4n$ ratings, which demands certain computational effort.

This time step value, Δt, must be carefully set since the $R(t)$ function, which describes the time evolution of the bubble radius can vary significantly depending on the non-dimensional parameters, and the applied disturbances, such as pressure and/or magnetic fields.

Small values of Δt could decrease the risk of a high value of $\dot{R}(t)$, thus eliminating the possibility of numerical collapse. However this would require a higher computational cost. With that said, it is easy to conclude that the numerical error for the solution method is of the order $O(\Delta t^5)$.

The time interval must be calibrated depending on the excitation frequency of the applied pressure and magnetic field (if oscillatory). A numerical time step depending on the proposed frequency takes form as $\Delta t = O(1/\omega)$. Likewise, we must note the fluid relaxation time. Considering a ferrofluid, the alignment of the particles and aggregates modify the relaxation time of the fluid. In this context, the time scales, including the magnetic one must be correctly analyzed.

Based on the analysis of Rayleigh cavity, an adequate time step for subsequent simulations was identified. It is given between $\Delta t_{Ray} = 10^{-3}$ and $\Delta t_{Ray} = 5.10^{-4}$. A convergence test was performed in order to understand how the system responds as the time step diminished.

It can be seen in figure 3.1 that as the time step increases the value of the average radius for a sinusoidal excitation considering small amplitude increases in a not convergent manner. On the other hand, for values of $\Delta t < 0.01$ that variable reaches an stable plateau. In this sense, there is no need to use a time step smaller than 10^{-3}. It would be an unnecessary increase in the computational cost for the same numerical solution of the governing equation.

Similarly, for very small values (smaller than 0.002), the system convergence would be impaired by an oscillatory motion, as seen in the insert of figure 3.1. This phenomena is explicitly related to the numerical residue, a characteristic of all computational codes that deals with the solution of nonlinear equations. The language used, Fortran 90, uses by default eight digits of precision. A very small number for the time step can generate computational instabilities, generating numerical oscillations.

Importantly, in a physical problem governed by differential equations in terms of time derivatives, the numerical solution passes through a time discretization process. Consequently, the adoption of a numerical time step Δt is part of the solution process. The physical parameters that

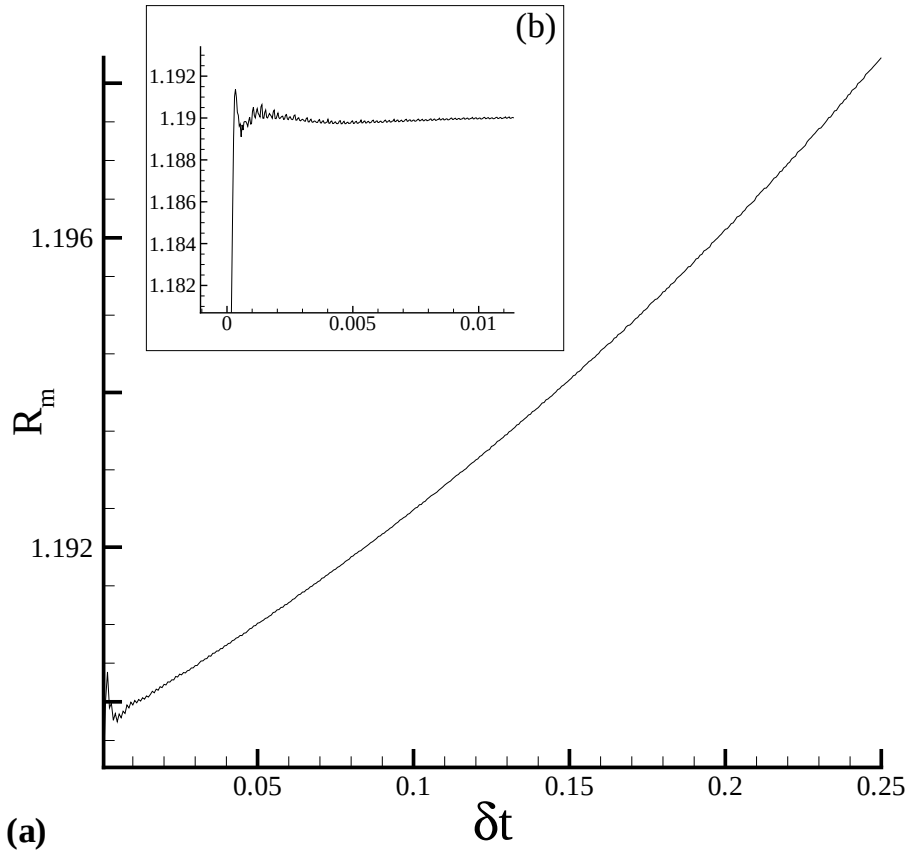

Figure 3.1: (a) Convergence of the numerical solution of the average radius as a function of the used time step; (b) The insert shows the magnified zone of the instability due the low time step used.

govern the behavior of a dynamic system serve as a good estimate of the order of magnitude of the involved time scales. As these parameters can be interpreted as typical time scales, some of these can serve as an estimate of the magnitude of the numerical time steps appropriate for solving certain differential equation.

3.2.1 Analytical Solution for Rayleigh's Cavity

Consider an infinite mass of incompressible, homogeneous fluid acting without external forces and at rest on a spherical portion of fluid, which is suddenly filled. The instantaneous pressure change was determined at any point of mass using the equation of fluid motion [50]. Likewise, the time for the cavity to be filled was also calculated.

Rayleigh [51] meticulously observed the conditions of collapse of a cavity in vacuum by developing a theoretical model that is used for calibration purposes in this study. Indeed, τ_c was determined as being the time of total collapse of the cavity. Expressed, in non-dimensional terms,

we have:

$$\tau_c = 0.915 R_0 \sqrt{\frac{\rho}{P_0}} \rightarrow \frac{\tau_c}{R_0 \sqrt{\frac{\rho}{P_0}}} = 0.915. \tag{3.6}$$

Considering a cavity, the dimensionless version of Rayleigh-Plesset equations becomes:

$$R\ddot{R} + \frac{3}{2}\dot{R}^2 = -1. \tag{3.7}$$

The numerical integration of equation 3.7 leads to the following system of first order differential equations:

$$\begin{cases} y = \dot{R} \\ \dot{y} = \frac{1}{R}[-1 - \frac{3}{2}y^2]. \end{cases} \tag{3.8}$$

The numerical solution of the bubble movement in a collapse condition is presented in figure 3.2. The error in the estimation of the time of collapse given by the numerical solution and the one predicted by the analytical solution is 0.082%. This, in a way, is a validation of the numerical calculation and shows that our numerical integration calibrated with the methodology of time step selection set out in this work, captures the bubble collapse time with great accuracy.

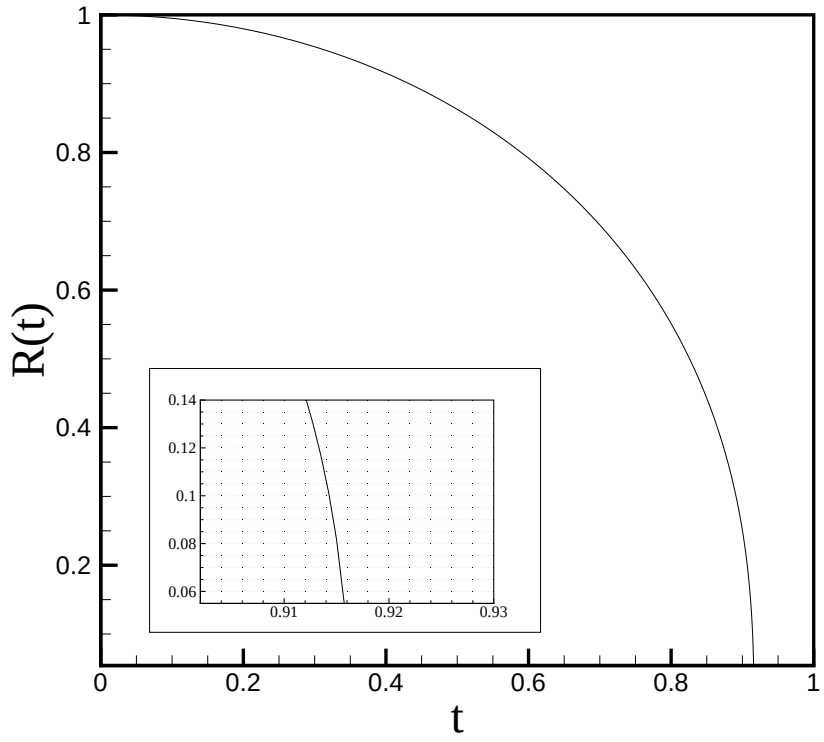

Figure 3.2: Computational solution of the time of collapse proposed for Rayleigh's cavity problem. The insert shows in details the bubble movement during the collapse imminence.

3.3 Adaptive Time Step

As stated before, in order to obtain the lowest possible computational requirement, time steps must be meticulously calibrated. For unstable regions where there is a sudden change in radius size or rapid variations of compression and expansion, it is necessary to set a smaller time step.

The estimated error obtained as we use a numerical method for solving ODEs is the key to implement an adaptive time step. As the adaptive time step is used in the fourth order Runge-Kutta, the need to capture each time step twice is required. One provides the value for y_1 using the complete time step. The other computes y_2 independently, using two time steps. The associated error between these two numerical mesures is given by:

$$\Delta_{err} = y_2 - y_1. \tag{3.9}$$

The first study in adaptive time steps was proposed by Fehlberg [49]. This method proposes the use of six functions (fifth order Runge-Kutta). Nevertheless, the combination of these functions must also result in the fourth order method.

The most general form of the method is expressed by:

$$k_1 = hf(x_n, y_n), \tag{3.10}$$

$$k_2 = hf\left(x_n + \frac{1}{5}h, y_n + \frac{1}{5}k_1\right), \tag{3.11}$$

$$k_3 = hf\left(x_n + \frac{3}{10}h, y_n + \frac{30}{40}k_1 + \frac{9}{40}k_2\right), \tag{3.12}$$

$$k_4 = hf\left(x_n + \frac{3}{5}h, y_n + \frac{3}{10}k_1 - \frac{9}{10}k_2 + \frac{6}{5}k_3\right), \tag{3.13}$$

$$k_5 = hf\left(x_n + h, y_n - \frac{11}{54}k_1 + \frac{5}{2}k_2 - \frac{70}{27}k_3 + \frac{35}{27}k_4\right), \tag{3.14}$$

$$k_6 = hf\left(x_n + \frac{7}{8}h, y_n + \frac{1631}{55296}k_1 + \frac{175}{512}k_2 + \frac{575}{13824}k_3 + \frac{44275}{110592}k_4 + \frac{253}{4096}k_5\right). \tag{3.15}$$

The approach of the $y(t)$ solution for the fifth order Runge-Kutta is obtained by equation:

$$y^*_{n+1} = y^*_n + \frac{2825}{27648}k_1 + \frac{18575}{48384}k_3 + \frac{13525}{55296}k_4 + \frac{277}{14336}k_5 + \frac{1}{4}k_6. \tag{3.16}$$

On the other hand, the approach of the $y(t)$ for the fourth order Runge-Kutta assumes

$$y_{n+1} = y_n + \frac{37}{378}k_1 + \frac{250}{621}k_3 + \frac{125}{594}k_4 + \frac{512}{1771}k_6. \tag{3.17}$$

The error estimation is, finally, given by:

$$\Delta_{err} = y^*_{n+1} - y_{n+1}. \tag{3.18}$$

1. Define $Re, We, Re_{mag}, \chi, n$ (polytropic coefficient) and ε;
2. Initial conditions and simulation time $R(0)$ and $G(0)$;
3. `While` $t(i-1) < b$ `do` ;
4. Compute $R_{min}(R(0), We)$;
5. Compute $k_1, k_2, k_3, k_4, k_5, k_6$ e $q_1, q_2, q_3, q_4, q_5, q_6$;
6. Forth order $\rightarrow g(i)$ and Fifth order $\rightarrow P(i)$;
7. Compute $error = \left| \left(\dfrac{g(i) - P(i)}{tolerance} \right) \right|$;
8. `If` $error > 1$ `then` $\rightarrow dt = htemp * seg$
9. `Compute new` $k_1, k_2, k_3, k_4, k_5, k_6$ and $q_1, q_2, q_3, q_4, q_5, q_6$;
10. `If` $error > 1$ `then` $\rightarrow dt = htemp * seg$;
11. `If` $error > parameter$ `then` $\rightarrow hnext = seg * htemp * parameter2$;
12. `If` $error < parameter$ `then` $\rightarrow hnext = htemp * parameter3$;
13. `If` $R(i) < R_{min}$ `then` $\rightarrow$ **COLAPSE**
14. `If` $hdid < dtm$ `then` $\rightarrow$ **END**
15. `If` $hdid > dtm$ `then` $\rightarrow$ `go to step 5.`

(3.19)

Figure 3.3: Algorithm to compute $R(t)$ as a function of the initial inputs.

These constants, given by Cash and Karp [32] provide smaller errors than the estimated by Fehlberg [49].

Here, in the scheme shown in 3.3, b detones the total time of the simulation, an user defined option. The minimum radius, R_{min} represents the minimum radius proposed [40] where the bubble should collapse. The variable *htemp* represents the temporary time step and the variable *hnext* is the next time step to be used in the following iteration, after the multiplication by the security parameters (*seg*) and tolerance (*parameter*2 and *parameter*3). Subsequently, the time step dt becomes *hdid* at the end of the iteration and is compared with the minimum time, *dtm*, defined by the user.

Even though the bubble collapse is not on the continuum mechanics formulation an asymptotic solution to predict the minimum radius before collapse can be developed. This theory [40, 41, 42] considers the most adverse condition of the flow when $Re \rightarrow \infty$. Considering that the ambient pressure is constant $p_\infty(t) = \tilde{p}$, the Rayleigh-Plesset equation might be written as:

$$\ddot{R}R + \frac{3}{2}\dot{R}^2 = -\frac{\Delta\tilde{p}}{\rho} + \frac{1}{\rho}\left(\Delta\tilde{p} + \frac{2\tilde{\sigma}}{R_E}\right)\left(\frac{R_E}{R}\right)^{3n} - \frac{2\tilde{\sigma}}{R\rho}. \tag{3.20}$$

The equation 3.20 migh be solved by the integrating factor method. In this case, the integrating factor is given by $2\dot{R}R^2$. Considering that, the left side of Rayeigh-Plesset equation can be seen as a product of two functions, becoming a separable ODE. Multiplying equation 3.20 by the integrating factor, we have:

$$2\ddot{R}\dot{R}R^3 + 3\dot{R}^3R^2 = -2\dot{R}R^2\frac{\Delta\tilde{p}}{\rho} + \frac{1}{\rho}2\dot{R}R^2\left(\Delta\tilde{p} + \frac{2\tilde{\sigma}}{R_E}\right)\left(\frac{R_E}{R}\right)^{3n} - \frac{4\dot{R}R\tilde{\sigma}}{R\rho}. \tag{3.21}$$

Considering an equilibrium constant $\tilde{H}$:

$$\tilde{H} = \left(\Delta\tilde{p} + \frac{2\tilde{\sigma}}{R_E}\right)R_E^3. \tag{3.22}$$

It is possible to write equation 3.21 as a function of its derivatives and integrate it considering its initial conditions: $\dot{R}(0) = 0$ e $R(0) = R_0$:

$$\frac{d}{dt}(R^3\dot{R}^2) = \frac{-2}{3}\left(\frac{\Delta\tilde{p}}{\rho}\right)\frac{d}{dt}(R^3) + \frac{2}{\rho}\tilde{H}\frac{d}{dt}(\ln R) - \frac{2\tilde{\sigma}}{\rho}\frac{d}{dt}(R^2). \tag{3.23}$$

Integrating, we obtain:

$$R^3\dot{R}^2 = \frac{-2}{3}\left(\frac{\Delta\tilde{p}}{\rho}\right)(R^3 - R_0^3) + \frac{2}{\rho}\tilde{H}\frac{d}{dt}\left(\frac{\ln R}{R_0}\right) - \frac{2\tilde{\sigma}}{\rho}(R^2 - R_0^2). \tag{3.24}$$

Its now possible to manipulate the equation and rewrite it as

$$\dot{R}^2 = \left(\frac{R_0^3}{R^3}\right)\left[\frac{2}{3}\left(\frac{\Delta\tilde{p}}{\rho}\right)\left(1 - \frac{R^3}{R_0^3}\right) + \frac{2}{\rho}\tilde{H}\frac{1}{R_0^3}\ln\left(\frac{R}{R_0}\right) - \frac{2\tilde{\sigma}}{\rho}\frac{1}{R_0}\left(\frac{R^2}{R_0^2} - 1\right)\right]. \tag{3.25}$$

In the imminence of collapse, in which $R << 1$, equation 3.25 can be written as:

$$\dot{R}^2 = \left(\frac{R_0^3}{R^3}\right)\left[\frac{2}{3}\left(\frac{\Delta\tilde{p}}{\rho}\right) + \frac{2}{\rho}\tilde{H}\frac{1}{R_0^3}\,ln\left(\frac{R}{R_0}\right) - \frac{2\tilde{\sigma}}{\rho}\frac{1}{R_0}\right]. \tag{3.26}$$

Since the bubble is not a cavity and its moles number is finite we must not use the condition of $\dot{R} \to \infty$. In this case, the minimum radius is never null. Thus, $\dot{R} = 0$ and at the collapse condition the bubble reaches the minimum radius. Equation 3.26 reduces to:

$$0 = \frac{2}{3}\left(\frac{\Delta\tilde{p}}{\rho}\right) + \frac{2}{\rho}\tilde{H}\frac{1}{R_0^3}\ln\left(\frac{R}{R_0}\right) - \frac{2\tilde{\sigma}}{\rho}\frac{1}{R_0}. \tag{3.27}$$

Isolating R_{min} and aplying the exponencial function on both sides:

$$\ln\left(\frac{R_{min}}{R_0}\right) = -\frac{R_0^3}{3\tilde{H}}\left(\Delta\tilde{p} + \frac{3\tilde{\sigma}}{R_0},\right), \tag{3.28}$$

or

$$R_{min} = R_0 e^{\frac{-R_0^3}{3\tilde{H}}}\Delta\tilde{p} + \left(\frac{3\tilde{\sigma}}{R_0}\right). \tag{3.29}$$

Since the mathematical modelling is written in its non-dimensional form, this stop criteria must also be written in a dimensionless version. Thus, the initial and minimum radius are both given by:

$$R^*_{min} = R_{min} R_E, \tag{3.30}$$

$$R^*_0 = R_0 R_E. \tag{3.31}$$

Substituing:

$$R^*_{min} = R^*_0 e^{\frac{(-R^*_0)^3 R^3_E}{3\tilde{H}}\left(\delta\tilde{p} + \frac{3\tilde{\sigma}}{R^*_0 R_E}\right)} = R^*_0 e^X. \tag{3.32}$$

Observing now how the term X can be written as a non-dimensional parameter:

$$X = -\frac{(R^*_0 R_E)^3 \Delta\tilde{p}}{3\Delta\tilde{p} R^2_E \left[\frac{2\tilde{\sigma}}{R_E \delta\tilde{p}} + 1\right]} \left[1 + \frac{3\tilde{\sigma}}{R^*_0 R_E \Delta\tilde{p}}\right]. \tag{3.33}$$

Using the Weber number, the equation 3.33 may be rewritten as:

$$X = -\frac{(R^*_0)^3}{3\left[\frac{2}{We} + 1\right]} \left[1 + \frac{3}{R^*_0 We}\right], \tag{3.34}$$

and simplified as:

$$X = -(R^*_0)^2 \frac{(1 + \frac{R^*_0 We}{3})}{We + 2}. \tag{3.35}$$

Thus, the minimum radius found by the asymptotic solution is given by:

$$R^*_{min} = (R^*_0) e^{-(R^*_0)^2 \left[\frac{(1 + R^*_0 We/3)}{We+2}\right]}. \tag{3.36}$$

3.4 Asymptotic Solution

In order to validate the numerical code developed, an asymptotic solution for small amplitudes of the pressure forcing and applied magnetic field has been proposed. In this section, a regular perturbation method is used in equation (2.107), considering the first order $\mathscr{O}(\varepsilon/Re_{mag})$ asymptotic solution. Under this limit, a variable change is made consisting in $R = 1 + r$. In a subsequent step a binomial expansion is used for $(1 + r)^{-1}$ and $(1 + r)^{-3}$ as:

$$\begin{aligned}(1 + r)^{-3n} &= 1 - 3nr + \frac{3}{2}[(1 + 3n)n]r^2 + \mathscr{O}(r^3) \\ (1 + r)^{-1} &= 1 - r + r^2 + \mathscr{O}(r^3).\end{aligned} \tag{3.37}$$

Substituting equation (3.37) in (2.107) and considering a MacLaurin expansion of the function $\ln(1+r)$ around $r=0$, we have $\ln(1+r) = r + \frac{r^2}{2}$ and

$$\ddot{r} + r\ddot{r} + \frac{3}{2}\dot{r}^2 = -\frac{4r}{We} - 3r - \varepsilon\sin(\omega t) - \frac{4\dot{r}}{Re} + \\ + \frac{4\dot{r}r}{Re} + \frac{1}{Re_{mag}}\left\{\frac{\chi}{2}\left[\ln(R_\infty) + \frac{r^2}{2} - r - \frac{C_1}{2}\right] - \frac{C_1}{8}\right\}. \tag{3.38}$$

Now it is possible to expand r as the following power series:

$$r = \sum_{k=1}^{\infty}\left(\frac{\varepsilon}{Re_{mag}}\right)^k r_k(t). \tag{3.39}$$

Substituting equation (3.39) in (3.38) a theoretical solution for r_1 is obtained and given by equation (3.40).

$$r_1(t) = e^{(2We+\lambda_1)t/ReWe}\frac{We[\lambda_2\lambda_3 - ReRe_{mag}\omega We(4+3We)\lambda_4 + \lambda_5]}{2(4+3We)\lambda_1(16\omega^2We^2 + Re^2[-4+(-3+\omega^2)We]^2)}. \tag{3.40}$$

The parameters λ_1, λ_2, λ_3, λ_4, λ_5 and Υ are given by equations (3.41), (3.42), (3.44), (3.45), (3.46), (3.43), respectively.

$$\lambda_1 = \sqrt{We[4We - Re^2(4+3We))]}, \tag{3.41}$$

$$\lambda_2 = -\Upsilon 16\omega^2We^2 + Re^2[-4+(\omega^2-3)We]^2, \tag{3.42}$$

$$\Upsilon = \frac{1}{\varepsilon}\left\{\frac{\chi}{2}\left[\ln(R_\infty) - \frac{C_1}{2}\right] - \frac{C_1}{8}\right\}, \tag{3.43}$$

$$\lambda_3 = 2(-1+e^{2\lambda_1 t/ReWe})We + \left[1 + e^{2\lambda_1 t/ReWe} - 2e^{(2We+\lambda_1)t/ReWe}\right]\lambda_1, \tag{3.44}$$

$$\lambda_4 = (-1+e^{2\lambda_1 t/ReWe})Re^2[-4+(\omega^2-3)We] + 4[-2We+\lambda_1] + 4e^{2\lambda_1 t/ReWe}(2We+\lambda_1), \tag{3.45}$$

$$\lambda_5 = 2ReRe_{mag}(4+3We)\lambda_1 e^{(2We+\lambda_1)t/ReWe}4\omega\cos(wt) + Re[-4+(\omega^2-3)We]\sin(\omega t). \tag{3.46}$$

Based on that solution, figure 3.4 shows the maximum bubble radius in steady state as a function of ε/Re_{mag}. The aim is to compare the numerical solution with the first order asymptotic solution. The parameters are $Re = We = \omega = 1$. We observe an error smaller than 1% for $\varepsilon/Re_{mag} \leq 0.4$. For instance, we have an error of 0.09% when $\varepsilon/Re_{mag} = 0.1$. This theoretical approach works as a validation of the proposed algorithm, therefore in the next sections we intend to use the developed code to explore other regimes that can not be captured by our asymptotic solution.

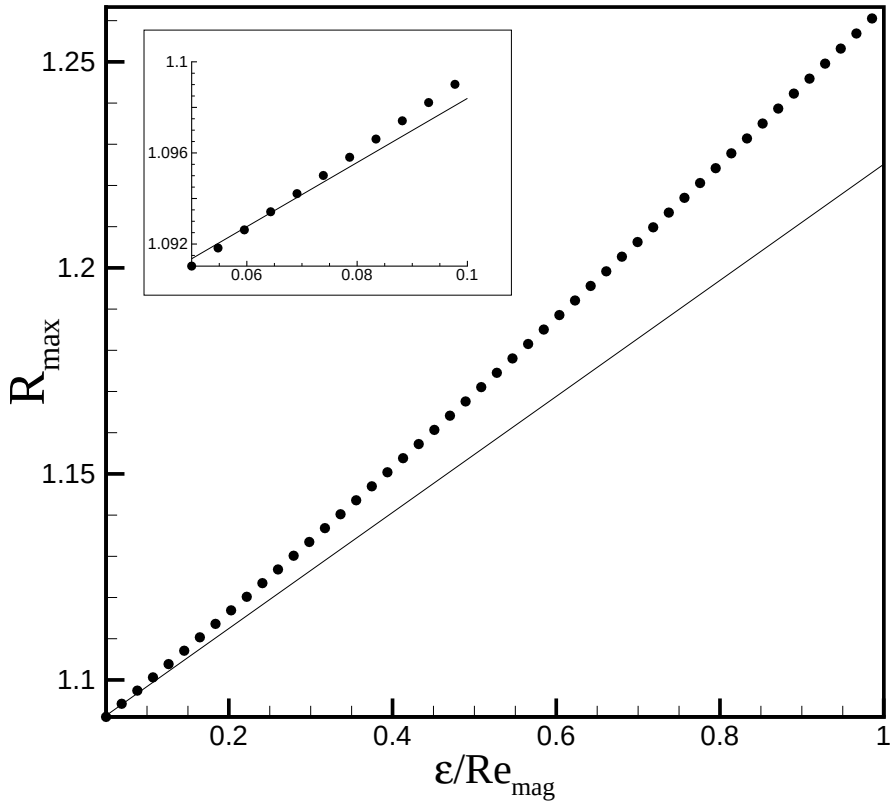

Figure 3.4: Comparison between the asymptotic solutions $\mathscr{O}(\varepsilon/Re_{mag})$ (filled line) and the numerical simulation (filled black circles) for the maximum radius obtained as a function of the excitation pressure amplitude ε and magnetic Reynolds number Re_{mag}.

Chapter 4

Constant Applied Field

This chapter shows the results for a bubble immersed in a ferrofluid and subject to a constant magnetic field. In this condition, the non-dimensional parameters are analysed and a hydrodynamic linear stability analysis is conducted. Thus, the collapse diagram is studied for both Newtonian and non-Newtonian cases and the vibrationa patterns are identified. With that in mind, a nonlinear control approach is used based on Neural Networks.

4.1 Magnetic Reynolds Number Influence

As a first result, it is observed how this new dimensionless parameter, Re_{mag}, modifies the bubble behavior. In Figure (4.1) it is possible to see how the magnetic field affects the bubble motion. In this case, for $Re_{mag} = 10$, the behavior is similar to what we would observe if the bubble was immersed in a Newtonian Fluid. Nevertheless, with $Re_{mag} = 0.1$ or in other words, with a high applied magnetic field, it is noted that the bubble behavior is completely stable and harmonic, showing a perfect limit cycle in the phase plot.

In order to understand how these patterns interfere regarding the bubble stability, it is important to discuss its response in the phase space, as shown in figure (4.1). For higher values of applied magnetic field, the bubble reacts as an harmonic sysem, showing only one energetic state. For $Re_{mag} = 1$, there is a deformation in the limit cycle, showing the distortion in the valley of the time response.

For low values of applied magnetic field, such as $Re_{mag} = 10$, the behavior approaches the one seen in the Newtonian case. Two energetic levels are present by the second limit cycle. This response represents a new frequency of oscillation, showing that two periods are present. When a magnetic field is applied, there are two mechanisms that describe the relaxation of a colloidal

ferrofluid [53]. The first mechanism is the relaxation due to the particle's hydrodynamic rotation and is called Brownian diffusion time.

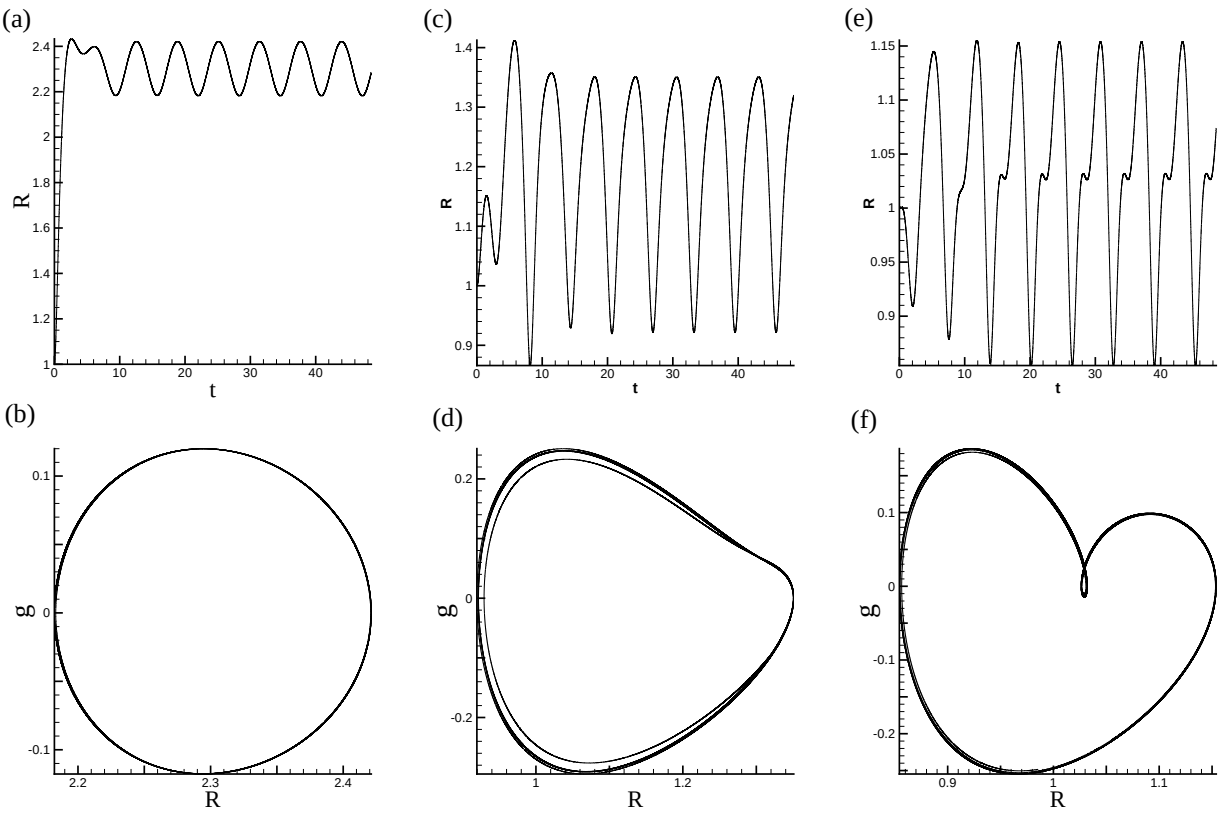

Figure 4.1: (a) and (b) represent the bubble response in time and phase plot, respectively, for $Re_{mag} = 0.1$; (c) and (d) show the bubble behavior in time and phase plot, respectively, for $Re_{mag} = 1$; (e) and (f) represent the response in time and phase plot for $Re_{mag} = 10$. In all cases, $Re = 10$, $We = 5$, $\varepsilon = 0.3$ and $\chi = 1$.

The Néel mechanism, on the other hand is related to the magnetic dipole rotation. In general, these mechanisms can be added to other time scales presented on the Mathematical Modeling section. The coupling of these time scales can modify the bubble behavior, increasing, for example, its amplitude of oscillation and avoiding the collapse. This result is shown in Figure (4.2). In this case, the amplitude of the oscillating bubble radius increases when the time scales are coupled. The bubble oscillation remains stable despite the bigger amplitude. When the applied magnetic field is increased, the time scales do not couple. In this case, the magnetic dipoles align faster than the inertial forces can act. On the other hand, by decreasing the magnetic field, the viscous effects become more present, hindering the bubble expansion and contraction movements. A key finding of the present investigation was that the nonlinear oscillatory motion of a gas bubble in a ferrofluid induced by a sufficiently large magnetic field can be attenuated. It happens when the magnitude of the magnetic force is comparable to the inertia force acting on the bubble interface. This magnetic effect is a direct consequence of an extra normal stress (magnetic pressure) produced in the surrounding polarized fluid under the action of a field [4].

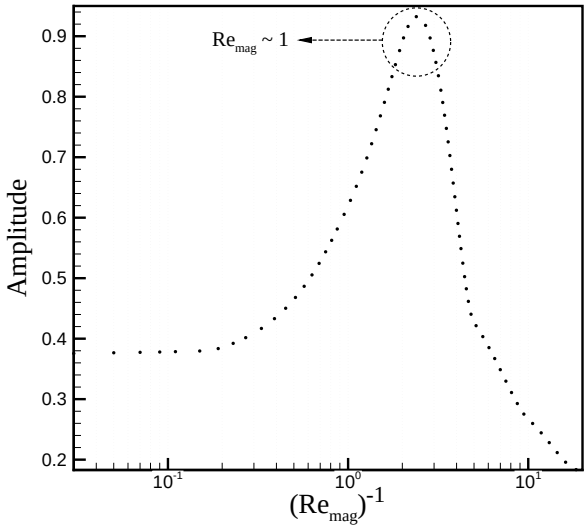

Figure 4.2: Amplitude of oscillation as a function of $1/Re_{mag}$. The dashed circle represents the higher values of amplitude, present where the time scales couple. In this case $Re = 10$, $We = 10$, $\varepsilon = 0.35$, $\omega = 1$ and $\chi = 1$.

Once the bubble is now subjected to an external magnetic field and immersed in a magnetic fluid, it is possible to analyze how the concept of collapse is modified by studying the collapse diagram. Under the influence of a magnetic field, a magnetic torque due to the presence of an external field acting on the magnetic particles causes the magnetization $\boldsymbol{M}$ to be out of phase with $\boldsymbol{H}$. In this situation, the expression for these magnetic torque, $\boldsymbol{T} = \mu_0 \boldsymbol{M} \times \boldsymbol{H}$, acting on the particles will try to rotate this magnetic domains, resulting in a higher resistance of the particles to rotate in the direction of the fluid vorticity which may result in an increase in the suspension effective viscosity [54, 13, 39, 56]. Based on the change of viscous effects due the application of a variable external field, it is expected that the collapse criteria is modified. When the applied magnetic field is increased, there is a stabilization on the bubble movement preventing the collapse. Even with a smaller magnetic field, $Re_{mag} = 1$, the result is more proeminent than in the case of the bubble immersed in a Newtonian fluid. It is interesting to see that we can capture this damping effect of the nonlinear responses by the application of an external field, which would be equivalent to increase the fluid viscosity.

4.1.1 Magnetic Susceptibility Influence

The response of the material to an applied field, characterized by the magnetization behavior is depicted by the suspension magnetic susceptibility. Its response describes along with the magnetic permeability, the magnetic behavior of the material. In some cases, such as for diamagnetic materials, susceptibility is small and negative. In other cases, the relationship between magnetization and applied field is nonlinear, so that the magnetic susceptibility varies with the intensity of this applied magnetic field.

Based on these considerations, a study regarding the influence of the magnetic susceptibility was made. Figure (4.3) shows the behavior of the bubble radius as a function of χ for different values of χ for $Re_{mag} = 1$. We note that for higher values of the magnetic susceptibility, the transient response leads to an increase in the oscillation values of the bubble radius. However the steady state response is directed to a more harmonic pattern. In addition to reaching higher values in the initial transient response, the bubble behavior at steady state is harmonic and represented by a limit cycle in the phase plane. The amplitude of oscillation in steady state is smaller, contributing for the bubble stabilization.

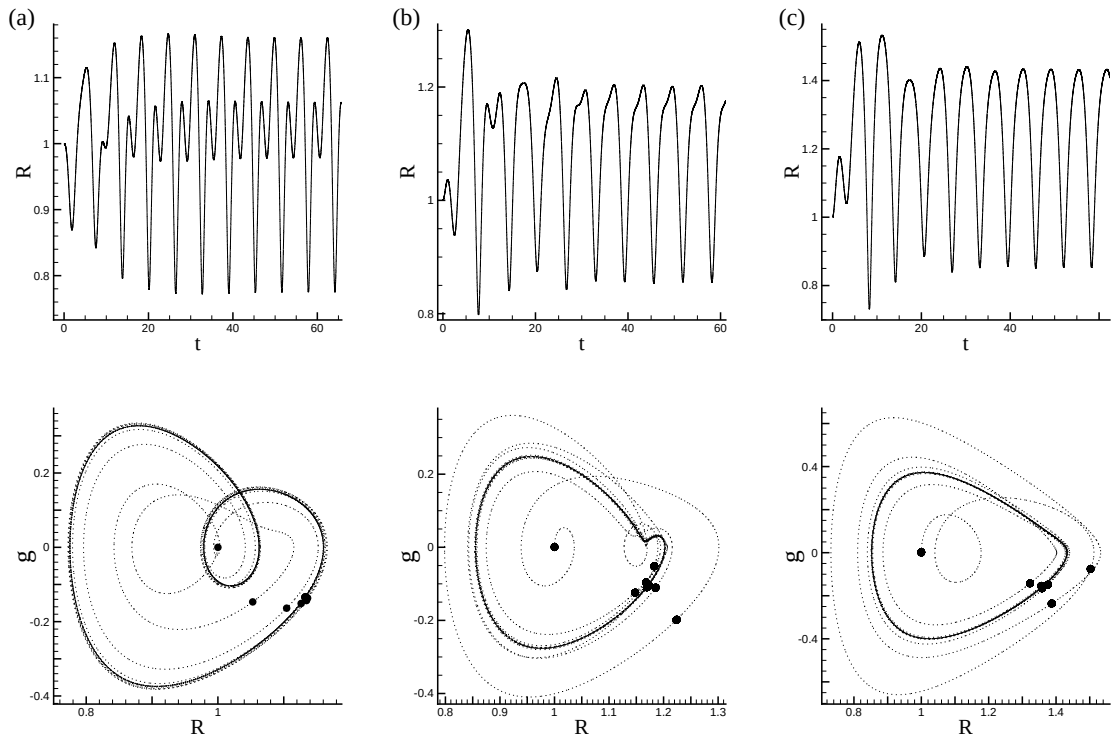

Figure 4.3: Bubble behavior for different magnetic susceptibilities. In (a) $\chi = 0.1$; (b) $\chi = 0.5$; and (c) $\chi = 1$. The top images show the time response and the images bellow show the phase plot and Poincaré section (black dots). For all tests $Re_{mag} = 1$, $Re = 20$, $We = 10$, $\varepsilon = 0.3$ and $\omega = 1$.

This behavior is directly related to the number of particles that align in the direction of the applied field and how this microstructural dynamic influences the motion of the bubble. In this case, when a small amount of particles align in the field direction, the bubble behavior is similar to the one observed in the case of a bubble immersed on a Newtonian Fluid. In this condition, the magnetic pressure is not enough to decrease the inertial movements. On the other hand, when $\chi = 1$, the magnetic pressure acts as if there was a decrease in the surrounding pressure around the bubble. Since this field is applied from outside it attracts the particles and therefore the fluid in the radial direction trying to expand the oscillating bubble. In other words, the bubble equilibrium

radius grow and the amplitude of oscillation is smaller. This change is even more noticeable in the phase plot. In (b) there is a second limit cycle, which represents a period doubling. We can see a second frequency of oscillation on the time response. This second limit cycle gets smaller with the increase of the magnetic susceptibility, until it reaches an almost harmonic response with only one limit cycle or, as we can see in the Poincaré section, one energy level.

In figure (4.4), with $Re_{mag} = 0.1$ and $\chi = 0.1$, the magnetic contribution is similar to other cases when both Re_{mag} and the χ are more proeminent. In this case, even using a high magnetic field, the amount of particles that align in the field direction is not enough to produce a considerable contribution. On the other hand, when $\chi = 1$, we can admit that the magnetic time scale couples with the inertial one and the magnetic field interacts with both pressure field and the viscous flow produced by the oscillatory motion of the bubble. With that in mind, it is possible to see an harmonic response, oscillating around a higher equilibrium radius but with small oscilattion amplitudes. In that case, we can consider that the magnetic contribution stabilizes the bubble motion. We also note that the coupling of these time scales can cause or prevent the collapse of the bubble.

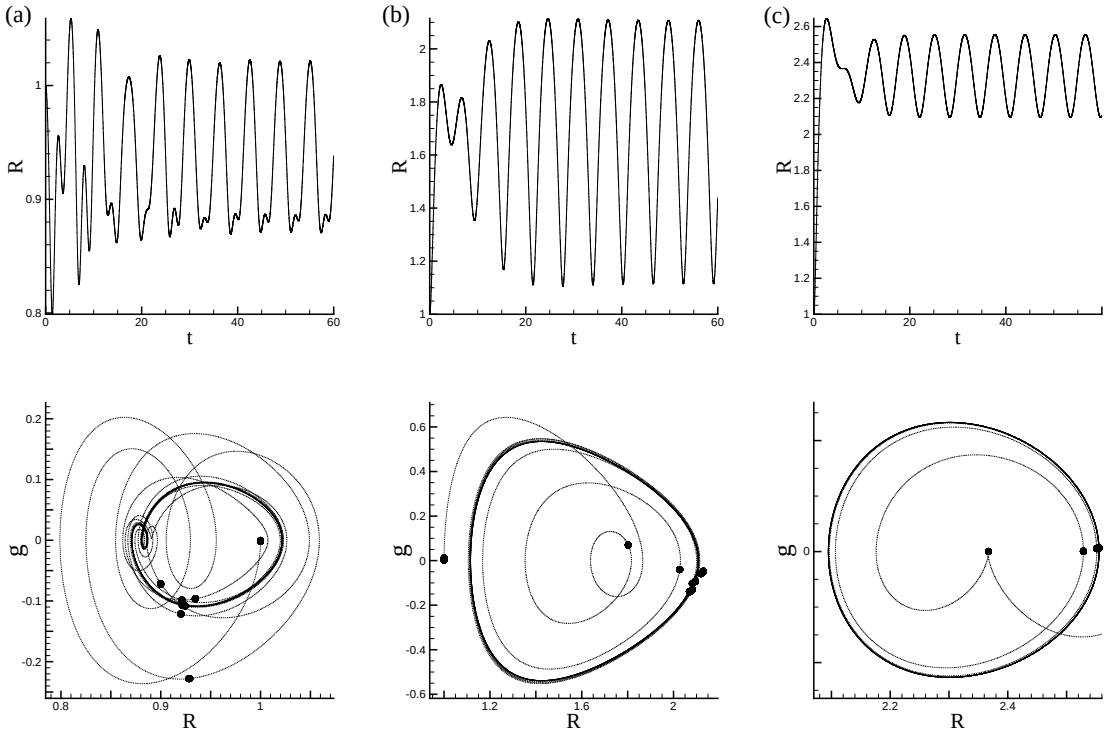

Figure 4.4: Bubble behavior for different magnetic susceptibilities. The top images show the time response and the images bellow show the phase plot and Poincaré section (black dots). For all tests $Re_{mag} = 0.1$, $Re = 20$, $We = 10$, $\varepsilon = 0.3$ and $\omega = 1$.

To sum up, it was noted that the behavior of the bubble varies depending on the magnetic susceptibility. However, the hypothesis of superparamagnetism indicates that the particles align

immediately with the application of the magnetic field. Thus, the magnetic susceptibility is indeed related to a spatial scale, conditioning homogeneity or anisotropy. With the increase of the susceptibility more particles respond to the applied field. In this context, with many accounting particles, i.e for large values of χ, there is a greater homogeneity in the magnetic suspension domain.

4.1.2 Acoustic Field Frequency Influence

The frequency of the acoustic field is also an important parameter of the problem since it's associated with the coupling of other time scales. When the frequency of the field increases, the bubble oscillation period ends not being sufficiently large so that there is a coupling between the viscous, inertial and magnetic forces. In this situation, the bubble begins to oscillate under incomplete periods, showing different frequencies as response.

In Figure (4.5), one can see a dynamic behavior with several degrees of freedom. Moreover, such rapid oscillation changes eventually prevents collapse. Thus, one has a precisely contrary response to the application of a magnetic field: it avoids collapse, but the behavior of the bubble radius becomes very nonlinear during its transient response.

The application of a magnetic field, as shown in figure (4.5) decreases the amplitude of oscillation of the bubble. Basically, the presence of a magnetic pressure, as mentioned before, reduces the effect of the acoustic pressure field. As the excitation frequency is higher than the natural frequency of oscillation of the bubble, the acoutic pressure effects are even smaller. This mechanism reduces the external excitation exerted on the bubble even more. Despite producing a small damping ratio, the transient period is quite fast when the applied magnetic field is high. The phase plots also show a very nonlinear transient but an harmonic response in steady state.

In figure (4.6), the frequency of excitation has been set to $\omega = 10$. In this case, the bubble responds even less to the acoustic field excitation. In this scenario, the amplitude of oscillation is even lower due to the uncoupling of the inertial and excitation time scales. Moreover, during one oscillation period other frequencies are noted (as rapid changes in the radius) that occur due to the high frequency of the acoustic field. In this situation, the application of a magnetic field causes the movement to become even more stable with very low oscillation amplitudes. Moreover, at higher frequencies, it is noted that the application of a magnetic field can prevent the collapse, in addition to stabilizing its movement.

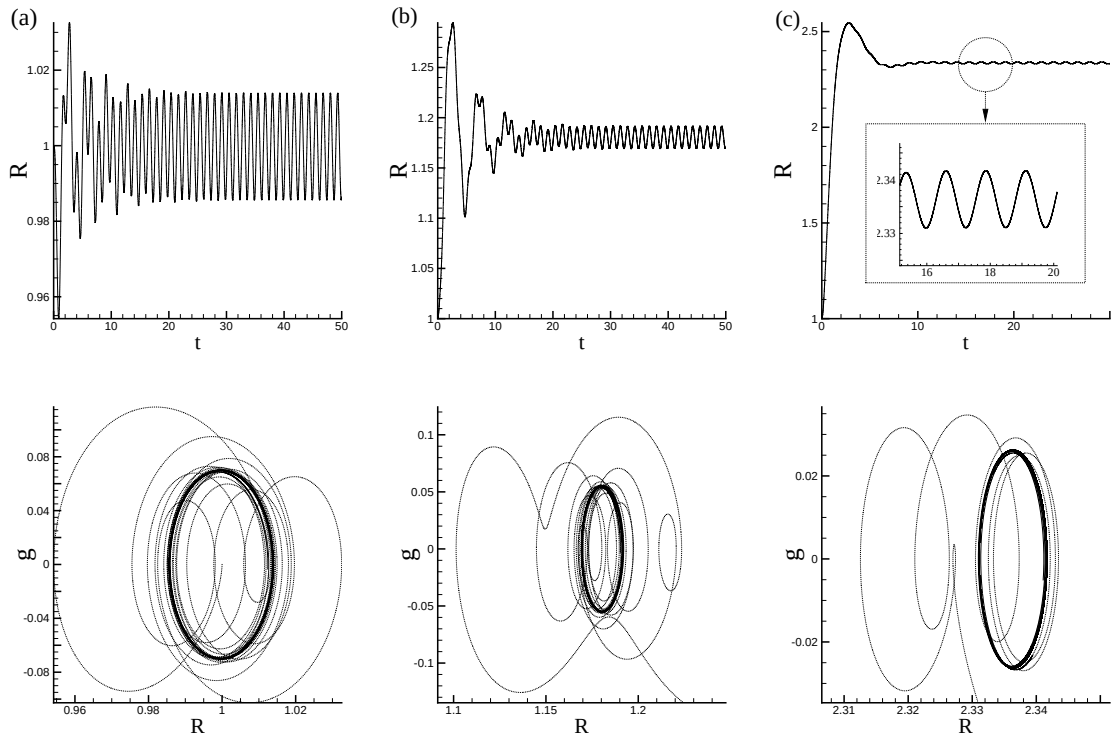

Figure 4.5: Bubble radius behavior (a) $Re_{mag} \to \infty$ and $\chi = 0$; (b) $Re_{mag} = 1$ and $\chi = 1$; and (c) $Re_{mag} = 0.1$ and $\chi = 1$. In all cases $Re = 10$, $We = 10$, $\omega = 5$ and $\varepsilon = 0.3$. The insert in (c) is a zoom from $t = 15$ to $t = 20$, with a steady state response.

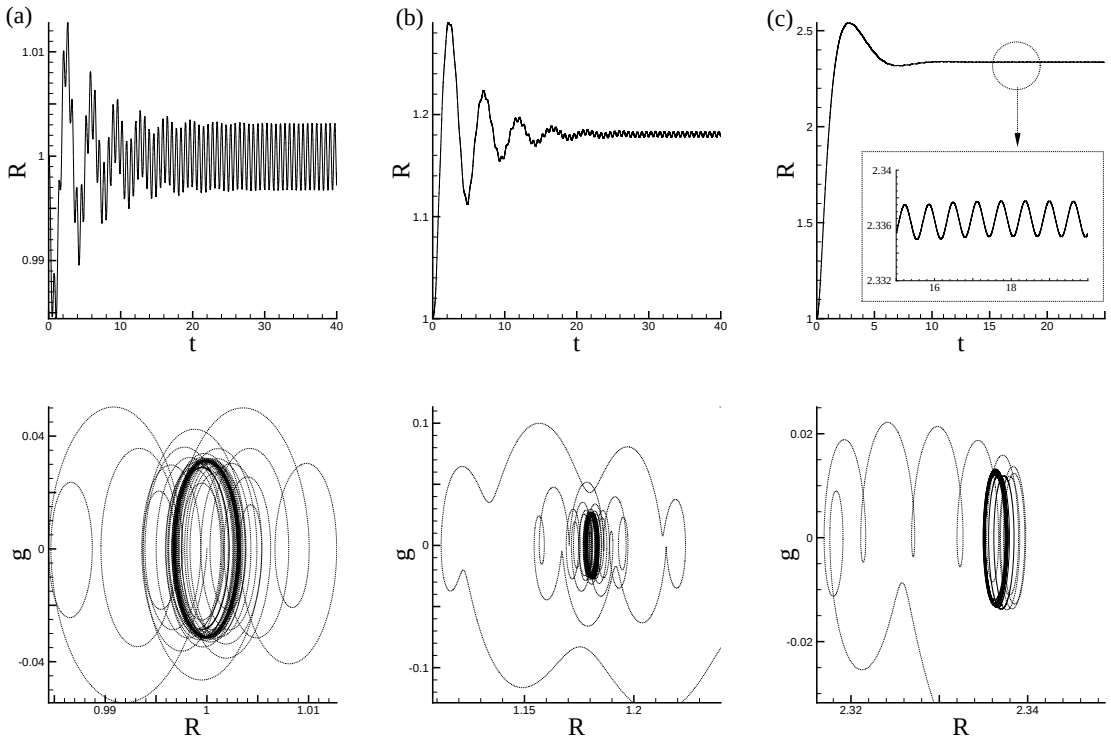

Figure 4.6: Bubble radius behavior (a) $Re_{mag} \to \infty$ and $\chi = 0$; (b) $Re_{mag} = 1$ and $\chi = 1$; and (c) $Re_{mag} = 0.1$ and $\chi = 1$. In all cases $Re = 10$, $We = 10$, $\omega = 10$ and $\varepsilon = 0.3$. The insert in (c) is a zoom from $t = 15$ to $t = 20$, with a steady state response.

4.1.3 Hydrodynamic Linear Stability Analysis

The importance of this analysis is to determine the influence of each physical parameter on the amplification or attenuation of a small perturbation around an equilibrium state of the system. It was noted that much of the physical interpretation of the results shown so far relies on the role that different typical time scales have in the bubble dynamics. The application of an external field changes the microscopic characteristics of the fluid. In this context, the non-dimensional numbers have a major role in stabilizing the bubble movement. In this particular problem we use a continuum mechanics formulation of the ferrohydrodynamics balance equations of a superparamagnetic fluid in order to capture how microstructural modifications in the suspension structure influence the macroscopic behavior of this oscillating bubble in its radial direction.

In this section a linear stability analysis will be developed from small amplitude disturbances within the bubble radius. Considering $R = 1 + \delta(t)$ MRP equation and excluding the sinusoidal excitation we have:

$$\begin{aligned}\ddot{\delta(t)}(1+\delta(t)) + \frac{3}{2}\dot{\delta(t)}^2 = \\ \frac{2}{We}\left[\frac{1}{(1+\delta(t))^3} - \frac{1}{(1+\delta(t))}\right] \\ + \left(\frac{1}{(1+\delta(t))}\right)^3 - 1 - \frac{4}{Re}\frac{\dot{\delta(t)}}{(1+\delta(t))} + \\ \frac{1}{Re^{mag}}\left\{\frac{\chi}{2}\left[\ln\left(\frac{R_\infty}{(1+\delta(t))}\right) - \frac{C_1}{2}\right] - \frac{C_1}{8}\right\}.\end{aligned} \tag{4.1}$$

Excluding the terms of higher order and considering a binomial expansion so that:

$$(1+R)^{-3} = 1 - 3R - \frac{3}{2}(1-3)R^2 + \mathscr{O}(R)^3, \tag{4.2}$$

$$(1+R)^{-1} = 1 - R + R^2 - \mathscr{O}(R)^3, \tag{4.3}$$

we have:

$$\begin{aligned}\ddot{\delta(t)} + \delta(t)\ddot{\delta(t)} + \frac{3}{2}\dot{\delta(t)}^2 = \\ \frac{2}{We}\left[-3\delta(t) - \frac{3}{2}(1-3)\delta(t)^2 + \delta(t) - \delta(t)^2\right] \\ +1 - 3\delta(t) - \frac{3}{2}(1-3)\delta(t)^2 - 1 - \\ \frac{4}{Re}\dot{\delta(t)}(1 - \delta(t) + \delta(t)^2) + \\ \frac{1}{Re^{mag}}\left\{\frac{\chi}{2}\left[(\ln(R_\infty) - 1 - \delta(t)) - \frac{C_1}{2}\right] - \frac{C_1}{8}\right\}.\end{aligned} \tag{4.4}$$

Now we insert a perturbation given by $\delta(t) = f_0 e^{st}$ and obtain the problem characteristic polynomial, given by

$$s^2 + \frac{4}{Re}s + \left(3 + \frac{\chi}{2Re_{mag}} + \frac{4}{We}\right) = 0. \tag{4.5}$$

In this case, the two roots or eigenvalues are given by:

$$s_{1,2} = -\frac{4}{Re} \pm \sqrt{\frac{16}{Re^2} - 4\left(3 + \frac{\chi}{2Re_{mag}} + \frac{4}{We}\right)}. \tag{4.6}$$

In this context, $s = \xi - i\omega$. The real part is responsible for the growth or reduction of the disturbances. On the other hand the imaginary part is associated with the disturbances phase and hence its speed of propagation. We can see from equation (4.6) that both roots give us stable behaviors, unless we have a negative magnetic susceptibility. If χ is negative, the material is diamagnetic. In this case, the magnetic field in the material is weakened by the induced magnetization.

One solution is the desired dispersion relation, in which there will probably be stable and unstable modes. This will be obtained for the calculated value in equation (4.6) with the negative sign. The other solution always provide stable modes, which confirm what our previous results have shown so far: the application of an external magnetic field tends to stabilize the oscillatory motion of the bubble.

However in order to present a careful analysis of the system we will consider in this section the case of a bubble immersed in a diamagnetic fluid, as studied experimentally by [57]. Therefore, the bubble movement will be considered locally stable when $\xi < 0$. For $\xi = 0$, we have the neutral stability condition, since the modes will not be amplified or attenuated in the course of time. In this context, this condition produces the so-called neutral stability curve. In our case, this curve will be a function of three dimensionless parameters: We, χ and Re_{mag} and their relation is given by

$$We = -\frac{8Re_{mag}}{6Re_{mag} + \chi}. \tag{4.7}$$

In figure (4.7), we can see the three stability points in both cases (a) and (b). In region A, all values lead to an unstable behavior. On the other hand, in region B, the roots real part is negative and the disturbance and oscillation are out of phase with each other. In region C, there is no imaginary part and the real one is always negative, leading to locally stable points. For that, there is a combination of values that generate only real responses, an stability criterion given by:

$$\frac{\chi}{Re_{mag}} \leq \frac{32}{Re^2} - 24 - \frac{8}{We}. \tag{4.8}$$

In this regard, it is noted again in this linear analysis that the application of a magnetic field stabilizes the nonlinear dynamic behavior of a bubble subjected to an acoustic field. This theoretical analysis helps us to confirm what our numerical results have shown so far.

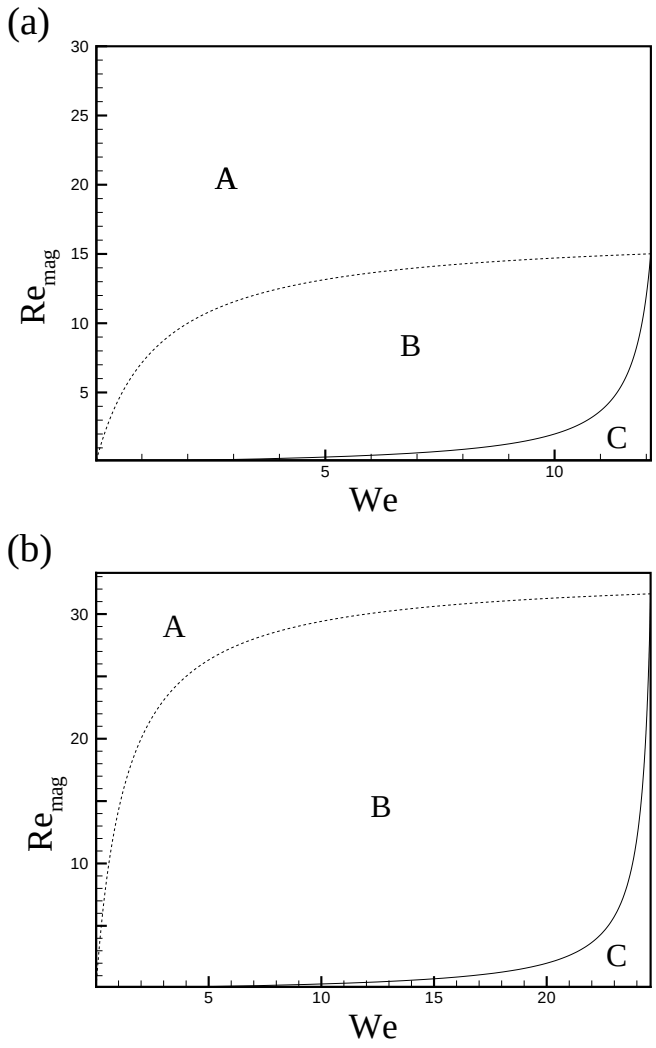

Figure 4.7: Neutral stability curve for (a) $\chi = -100$ and (b) $\chi = -200$. The three regions represent: **A** unstable solution; **B** stable with complex roots; and **C** stable.

4.2 Collapse Diagram

The attenuation of collapse can be seen in figure (4.8). As mentioned before, the application of a magnetic field can stabilize the bubbles motion. In this context, a decrease in Re_{mag} or increase in the magnetic susceptibility, χ, may change the bubble response due to an external pressure forcing.

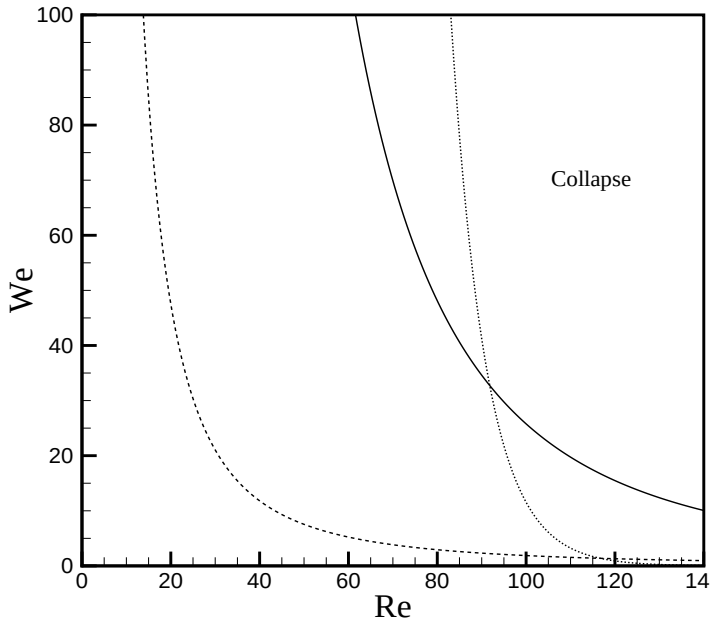

Figure 4.8: Collapse diagram for $Re_{mag} = 1$ and $\chi = 1$ (dashed line), $Re_{mag} = 1$ and $\chi = 3$ (dotted line) and $Re_{mag} \to \infty$ (solid line), as a function of Re and We for $\varepsilon = 0.3$ and $\omega = 1$.

However, this behavior differs from the previously noted, where the presence of the magnetic field transforms the bubble motion in an harmonic oscillation. This phenomenon is explained due to the abrupt transient which is also present in the magnetic case. Whereas the bubble is at equilibrium and both fields are applied at $t = 0$, there is a lag until it reaches a steady state oscillatory regime. During this short period of time, viscous, inertial and magnetic forces are competing without coupling causing abrupt changes in the radius. These changes end up generating high values of the radius derivative, implying in a higher probability of collapse. Nevertheless, it is noted that when the magnetic force is dominant ($\chi = 3$), the magnetic pressure acts trying to compensate the mechanical pressure generated by the acoustic field, preventing the bubble collapse. To sum up, depending on the parameters, the breakdown may be induced or prevented, but the bubble movement remains harmonic in both cases, as seen in figure (4.9).

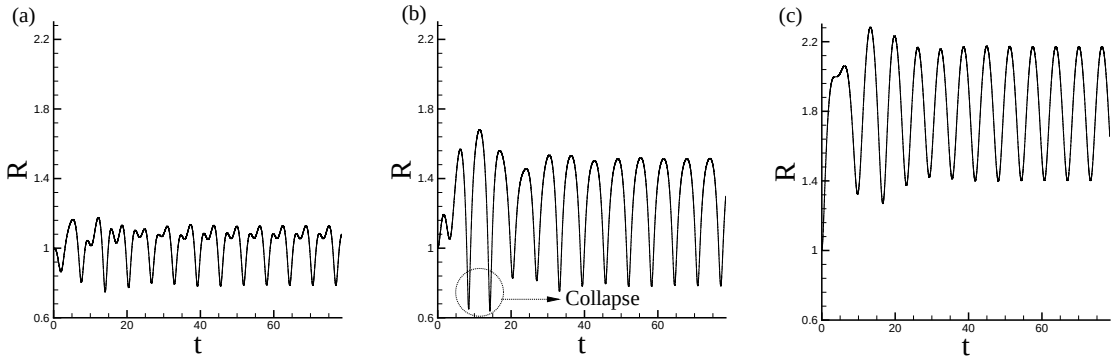

Figure 4.9: Bubble radius behavior without collapse criteria for (a) $Re_{mag} \to \infty$ and $\chi = 0$; (b) $Re_{mag} = 1$ and $\chi = 1$; and (c) $Re_{mag} = 1$ and $\chi = 3$. In all cases $Re = 30$, $We = 30$, $\omega = 1$ and $\varepsilon = 0.3$. In (b) we can see that the transient would cause collapse, even though the response is less nonlinear.

4.3 Vibrational Patterns

The nonlinearity of the MRP equation increases the number of degrees of freedom. That means that even though the system is more stable, it may be possible to find new patterns of vibration. When the Magnetic Reynolds number is unitary, for example, the bubble movement approaches an harmonic pattern. It is observed that inspite of preventing the collapse, the application of magnetic fields can also increase the amplitude of the transient response. In this context, new vibrational patterns appear, as seen in figure (4.10).

These vibrational patterns can be analyzed by different dynamical systems approach of such as Discrete Fourier Transform (DFT), Poincaré section, phase plot, Lyapunov exponents and wavelets transform as shown in 17. Each one of these approaches promotes gain of informations when characterizing a nonlinear dynamic system. For instance, the frequency response give us information about the energy stored in every harmonic. Since the excitation frequency used was $\omega = 1$, we note that the biggest amount of energy is present in the first harmonic of a time series. On the other hand, deformations in the time response also can induce spectral spreading in which the energy of the system spreads along different harmonics. That means that in some part of the system response, there is a frequency variation. That frequency variation is also seen in the phase plot as a shape deformation in the limit cycle. In this case, there is no second limit cycle, pointing out that no period doubling is presented. The Poincaré section is another interesting approach to be used, specially when the system is periodic. The stability of a periodic orbit of the original system is closely related to the stability of the fixed point of the corresponding Poincaré map. We can see that there is a difference in the energy levels seen in the phase plot.

That analysis might leads us to think that the bubble motion is chaotic, due to the nonlinearity of the equation. In order to verify if there is a chaotic behaviour in this context, that is for a spherical oscillating bubble immersed in a magnetic field and subjected to a pressure forcing, the Lyapunov exponents must be obtained.

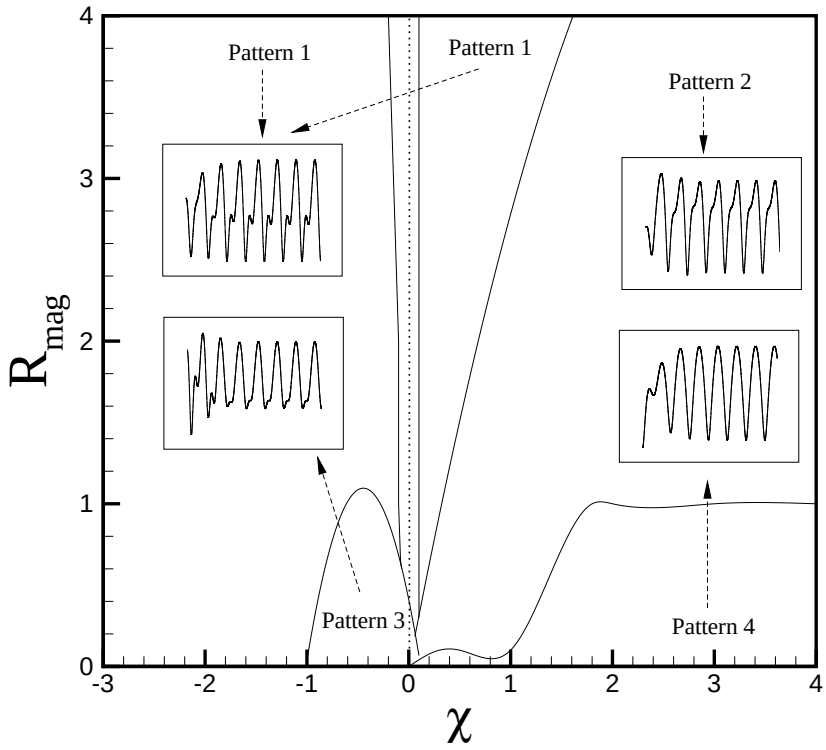

Figure 4.10: Identified vibrational patterns as a function of Re_{mag} and χ. For all cases, $Re = 10$, $We = 10$ e $\varepsilon = 0.3$.

The Lyapunov exponents are considered to be a dynamic measure of the complexity of attractors and can be used for the characterization of chaos and bifurcations, which are very common consequences of high nonlinearity in dynamic systems, such as the transient-oscillatory motion of bubbles in complex fluids [58]. Behnia [59] define the Lyapunov exponents as:

> *Consider two different neighboring points in the phase space in time $t = 0$ and t, with distances in the i direction defined as $||\delta x_i(0)||$ and $||\delta x_i(t)||$. The Lyapunov exponent will reflect the average growth (λ_i) of these initial distances.*

$$\frac{||\delta x_i(t)||}{||\delta x_i(0)||} = 2^{\lambda_i t} \qquad (t \to \infty) \tag{4.9}$$

or

$$\lambda_i = \lim_{t\to\infty} \frac{1}{t} log_2 \frac{||\delta x_i(t)||}{||\delta x_i(0)||} \tag{4.10}$$

Based on that, we migh find three different behaviors of λ:

- If $\lambda < 0$, the trajectories are close (stable oscillation)

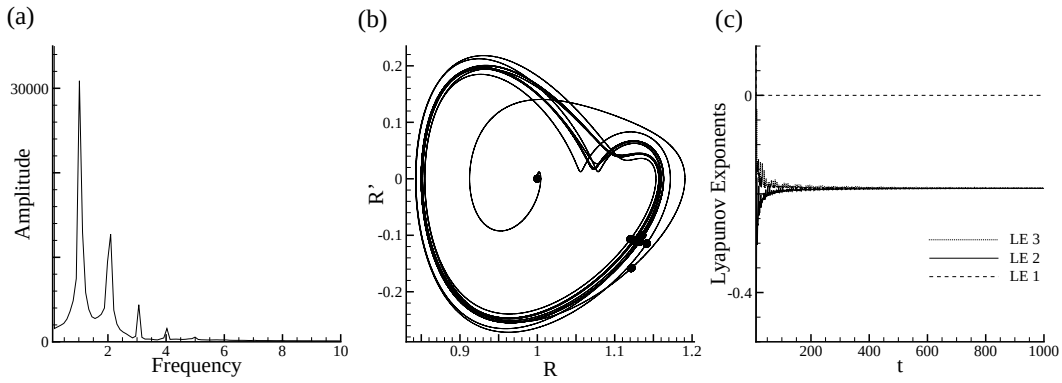

Figure 4.11: Bubble response using different dynamical system approaches to analysis. (a) Shows the DFT; (b) the phase plot and Poincaré section; (c) shows the three Lyapunov exponents. In all cases $Re = 10$, $We = 10$, $\varepsilon = 0.3$, $\omega = 1$, $\chi = 0.3$ and $Re_{mag} = 1$.

- If $\lambda = 0$, then the energy levels maintain their relative positions (stable attractor)
- If $\lambda > 0$, it implies that the energy orbits do not remain nearby (unstable attractor)

To sum up, the existence of positive Lyapunov exponents indicates that there is a chaotic behavior towards infinitesimal differences. In order to compute the Lyapunov exponents, we need to transform the magnetic version of Rayleigh-Plesset equation in an autonomous system, given by Equation 4.11.

$$\begin{cases} \frac{dx}{dt} = y \\ \frac{dy}{dt} = \frac{1}{x}\left[-\frac{3}{2}y^2 + \frac{2}{We}\left(\frac{1}{x^3} - \frac{1}{x}\right)\right] - \frac{1}{x} - \frac{\varepsilon sin(\omega z)}{x} + \frac{1}{x^4} - \frac{4}{Re}\frac{y}{x^2} + \frac{1}{Re_{mag}}\left[\frac{\chi}{2}\left(\ln(5) - \ln(x) - \frac{3}{8}\right) - \frac{3}{32}\right] \\ \frac{dz}{dt} = 1 \end{cases} \tag{4.11}$$

Considering different values of Re, We, ε, Re_{mag}, χ and the initial conditions it is possible to test the chaotic behavior of the bubble using a Matlab Lyaponov Exponents Toolbox. The output of the Matlab LET code [60] may give different behaviors, which can be classified as periodic cycles or stable equilibrium, nonlinear chaotic and pure random processes. In order to compute the bubble vibrational pattern a neural netowork can be trainned. This tool is used in nonlinear systems as a family of statistical learning models inspired by biological neural networks (the central nervous systems of animals, in particular the brain) and are used to estimate or approximate functions that can depend on a large number of inputs and are generally unknown. In practical applications, the use of neural networks can help to identify how the bubble is vibrating and, from that, the dimensionless parameters of the system.

4.4 Neural Networks

As said in the previous section, in machine learning and cognitive science, artificial neural networks (ANNs) are a family of statistical learning models inspired by biological neural networks (the central nervous systems of animals, in particular the brain) and are used to estimate or approximate functions that can depend on a large number of inputs and are generally unknown [61].

This is a very interesting tool to use in pattern identification. In this case, considering the new technologies been used, two networks were trainned in order to identify the bubble vibrational patterns.

For the trainning of both networks, the Scaled Conjugate Gradient method was used in the Matlab Neural Network Toolbox. The basic conjugate gradient backpropagation algorithm adjusts the weights in the steepest descent direction (negative of the gradient). This is the direction in which the performance function is decreasing most rapidly. Even though the Scaled Conjugate Gradient needs more storage than the other second order algorithms, its convergence is more rapid. This algorithm is based upon a class of optimization techniques well known in numerical analysis as the Conjugate Gradient Methods [62]. From an optimization point of view, learning in a neural network is equivalent to minimizing a global error function, which is a multivariate function that depends on the weights in the network. This perspective gives some advantages in the development of effective learning algorithms because the problem of minimizing a function is well known in other fields of science, such as conventional numerical analysis.

Considering the use of a logarithmic or tangential transfer function the results obtained by the neural network as patterns are not integer numbers and those errors can lead to misidentifications. For that approach, ten tests were made for both harmonic and Lyapunov exponents inputs. In the case of the harmonic input, the DFT response containing both amplitude and frequency information from $\omega = 0$ to $\omega = 10$ were given as trainning set. For each case, the targets were given as the correct patterns. In the second network, using Lyapunov exponents, the input is given as the three exponents obtained from the autonomous system as shown in figure 4.12.

For the first network, based on the frequency spectrum, 95 neurons were set in the hidden layer. The network was trainned during 100 epochs for each test. In the first layer a logarithmic transfer function was used and in the second layer a linear transfer function. In the case of the second network, trainned with the Lyapunov exponents, 20 neurons were used in the hidden layer and the network was trainned for 1000 epochs. In the first layer a tangential transfer function was used and in the second layer a linear transfer function.

The performance of the pattern identification using Neural Networks was analyzed based on the normalized error. In this case, it was defined as the normalized absolute error between the identified pattern and the correct one:

$$E = \frac{|P_i - P_c|}{4} 100\%, \tag{4.12}$$

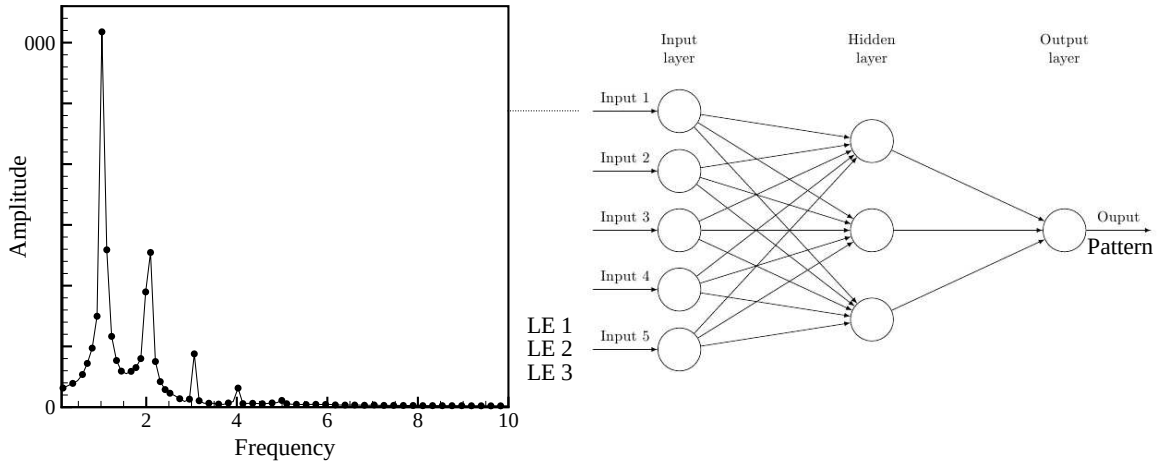

Figure 4.12: Typical schematic of a neural network.

where P_i is the pattern identified by the network and P_c is the correct pattern.

In table 4.1 we can see an example related with three selected results between the ten tests performed. In this case, the higher relative error is 13.55%. Considering a bigger validation set, the error propagation is not going to be alarming. On the other hand, from table 4.2, we can see the larger relative error when using lyapunov exponents as the main information to train the neural network. Nevertheless, this information is not enough to decide which method would be better to use.

Table 4.1: Identified pattern and normalized error for the 3 of the 10 tests using the harmonic input.

	Test 1	Test 2	Test 3
Pattern 1	1.008 (0.2 %)	1.013 (0.33 %)	1.024 (0.60 %)
Pattern 2	1.905 (2.38 %)	1.795 (5.13 %)	1.729 (6.78 %)
Pattern 3	2.894 (2.65 %)	3.127 (3.18 %)	3.075 (1.88 %)
Pattern 4	4.237 (5.93 %)	4.135 (3.38 %)	3.967 (0.83 %)

Table 4.2: Identified pattern and normalized relative error for the 3 of the 10 tests using Lyapunov exponents input.

	Test 1	Test 2	Test 3
Pattern 1	1.335 (8.38 %)	1.387 (9.68 %)	1.430 (10.75 %)
Pattern 2	2.183 (4.58 %)	2.035 (0.88 %)	2.088 (2.20 %)
Pattern 3	3.099 (2.48 %)	2.906 (2.35 %)	3.118 (2.95 %)
Pattern 4	4.342 (8.55 %)	3.906 (2.35 %)	3.783 (5.43 %)

We can see from figure 4.13 that even though the results from tables 4.1 and 4.2 have shown that the Lyapunov exponents can lead to more missidentifications, on the average, the results are more accurate and carry some relevant informations. The tests carried out here have demonstrated

that the use of less information as input, such as the Lyapunov exponents, and more epochs of trainning may be more efficient. In this condition, the network has more time to adjust the neurons weights. In general, the patterns have small distinctions among themselves and the use of the frequency spectrum ends up not being the best tool. This is because the differences in bandwidth and amplitude of each harmonic do not change much. For this reason, the network ends up having difficulties in storing the primary characteristics of each pattern. If the patterns presented more non-linear characteristics as shown in other studies [61], the use of the frequency spectrum would be more appropriate.

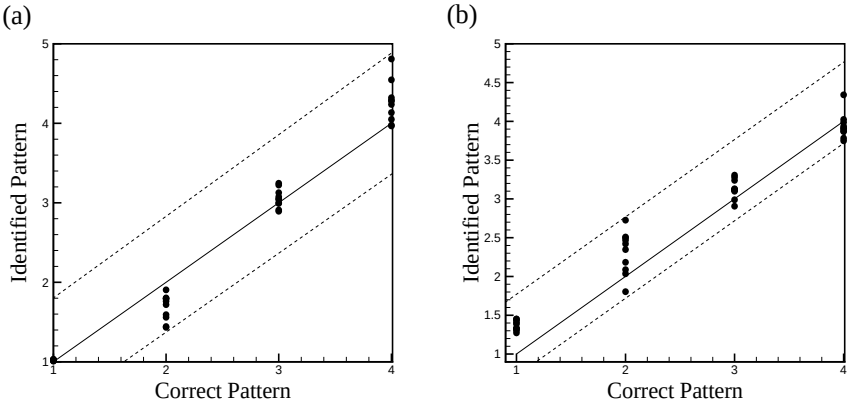

Figure 4.13: Comparison between both networks explored in the present work. (a) Result of 10 tests made with different weights initial conditions for the frequency spectrum input; (b) Results of 10 tests made with different weights initial conditions for the Lyapunov exponents input;

In order to consider the pattern identification, the obtained pattern was rounded to an integer. In this context, the higher the error obtained in the previous approach, the greater the chances for the neural network to misidentify the pattern (considering the rounding).

Table 4.3: Identified pattern for the 10 tests for the harmonic input. In this context, the neural network idenfity accurately the pattern in 90% of cases.

	Test 1	Test 2	Test 3	Test 4	Test 5	Test 6	Test 7	Test 8	Test 9	Test 10
Pattern 1	1	1	1	1	1	1	1	1	1	1
Pattern 2	2	2	2	1	2	2	2	2	1	2
Pattern 3	3	3	3	3	3	3	3	3	3	3
Pattern 4	4	4	4	5	5	4	4	4	4	4
Correct Identification	100 %	100 %	100 %	50 %	75 %	100 %	100 %	100 %	75 %	100 %

As we can see from tables 4.3 and 4.4, the Lyapunov exponents give a robust way for examining the bubble dynamic system explored in this work with neural network. The neural network correctly identified the vibrational pattern in 95 % of the cases. This is a consequence due to the fact that the network trained with the Lyapunov exponent has less information to be used in training (only 3 numbers), whereas in the case of frequency spectrum 95 points were used for each input. In addition, the exponents have been more sensitive to the changes of the patterns. This shows that the DFT may not be the most appropriated approach for this type of analysis in the absence

Table 4.4: Identified pattern for the 10 tests for the harmonic input. In this context, the neural network idenfity accurately the pattern in 95% of the cases.

	Test 1	Test 2	Test 3	Test 4	Test 5	Test 6	Test 7	Test 8	Test 9	Test 10
Pattern 1	1	1	1	1	1	1	1	1	1	1
Pattern 2	2	2	2	3	2	2	2	2	3	2
Pattern 3	3	3	3	3	3	3	3	3	3	3
Pattern 4	4	4	4	4	4	4	5	4	4	4
Correct Identification	100 %	100 %	100 %	100 %	75 %	100 %	100 %	100 %	75 %	100 %

of pattern being highly nonlinear. Indeed, from a practical point of view, changes in harmonics amplitude are not very significant in these cases.

In pratical problems that make use of the cavitation phenomena and ferrofluids, this identification opens application possibilites in different fields, such as biomedical and naval industries. In the cavitation study, characterizing the bubble freedom degrees in its nonlinear motion is very important for predicting premature collapse. In this context, using neural networks in order to identify cavitation vibrational modes seems to be very promising for a complete characterization of bubble dynamics.

Chapter 5

Oscillatory Magnetic Field

This chapter presents the results obtained for a bubble immersed in a magnetic fluid under the action of an oscillating magnetic field. In this situation, new vibrational modes are analyzed and the decorrelation between the excitation frequencies of acoustic and magnetic fields lead the bubble to a chaotic behavior.

5.1 Introduction

An oscillating magnetic field differs from an static magnetic field since it is time dependent. In order to understand how the oscillatory magnetic field would interact with the static magnetic field, two different conditions were proposed. In the first one, only the oscillatory contribution would be study. In the second one, both static and oscillatory would be used in order to see how the bubble would react.

5.2 First Field Condition

In this context, the H_0 would be replaced by $H(t)$, in which $H(t) = H_0 \sin(w_{mag}t)$. Therefore, equation 2.43 is rewritten as:

$$\frac{2\dot{R}R + R^2\ddot{R}}{R} - \frac{2\dot{R}^2R^4}{4R^4} = \frac{p_l(R) - p_\infty}{\rho} - \frac{1}{\rho}\left[\mu_0\left(\frac{-3\mu_r^2 H(t)^2}{8}\right)\right]$$
$$+\frac{1}{\rho}\mu_0\chi\left[\frac{-\mu_r H(t)^2}{3} - \frac{17\mu_r H(t)^2}{12} + \frac{H_0^2}{2}\ln(R_\infty) - \frac{H(t)^2}{2}\ln(R)\right]. \quad (5.1)$$

After the same algebric manipullations presented in the Mathematical Modelling chapter, the MRP equation can be written as:

$$R^*\ddot{R}^* + \frac{3}{2}(\dot{R}^*)^2 = \frac{2}{We}\left[\frac{1}{(R^*)^{3n}} - \frac{1}{R^*}\right] - 1 - \varepsilon^* sen(\omega^* t^*)$$
$$+\frac{1}{(R^*)^{3n}} - \frac{4}{Re}\frac{\dot{R}^*}{R^*} + \frac{\sin(\omega_{mag} t)}{Re^{mag}}\left\{\frac{\chi}{2}\left[\ln\left(\frac{R^*_\infty}{R^*}\right) - \frac{C_1}{2}\right] - \frac{C_1}{8}\right\}. \quad (5.2)$$

In practical applications, it would be the same as having the exclusive application of a sinusoidal magnetic field.

5.2.1 Frequency Coupling Analysis

The addition of one more frequency at the system also adds a new time scale. Being a highly nonlinear system, it is expected that the application of an oscillating magnetic field will influence the movement of the bubble. However, this should only occur when the time scales are coupled. Otherwise, if the time scale of the oscillating magnetic field is much bigger than the bubble oscillation time, the results should be similar to the ones obtained for a bubble immersed in a Newtonian fluid [61].

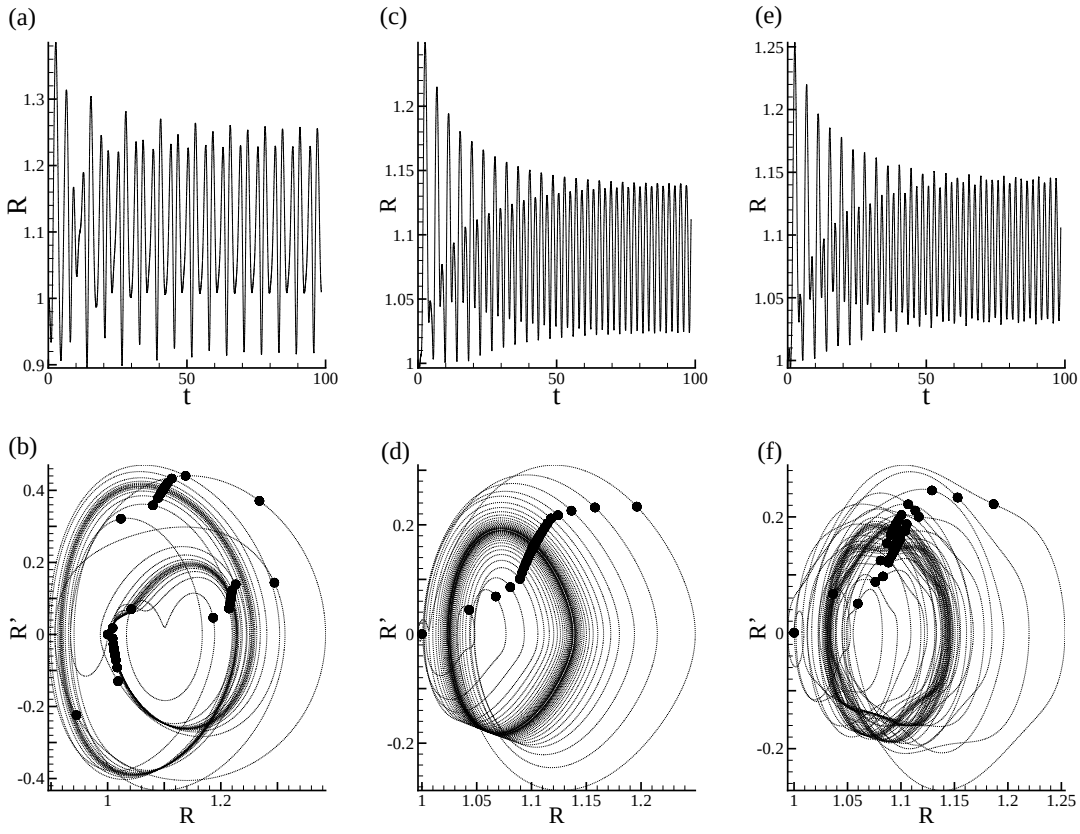

Figure 5.1: Bubble response for $\varepsilon = 0.4$, $Re = 20$, $We = 20$, $\omega = 3$, $Re_{mag} = 1$, $\chi = 1$ when (a) $\omega_{mag} = 1$ in time and (b) phase plot with Poincaré section; (c) $\omega_{mag} = 3$ in time and (d) phase plot with Poincaré section; and (e) $\omega_{mag} = 5$ in time and (f) phase plot with Poincaré section;

It is possible to see from figure 5.1(a,b) that when the magnetic frequency is smaller than the

pressure forcing one, the bubble reacts the same way as when it is immersed in a Newtonian fluid. That happens because the bubble oscillation time is much smaller than the magnetic one. In this case, when the particles align in the field direction, the bubble has already oscillated during several periods. Thus, since it is a sinusoidal field, when the particles align, the field starts to decrease and there is a relaxation in the fluid, allowing the movement of the bubble.

On the other hand, when the magnetic frequency is the same as the pressure one, as shown in 5.1(c,d), there is a coupling between these mechanisms. It is observed that there is a transient in which the bubble changes from a stacionary condition to a state of reaction of several different mechanisms. In this context, after the transient, there is a stabilization and an harmonicity is observed in the movement thereof. This can be observed even in the phase space, in which a limit cycle is observed with no period doubling or bifurcations. When the magnetic frequency increases, the coupling mechanisms decrease and the movement of the bubble, although stabilized, suffer from some variations in frequency. It is interesting to see that since the magnetic field acts much faster in this case, the bubble still reacts to its actions. However, the bubble sees it as if a weaker magnetic field has been imposed.

5.2.2 Magnetic Parameters Interaction

Similarly to the case of the static field, the magnetic parameters are of great influence on the system. Note from figure 5.2 that when the applied field has high intensity with $\chi = 1$, there is an attenuation in the bubble oscillation amplitude. However, there is a period doubling. On the other hand, when the magnetic susceptibility is small (ie. $\chi = 0.1$) the magnetic particles do not align in the field direction and the behavior is similar to the case when $Re_{mag} = 0.1$ and $\chi = 1$. This shows us that the applied field and the magnetic susceptibility are two complementary parameters. In general, if few particles are magnetized, the result is similar to the case when a low field is applied in a medium with high susceptibility.

The condition shown in (5.2c) lead us to think that the application of a specific magnetic field and susceptibility migh lead the bubble to a nonlinear behavior or even chaotic, due to time scales uncopling.

5.3 Second Field Condition

In this case, as explained before, there is an static field and an oscillating field in addition. Yoshimura [63] classified the effects of magnetic fields on microbial growth and reproduction. In biology, the use of static and oscillating magnetic fields may modify the growth (or destruction) of microorganisms. Moore [64], for example, showed that the population of *Pseudomonas aeruginosa* and *Candida albicans* increased when the frequency of the aplied oscillatory magnetic field increased. On the other hand, the cell population of *Streptococcus themophilus* reduced from $25,000$ cells$/ml$ to 970. In this condition, in order to not affect the living microorganisms or try to compensate one field action, both static and oscillating fields are applied. This aims to keep

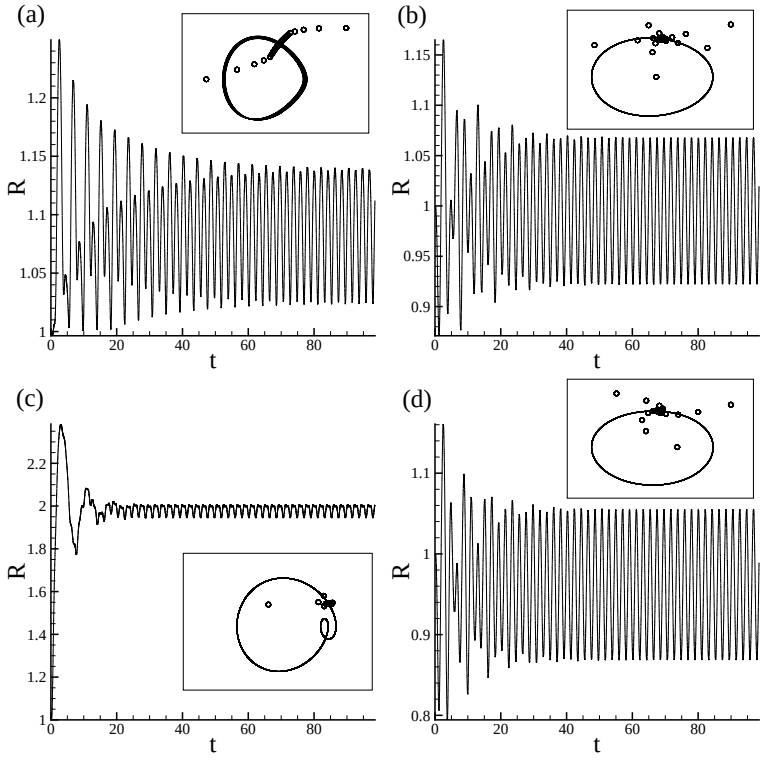

Figure 5.2: Bubble response for $\varepsilon = 0.4$, $Re = 20$, $We = 20$, $\omega = 3$, $\omega_{mag} = 3$ when (a) $Re_{mag} = 1$, $\chi = 1$; (b) $Re_{mag} = 1$ and $\chi = 0.1$; (c) $Re_{mag} = 0.1$ and $\chi = 1$; (d) $Re_{mag} = 0.1$ and $\chi = 0.1$.

the medium intact in biologial aspects.

For that, H_0 is replaced by $H(t) = H_0[1 + \sin(w_{mag}t)]$ and the MRP equation becomes:

$$R^*\ddot{R}^* + \frac{3}{2}(\dot{R}^*)^2 = \frac{2}{We}\left[\frac{1}{(R^*)^{3n}} - \frac{1}{R^*}\right] - 1 - \varepsilon^* sen(\omega^* t^*)$$
$$+\frac{1}{(R^*)^{3n}} - \frac{4}{Re}\frac{\dot{R}^*}{R^*} + \frac{(1 + 2sin(\omega_{mag}t) + \sin(\omega_{mag}t)^2)}{Re^{mag}}\left\{\frac{\chi}{2}\left[ln\left(\frac{R^*_\infty}{R^*}\right) - \frac{C_1}{2}\right] - \frac{C_1}{8}\right\}. \quad (5.3)$$

5.3.1 Magnetic Frequency Influence

Considering the sum of both oscillatory and static fields, the magnetic contribution is superior than other cases. Accordingly, it is possible to see in figure 5.3 a bifurcation diagram involving the two frequencies: magnetic and non-magnetic.

It is noted the existence of new modes of vibration. In this context, observing figure 5.4 one may see patterns with smaller amplitudes, for example, as seen in patterns 1 and 2. On the other hand, the application of an oscillatory field in addition with the static one may lead to the nonlinear behavior seen in pattern 6. In this pattern, specifically, the harmonic oscillation is modulated by another frequency. That behavior is normally seen in the FM radio waves, for example. In this case, there are two leading frequencies: one related to the oscillation and another related to the

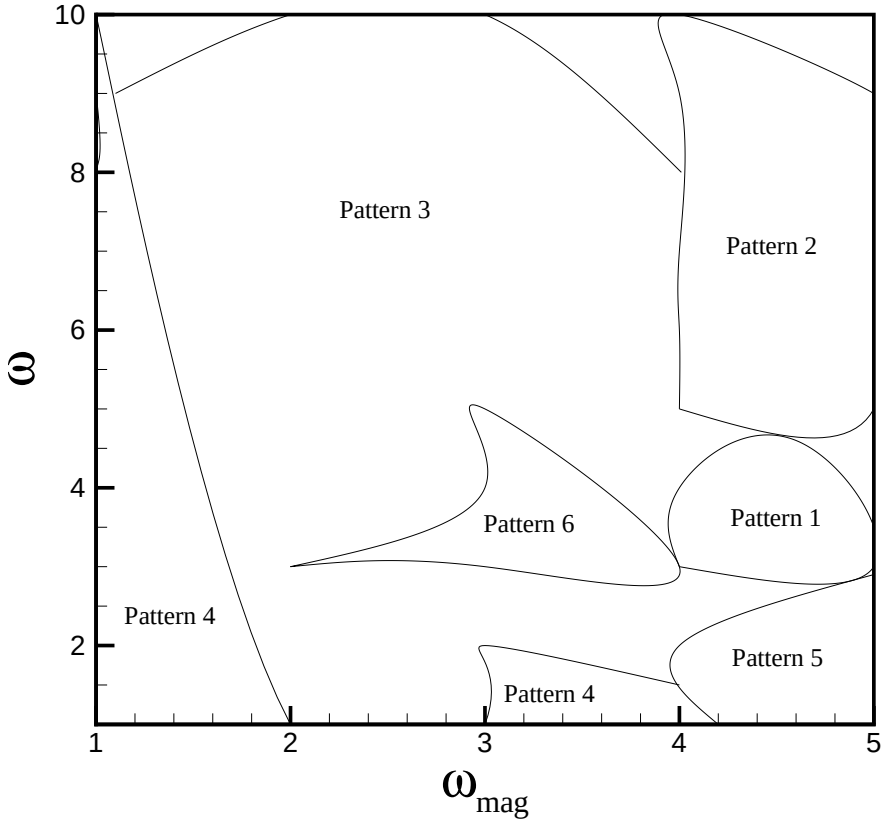

Figure 5.3: Bifurcation diagram as a function of ω and ω_{mag} for $Re = 60$, $We = 20$, $Re_{mag} = 1$, $\chi = 1$ and $\varepsilon = 0.8$.

modulation [65].

This shows us the importance of frequency coupling. In order to control the bubble motion, the application of both oscillatory and static field is the best option, since several new patterns appear. On the other hand, the system becomes more sensibe to the parameters. This sensitivy to initial conditions migh lead the bubble to a chaotic behavior, specially because of the presence of new parameters concerning different physical mechanisms.

5.4 Chaos Analysis

A chaotic time-series analysis can give us a profound insight into the complex hydrodynamics of gas liquid systems. In this context, the study of bubble behavior has been the center of attention and it is shown that this phenomenon exhibits highly complex and chaotic dynamics both experimentally [66, 67, 68] and numerically [69, 70].

As said before, the existence of a positive Lyapunov exponent is the indicator of chaos, showing that neighboring points with infinitesimal differences at the initial state abruptly separate from

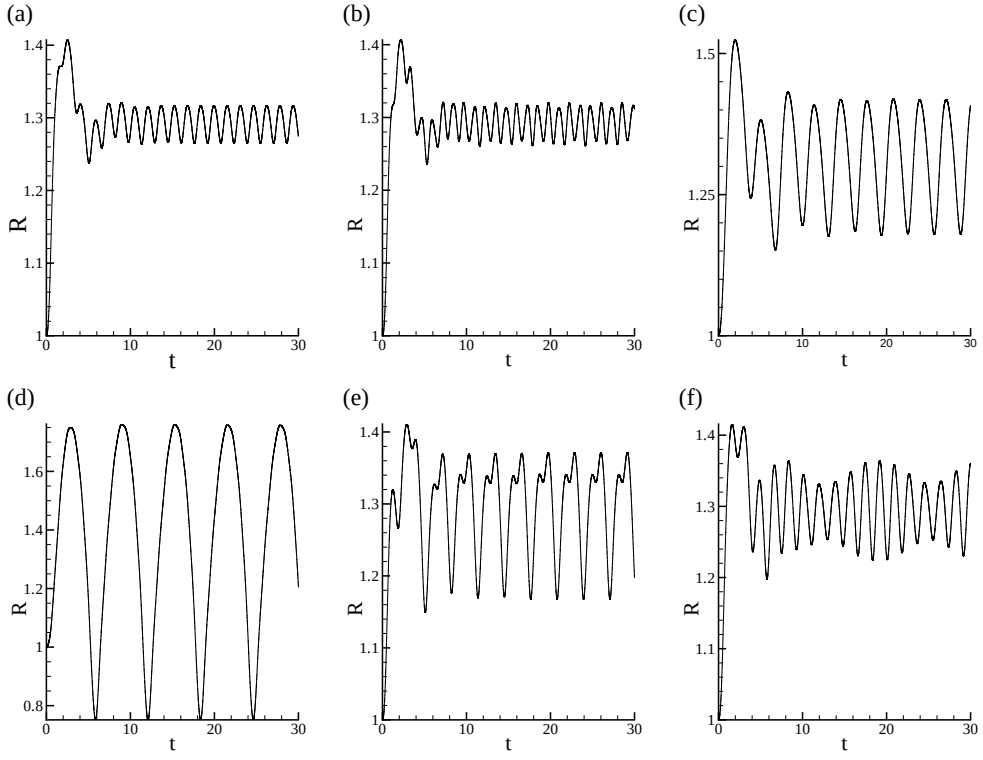

Figure 5.4: (a) Pattern 1; (b) pattern 2; (c) pattern 3; (d) pattern 4; (e) pattern 5 ; (f) and pattern 6 obtained from different combinations of ω and ω_{mag} for ω_{mag} for $Re = 60$, $We = 20$, $Re_{mag} = 1$, $\chi = 1$ and $\varepsilon = 0.8$.

each other in the ith direction.

In our case, the bubble governing system is non-autonomous. Considering the autonomous version, we transform the system to a 3−dimensional model in the phase space. Since our third variable $dz/dt = 1$, one of the Lyapunov exponents will always be null. The Lyapunov spectrum, applied in this work, can be used to give an estimate of the rate of entropy production and of the fractal dimension of the considered dynamical system. In particular from the knowledge of the Lyapunov spectrum it is possible to obtain the so-called Kaplan-Yorke dimension [71], given by:

$$D_{KY} = k + \sum_{i=1}^{k} \frac{\lambda_i}{|\lambda_{k+1}|}, \tag{5.4}$$

where k is the maximum integer such that the sum of the k largest exponents is still non-negative.

Actually, the inverse of Lyapunov exponents can be seen as a characteristic timescale: the Lyapunov time. Another way to compute the complexity of a dynamical system is analyzing its entropy. Yakov Sinai was the first to come up with a mathematical foundation for quantifying the complexity of a given dynamical system [72]. Inspired by Shannon's entropy in information theory, and in the framework of Kolmogorovs Moscow seminar, Sinai introduced the concept of entropy for so-called measure preserving dynamical systems, today known as Kolmogorov-Sinai entropy. This entropy turned out to be a strong and far reaching invariant of dynamical systems. Summing up,

the Kolmogorov-Sinai entropy measures the unpredictability of a dynamical system. The higher the unpredictability, the higher the entropy. It has been anticipated that the magnetic field can be used to control the growth or collapse of bubbles in conducting fluids [73].

Based on that, the dynamic of the oscillating bubble has been observed using tools of dynamic system analysis. In the first test, a non-magnetic test was made. In this context, the bubble is immersed in a Newtonian fluid and the frequency of the pressure forcing is $\omega = 3$. In figure 5.5, we can see three different types of oscillation in the same signal. The phase plots bellow show the response from $0 \leq t \leq 250$, $250 \leq t \leq 500$ and $500 \leq t \leq 550$. The bubble collapsed at $t = 550$ due to an amplification in its energy, as can be seen from the phase plot. We may notice that the bubble response passes through transients at the beginning of each period, but tends to reach a stable and harmonic response until the next period.

In figure 5.6 we can see the bubble response in frequency spectrum, Poincaré section and Lyapunov spectrum. The peak of higher energy in the frequency spectrum is located on the pressure forcing frequency ($\omega = 3$). As expected there are positive Lyapunov exponents in the Lyapunov spectrum, showing a chaotic behavior of the bubble. The Lyapunov dimension is not always null in this case.

When a static magnetic field is added, the behavior appears to stabilize, as shown in figure 5.7 but if we analyse the signal for long enough, after $t = 258$, the bubble energy starts to grow in a nonlinear way. This sensitivy to initial conditions is a characteristic of chaotic systems. In the first phase plot, that represents $0 \leq t \leq 258$, after the transient, the bubble movement is characterized by a limit cycle. On the other hand, in the second phase plot, there is an unstable equilibrium point.

In figure 5.8, the frequency spectrum, Poincaré section and Lyapunov spectrum is shown. The Poincaré section shows some points in the unstable equilibrium point but, after some time, there are other energy levels at bigger R and R', what lead the bubble to collapse. Again, there are positive Lyapunov exponents in the spectrum on the initial transient.

On the other hand, when an oscillatory magnetic field is applied, the amplitude of oscillation of the bubble decreases significantly, as seen in figure 5.9. In this context, the bubble does not collapse and the magnetic field tends to stabilize its motion at every time. The time response was divided in three periods: $0 \leq t \leq 258$, $258 \leq t \leq 510$ and $510 \leq t \leq 700$. On every period, even though the response is not harmonic, it is very similar as we can see in the three phase plots presented. The phase plot shows a period doubling at the very first limit cycle and the addition on a third one with some deformation. The insert shows us that there are more than one frequency of oscillation and a deformation in the time response between these two frequencies.

Even though there are positive Lyapunov exponents, as seen in figure 5.10, the amplitude of the harmonic in $\omega = 3$ decreases, which is also shown in the time response as a decrease in the bubble amplitude of oscillation. In this case, even in a chaotic motion, the bubble does not collapse. Indeed, its collapse is prevented when immersed in a magnetic fluid, subject to extreme conditions.

When the frequency of the magnetic field increases, the bubble behavior becomes even more

non-linear, but again there is no collapse. In fact, the amplitude of oscillation tends to decrease with time. Being a highly nonlinear system, any rapid decoupling caused by the application of the oscillating magnetic field generates major disruption. Under these conditions, a particle that has been convected due to the oscillatory motion of bubble and end up taking longer to align could cause large variations in the system. However, since the magnetic time scale is very small, the system tends to rapidly return to its equilibrium state.

The responses in frequency, Poincaré section and Lyapunov spectrum, shown in figure 5.12, are very similar to the ones found when other values of ω_{mag} were applied. Nevertheless, there are small variations in the frequency spectrum generated by the spectrum spreading of power in the frequency of the pressure forcing and the magnetic field.

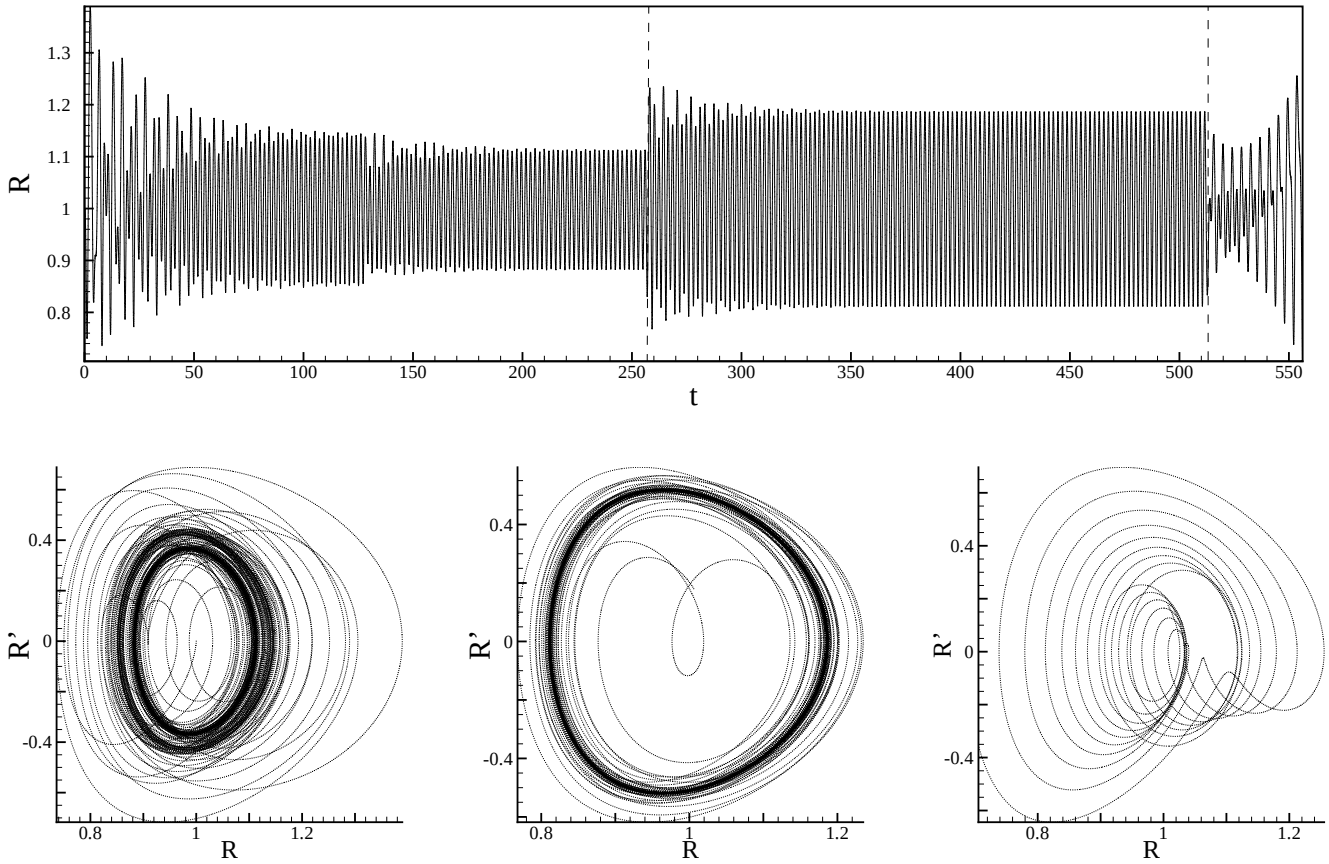

Figure 5.5: Bubble response in time and phase plots for $Re = 60$, $We = 20$, $\omega = 3$ and $\varepsilon = 0.8$ when immersed in a Newtonian fluid.

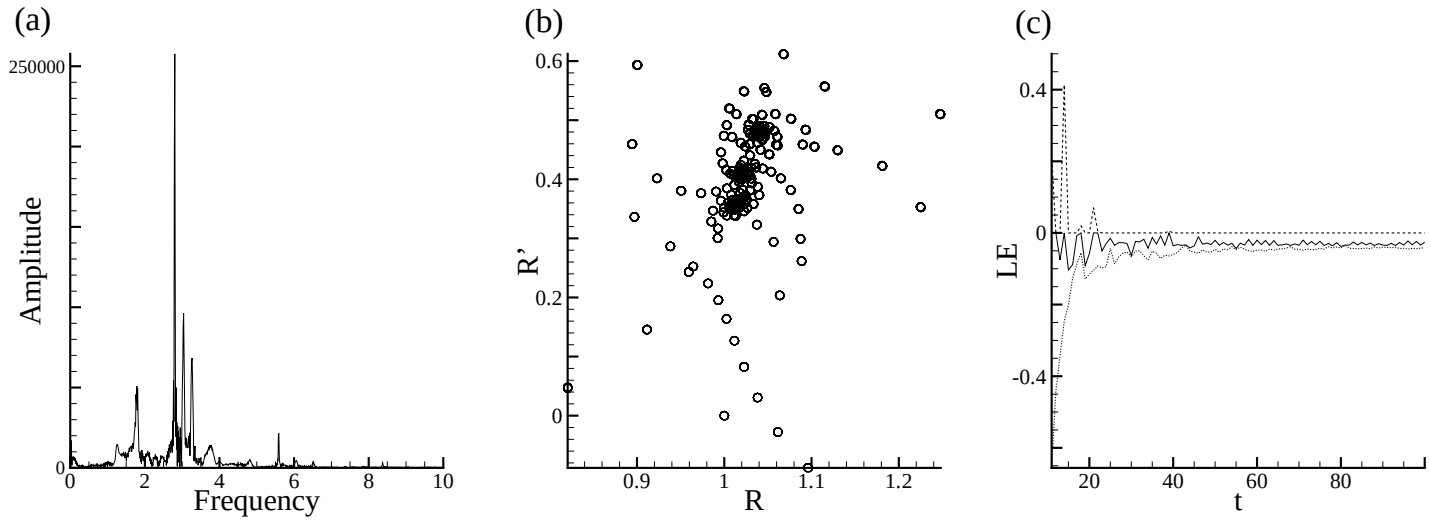

Figure 5.6: Bubble response in frequency spectrum, Poincaré section and Lyapunov spectrum for $Re = 60$, $We = 20$, $\omega = 3$ and $\varepsilon = 0.8$ when immersed in a Newtonian fluid.

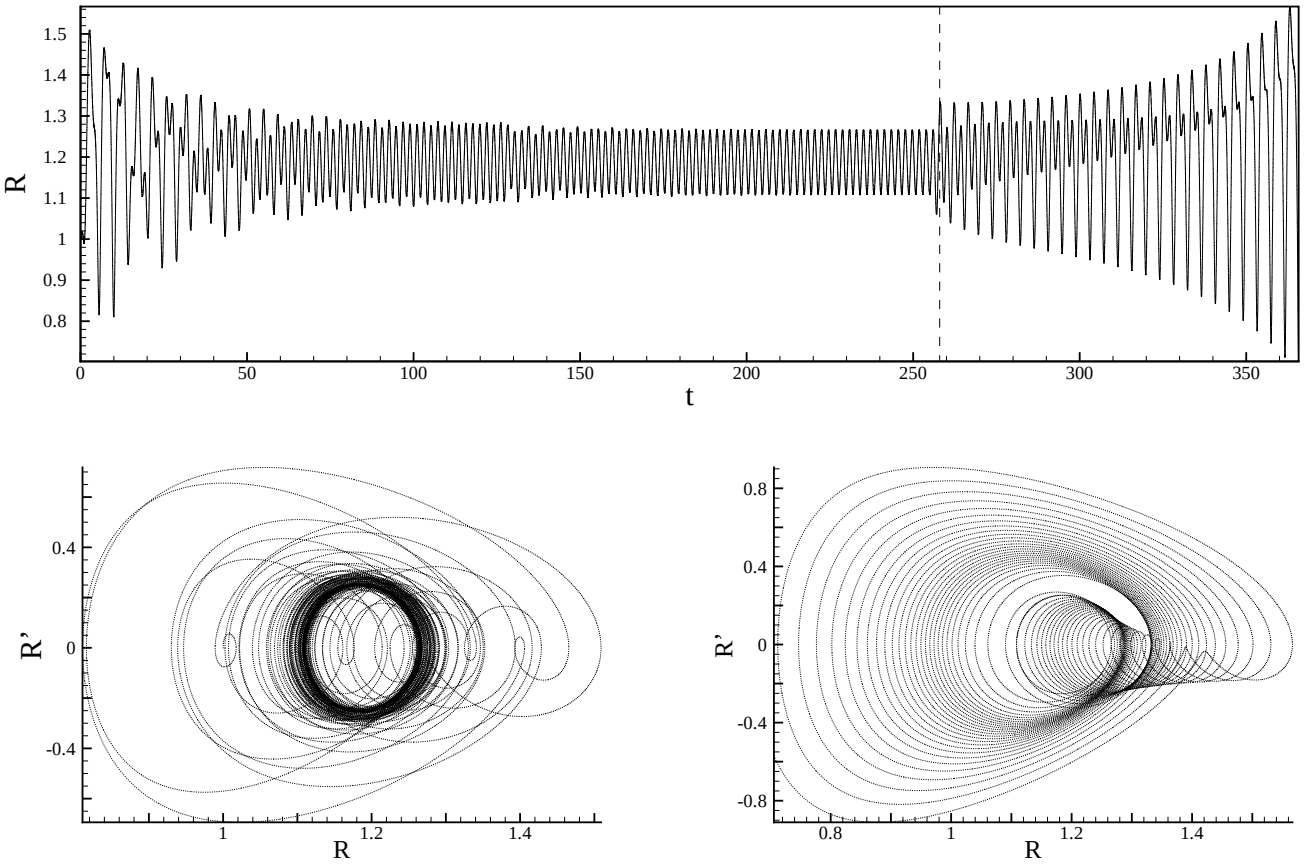

Figure 5.7: Bubble response in time and phase plots for $Re = 60$, $We = 20$, $\omega = 3$, $\varepsilon = 0.8$, $Re_{mag} = 1$ and $\chi = 1$ when immersed in a magnetic fluid.

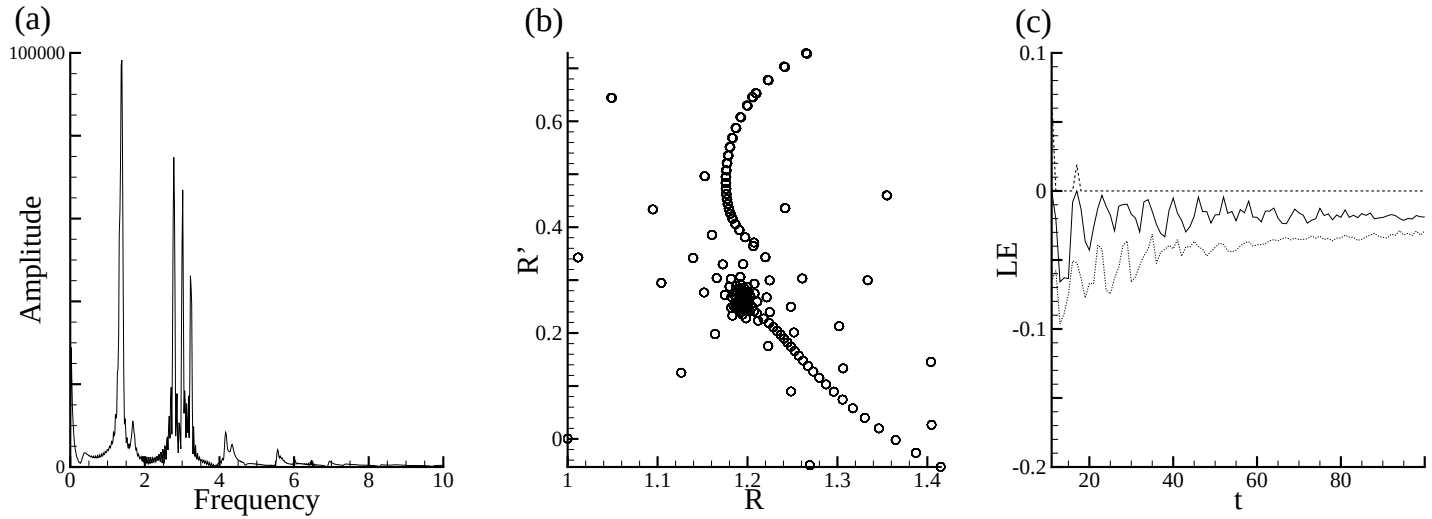

Figure 5.8: Bubble response in frequency spectrum, Poincaré section and Lyapunov spectrum for $Re = 60$, $We = 20$, $\omega = 3$, $\varepsilon = 0.8$, $Re_{mag} = 1$ and $\chi = 1$ when immersed in a magnetic fluid.

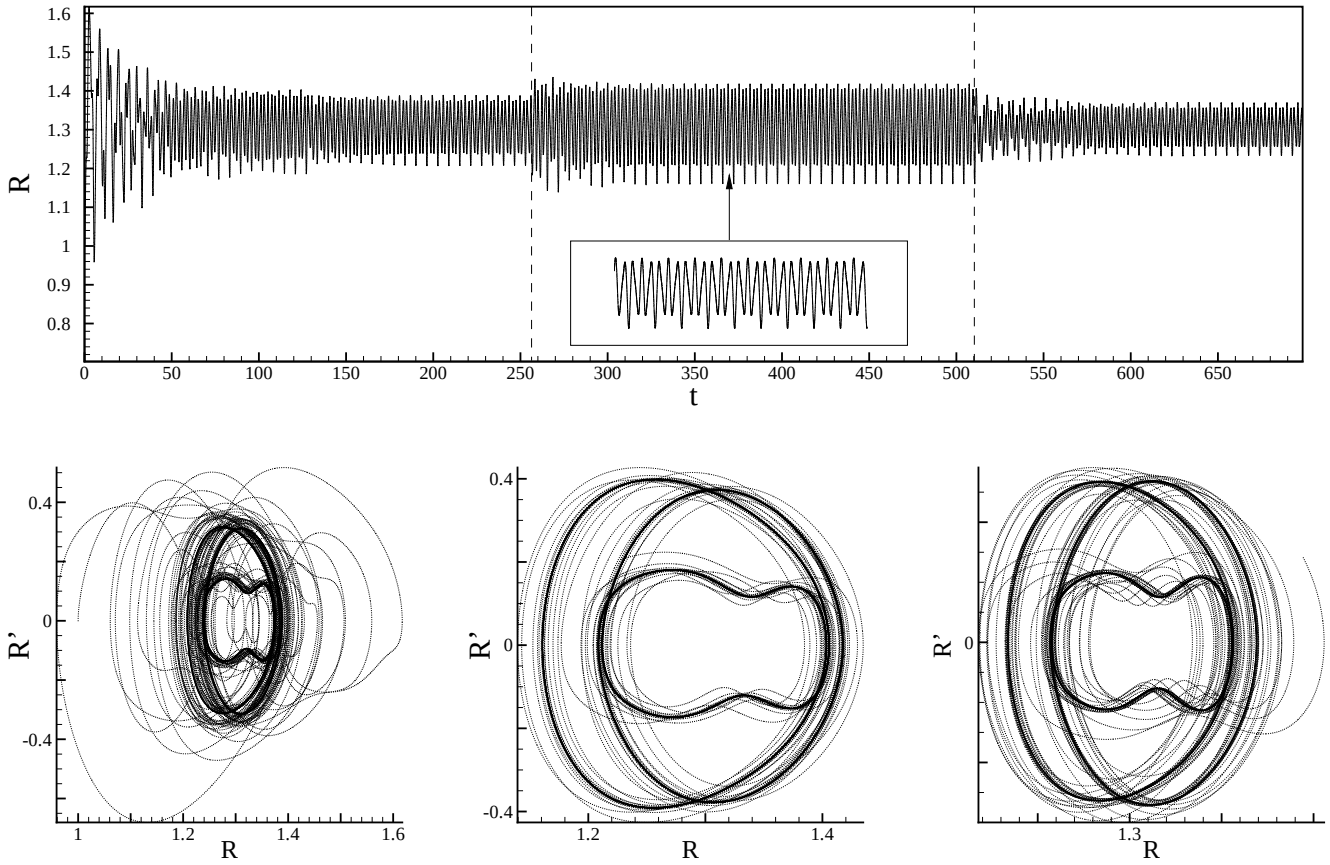

Figure 5.9: Bubble response in time and phase plots for $Re = 60$, $We = 20$, $\omega = 3$, $\varepsilon = 0.8$, $Re_{mag} = 1$, $\chi = 1$ and $\omega_{mag} = 5$ when immersed in a magnetic fluid.

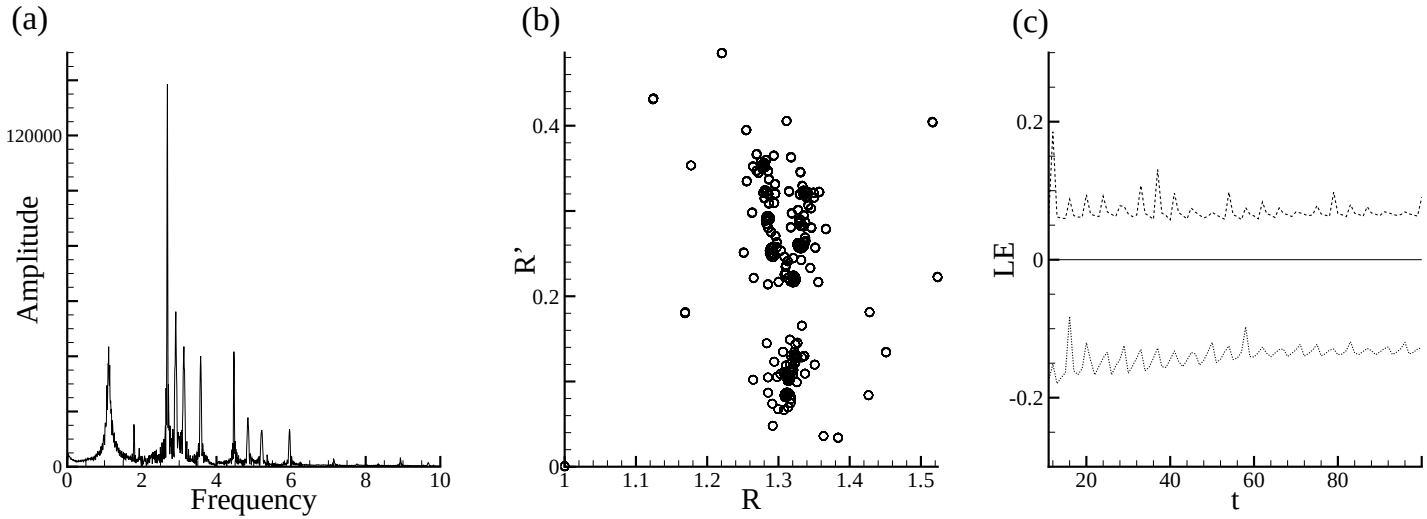

Figure 5.10: Bubble response in frequency spectrum, Poincaré section and Lyapunov spectrum for $Re = 60$, $We = 20$, $\omega = 3$, $\varepsilon = 0.8$, $Re_{mag} = 1$, $\chi = 1$ and $\omega_{mag} = 5$ when immersed in a magnetic fluid.

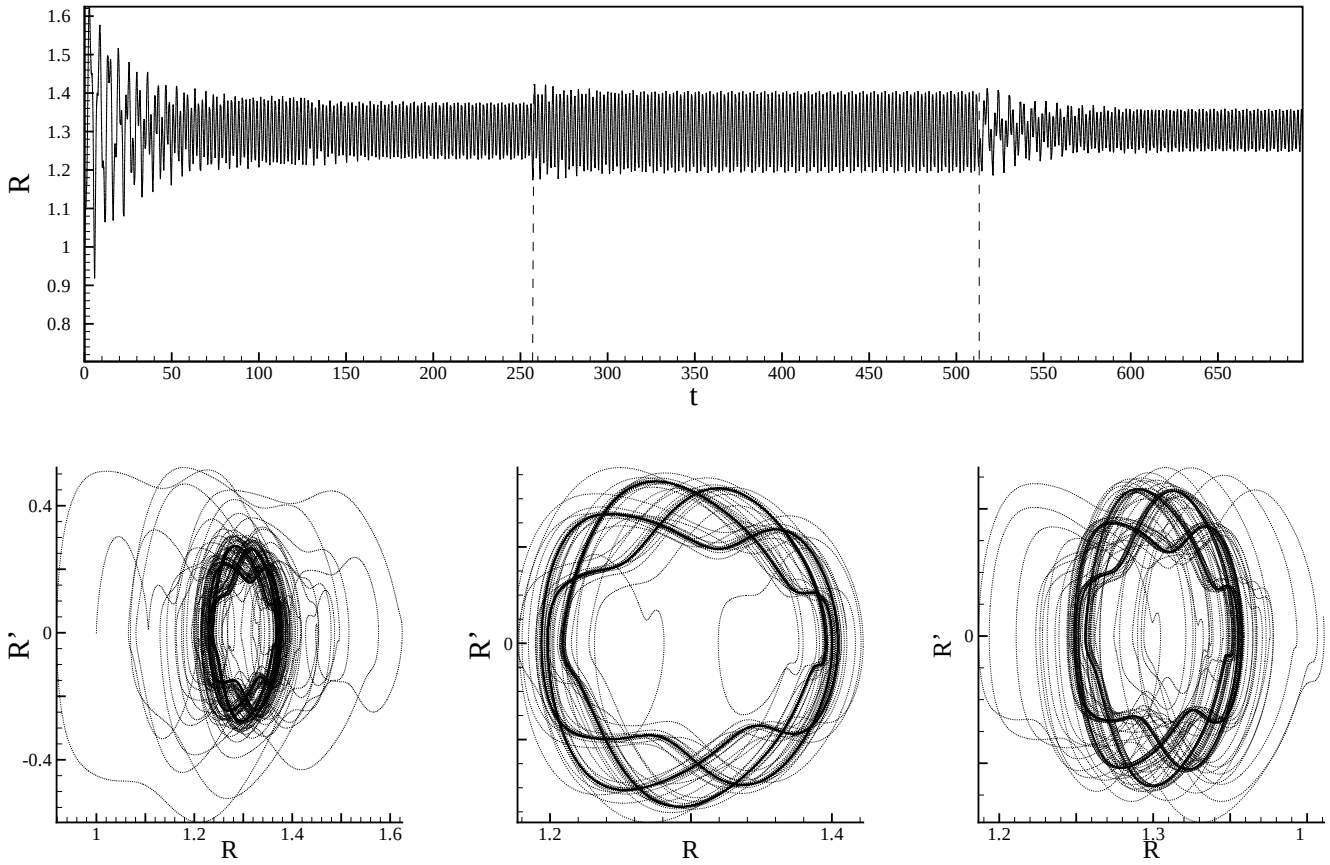

Figure 5.11: Bubble response in time and phase plots for $Re = 60$, $We = 20$, $\omega = 3$, $\varepsilon = 0.8$, $Re_{mag} = 1$, $\chi = 1$ and $\omega_{mag} = 10$ when immersed in a magnetic fluid.

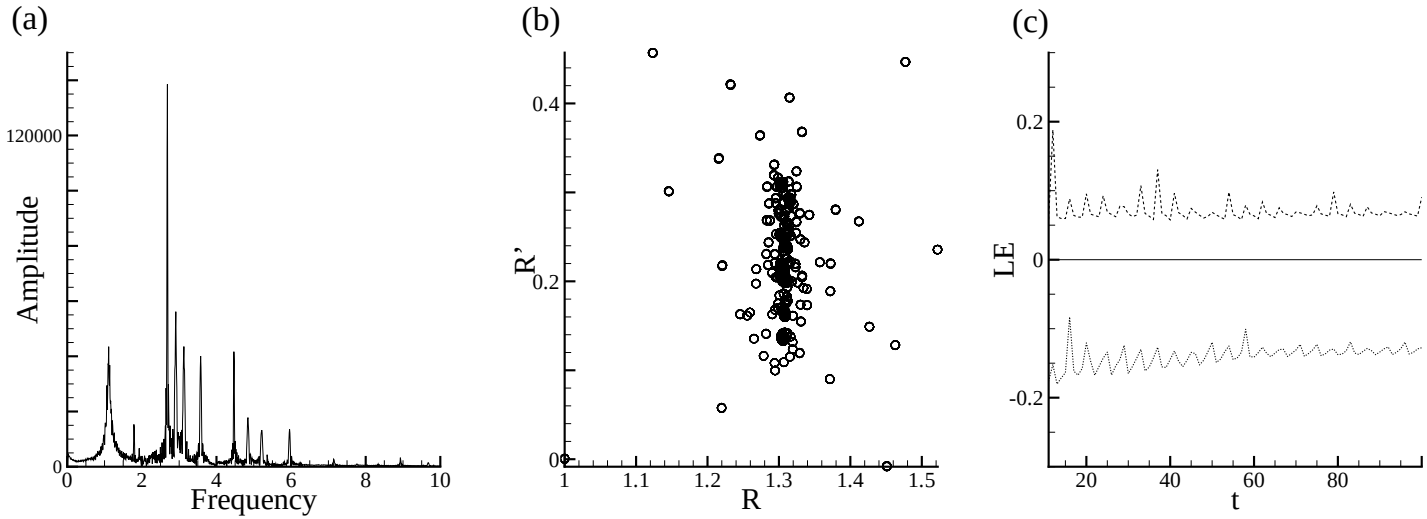

Figure 5.12: Bubble response in frequency spectrum, Poincaré section and Lyapunov spectrum for $Re = 60$, $We = 20$, $\omega = 3$, $\varepsilon = 0.8$, $Re_{mag} = 1$, $\chi = 1$ and $\omega_{mag} = 10$ when immersed in a magnetic fluid.

Another study can be done with respect to correlation between two variables. In this case, the correlation of the signal $R(t)$ with $R(t+\tau)$, where τ scales with the system period of oscillation. This approach, called scatter diagram or delay methods, can be used for both conditions: stationary and oscillatory.

Observing figure (5.13), it is possible to see a perfect strong positive correlation between both variables. That means that the magnetic effects, when added with a stationary and an oscillatory part, increases the system memory, as expected.

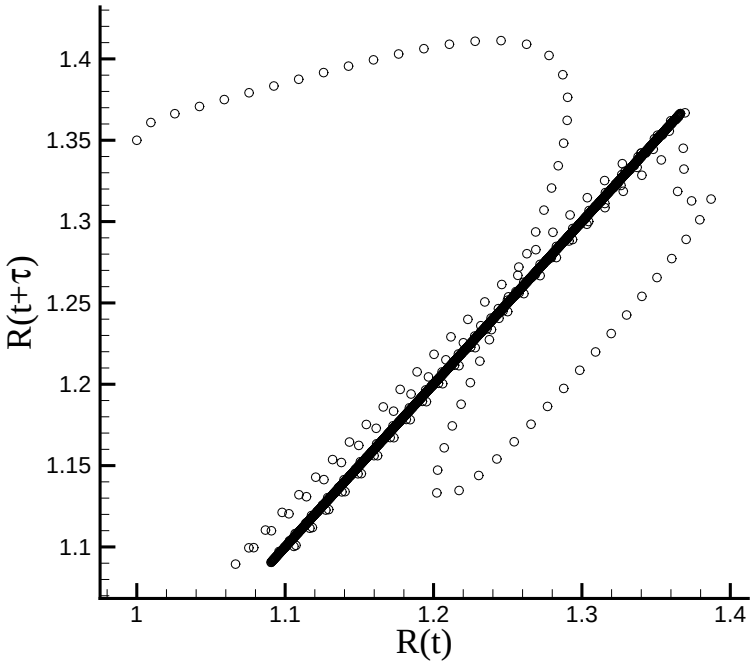

Figure 5.13: Scatter diagram for $R(t)$ and $R(t+\tau)$ when $Re = 10$, $We = 10$, $\omega = 2$, $\varepsilon = 0.3$, $Re_{mag} = 1$, $\chi = 1$, $\omega_{mag} = 4$ shows a perfect strong positive correlation.

However, figures (5.14) and (5.15) shows a weaker correlation between both variables. In this condition, with a static magnetic field, there is no coupling between the magnetic effects and the inertial ones. Indeed, the magnetic effects are less proeminent and less memory is added to the system, weakinning the correlation. The same behavior is observed when only the oscillatory magnetic field is applied.

It was noted that the coupling of time scales is very sensitive. Thus, the application of a magnetic field with both static and oscillatory parts allows the fluid to be permanently magnetized. Furthermore, when the oscillatory part couples with the bubble oscillation, it responds as if a stronger magnetic field is applied.

When no magnetic field is applied, the correlation is even weaker, due the lack of memory of the system, as seen in figure (5.16).

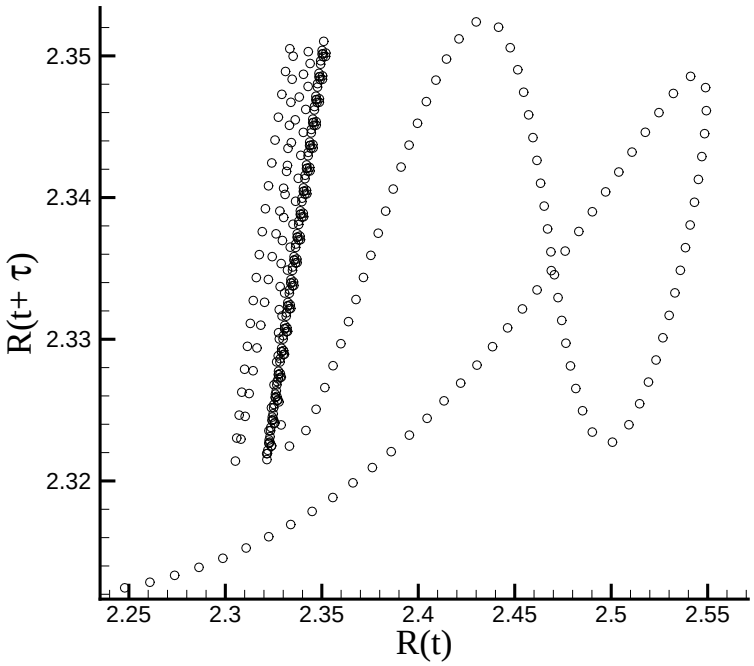

Figure 5.14: Scatter diagram for $R(t)$ and $R(t+\tau)$ when $Re = 10$, $We = 10$, $\omega = 3$, $\varepsilon = 0.3$, $Re_{mag} = 0.1$, $\chi = 1$.

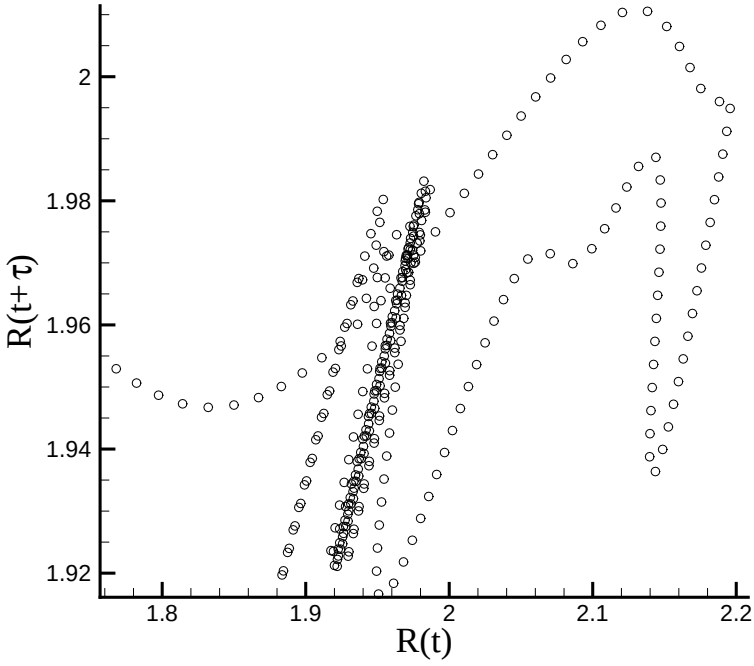

Figure 5.15: Scatter diagram for $R(t)$ and $R(t+\tau)$ when $Re = 10$, $We = 10$, $\omega = 3$, $\varepsilon = 0.4$, $Re_{mag} = 0.1$, $\chi = 1$, $\omega_{mag} = 3$.

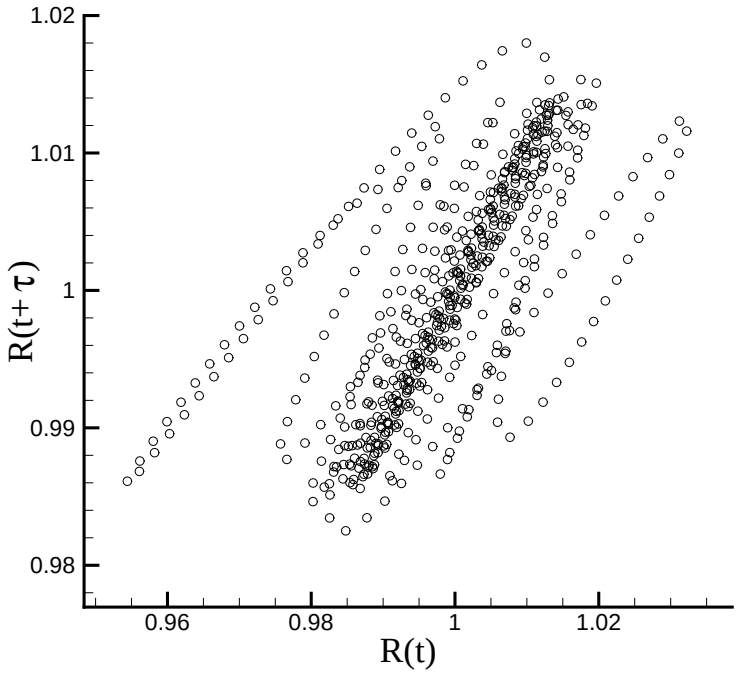

Figure 5.16: Scatter diagram for $R(t)$ and $R(t+\tau)$ when $Re = 10$, $We = 10$, $\omega = 3$, $\varepsilon = 0.4$.

Chapter 6

Ferrofluid Magnetization

This chapter aims to compare the superparamagnetism hypothesis used in the mathematical modelling of MRP equation with a magnetization model. In this context, the magnetic stress tensor is modified and the Langevin model for equilibrium magnetization is used.

6.1 Introduction

The mathematical formalization of the balance equations of Ferrohydrodynamics began with the simplified hypothesis of superparamagnetism. In this condition, the system of governing equations does not demand the resolution of the magnetization evolutive equation nor the angular momentum equation, since $\boldsymbol{M} = \chi \boldsymbol{H}$. Indeed, besides all the differences between the superparamagnetic model and the magnetization evolution equation, maybe the most important one is the presence of a linear relaxation term τ_s that accounts for deviations from the equilibrium state.

Indeed, in systems where the magnetic moment relaxation rate plays an important role, the magnetization on the linear momentum balance must be used. This model has proven to be far more robust than the superparamagnetic one, in which particles align with the field immediately. In this context, an analysis of the magnetization of the fluid through finite difference method is made. However, there is no coupling with the MRP equation. Therefore, it is considered a virtual bubble always oscillating in a harmonious and sinusoidal way.

6.2 Mathematical Modelling

This study intents to compute the magnetization effects in the stress tensor when a phenomenological equation for the magnetization is used. In this consideration, the particles take a period of time to align in the field direction.

Observing equation 2.92 and disconsidering the term referring to $\sigma_{\theta\theta}$, we have:

$$R^*\ddot{R}^* + \frac{3}{2}(\dot{R}^*)^2 = \frac{2}{We}\left[\frac{1}{(R^*)^{3n}} - \frac{1}{R^*}\right] - 1 - \varepsilon^* sen(\omega^* t^*) + \frac{1}{(R^*)^{3n}} - \frac{4}{Re}\frac{\dot{R}^*}{R^*} + 2\int_R^\infty \frac{\sigma_{rr}^*}{r}dr + \sigma_{rr}^*. \tag{6.1}$$

Considering now the magnetic stress tensor as:

$$\sigma_{mag} = \mu\frac{H^2}{2}\boldsymbol{I} + \boldsymbol{BH} = \mu_0\left(\frac{H^2}{2}\boldsymbol{I} + \boldsymbol{HH} + \boldsymbol{MH}\right). \tag{6.2}$$

And its radial component:

$$\sigma_{rr} = \mu_0\left(\frac{H_r^2}{2} + H_r + M_r H_r\right) = \mu_0\left(\frac{3H_r^2}{2} + M_r H_r\right), \tag{6.3}$$

where $\boldsymbol{H}$ is the applied magnetic field, $\boldsymbol{M}$ is the magnetization vector and $\boldsymbol{B}$ is the magnetic induction vector. As explained before, in the Mathematical Modelling chapter, it is essential to determine the field $\boldsymbol{H}$.

On the other hand, the phenomenological equation for magnetization may be written as [74]:

$$\frac{\partial \boldsymbol{M}}{\partial t} + \boldsymbol{v}\cdot\nabla\boldsymbol{M} = \left(\frac{1}{2}\nabla\times\boldsymbol{v} + \boldsymbol{\omega}\right)\times\boldsymbol{M} + \frac{1}{\tau_s}(\boldsymbol{M_0} - \boldsymbol{M}) \tag{6.4}$$

where $\boldsymbol{M_0}$ is the magnetization of equilibrium in a magnetic field $\boldsymbol{H}$, given for dilute fluids from the Langevin superparamagnetic relationship, and $\boldsymbol{M}$, as previously defined, is the actual magnetization at a given instant of time. Thus, τ_s is the magnetic relaxation time constant and $\boldsymbol{\omega} = 1/\zeta\boldsymbol{M}\times\boldsymbol{H}$, where ζ is given by:

$$\zeta = \frac{\rho}{J\tau_s\mu_0} \tag{6.5}$$

where ρ is the fluid density, J is the polar moment of inertia of the particles and μ_0 is the magnetic permeability. Physically interpreting equation 6.4 we may note that the term on the left side is associated with the material derivative of the magnetization vector field, the first term on the right side represents a transport by the rotation of the particles that compose the magnetic fluid and the transport of magnetization by the action of the vorticity of the fluid.

The magnetization on the linear momentum balance has a wide applicability to systems where the relaxation rate of the magnetic moment plays an important role. In this approach, important physical parameters of the suspension appear explicitly on the mathematical formulation. The combination of these parameters (ϕ, τ_s, α). In the present model, a transient response of the magnetization is considered and the convective contribution is accounted. Since in this case the bubble has only radial motion, then equation 6.4 might be written as:

$$\frac{\partial M_r}{\partial t} + v_r\frac{\partial M_r}{\partial r} = \frac{1}{\tau_s^*}(M_{0,r,} - M_r), \tag{6.6}$$

where τ_s^* is the non-dimensional magnetic relaxation time ($\tau_s^* = \tau_s/\tau_h$, being τ_h a hidrodynamic time scale) and $M_{0,r}$ may be modeled as:

$$M_{0,r} = M_d^* \mathscr{L}(\alpha)\phi, \tag{6.7}$$

where M_d^* is a physical non-dimensional parameter that represents the magnetization magnitude order of the material, ϕ is the volume fraction of particles and $\mathscr{L}(\alpha)$ is the Langevin function of the α parameter representing the interation between particles and magnetic field, given by:

$$\alpha = \frac{\mu_0 m H_0}{k_B T}, \tag{6.8}$$

where μ_0 is the vacuum magnetic permeability, H_0 is a typical intensity of the applied magnetic field, k_B is the Boltzmann constant and T is the fluid absolute temperature.

Indeed, a rigorous definition of the time scale τ_s is given by

$$\tau_s = \frac{\tau_N \tau_B}{\tau_N + \tau_B}, \tag{6.9}$$

where τ_N is the Néel characteristic time scale, associated with the time that the particle dipole moment takes to flip and align with an external applied field $\boldsymbol{H}$. For now on, τ_s^* will be replaced by τ_s in order to provide a clear nomenclature. The Brownian rotational time scale, on the other hand, is represented by τ_B. When $\tau_N \ll \tau_B$, $\tau_s \to \tau_N$ and when $\tau_B \ll \tau_N$, $\tau_s \to \tau_B$. While $\tau_N \sim e^d$, being d the particle diameter, the Brownian time scales with $\tau_B \sim d^3$. In this sense, $\tau_N \ll \tau_B$ for nanosized particles. In this asymptotic limit the particles may be interpreted as small gyroscopes and their magnetic dipole moments may flip regardless their rotational motion. It is also important to notice that in this limit the physics is restricted to Brownian suspensions where the Péclet number ($Pe = Ud/\mathscr{D}$) must be always much less than 1. Here, U is a typical velocity and $\mathscr{D}$ is the isotropic diffusional Stokes-Einstein coefficient. In the other asymptotic limit, $\tau_B \ll \tau_N$, the magnetic dipoles are fixed in each particle and Pe might be arbitrary. Under the perspective of continuum mechanics, the assumption of fixed dipole moments ($\tau_B \ll \tau_N$) leads to a more physically consistent model. From a phenomenological perspective, the Néel relaxation time scale lies on non-continuum mechanims in the realm of quantum mechanics.

We may observe from figure 6.1 that the suspension may be dominated by different time scales. In general, small particles lead to $\tau_s = \tau_N \ll \tau_B$. Defining a Magnetic Péclet number as $Pe_{mag} = \tau_N/\tau_h$ and being $Pe = \tau_B/\tau_h$ we may conclude that in a suspension of nanosized particles $Pe \ll 1$ and $Pe_{mag} \ll 1$. In order to couple the hydrodynamic time scale with the magnetic relaxation time, $Pe_{mag} \sim 1$. In this sense, the flow time scale should be extremely fast. From a practical point of view, when one considers a simple shear (in a rheometer, for example), $\tau_h = 1/\dot{\gamma}$. In this condition, $\dot{\gamma}$ should be extremely high. Since $\tau_N \ll \tau_B$, $Pe \to \infty$.

However, when there is a formation of aggregates or micro-sized particles are used, the flow time scale migh become important. In this condition, when coupling is considered, $Pe \gg 1$ and $Pe_{mag} \ll 1$. Three asymptotic limits can be explored as seen in 6.2. In this context, τ_s will be assumed as Pe or Pe_{mag} depending on the suspension characteristics.

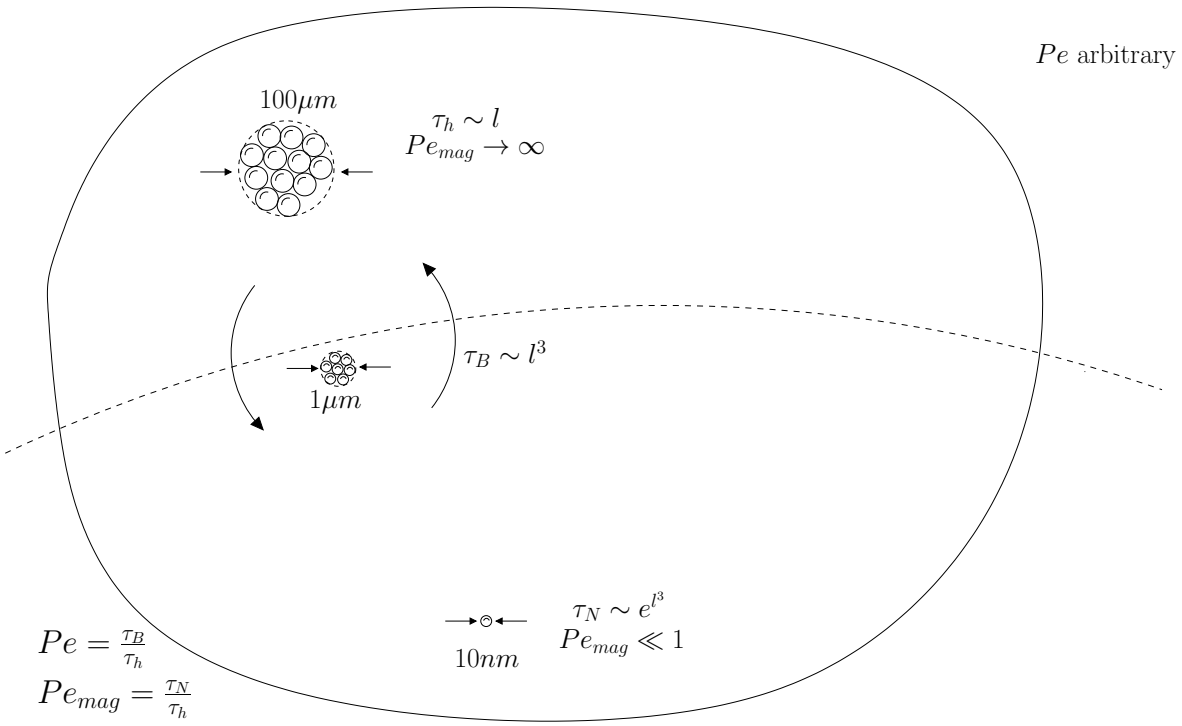

Figure 6.1: Schematic example of the transition between multiple time scales and its relation with the particles size.

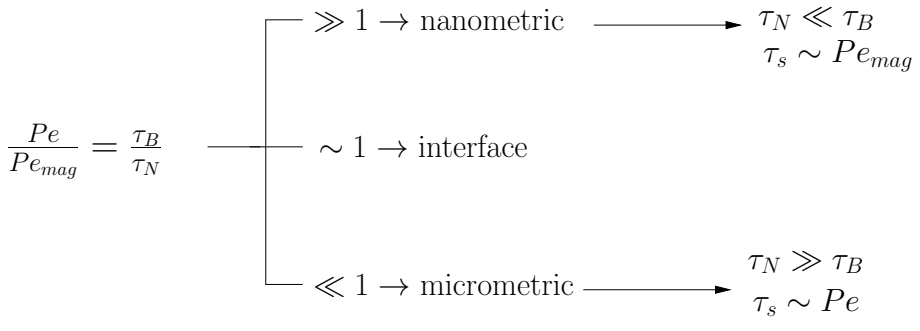

Figure 6.2: Three asymptotic limits obtained by the comparison between Pe and Pe_{mag}.

In this regard, it is noted that for suspensions in which $\tau_N \ll \tau_B$, there is only one main time scale. Thus, the flow does not interact with the particles as $\tau_h \gg \tau_N \to Pe_{mag} \ll 1$. Acording to Sobral and Cunha [75] for nanosized particles $\tau_N \sim 0.1ns$, whereas $\tau_B \sim 10^3 ns$. In this application, in order to compute the coupling between the hydrodynamic scale and the magnetic ralaxation time, the flow must be extremely fast and $Pe \sim 10^4$. On the other hand, if we consider micro-composites of nanoparticles $\tau_B \ll \tau_N$ and $Pe_{mag} \ll 1$. Given that, the coupling between hydrodynamic and magnetic time scales is easier to obtain from a practical perspective when using microsized particles.

This discussion shows that the microstructure of a magnetic suspension is governed by several

mechanisms with multiple time scales. With this in mind, the interface between continuum and non-continuum mechanics becomes tenuous. Like many other physical problems, the mutiplicity of time scales allows the study of a rich and highly nonlinear dynamics.

6.3 Numerical Modelling

This nonlinear behavior of the bubble dynamics does not allow the equations to be solved analytically and in order to optimize the analysis of these nonlinear ordinary differential equation, a computer simulation was used. A finite-difference method in Fortran 90 was proposed. It is a numerical method for approximating the solutions to differential equations using finite difference equations to approximate derivatives. In this case, a bubble sinusoidal motion uncoupled with the flow is used.

Considering equation 6.6 and using a backward difference, it is possible to achive and always stable an convergent scheme as shown bellow:

$$\frac{M_r^{t+1} - M_r^t}{\Delta t} = -\left\{\frac{[1 + 2\varepsilon sin(\omega t) + \varepsilon^2 sin^2(\omega t)]\omega\varepsilon cos(\omega t)}{r^2}\right\}\left(\frac{M_{i+n}^{t+1} - M_{i-1}^{t+1}}{2\Delta r}\right) + \frac{1}{\tau_s}(M_d(L(\alpha))\phi - M_r^{r+1}). \tag{6.10}$$

where t is the current time step, $t+1$ is the next time step and i represents a certain node. In this condition, it is possible to consider the following constants:

$$C_1 = \left\{\frac{[1 + 2\varepsilon sin(\omega t) + \varepsilon^2 sin^2(\omega t)]\omega\varepsilon cos(\omega t)}{}\right\}, \tag{6.11}$$

$$C_2 = \frac{1}{\tau_s}, \tag{6.12}$$

$$A = M_d\mathscr{L}(\alpha)\phi. \tag{6.13}$$

With this discretization is noted that the node i depends on the nodes $i-1$ and $i+1$. For this reason, a linear system of type $\boldsymbol{Ax} = \boldsymbol{b}$ is mounted, as shown bellow:

$$\begin{bmatrix} 1 & 0 & 0 & 0 & 0 & 0 & 0 & 0 & 0 & 0 \\ C_1 & 1+C_2 & C_1 & 0 & 0 & 0 & 0 & 0 & 0 & 0 \\ 0 & C_1 & 1+C_2 & C_1 & 0 & 0 & 0 & 0 & 0 & 0 \\ 0 & 0 & C_1 & 1+C_2 & C_1 & 0 & 0 & 0 & 0 & 0 \\ 0 & 0 & 0 & C_1 & 1+C_2 & C_1 & 0 & 0 & 0 & 0 \\ 0 & 0 & 0 & 0 & C_1 & 1+C_2 & C_1 & 0 & 0 & 0 \\ 0 & 0 & 0 & 0 & 0 & C_1 & 1+C_2 & C_1 & 0 & 0 \\ 0 & 0 & 0 & 0 & 0 & 0 & C_1 & 1+C_2 & C_1 & 0 \\ 0 & 0 & 0 & 0 & 0 & 0 & 0 & C_1 & 1+C_2 & C_1 \end{bmatrix} \begin{bmatrix} M_1^{t+1} \\ M_2^{t+1} \\ M_3^{t+1} \\ M_4^{t+1} \\ M_5^{t+1} \\ M_6^{t+1} \\ M_7^{t+1} \\ M_8^{t+1} \\ M_9^{t+1} \\ M_10^{t+1} \end{bmatrix} = \begin{bmatrix} 0 \\ M_2^t + C_2A \\ M_3^t + C_2A \\ M_4^t + C_2A \\ M_5^t + C_2A \\ M_6^t + C_2A \\ M_7^t + C_2A \\ M_8^t + C_2A \\ M_9^t + C_2A \\ M_10^t + C_2A \end{bmatrix} \tag{6.14}$$

```
1.  Define Re, We, Re_mag, χ, n (polytropic coefficient) and ε;
2.  Define α, ε, τ_s, φ, ω, M_d, Re_mag and χ;
3.  Define dt, the time step and L, the size of the mesh;
4.  Define the initial and boundary conditions;
5.  Define constants: C_1, C_2, C_3;
6.  do p = 1, 1000;
    do i = 2, n − 1;
    A(i, i) = 1 + C_2;
    A(i, i + 1) = C_1(i);
    A(i, i − 1) = C_1(i);
    b(i) = M(i − 1) + C_2 C_3;
    end do ;
    end do ;
10. call linear system;
11. Compute M(i);
```

(6.15)

Figure 6.3: Algorithm to compute the magnetization and the magnetic contribution of the problem

To solve the linear system shown in Equation 20 with $n \times n$ matrix, the TDMA (Tri-Diagonal Matrix Algorithm), also known as Thomas Algorithm was used. It is a simplified form of Gaussian elimination that can be used to solve tridiagonal systems of equations. Finally, the trapezoidal rule is used for the numerical integration of equation **??**. An algorithm of the numerical solution is shown in 6.3:

6.4 Parameters Influence on the Magnetization

As said before, when a paramagnetic or ferromagnetic material is stressed by a magnetic field the magnetic dipoles within the material will attempt to align their magnetic dipole moment parallel to the direction of the applied field. Ferromagnetic materials display a strong magnetic interaction between neighboring molecules, while paramagnetic materials display only weak interactions between neighboring material molecules.

The initial slope of the magnetization curve, χ, is the magnetic susceptibility and is given as:

$$\chi = \frac{\boldsymbol{M}}{\boldsymbol{H}} = \frac{\pi}{18}\frac{\mu_0 \phi M_d^2 d^3}{k_B T}, \tag{6.16}$$

where d represents the particle diameter, k_B is the Boltzmann constant, T is the temperature, ϕ is the volumetric fraction of particles, M_d is the solid particles magnetization and μ_0 is the magnetic permeability of free space. The susceptibility describes the magnitude of magnetic response shown by a magnetic material at low field strengths. A large value of χ, as said before, corresponds to strongly magnetic materials, while a small value corresponds to a weakly magnetic material.

Based on the proposed code, several results are obtained when the physical parameters are changed. Each parameter changes the system behavior in a different way. Changing the volumetric fraction of particles can increase the magnetization drastically as shown in figure 6.4. It is known that when the magnetic field is applied to a magnetic fluid, its rheological properties will change. For diluted ferrofluids where there are almost no interaction between particles the Brownian rotation is hindered by the magnetic field, so its effective viscosity is increased [76]. The transient time also decreases.

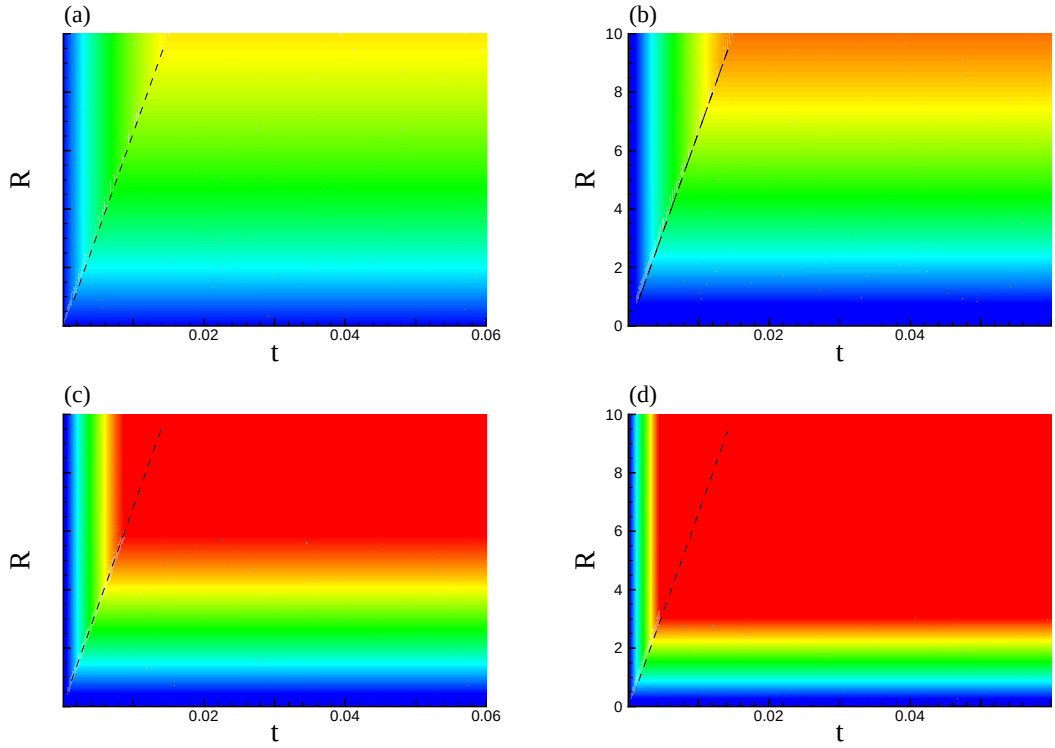

Figure 6.4: Diagrams of R versus time for different particle volume fraction with $\alpha = 1$, $\varepsilon = 0.5$, $\omega = 1$, $\tau_s = 1 \times 10^{-2}$ and $M_d = 0.5$. (a) Represents $\phi = 1\%$, (b) $\phi = 3\%$, (c) $\phi = 5\%$ and (d) $\phi = 8\%$. The diagonal lines represent the transient time. The range varies from 0 to 1 (blue to red).

The increase of particles in the fluid, also changes the corresponding susceptibility, as proposed by Shliomis [53]. When the volumetric fraction of particles is greater then 10%, a necessary correction is made in equation 6.16. In this case:

$$\frac{\chi(2\chi+3)}{\chi+1} = \frac{\pi}{6}\phi\frac{\mu_0 M_d^2 d^3}{k_B T} = \alpha \tag{6.17}$$

Since the corresponding susceptibility is bigger, the increase of the volume fraction increase the magnetic time, which correspond to the alignment time.

Even though Curie's law for the initial susceptibility shows that it depends linearly on the particle concentration, there is an essential deviation from the Langevin formula. This is caused

by particle-particle interaction [77], which was not considered in this work, but should be observed at high concentrations [33].

Changing the interaction between the particles and the field also allow us to control the applied magnetic field, increasing the magnetization, as shown in 6.5.

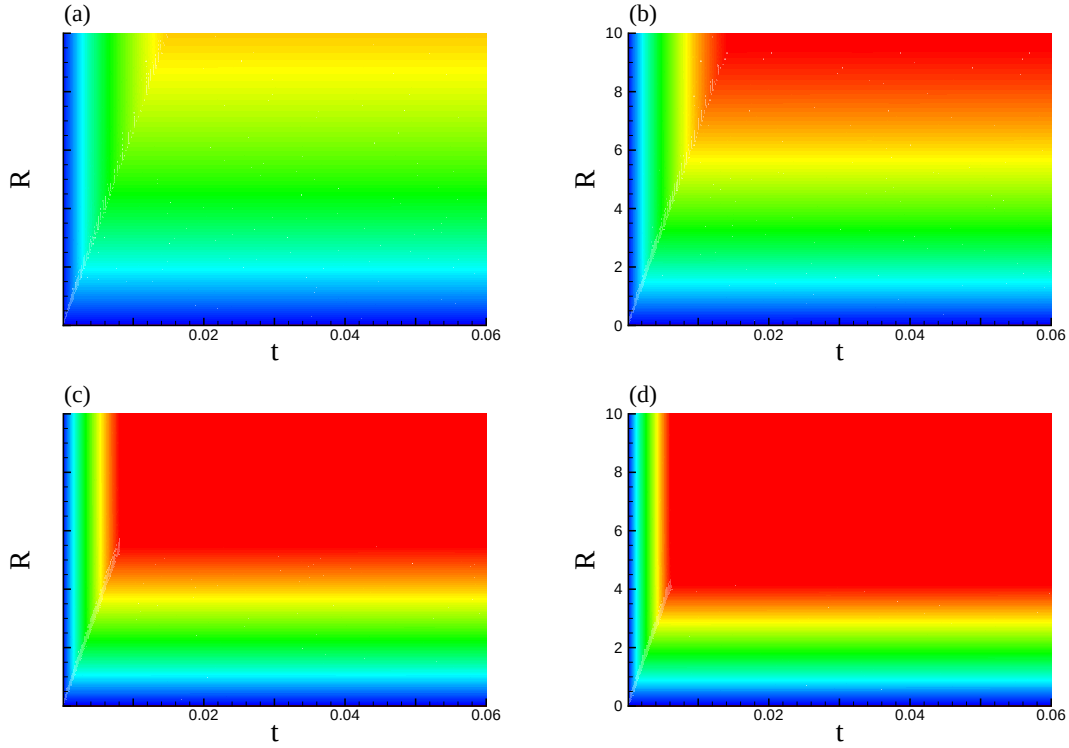

Figure 6.5: Diagrams of R versus time with $\phi = 5\%$, $\varepsilon = 0.5$, $\omega = 1$, $\tau_s = 1 \times 10^{-2}$ and $M_d = 0.5$ for (a) $\alpha = 1$, (b) $\alpha = 3$, (c) $\alpha = 5$ and (d) $\alpha = 8$. The diagonal lines represent the transient time. The range varies from 0 to 1 (blue to red).

The increase of the applied magnetic field decreases the magnetic time, but do not change the transient time. Changing the magnetic relaxation time, on the other hand, modificates the transient time, as shown in 6.6.

When the magnetic relaxation time decreases, the transient time represented by the diagonal line slope also decreases. This is due the alignment of the particles that takes less time to occur. In quasi-equilibrium ferrohydrodynamics, $\boldsymbol{M}$ is collinear with $\boldsymbol{H}$, as in ferrohydrostatics. The viscous stress tensor is then symmetric, and it is immaterial whether relaxation is dominated by the Néel or Brownian relaxation mechanism [39]. When $\boldsymbol{M}$ does not align with $\boldsymbol{H}$, there exists a nonequilibrium state of magnetization and a concomitant state of asymmetric stress. Brownian relaxation is faster than Néel relaxation for particles of sufficiently large size. Note that the assumption of $\tau_s \ll \tau_h$ is not directly related with Pe. In other words, we may have $\tau_s \ll \tau_h$ for arbitrary Pe number ($Pe \sim 1$ or $Pe \gg 1$).

The amplitude and frequency do not generate many changes in magnetization, as shown in

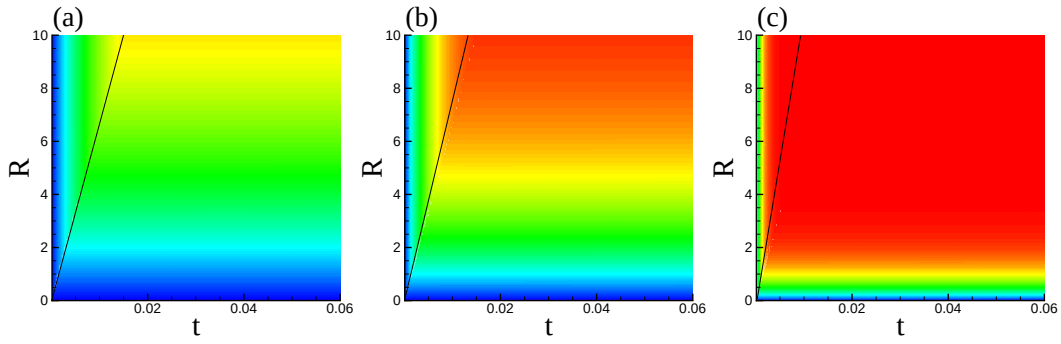

Figure 6.6: Diagrams of R versus time with $\alpha = 1$, $\phi = 5\%$, $\varepsilon = 0.5$, $\omega = 1$ and $M_d = 0.5$ for (a) $\tau_s = 4 \times 10^{-2}$; (b) $\tau_s = 2 \times 10^{-2}$ and (c) $\tau_s = 5 \times 10^{-3}$. The diagonal lines represent the transient time. The range varies from 0 to 1 (blue to red).

6.7. First, the disturbance generated by the oscillatory motion of the bubble is not very relevant in contrast to the mesh size

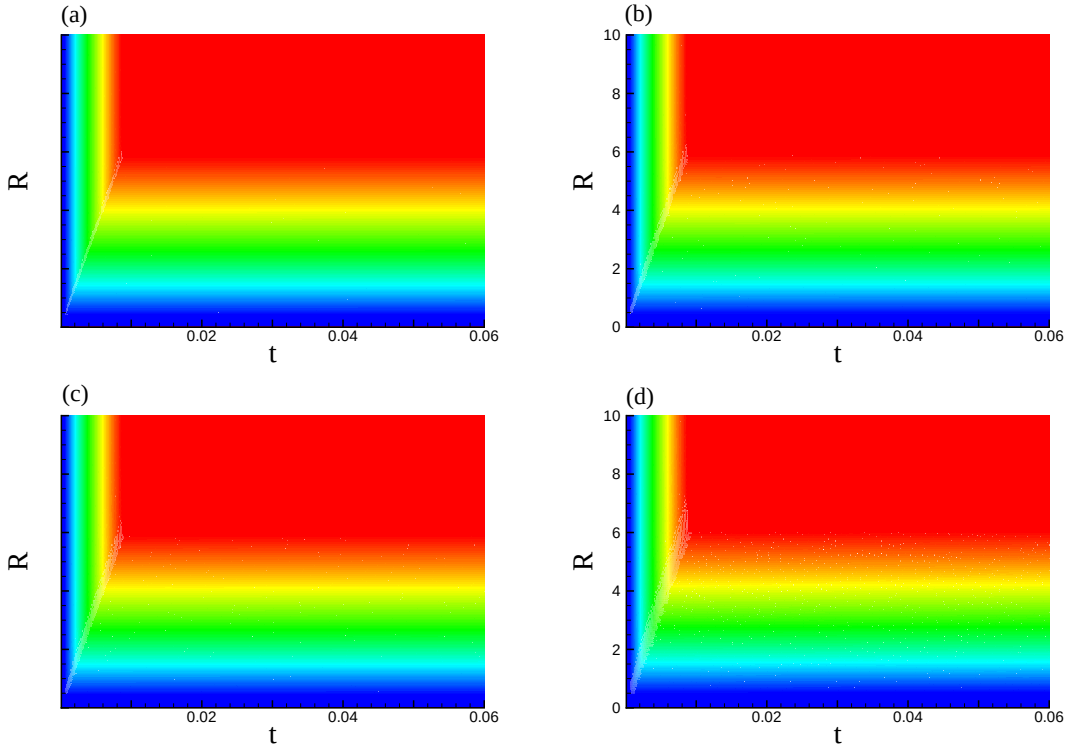

Figure 6.7: Diagrams of R versus time with (a) $\omega = 1$ and $\varepsilon = 0.3$, (b) $\omega = 3$ and $\varepsilon = 0.3$, (c) $\omega = 1$, $\tau_s = 1 \times 10^{-2}$ and $\varepsilon = 0.7$ and (d) $\omega = 3$ and $\varepsilon = 0.7$ with $\alpha = 1$, $\phi = 5\%$, $\varepsilon = 0.5$, $\omega = 1$, and $M_d = 0.5$. The diagonal lines represent the transient time. The range varies from 0 to 1 (blue to red)

On the other hand, when the factor M_d is increased, there is a change in transient, shown in figure 6.8, since this magnetization factor has a behavior similar to the decrease in relaxation time.

In other words, the capacity of the fluid particles to be magnetized increases considerably.

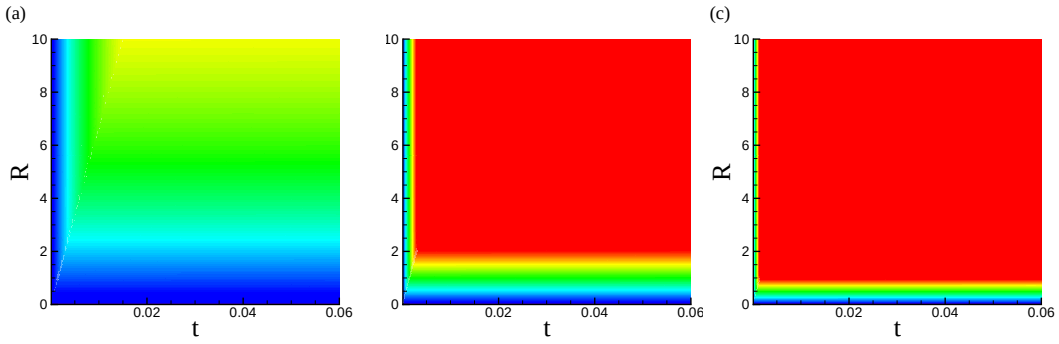

Figure 6.8: Diagrams of R versus time with (a) $M_d = 0.5$, (b) $M_d = 2.0$, (c) $M_d = 4.0$ for $\alpha = 1$, $\phi = 5\%$, $\varepsilon = 0.5$, $\tau_s = 1 \times 10^{-2}$ and $\omega = 1$.

To sum up, it is possible to conclude that the magnetic relaxation time is one of the main parameters that control the magnetization. The reduction thereof causes the particles to align more quickly in the field direction, approaching the superparamagnetic behavior. Furthermore, the M_d factor is also extremely important in increasing or decreasing the magnetization. The variation of the volume fraction of particles has a very similar behavior to the Langevin parameter, α, increasing in direct proportion, although more discretly, the magnetization. Indeed, the alignment characteristics of magnetic dipoles of the fluid can be easily controlled by the applied field and the type of particles employed.

Chapter 7

Experimental Analysis of a Rising Bubble

In order to visualize the bubble in a ferrofluid, an experimental setup was designed. This chapter aims to explore the results obtained with these experiments for a bubble rising in different fluids inclusing a magnetorheological suspension and a ferrofluid with high particle magnetization.

7.1 Introduction

Multi-phase fluids play an important role in many natural and industrial processes such as combustion/chemical reaction, petroleum refining and boiling. The rising of a single bubble in a viscous liquid due to buoyancy forces is one typical multi-phase flow. A fundamental understanding of the bubble rising physics is essential in various practical applications, ranging from the rise of steam bubbles in boiler tubes to gas bubbles in oil [78]. Indeed, it is very difficult to study a bubble under low Stokes velocity.

As a result of that difficulty, approximate theoretical solutions have been derived in the limit of very small bubble deformations (low Bond number) for either high [79] or low [80] Reynolds numbers, where the bubble shape is relatively stable. That is the condition used in this work for all the simulations and code development.

This spherical shape is completely related to the bubble size. The fact that gas bubbles with volumes exceeding about one centilitre take a spherical-cap shape when they rise steadily through liquid of small viscosity appears to have been noticed first by Taylor and Davies [81].

So far, we have used the Weber number as the non-dimensional parameter related to the superficial tension. However, the rising of a bubble in a viscous fluid under the influence of gravitational forces can be generally grouped in three different regimes: spherical, ellipsoidal, and spherical cap. These regimes are achieved depending on the values of two important non-dimensional quantities, the Bond and Morton numbers:

$$Bo = \frac{g\Delta\rho d^2}{\sigma}, \tag{7.1}$$

and

$$Mo = \frac{g\Delta\rho\eta_l^4}{\sigma^3\rho_\ell^2} \tag{7.2}$$

where d is the bubble diameter, ρ_ℓ is the liquid density, η_l is the liquid viscosity, $\Delta\rho = \rho_\ell - \rho_g$ is the density difference between continuous medium and the dispersed fluid and g is the gravitational acceleration. The Bond number, Bo is the ratio of the body forces (effective gravitational forces) and the surface tension forces, but it could also be considered as a dimensionless size value of the bubble [82]. The physical parameter Mo provides a description of the properties of the surrounding fluid, mainly focusing in viscosity and surface tension. A general classification of the bubble is usually done depending on final shape or by the primary forces acting on the system [83].

However, the transition areas from regime to regime are still not well defined. A brief description of each of the three main regimes: Spherical, ellipsoidal, and spherical cap is provided as follows [84].

- Spherical regime: This regime is dominated by surface tension and viscous forces. Original size of the bubble is small, usually less than $1.3mm$. The shape of the bubble remains spherical or nearly-spherical. Usually the ratio of minor to major axis is less than 10%. In this regime, the terminal velocity is proportional to the size of the bubble.

- Ellipsoidal regime: This regime is mainly dominated by surface tension. Bubble size is intermediate, typically from 1.3 to 6 mm, and the range for Bo is $0.25 < Bo < 40$. Final shape is usually oblate with convex interface if looking from inside. Generally, there is no fore-and-aft symmetry. In this regime, there is little viscous resistance to internal circulation, therefore drag and terminal velocity are very sensitive to contamination.

- Spherical cap regime: This regime is governed by inertia force. Bubble size is large, usually bigger than 6 mm. $Bo > 40$ and $Re > 1:2$. In this regime, terminal velocity of bubble is proportional to size. In addition, large inertia creates higher deformation by creating high pressure on the front and rear and low pressure at the sides

Besides the bubble shape, many experiments performed over the last 50 years have demonstrated that millimetric bubbles rising in low viscosity liquids do not generally follow a straight trajectory [85]. In the regime where bubbles exhibit approximately oblate spheroidal shapes, they rather rise in zigzag within a given vertical plane or spiral around a vertical axis. In pure water the transition from straight path to zigzag path occurs when the equivalent diameter of the bubble exceeds 1.8 mm, which corresponds to a rise Reynolds number of about 660 and an aspect ratio about 1.85 [86].

7.2 Experimental Setup

In order to generate the bubbles accurately and in a controlled way, a syringe pump was developed. For that, a microcontroller (Arduino) was programmed to control a stepper motor. This stepper motor was connected to a linear actuator that pushes the glass syringe. In order to controll the motor, the Easy Driver hardware was used. This driver has an H-bridge design internally, which is an electronic circuit that enables a voltage to be applied across a load in either direction. In other words, it allows DC motors to run forwards and backwards. A LCD display is used to inform the user if the motor is running forward or backward and other relevant information. The apparatus can be seen in figure 7.1.

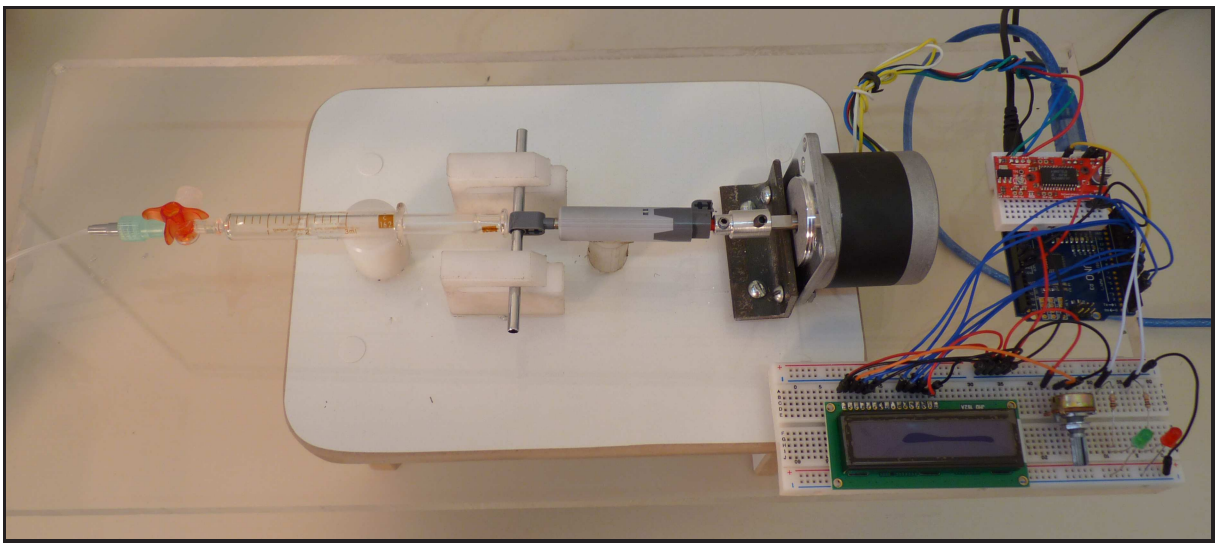

Figure 7.1: Experimental bench working as a syringe pump. The electronic part controls the stepper motor step. This motor is connected to a linear actuator that pushes the syringe with velocity proportional to the motor rotation speed and the amount of steps.

The eletronic circuit and the protoboard figure produced by *Fritzing* can be seen in **Appendix II**. Two leds were added to show the user the motor action if the LCD is not connected. In order to control the LCD contrast, a $10k\Omega$ potentiometer is used. The electrical circuit and the three modes of operation of the LCD are shown in figure 7.2. The LCD is programmed to initiate the process and then inform the user if the motor is running forward or backward. Between this two modes, the system waits for 10 seconds, which is also shown in the LED screen. The syring is connected to an acrylic tank in which the fluid is added.

The dimension on the tank must be calculated regarding the physical non-dimensional parameter called Stokes number. If we consider the bubble as a flotating particle, it is possible to define two time scales. One related to the bubble relaxation time and the other one related to the time the bubble needs to rise a distance a, which is its radius. These two time scales are given respectively by:

$$t_r = \frac{m}{6\pi\mu a} \tag{7.3}$$

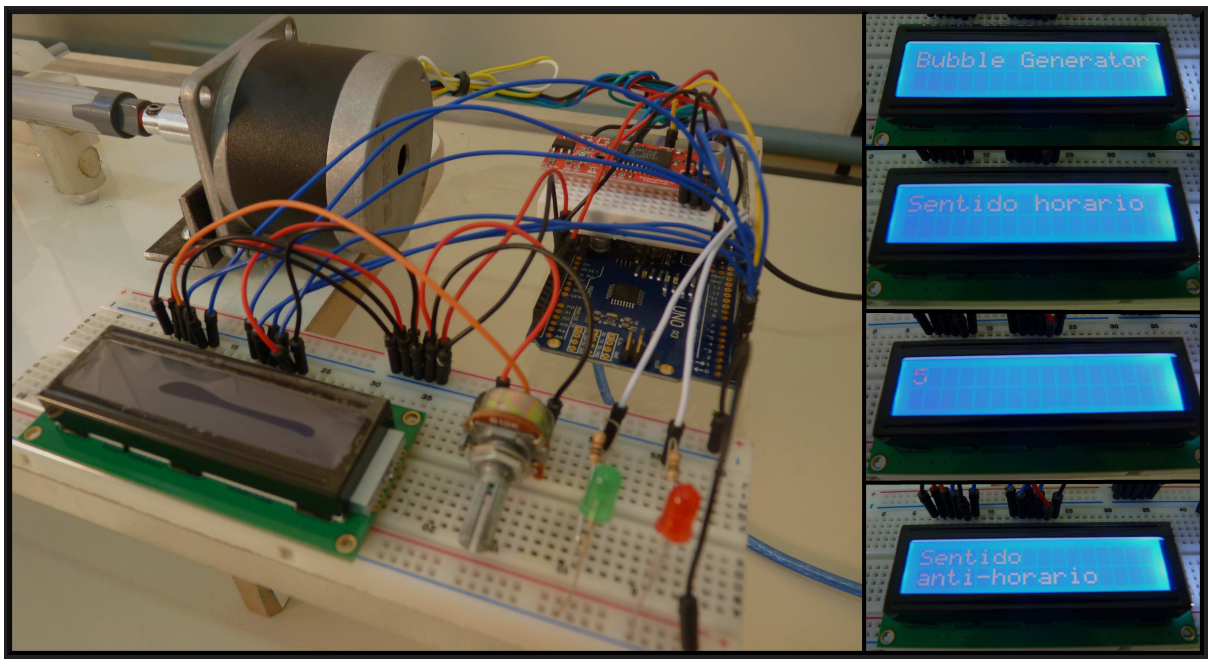

Figure 7.2: Electronic part of the experimental bench. The Arduino is connect to an H-bridge (Easydriver), stepper motor, LCD screen and leds. The LCD screen works in four different modes: (a) initialization mode, (b) clockwise , (c) countdown and (d) counterclockwise. The contrast of the LCD screen is controlled by a potentiometer.

and

$$t_c = \frac{a}{U_t}, \tag{7.4}$$

where m is the bubble mass, a is its radius, μ is the viscosity of the fluid and U_t is the terminal velocity. Now, considering that $St_a = t_r/t_c$ and using equations 7.3 and 7.4 we define that:

$$St_a = \frac{mU_s}{6\pi\mu a^2}, \tag{7.5}$$

and for the case of creeping flow ($Re \ll 1$) the particle terminal velocity reduces to Stokes terminal velocity given by:

$$U_s = \frac{2}{9}\frac{\Delta\rho}{\mu}ga^2. \tag{7.6}$$

Supposing a single isolated small bubble, which is approximately a perfect sphere due to surface tension dominant effect on its shape and $\mu = 100cP$, the Stokes solution is a good approximation.

$$U_s = 0.0747\frac{m}{s} \tag{7.7}$$

and

$$St_a = 2.36 \times 10^{-4}. \tag{7.8}$$

Now if this Stokes number is compared with a Stokes number related to the tank height, H, where:

$$St_H = \frac{mU_s}{6\pi\mu aH}. \tag{7.9}$$

this leads to

$$\frac{St_H}{St_a} = \frac{a}{H} \tag{7.10}$$

Considering that St_H must be smaller than 0.1, so the bubble reaches its terminal velocity within the height of the column. In this condition, the critical tank heigh H_c should be:

$$\frac{H_c}{a} = \frac{St_a}{St_H}. \tag{7.11}$$

We may observe that if the bubble is small enough, it quickly reaches the Stokes terminal velocity. Besides, considering creeping flow, $U_s \sim U_t$, where U_t is the terminal velocity. In this condition $H/a \ll 1$. Based on that, the whole bench can be seen in figures 7.3 and 7.4.

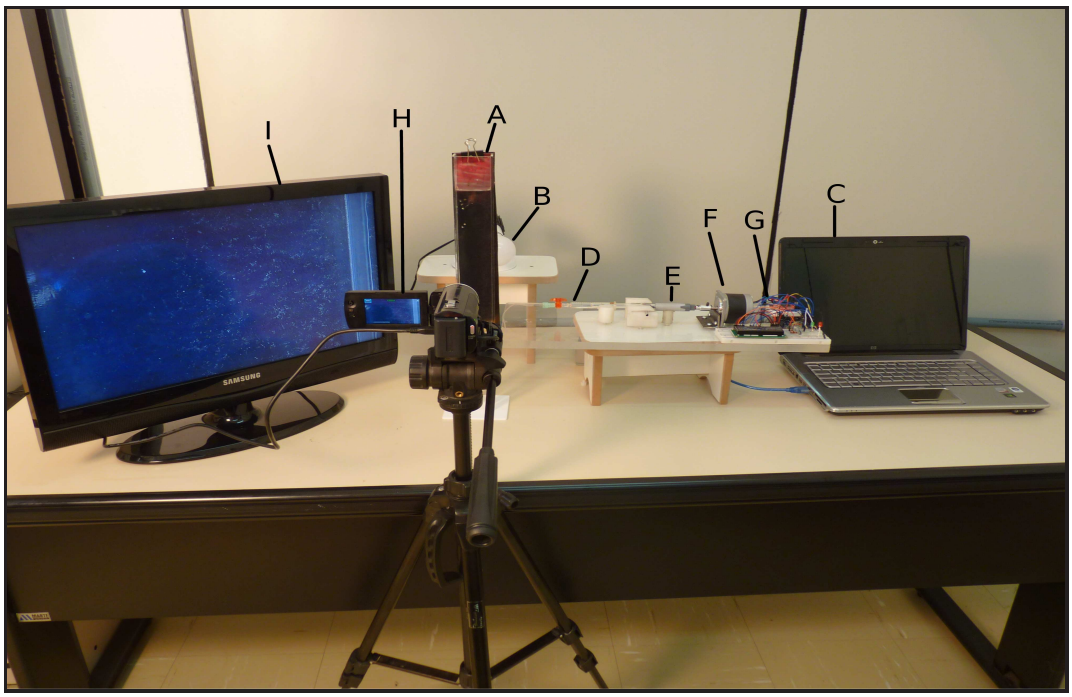

Figure 7.3: The whole experimental setup. **A** shows the fluid column, **B** is the back LED light used to iluminate when using opaque liquids, **C** represents the computer used to control the microcontroller, **D** is the syringue, **E** shows the linear actuator, **F** is the stepper motor, **G** shows the electronic devices, **H** is the HD camera and **I** is the monitor of visualization.

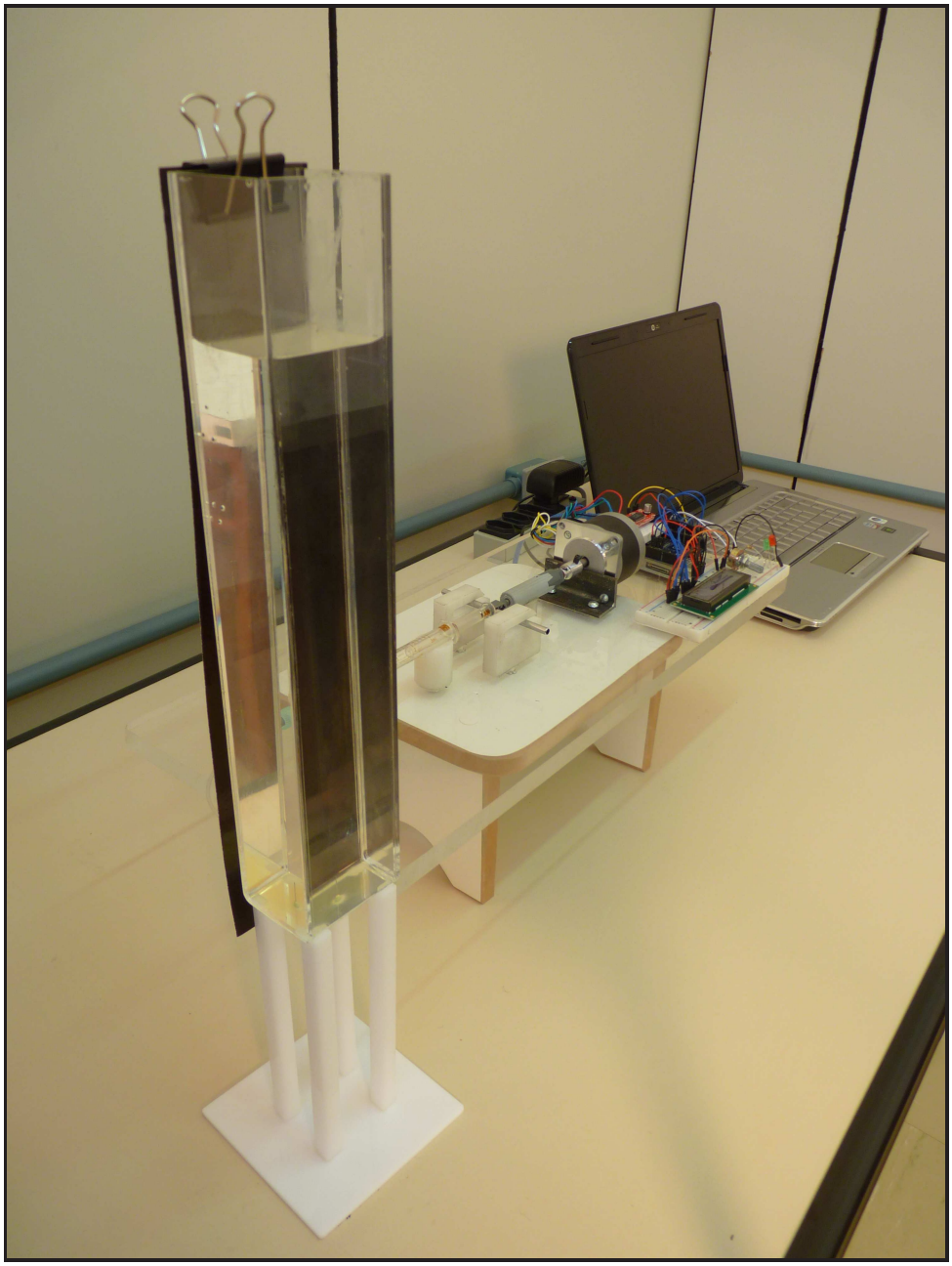

Figure 7.4: The experimental bench apparatus seen from another point of view. In this image is possible to see the test column. The black paper on background facilitates the visualization due the contrast.

The magnet used in order to apply a magnetic field is shown in figure 7.5. This magnet made from a combination of neodymium, iron and boron is extremely strong, but fragile at temperatures above 120^oC and has typical values of remanence and coercitivity $0.38T$ and $600kA/m$, respectively.

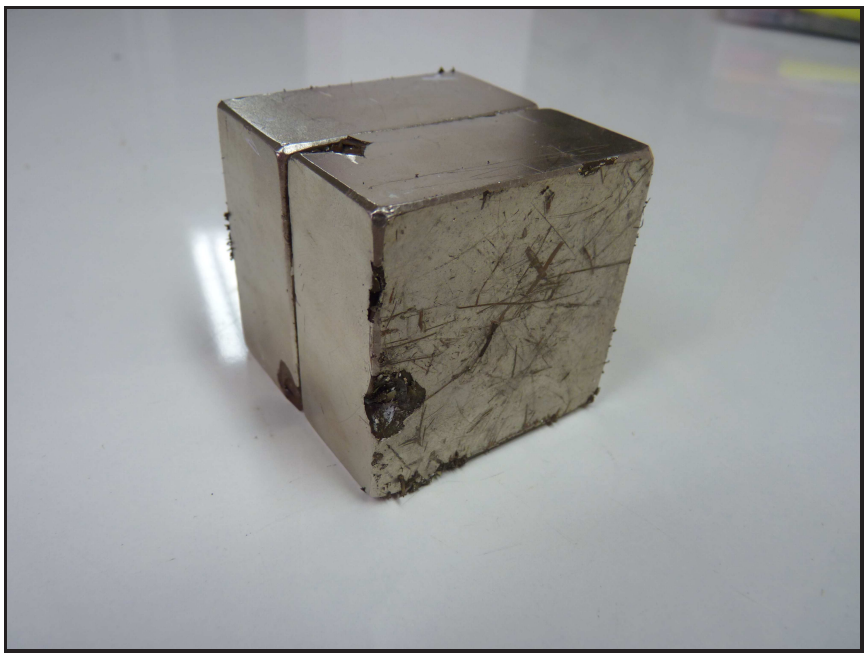

Figure 7.5: Neodymium magnet used as a constant applied magnetic field in the experiments

In order to compute the decay of the field produced by the magnet, two different gaussmeters were used: a LakeShore 410 Gaussmeter and F.W.Bell 5070 Gaussmeter, shown in figures 7.6(a) and 7.6(b). Both equipments measure the strength of the magnetic field at a point in space based in the Hall Effect. The Hall generator is a device commonly used to measure flux density. It is a thin slice of a semiconductor material to which four leads are attached at the midpoint of each edge. A constant current Ic is forced through the material. In a zero magnetic field there is no voltage difference between the other two edges. When flux lines pass through the material the path of the current bends closer to one edge, creating a voltage difference known as the Hall voltage V_h. In an ideal Hall generator there is a linear relationship between the number of flux lines passing through the material (flux density) and the Hall voltage. The Hall voltage is also a function of the direction in which the flux lines pass through the material, producing a positive voltage in one direction and a negative voltage in the other. If the same number of flux lines pass through the material in either direction, the net result is zero volts. This sensitivity to flux direction makes it possible to measure both static (dc) and alternating (ac) magnetic fields.

This voltage is also a function of the angle at which the flux lines pass through the material. The greatest Hall voltage occurs when the flux lines pass perpendicularly through the material. Otherwise the output is related to the cosine of the difference between 90^o and the actual angle.

The decay of the field produced by the magnet is shown in figure 7.6. It is possible to see that for $d \geq 3cm$, the measured values can be fitted by a function of type $1/r^2$. However, when $d \leq 3cm$ it is more appropriate to fit the gaussmeter behavior by a exponencial fit. For the F.W.Bell 5070

(a) LakeShore 410 Gaussmeter

(b) F.W.Bell 5070 Gaussmeter

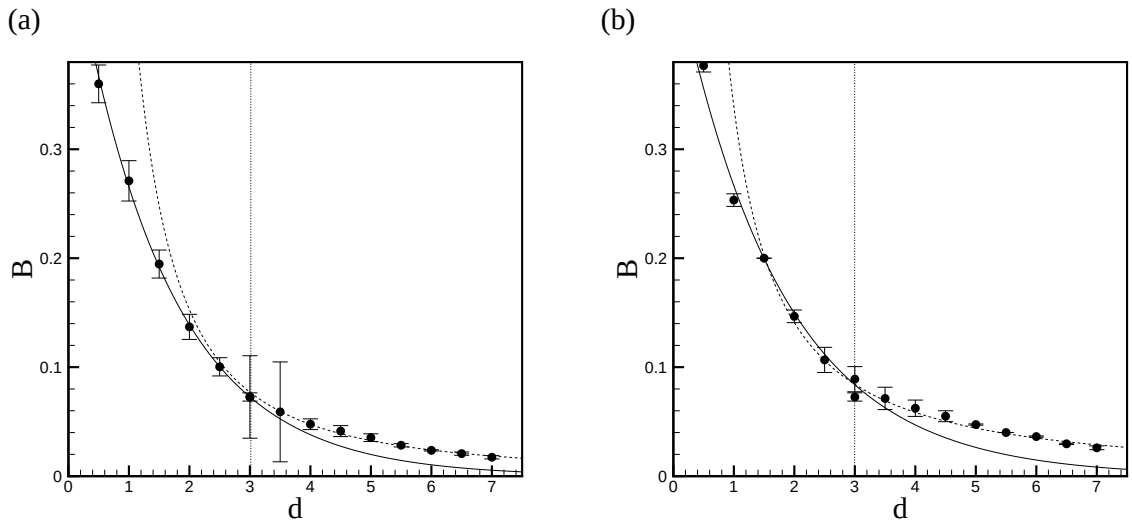

Figure 7.6: Field decay measured with the F.W.Bell 5070 Gaussmeter (empty circles and dashed line) and the LakeShore 410 Gaussmeter (filled circles and solid line). The $1/r^2$ behavior is shown for $d \geq 3cm$.

Gaussmeter, the fits are given by:

$$\boldsymbol{B} = \begin{cases} e^{(-0.65d+1.62)}, & \text{if } d \leq 3.0cm \text{ (near-field configuration)} \\ 1.59d^{-1.69}, & \text{if } d \geq 3.0cm \text{ (far-field configuration)} \end{cases} \tag{7.12}$$

and for the LakeShore 410:

$$\boldsymbol{B} = \begin{cases} e^{(-0.58d+1.55)}, & \text{if } d \leq 3.0cm \text{ (near-field configuration)} \\ 1.22d^{-1.26}, & \text{if } d \geq 3.0cm \text{ (far-field configuration)} \end{cases} \tag{7.13}$$

It is interesting to notice that the near-field configuration could also be fitted if we consider

other harmonics besides $1/r^2$. However, at certain small distance d, this series diverges. For this reason all the simulations experiments regarding particle-particle magnetic interaction should be made with dilute suspensions. If the particles are at a critical distance d_{cr}, the decay of the magnetic forces and torques, represented respectively by $1/r^3$ and $1/r^4$ would produce errors. However, in numerical simulations of many bodies problems, a near-field repulsion force (fictitious lubrication) is used to avoid the particles overlapping.

In addition to using gaussmeters, it is also possible to calculate analytically the field generated by a permanent magnet [87]. In order to conduct this calculation, the magnet is positioned as shown in figure 7.7.

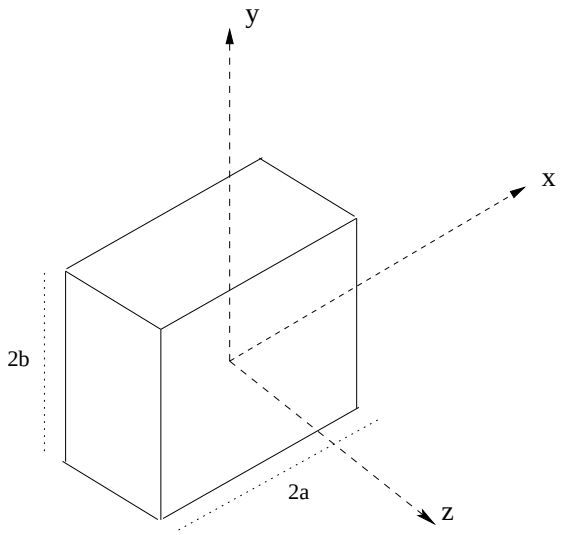

Figure 7.7: Schematic of the permanent magnet position for the analytic calculation.

The fields in the x and y directions will not be considered. However, the H_z component is given by:

$$H_z = \frac{J}{4\pi\mu_0}\left[tan^{-1}\left(\frac{(x+a)(x+b)}{z(x+a)^2+(x+b)^2+z^{2^{1/2}}}\right)+tan^{-1}\left(\frac{(x-a)(x-b)}{z(x-a)^2+(x-b)^2+z^{2^{1/2}}}\right)\right]$$
$$\frac{J}{4\pi\mu_0}\left[-tan^{-1}\left(\frac{(x+a)(x-b)}{z(x+a)^2+(x-b)^2+z^{2^{1/2}}}\right)-tan^{-1}\left(\frac{(x-a)(x+b)}{z(x-a)^2+(x+b)^2+z^{2^{1/2}}}\right)\right], \quad (7.14)$$

where $J/\mu_0 = M$. Considering that the remanent magnetization of the neodymium is $M = 1.1T$, $a = b = 2.5cm$, it is possible to compare the analytical solution with the values measured by the gaussmeters. This comparison is shown in figure 7.8.

It can be seen that there is a good correlation between the results. However, we may notice that the analytical solution is not adequate in the near-field region due to the exponencial behavior of this region.

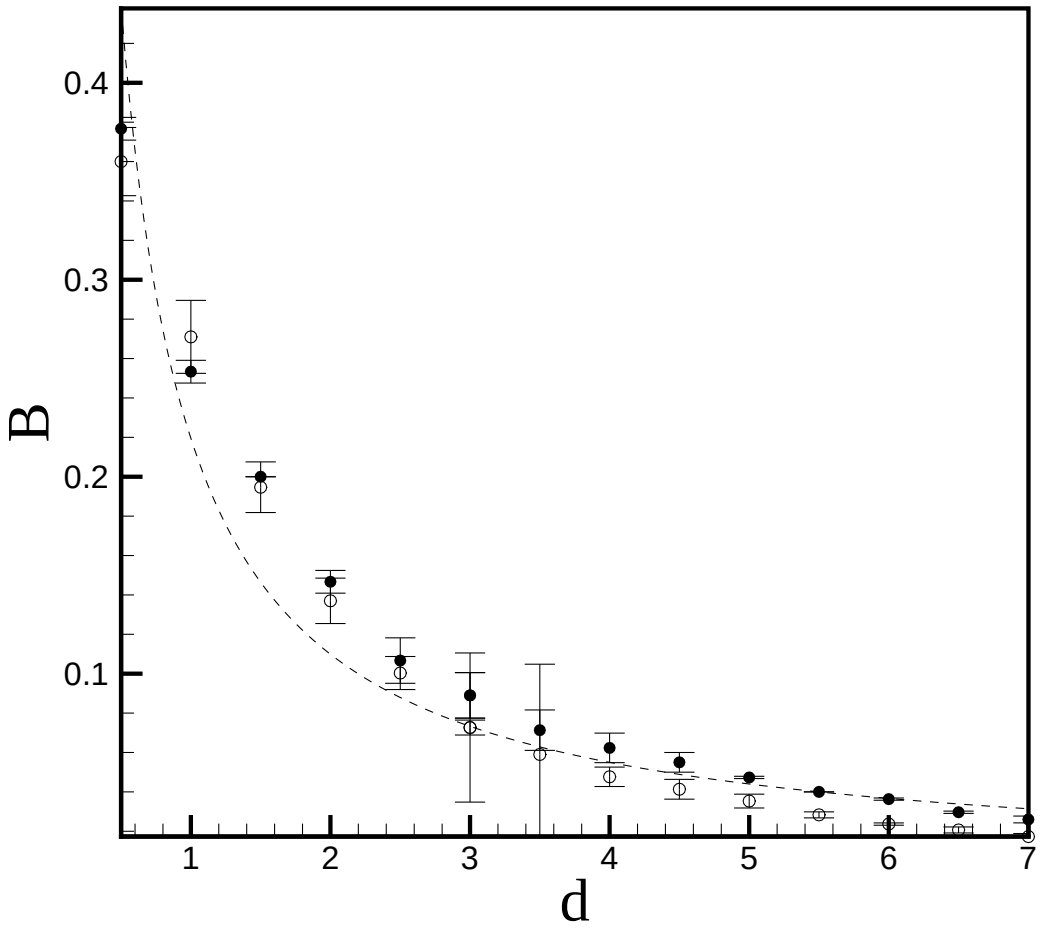

Figure 7.8: Field decay comparison between the analytic solution (dashed line) and the values measured by F.W.Bell 5070 Gaussmeter (filled circles) and the LakeShore 410 Gaussmeter (blank circles). The $1/r^2$ behavior is shown for $d \geq 3cm$.

7.3 Fluids Characterization

7.3.1 Viscosity Measurements

In order to characterize the viscosity of the fluids used in the experiments, an Anton-Paar Physica MCR 301 rheometer is used to measure the viscosity. The rheometer, shown in figure 7.10 is installed on a robust table and isolated from vibrations. It allow us to study both Newtonian and non-Newtonian fluids with or without the influence of magnetic fields in simple and oscillatory shears. The temperature of the plates is kept constant due to a Peltier system. When a magnetic field is applied, this system cannot be used, due to the electrical components and the temperature is controlled with a thermal bath from Lauda.

The rheometer is supplied with compressed air from a Schulz compressor. The air is previously

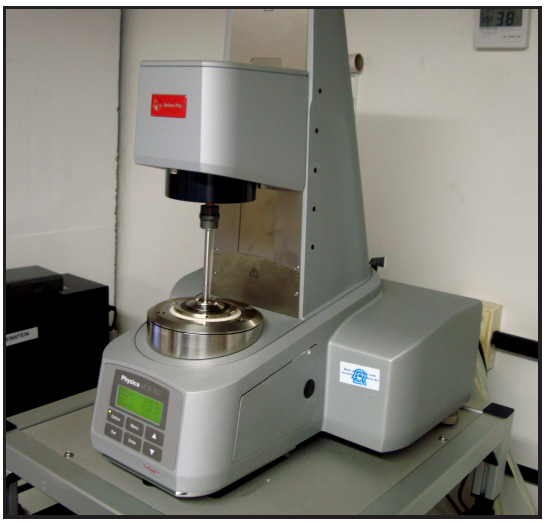

(a) Anton-Paar Physica MCR 301 Rheometer

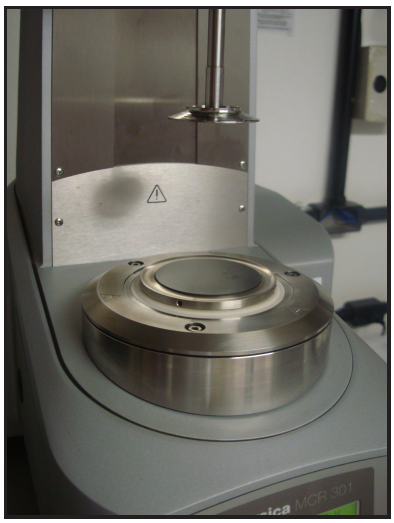

(b) Rheometer plates

cleaned and dehumidified by several filters (as shown in figure 7.9). Depending on the viscosity of the fluid, the shear rate can reach values around $5000s^{-1}$, which overcomes most viscometers standards.

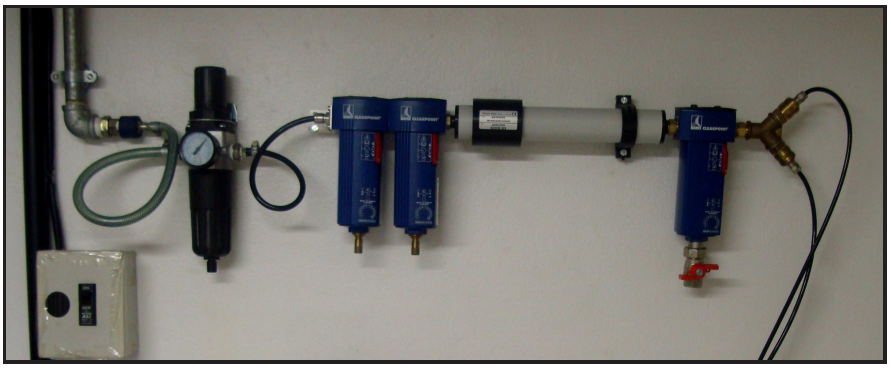

Figure 7.9: Filters used to clean and dehumidified the compressed air from the Schulz compressor

The physical measuring principle of rheometry is used to determine macroscopic material functions of a sample behavior. However, such functions are the sum result of the sample microscopic structure parameters. The rotational tests conducted using an Anton-Paar rheometer are possible due to the dynamic EC motor that controls the shear rate imposed. Besides, a Peltier system is used to maintain the temperature of the sample from -150^oC up to 1000^oC. In this context, to conduct the experiments, the sample is loaded into a gap between two parallel plates. The upper disc rotates due to the movement of an ultra-low inertia motor, coupled to an ultra-high precision position encoder, which can be seen in figure 7.10.

The size of the gap is determined due to the fluids viscosity. For the magnetic fluids used to generate bubbles the gap and the volume of the sample is shown in table 7.1. In order to obtain the sample volume, we must use the rotational plate diameter $d_{PP50} = 49.963mm$.

When the fluid is sheared in the rheometer it is governed by Continuity and Navier-Stokes equations. For that, both stationary and rotational disks are used as boundary conditions. The

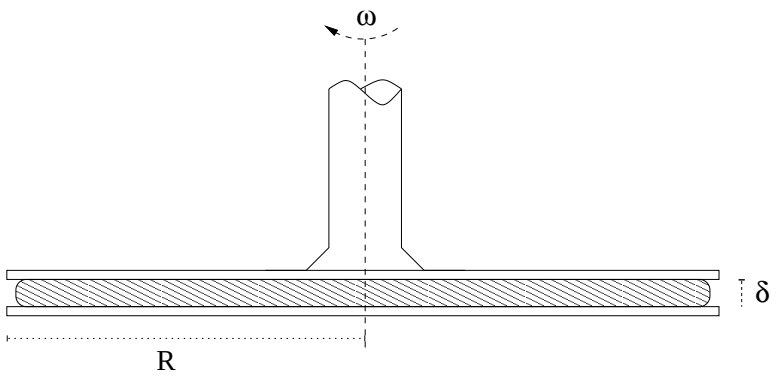

Figure 7.10: Rheometer plates schematic. The rotational plate (with radius R) is positioned at a distance δ from the stationary plate and rotates with angular velocity ω. The fluid sample is added between both plates.

Fluid	Gap [mm]	Sample Volume [ml]
Ferrofluid # 1	0.4	0.784
Magnetorheological Suspension	0.4	0.784
Ferrofluid # 2	0.7	1.372

Table 7.1: Adequate gaps and sample volume for fluids used.

mechanical quantity to be controlled in the experient is the torque, which must be within the range indicated by the manufacturer ($200mNm$ - $0.1\mu Nm$). The torque is based on the force acting on the element of fluid. In this case, the shear rate is a function of the disk radius, the angular velocity and the gap between the rotational and static disc:

$$\dot{\gamma} = \frac{\omega r}{\delta}, \tag{7.15}$$

where ω is the angular velocity and δ is the gap size. Said that, the torque is then, given by:

$$\mathscr{T} = \int_0^R r\eta\dot{\gamma}2\pi r dr, \tag{7.16}$$

so

$$\mathscr{T} = \frac{\eta\dot{\gamma}R^3\pi}{2}. \tag{7.17}$$

Based on that information, the magnetic fluids used are tested. The uncertainty of the viscosity measurements obtained by the rheometer was considered the maximum between the standard deviation of the measurements obtained for each shear rate and the one calculated by the rheometer torque expression in equation 7.17:

$$\Delta\eta = \frac{\partial\eta}{\partial\mathscr{T}}\Delta\mathscr{T} + \frac{\partial\eta}{\partial R}\Delta R + \frac{\partial\eta}{\partial\dot{\gamma}}\Delta\dot{\gamma}. \tag{7.18}$$

7.3.1.1 Ferrofluid #1

Ferrofluid #1 is a mixture of EFH3 (commercial ferrofluid manufactured by Ferrotec) and mineral oil (commercialized by VETEC) . Both fluid characteristics can be seen in table 7.2:

Fluid	Viscosity [cP]	Volumetric Fraction [%]	Density [g/mL]	Magnetization [Gauss]
EFH3	12	11.8	1.42	650
Mineral Oil	156 cP	-	≈ 0.85	-

Table 7.2: Properties of the fluids used as base to synthesize the ferrofluid #1

In order to measure the fluid viscosity, three tests are conducted for different shear rates. For each shear rate, the viscosity is measured in time ($0 \leq t \leq 300$), as seen in figure 7.11(a). For each realization, a time average was taken and an ensenble average was made from these, as shown in figure 7.11(b).

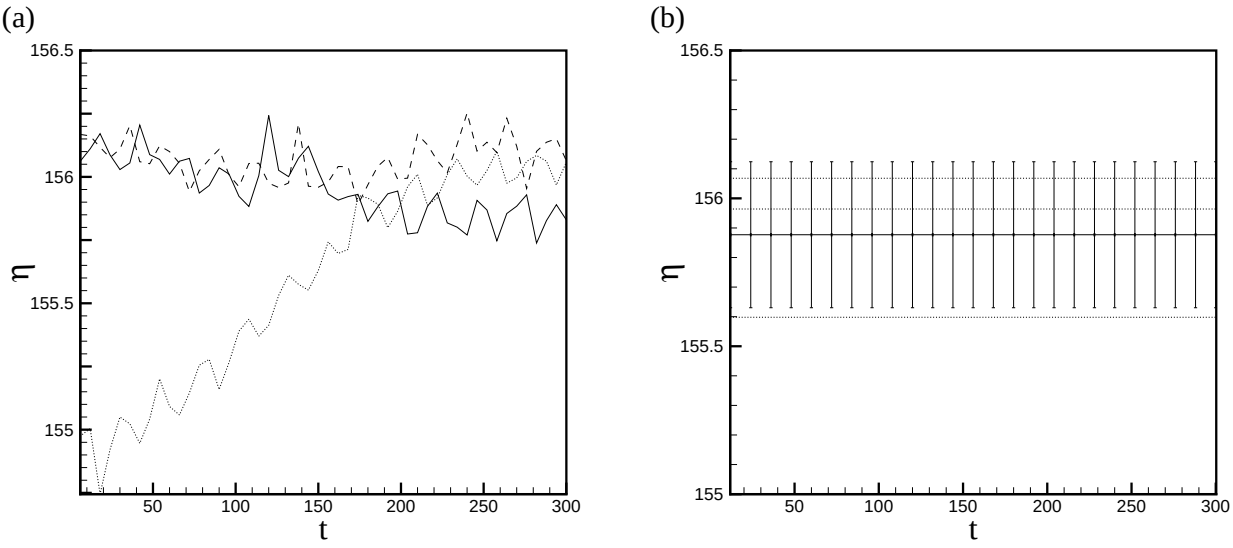

Figure 7.11: (a) The viscosity η is shown as a function of time for the first (dotted line), second (dashed) and third (solid line) realizations. (b) The time avarage of each realization is shown in dotted lined and the ensenble average by the solid line.

With the ensenble avarage of each shear rate, the fluid viscosity can be obtained. For ferrofluid #1, we made three realizations for $\dot{\gamma} = 50$, $\dot{\gamma} = 100$ and $\dot{\gamma} = 500$. The Newtonian fluid behavior can be seen in figure 7.12. This is consistent with expected, since there is no applied field.

7.3.1.2 Magnetorheological Suspension

The magnetorheological suspension (MRS) is a mixture of mineral oil and magnetic microparticles ($d \approx 100\mu m$). The magnetic particles used in the experiment were maghemite nanoparticles (mean diameter equal to $4nm$) immersed in styrene-divinylbenzene spherical micron-sized polymer

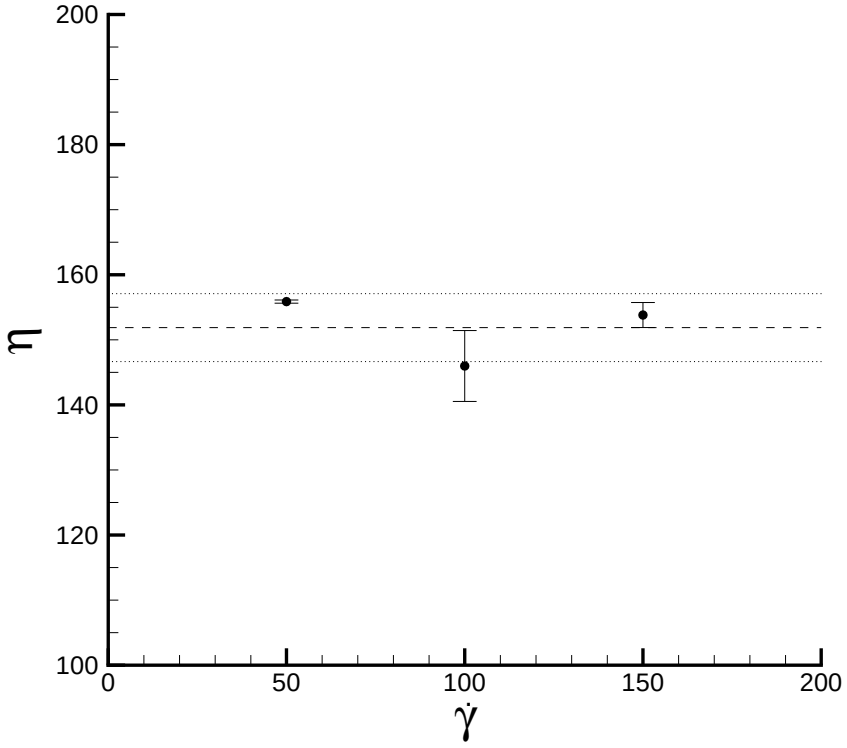

Figure 7.12: (a) The viscosity η of the ferrofluid is shown as a function of time for the first (dotted line), second (dashed) and third (solid line) realizations. (b) The time avarage of each realization is shown in dotted lined and the ensenble average by the solid line.

templates with mean diameter of $100\mu m$. The difference from a MRS and a ferrofluid is basically the stability of the suspension. While in the ferrofluid there is Brownian motion, this mechanics is not effectively in the MRS due to the particle size.

When subjected to a magnetic field, the MRS greatly increases its apparent viscosity, to the point of becoming a viscoelastic solid, depending on the volumetric fraction of particles. In this case, there are 758 ppm in volume so the fluid is not opaque.

For the MRS, we made three realizations for $\dot{\gamma} = 20$, $\dot{\gamma} = 100$ and $\dot{\gamma} = 500$. It is possible to see from figure 7.13 that the fluid has a Newtonian behavior. Again, that is expected because there is no applied field and the suspension is very dilluted.

We may observe on figure 7.14 the magnetorheological suspension amplified with a Olympus 30 UC microscope. Note on the far left of the figure, the presence of dimers and trimers when the suspension is subjected to shear rate of $\cot\gamma = 300$. These type of chains are the most proeminet in diluted suspensions. However, when we apply a magnetic field (middle figure), there is an agglomeration of these particles, increasing the length of the chains. For this reason, the viscosity increases when the field is applied. These agglomerates generate a flow resistance. In far right, the figure shows the same suspension 24 hours after the application of the magnetic field. It is

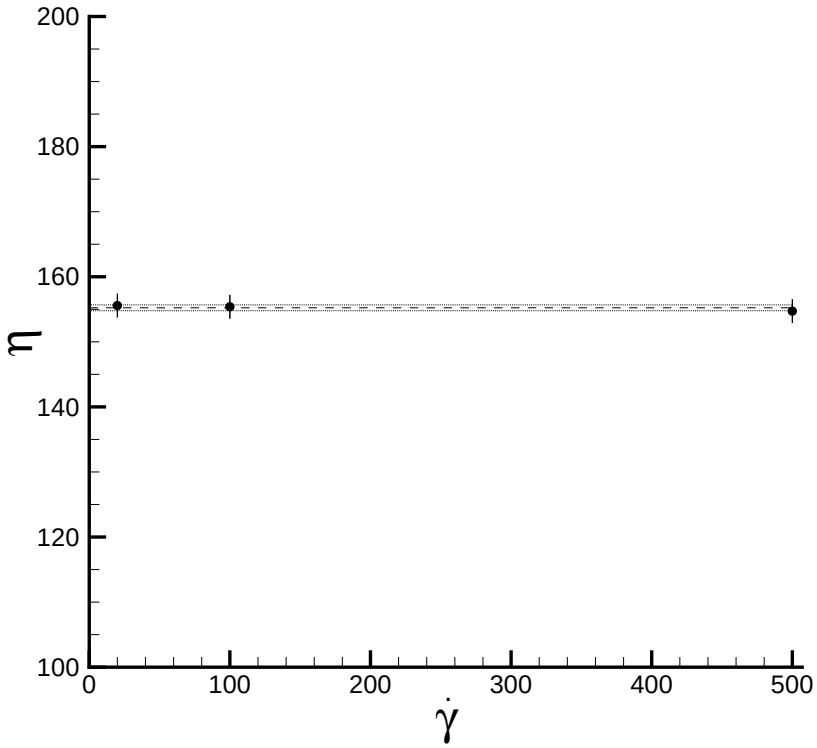

Figure 7.13: (a) The viscosity η of the magnetorheological suspension is shown as a function of time for the first (dotted line), second (dashed) and third (solid line) realizations. (b) The time avarage of each realization is shown in dotted lined and the ensenble average by the solid line.

observed that there is still a residual magnetization (due to hysteresis) since the particles become small magnets.

Figure 7.14: The far left figure shows the suspension under a shear ($\dot{\gamma} = 300$). The figure in the midle presents the magnetorheological suspension when there is an applied magnetic field. The far right figure shows the same suspension 24 hours after the application of the magnetic field.

7.3.1.3 Ferrofluid #2

The ferrofluid #2 is a mixture of EFH3 (commercial ferrofluid manufactured by Ferrotec) and silicon oil. Both fluid characteristics can be seen in table 7.3. For the ferrofluid #2, we made two realizations for $\dot{\gamma} = 10$, $\dot{\gamma} = 20$, $\dot{\gamma} = 50$ and $\dot{\gamma} = 100$. The non-Newtonian behavior can be seen in figure 7.15.

Fluid	Viscosity [cP]	volumetric Fraction [%]	Density [g/mL]	Magnetization [Gauss]
EFH3	12	11.8	1.42	650
Silicon Oil	60,000 cP	-	≈ 0.97	-

Table 7.3: Properties of the fluids used as base to synthesize the ferrofluid #2

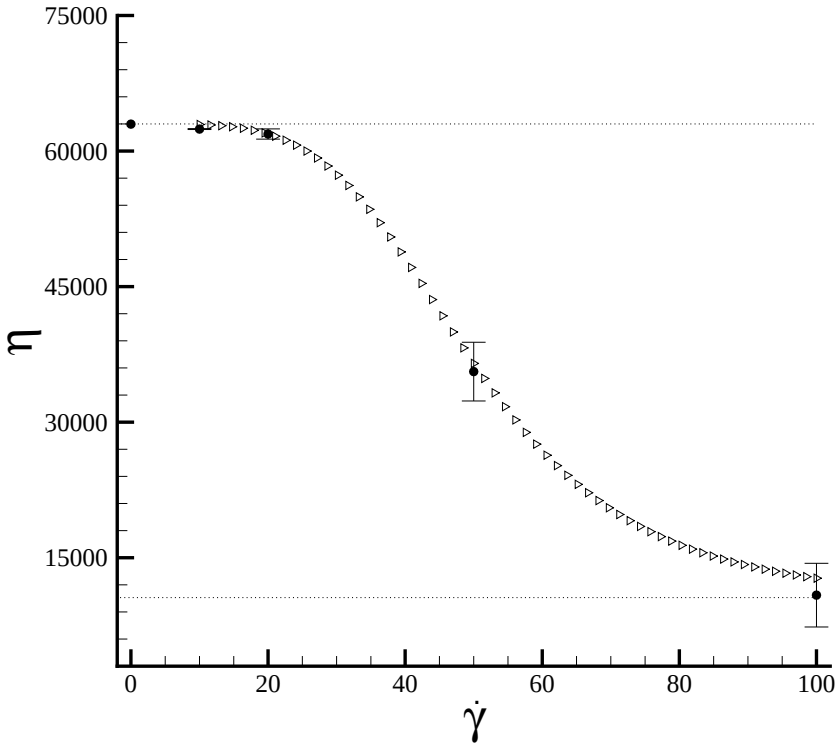

Figure 7.15: (a) The viscosity η of the magnetorheological suspension is shown as a function of time for the first (dotted line), second (dashed) and third (solid line) realizations. (b) The time avarage of each realization is shown in dotted lined and the ensenble average by the solid line.

The viscosity can be fitted by a Cross Model [88] given by:

$$\eta = \eta_\infty + \frac{(\eta_0 - \eta_\infty)}{1 + (0.02\dot{\gamma})^{4.2}} \tag{7.19}$$

This model basically represents two plateaus (the zero-shear Newtonian plateau and the infinite-shear Newtonian plateau) and a shear-thinning region. It is extremely difficult to synthesize pure

silicone oil with high viscosity. For this reason, it is common to add long chain macromolecules. However, when the macromolecules are not deformed, or at rest, the fluid behaves as a Newtonian one. As these macromolecules have a high molecular weight, there is a relaxation mechanism generating the shear thinning behavior. That effect, called reptation [89] describes the effect of polymer chain entanglements on the relationship between molecular mass and chain relaxation time (or similarly, the polymer zero-shear viscosity). This memory effect varies directly with the molecular weight (M) with $\tau \sim M^{3.4}$ [90].

At low shear rates the flow does not interact with the polymer molecules. In this situation the molecules relaxes faster than the variations of the flow maintaining its original form. However, as the shear rate increases, also does the macromolecule deformation, which occurs in the flow direction. The viscosity decreases with the increasing shear rate until the threshold at which the molecule reaches its maximum elongation.

7.3.2 Surface Tension

The surface tension of the bubbles is measure using a Lauda TVT2 tensiometer, shown in figure 7.16. The measuring principle here is the drop volume technique. Actually, on the simple balance between Arquimedes' buoyancy force and interfacial surface when a small drop is generated and its detachments from the edge of a capillary tube. By this principle is possible to make measurements of surface tension between gas-liquid and interfacial tension between liquid-liquid. The mechanical arm of the tensiometer pushes the syringe plunger, which presses the fluid into the capillary. The drop remains attached to the capillary due to superficial tension. The temperature is controlled and kept constant (24 degree Celsius) by using a Lauda thermal bath.

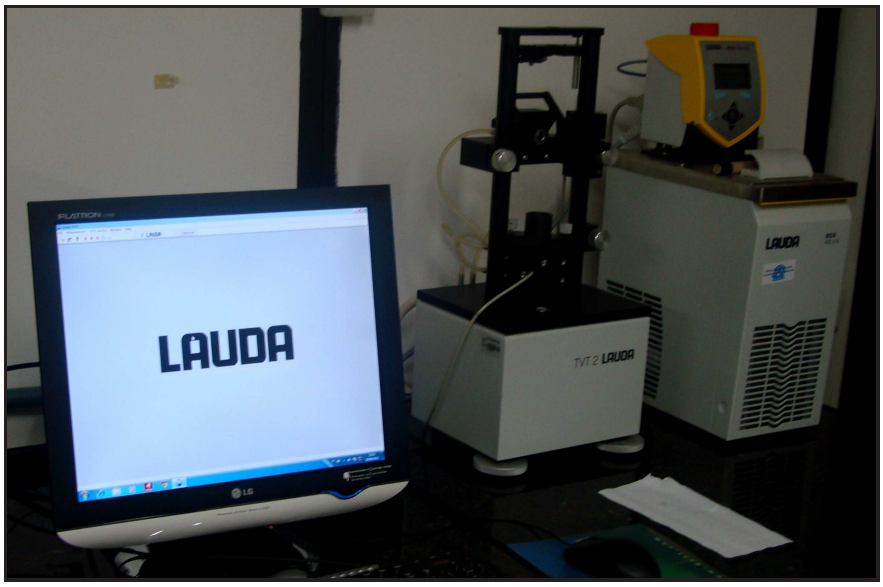

Figure 7.16: Figure shows the computer with the special data aquisition software, the tensiometer and the thermal bath: all from Lauda.

With the gradual increase in the drop volume, it detaches from the capillary. The superficial

tension is given by:

$$\sigma = \frac{\Delta\rho V g}{2\pi R} F \tag{7.20}$$

where V is the drop volume, g is the gravity acceleration, $\Delta\rho$ is the difference of both fluids density, R is the capillary radius and F is a correction factor given by the manufacturer. The capillary is immersed in a glass container which is filled with a fluid. In this case, the fluid is air. If the liquid in the syringe has greater density, the straight capillary should be used. If this fluid has the lower density, a reserve capillary must be used. In this case, the drop is formed under the light barrier, and rises to the top because of the difference in specific gravity. The formed drop is detected when passing through the light barrier and the critical drop volume and time is measured.

In standard mode of operation, the only adjustable parameter is the drop formation rate, which remains constant throughout the experiment. Thus, all the drops have the same formation time. This was the mode used in all tests, performed at a temperature of 24^oC, which is kept constant with a Lauda Thermal Bath, with the straight capillary ($r = 1.38mm$). The average results are given in table 7.4, for two different tests. For each test, we consider five realizations of drops formation (cycles of drop formation) and, for each realization we average over five drop volume formations.

Fluid	Surface Tension [mN/m]	Volume [μl]
Ferrofluid #1	30.36 ± 0.8	20.16
Magnetorheological Suspension	30.62 ± 0.27	20.34

Table 7.4: Surface tension obtained for both tested fluids as a function of the drop volume.

7.4 Experimental Results

7.4.1 Mineral Oil

When using a mineral oil of $\mu = 156cp$, depending on the velocity set in the stepper motor, the bubble may deform. In this context, we show figure 7.17. An edge detection algorithm was used in order to observe the bubble shape. It is possible to see two different types of bubbles: the spherical cap and ellipsoidal. This is related to the high Reynolds number obtained due to the motor velocity.

Using the software CVMOB [91], it is possible to measure the bubble risen velocity and its radius. At first, the bubble horizontal and vertical diameters are, respectively: $0.00271m$ and $0.00296m$. The deformation parameter "D" proposed by Taylor [92] is used to quantify bubble shape deviation form a spherical shape:

$$D = \frac{|b - a|}{b + a} \tag{7.21}$$

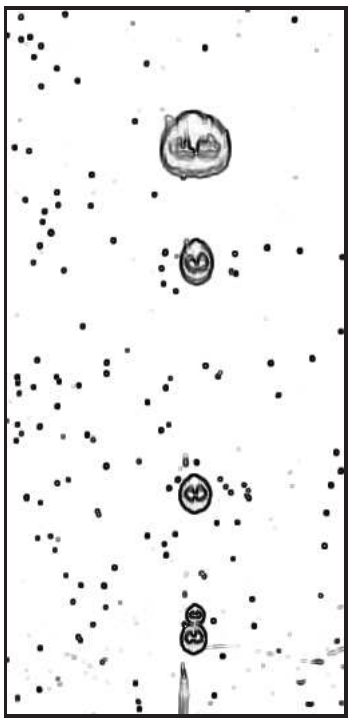

Figure 7.17: A Sobel edge detection algorithm is used to identify different bubble shapes. In this case, one may see the spherical cap, ellipsoidal and spherical.

where b and a denote the semi-axis along x and y retrospectively. For values of D smaller than 10% the bubble is considered spherical. In this case, the system is not at low Reynolds number and the bubbles end up not coalescing, as seen in figure 7.18. However, for this specific bubble $D \approx 5\%$. For a given bubble, for example, considering a constant risen velocity of $0.0576m/s$ and the mineral oil density of $\rho = 850kg/m^3$ at 25^oC, the *particle* Reynolds is ≈ 1. The Bond number, on the other hand, is ≈ 1 indicating a non-trivial balance between the two effects. In these cases, there is a certain deformation of the bubble spherical shape.

Considering $Re = 1$ and $Bo = 1$, the bubble is still in spherical shape what can be confirmed by the diagram proposed by Clift [84] (where the Bond number is called Eötvös, pronounced as Ertversh). This diagram can be seen in figure 3.

It is interesting to notice that these results are not valid for extreme values of density ratio ($\gamma = \rho_b/\rho_\ell$) or viscosity ratio $\kappa = \mu_b/\mu$, found for liquid drops falling through gases. Thus, if the walls of the container affects the bubble (or drop), this diagram is not valid. If the bubble or drop is sufficiently large, it fills most of the container cross section and the "slug flow" regime results.

7.4.2 Magnetorheological Suspension

A magnetorheological suspension is formed by microscale iron particles. Unlike the ferrofluid in which the particles are nanometric, the magnetorheological suspension is not stable. They cannot be considered an equivalent continuum fluid, but can be seen as a biphasic system with magnetic properties. These suspensions are interesting to make flow visualizations, since it is possible to see

Figure 7.18: Bubble interaction without coalescence. The contact time needed for these bubbles to coalesce is not enough. In this condition, both bubbles react as two particles interacting with reversibility.

these particles in the naked eye.

However, since the particles are larger particles, they are quickly attracted by an applied field. In this sense, the attraction of these particles produces a velocity field perpendicular to the bubble upward movement. For this reason, the bubble tends to modify its trajectory, as can be seen in figure 7.20.

A monitoring fluid particles was done through the software CVMOB. In this regard, we note that these small volumes are attracted to the field because of the attraction of the magnetic particles. This is why the bubbles passing end up having its trajectory modified. This change in trajectory can be seen in figure 7.19.

However, the bubble deformation in the x direction is not considerable. For instance, the initial average diameter of the bubble is $d_i = 0.002275m$ with a deformation coefficient of $D_i = 7.9\%$. After rising $5.5cm$, the diameter is $d_f = 0.002345m$ with $D_f = 5.5\%$. However, in situations where a higher magnetic field is applied or the concentration of particles is greater, there may be a distortion in the bubble shape. In this case, $Re \approx 0.4$, $Re_{mag} \approx 0.021$ and $Bo \approx 0.6$. Under these conditions, the magnetic effects dominate the inertial effects

7.4.3 Ferrofluid #1

The first ferrofluid was made with mineral oil and EFH3 (particle volume fraction of $\approx 252.86ppm$). The ferrofluid EFH3 is very opaque and the visualization gets worse exponentially as the volume fraction increases. The application of a magnet in the left side of the container do not affect the bubble trajectory or velocity. When there is no applied magnetic field, the initial defformation ratio of a bubble with avarage diameter $d = 0.00157m$ is $D_i \approx 17\%$. When the bubble

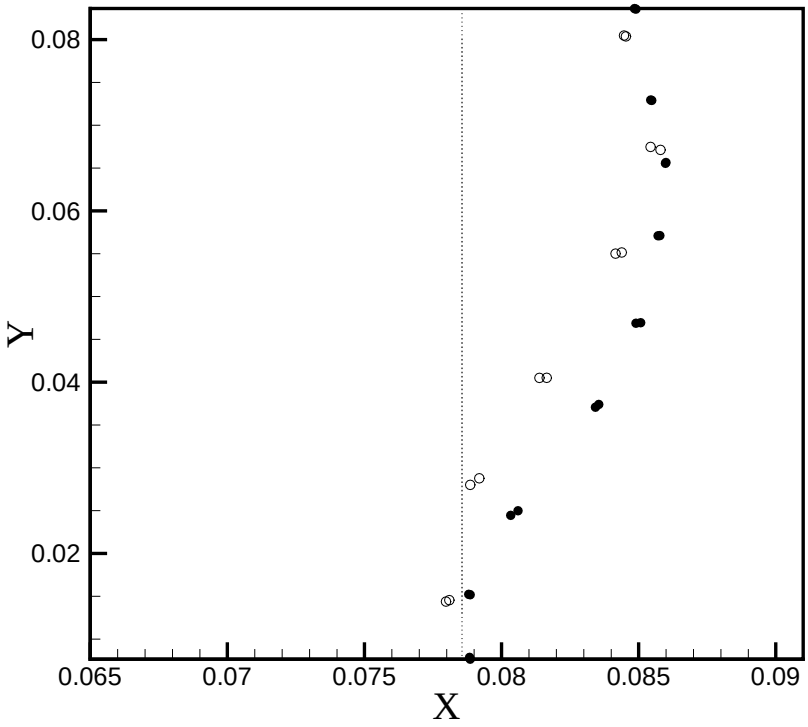

Figure 7.19: The trajectory of two rising bubbles immersed in the magnetorheological suspension. It is possible to observe that the bubble modifies its trajectory in x in 3.5 times its diameters.

rises $h = 2.4cm$, this quocient becomes $D_f \approx 25\%$.

When the magnetic field is applied, considering a bubble of diameter $d \approx 0.00160m$, the deformation ratio changes to $D_i \approx 3\%$ and $D_f \approx 3.5\%$. This shows, once again, a stabilization in the movement of the bubble with the application of magnetic field. In this sense, when the field is applied, the particles tend to align in its direction, generating a resistance to tangential movements.

In addition, we analyzed two bubbles with average diameters of $d_1 = 0.001815m$ and $d_2 = 0.001835m$. In this case, d_1 is the diameter of a bubble immersed in ferrofluid without any applied field. On the other hand, d_2 is the diameter of a bubble immersed in ferrofluid with a field applied in left side of the column. The relation between the Stokes velocity of both bubbles is given by:

$$\frac{U_{s1}}{U_{s2}} = \left(\frac{d_1}{d_2}\right)^2 = 0.9783 \tag{7.22}$$

where U_{s1} is the Stokes velocity of the first bubble and U_{s1} is related to the second bubble. This means that there is a variation of 2.22% in the bubbles Stokes velocity due to size differences. However, the rising velocity of the first bubble, when there is an applied field, is $U_1 = 0.049m/s$. When there isn't any applied field, the second bubble velocity is $U_2 = 0.038m/s$. This represents

Figure 7.20: The trajectory of small volumes of fluid (represented by the different colors) are analyzed over time by CVMOB software in two different cases. Note that the flow tends to move toward the magnet, due to the attraction of the magnetic particles.

a difference of $28,94\%$, as shown in figure 7.21 The application of the magnetic field generates a change in the flow around the bubble. In addition, the magnetic fluid begins to present its non-Newtonian behavior.

The magnetic particles tend to align and be attracted in the direction of the applied field. In this sense, the approach of the magnet generates a transverse flow. However, since the magnet is applied in $h \approx 40cm$, the velocity field has a component in the z direction (related to the column heigh). Thus, as the bubble rises to a height of $60cm$, its velocity ends up being modified by the flow movement in the magnet direction. Furthermore, the application of the magnetic field tends to reduce the bubble deformation coefficient. Therefore, when the bubble is more spherical it has less area perpendicular to the flow, reducing drag.

When there is no applied field, $Re = 0.4$ and $Bo = 0.9$. When the field is applied, we have $Re = 0.5$ and $Re_{mag} = 0.025$. For both cases, the bubble is still in the spherical region of the Clift diagram.

7.4.4 Ferrofluid #2

The second ferrofluid made with silicon oil and EFH3 (particle volume fraction of $\approx 103.25ppm$) joins the non-Newtonian mechanisms of macromolecules and magnetic effects. The higher fluid viscosity allows the bubble to have more time to react to magnetic effects. However, the same long relaxation time decelerates the alignment movement of the particles in the field direction. It

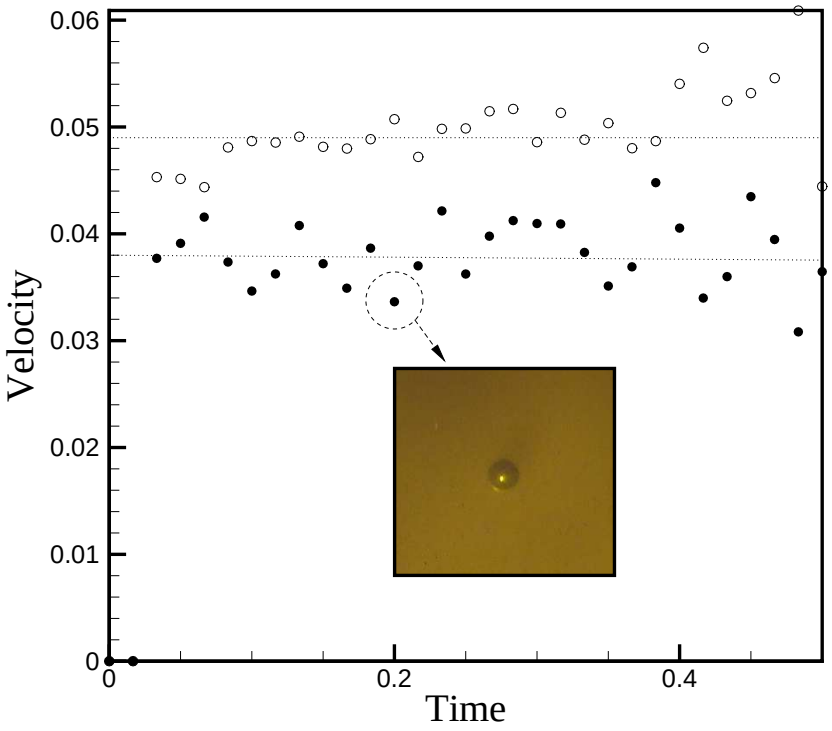

Figure 7.21: Bubble velocity over time for both cases: when a magnetic field is applied (blank circles) and when there is no applied field (black circles).

is possible to see in figure 7.22 that the particles are aligned in the field direction when that one is applied on the left side of the test column.

Figure 7.22: Particles alignment of approximately 45 degrees due to the application of a magnetic field.

In this context, the viscous effects compete with the torque generated by aggregates due to the

alignment tendency. This ends up generating a resistance to the bubble movement. It is observed in figure 7.23 the bubble trajectory in both cases: in the presence and absence of magnetic applied field.

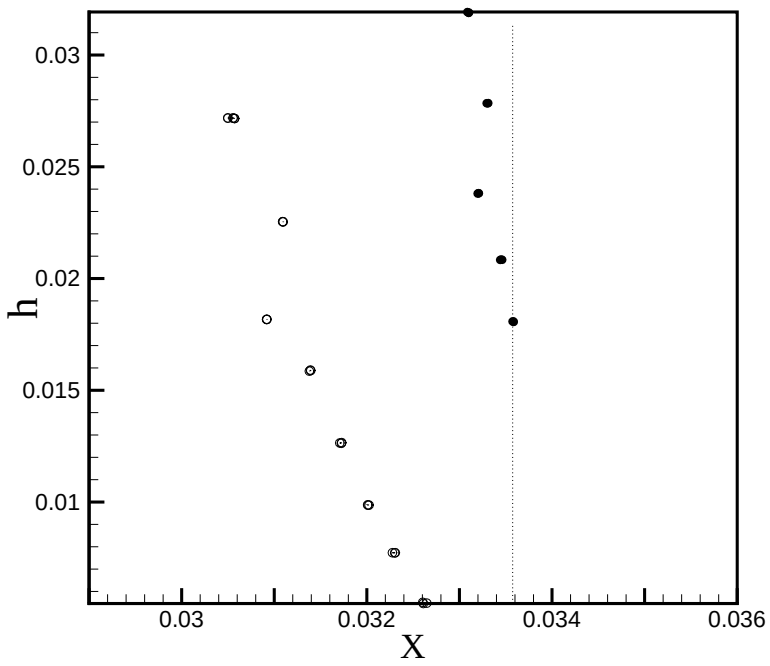

Figure 7.23: Bubble trajectory deviation. In this case, this deviation is 40% of its initial diameter, due to the size of the bubble and characterization of creeping flow.

It is possible to see that when there is the application of a magnetic field, the bubble tends to be taken in the same direction. This is due the alignment of particles in the direction of the field, generating a crossflow movement of the bubble.

Even considering a bubble of average diameter $d = 0.00975m$, due to the high viscosity of the fluid, the Reynolds number is very low ($Re \approx 0.0005$) and the deformation coefficient is $D = 2\%$. The Magnetic Reynolds number is $Re_{mag} = 0.00011$. This condition of creeping flow results in reversibility. In this condition, if two bubbles interacting possess a very high surface tension ($B \to \infty$) they would not coalesce. Rather, they would interact in the same way as observed in figure 7.18. However, in that case, that interaction is due to the value of the Reynolds number, which does not characterize creeping flow.

7.5 Bubble Interaction

The coalescence of a pair of bubbles occurs in two stages: (i) the draining of the intervening film of continuous-phase liquid to a critical thickness, h, which is thought to be between 10 and 100 nm [93]; (ii) the rupture of the remaining film by a mechanism which is not understood and

may involve non-continuum effects. The first of these steps is ordinarily the slower and hence determines the overall duration of the coalescence process.

A number of attempts have been made to describe the film-drainage stage mathematically [94, 95, 96, 97] and several detailed experiments have been carried out [98, 99, 100]. Among the difficulties encountered are: (i) if a realistic zero-tangential-stress boundary condition is applied to the draining film and surface tension is correctly included, a singular perturbation problem is generated which requires matched asymptotic expansions for its solution; (ii) if the bubbles collide with appreciable velocity, circulation patterns within the bubbles impose on the interface shear stresses, which assist drainage, greatly increasing computational difficulties; (iii) the area of the draining film varies with time: collisions at low relative velocities, being associated with initially small film areas, are more likely to lead to coalescence than collisions at high relative velocities, which involve large deformations of the bubbles and hence the rapid formation of a large-area, slowly draining film [101].

In this context, considering that two bubbles are pressed together by a steady force, F, the time τ required for the films to drain to the rupture thickness h is a classical lubrication problem and can be given by:

$$\tau = \frac{3\pi\mu S^4}{2F^2 h} \tag{7.23}$$

where μ is the dynamic viscosity of the continuous phase, S is the radius of the film and F is the force pressing the bubbles together. Considering the pressure within the deformed bubbles we have

$$F = 4\pi S^2 \frac{\sigma}{d} \tag{7.24}$$

where σ is the surface tension and d the bubble diameter. Based on that information, two bubbles rising under buoyancy in a silicon oil $(100,000cP)$ were analysed. The results are seen in figures 7.24 and 7.25.

In this case the bubbles start to rise due to buoyancy forces after being released. Subsequently, a wake is formed behind each bubble, and a pressure gradient is generated at the bottom surface of the bubbles at the same time. The trailing bubble is immersed in the wake of the leading one and interacts with the wake flow, which results in a stretch deformation in the vertical direction. It can be observed in figure 7.24 that the shape of the trailing bubble becomes a prolate ellipsoid which differs from that of the leading bubble of oblate shape.

The bottom of the leading bubble is progressively flattened whereas the top remains spherical. As time increases, the leading bubble develops towards an oblate ellipsoidal cap shape while the trailing one is deformed into a prolate shape due to the interaction of bubble-bubble and bubble-fluid. After that, the trailing bubble goes up faster due to the upward flow in the wake of the leading one and the recirculation at the side of the bubbles. The leading bubble appears to wrap itself around the trailing one as the bubbles move closer together. Finally, two bubbles coalesce

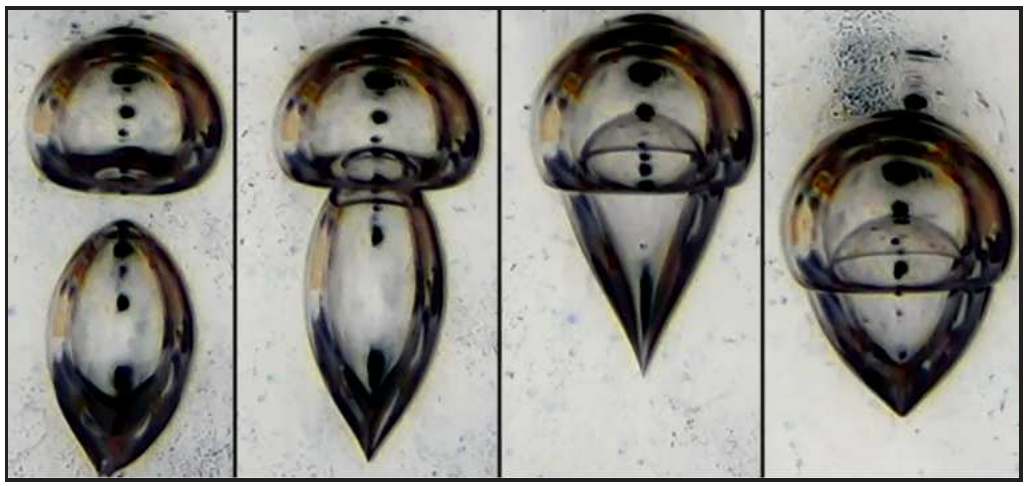

Figure 7.24: Bubble interaction in creeping flow. In this condition, two bubbles immersed in silicon oil interact and end up coalescing.

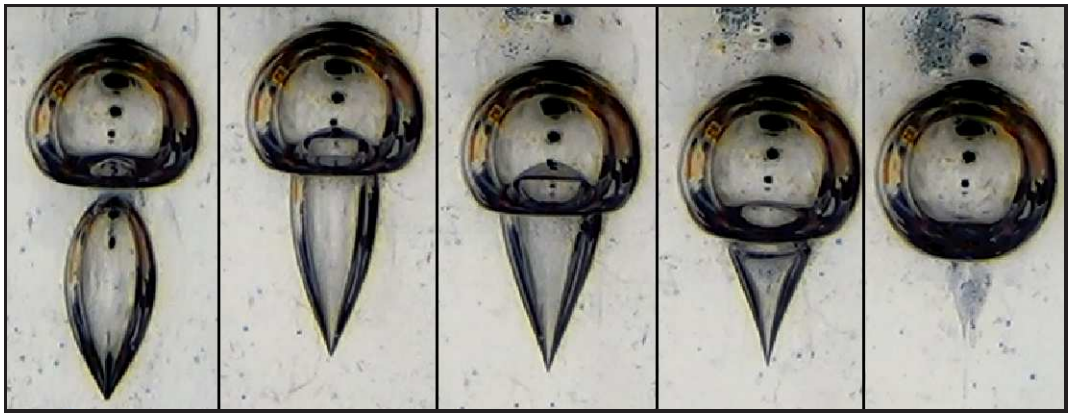

Figure 7.25: Bubble interaction in creeping flow. In this condition, two bubbles immersed in silicon oil interact and end up coalescing into a spherical shape bubble.

to form a bigger bubble. Another interesting feature to note is that the region of high curvature develops at the back of the trailing bubble, which results in a taper shape on the bottom of coalesced bubble. The reason for causing this pattern can be given as follows. For a fixed Morton number the surface tension of the bubble decreases with decreasing the density ratio. The smaller tension allows a tail with a region of high curvature on a bubble to develop in a steady extensional flow. The wake flow of the leading bubble resembles an extensional flow. The Morton number is a dimensionless number used together with the Eötvös number or Bond number to characterize the shape of bubbles or drops moving in a surrounding fluid or continuous phase and is given by:

$$Mo = \frac{g\mu^4 \Delta\rho}{\rho_l^2 \sigma^3} \tag{7.25}$$

where μ is the liquid viscosity, σ is the bubble surface tension, ρ_l is que fluid density and $\Delta\rho$ is the difference of density from both liquid and gas.

Chapter 8

Conclusions

This work investigated the oscillatory motion of a bubble immersed in a magnetic fluid subjected to an harmonic pressure and an external magnetic field. The governing equation for the radial movement of the oscillating bubble, in this context, called the Magnetic Rayleigh-Plesset equation (MRP) provides a highly nonlinear response. In this sense, several characteristic responses have been studied.

This study aimed to analyze these characteristic responses using an original methodology in order to seek the possible physical interpretations of how the main parameters of the problem influence the bubble response. To physically interpret how the oscillatory behavior of the bubble is modified due the system non-dimensional parameters, different dynamical system approaches have been used. Among these approaches, we may recall the use of collapse diagram, frequency spectrum alaysis, Lyapunov exponents, phase space analysis, bifurcation diagrams and scatter diagrams. These approchaes are able to provide important informations regarding the bubble behavior under different physical aspects. Furthermore, they proved to be very effective from the stability analysis point of view.

In the first part of this work, we studied how the equation of Rayleigh-Plesset is modified when the bubble is immersed in a magnetic fluid. For this, a new version of equation (MRP) was developed using the Maxwell's stress tensor. The applied magnetic field followed the model proposed by Rosensweig [39], considering only radial oscillations. The non-dimensional mathematical modeling has proved to be extremely robust, adding two new parameters: the Magnetic Reynolds number and the fluid magnetic susceptibility.

To solve the governing equation of the problem, we used a fifth order Runge-Kutta method with adaptive time step. This method proved to be extremely efficient, reducing the time required for the iterations with small time steps in up to 80%. In order to validate the code, an asymptotic solution was developed. In this situation, it was observed that for small values of (ε/Re_{mag}), the asymptotic solution perfectly couples the numerical one.

Based on these findings, it was observed how a static magnetic field modifies the bubble behavior. In this regard, it is noted that the application of a steady magnetic field increases the stability of the bubble, preventing the collapse and increasing its periodicity. This behavior was

also supported by the hydrodynamic linear stability analysis conducted.

It was noted that the non-dimensional parameters are extremely sensitive. Indeed, a study based on the changes in the bubble oscillation as a function of the Magnetic Reynolds, magnetic susceptibility and frequency of the pressure field was made. We observed, for example, that the application of a stronger magnetic field is valid only when the magnetic susceptibility is fairly significant, which is controlled by the volume fraction of particles in the ferrofluid.

The variation in these parameters generated several vibrational patterns that have been shown in a bifurcation diagram. Subsequently, by applying the results obtained in an intelligent learning system based on neural networks, a pattern recognition system was developed. This methodology has become quite efficient and promising for practical applications.

In order to better control the suspension behavior an oscillatory magnetic field was proposed. Therefore, two cases were considered: a sinusoidal oscillating field and the combination of a static and an oscillatory magnetic field. Under the first condition, we observed that when there is a frequency coupling the system becomes more stable. However, it is noted that this coupling is extremely sensitive. The choice of a magnetic field oscillatory frequency, ω_{mag} higher or lower than the frequency of the pressure field, ω does not generate periodic responses. In addition, these responses have different levels of energy and a spectrum spreading in several frequencies.

It is also noteworthy that the existence of a coupling or decoupling generates new vibrational patterns that can be better observed in a bifurcation diagram relating ω and ω_{mag}. Among these patterns, there is the presence of chaotic conditions, which was confirmed by the existence of positive Lyapunov exponents. Under these conditions, the initial condition influences the movement of the bubble that becomes unpredictable. We note that the change of the control parameters increases or decreases the correlation between a signal $R(t)$ and $R(t+\tau)$ analyzing the scatter diagram.

With the validation of these dynamic system approaches, proving that the application of magnetic fields tend to stabilize the bubble oscillating movement, we were able to investigate the fluid where the bubble is immersed. We observed that the application of an oscillatory shear coupled with a magnetic field ends up changing the alignment of the particles joining magnetic and hydrodynamic effects. In this condition, we observed rapid fluctuations in the magnetization of the suspension, which significantly modifies the movement of the bubble and is one of the responsibles for the time scales coupling. This change was more prominent for more concentrated suspensions. For this reason, the trained neural network was successful with the increase of the particles volume fraction. Even then this network has proven to be extremely effective for observation of hydrodynamic mechanisms, guessing the volume fraction correctly in 100% of the cases.

Still considering the ferrofluid where the bubble is immersed, a magnetization study was done using a finite differences method. Indeed, the magnetic contribution in MRP equation regarding the magnetic stress tensor was analyzed. It was possible to compare the superparamagnetic model with the model proposed using a phenomenological evolutive equation for the suspension magnetization. In this condition, the variation of magnetic parameters such as ϕ, α and the magnetic relaxation time τ_s was analysed. From this study, it was observed that the use of a superamagnetic

model results in the same magnetization behavior than other models when the fluid vorticity is not coupled with the suspension magnetization (and in the absence of internal magnetic torques $\mu_0 \boldsymbol{M} \times \boldsymbol{H}$). However, in this case one can only control the magnetic susceptibility. It is suggested an investigation of how the magnetic stress tensor asymmetry can contribute to a more robust mathematical modeling.

In order to verify the sphericity condition proposed, the purely radial movement condition and study the behavior of the bubble when immersed in a ferrofluid, an experimental bench was designed. The use of a microcontroller has proven suitable for these experiments. Therefore, three magnetic fluids were synthesized: A ferrofluid based in mineral oil, a magnetorheological suspension and a ferrofluid sintetized with a high viscosity silicone oil. They were all excited with a static magnetic field provided by a neodymium magnet. The magnetization of this magnet was tested with two gaussmeters and calculated analytically. It was observed that the decay follows a power law only for the far-field condition. In the near-field conditions, there was an exponencial fit, which is also used in many bodies computer simulations to provide a repulsion force or fictious lubrication.

These three fluids were characterized with the aid of a rotating disk rheometer and a tensiometer. It was observed that the presence of the magnetic particles did not modify the base fluid characteristics significantly, due to the low volume fraction of particles.

We noted that for small bubbles, the condition of no tangential deformation is valid. It was also observed that the interaction that generates coalescence between bubbles occurs only at low Reynolds numbers (creeping flow). In situations where the Reynolds number is more significant, there is an interaction similar to the one observed in particle-particle interaction without reversibility. It is also noted that even with the application of high magnetic fields (around 4000 G), there is no significant deformation of the bubble shape, corroborating the results obtained numerically. However, the application of these fields has shown important hydrodynamic effects, since the alignment of the particles significantly alters the flow and therefore the bubble rise velocity.

Overall, we concluded that the considerations made for the mathematical and numerical modeling were appropriate. Furthermore, it was observed that the application of magnetic fields significantly increases the control over the bubble and prevents collapse. Note that the coupling of time scales, which can be controlled by non-dimensional parameters, allows the bubbles to be used in many different applications. The use of ferrofluids and magnetic fields in propulsion systems, for example, can prevent the collapse of the bubbles formed due to the blade rotational movement, preventing collapse and cavitation erosion. The delivery of drugs can be made by controlling the bubble movement to the appropriate location by magnetic fields and exciting it with an acoustic field. To sum up, the fact that an extremely complex system can be controlled allows new fields of study and new applications to emerge.

8.1 Future Works

In order to continue the study, we suggest some future works. First of all, it is possible to investigate the effect of the aymmetry in the magnetic stress tensor, produced by the internal torques $\boldsymbol{M} \times \boldsymbol{H}$. In this sense, more sophisticated magnetization models could be used considering the phenomenological magnetization equation. Besides, the finite difference method used to solve that problem could be coupled to the MRP equation. At each time step, we would have the fluid magnetization and thus would be possible to calculate the bubble radius as a function of these updated magnetic effects.

In this asymmetric condition, $\boldsymbol{M}$ and $\boldsymbol{B}$ are not collinear. This means that the microscopic dipoles are not aligned with the macroscopic field, which therefore causes a torque on each dipole. In this condition, it is interesting to consider the magnetization in both r and θ directions. Thus, it is possible to compute the vorticity term $\boldsymbol{M} \times \boldsymbol{H}$, which represents exactly the torques acting on the dipolar matter due to an applied field, represented as $\boldsymbol{\varepsilon} : \boldsymbol{\sigma} = -\boldsymbol{\mu_0} \boldsymbol{M} \times \boldsymbol{H}$. With these studies, all dynamic system approaches presented here can be used. Besides, an autocorrelation function can be used proposed aiming to understand how the magnetism adds memory to the system. Furthermore, the magnetic relaxation time τ_s can be explored. In this sense, a coupling between the time scales may modify the behavior of the ferrofluid magnetization.

From the viewpoint of signal processing, it is also possible to perform a preprocessing to better evaluate the frequency response. In this sense, the frequency signature can be extracted and only the modifications present in each vibrational pattern can be analyzed. Moreover, it is noted that there are other tools such as wavelet and spectrogram that may be better for certain applications.

In the case of experimental work, it is possible to use a piezoelectric actuator to excite the bubble. As the fluids are incompressible, the use of amplifiers will not show much result. However, exciting the fluid itself, in which the bubble is immersed in it is possible to simulate the application of an acoustic field.

Finally, one can use these concepts to the production of microfluidic systems. One example, would be to simulate the delivery of drugs or bubbles in specific locations of a capilar by the use magnetic fields. Subsequently, exciting the bubble with acoustic fields may lead it to colapse, which would administer the medication or cause erosion in cancer cells, for example. To sum up, there are several research fronts that may use the results presented here not only as final conclusions, but also as an introduction to more advanced researches.

BIBLIOGRAPHIC REFERENCES

[1] ISHIMOTO, J. et al. Bubble behavior in magnetic fluid under a nonuniform magnetic field. *JSME International Journal Series B*, v. 38, n. 3, p. 382–387, 1995.

[2] NAKATSUKA, K. et al. Visual observation of the effect of magnetic field on moving air and vapor bubbles in a magnetic fuid. *J. of Magnetism and Magnetic Materials*, v. 201, p. 256–259, 1999.

[3] NAKATSUKA, K. et al. Theoretical and experimental study of mhd (magnetohydrodynamic) micropump. *Sensors and Actuators*, v. 80, p. 84–89, 2000.

[4] CUNHA, F. R.; SOARES, A. J.; MORAIS, P. C. The dynamic behavior of a collapsing bubble in a magnetic fluid. *J. of Magnetism and Magnetic Materials*, v. 252, p. 271–275, 2002.

[5] HUTZLER, S. et al. Juggling with bubbles in cylindrical ferrofuid foams. *Philisophical Magazine Letters*, v. 82, n. 5, p. 297–301, 2002.

[6] MARMOTTANT, P.; HILGENFELDT, S. A bubble-driven microfluidic transport element for bioengineering. *J. American Chemical Society*, v. 101, n. 26, 2004.

[7] ANDREOTTI, M.; CUNHA, F. R. A study of the effect of polymer solution in promoting friction reduction in turbulent channel flow. *J. of Fluids Engineering - Transitions of the ASME (AIP - American Institute of Physics)*, v. 129, p. 491, 2007.

[8] BLAKE, J. R.; GIBSON, D. C. Cavitation bubbles near boundaries. *Annu. Rev. Fluid Mech*, v. 19, p. 99–123, 1987.

[9] NAUDÉ, C. F.; ELLIS, A. T. On the mechanism of cavitation damage by non-hemispherical cavities. *Trans. ASME D: Basic Eng.*, v. 83, p. 99–123, 1961.

[10] PLESSET, M. S.; CHAPMAN, R. B. Collapse of an initially spherical vapor cavity in the neighborhood of a solid boundary. *Division of Engineering and Applied Science California Institute of Technology*, 1970.

[11] REYNOLDS, O. The causes of the racing of the engines of screw steamers investigates theoretically ans by experiment. *Trans. Inst. Naval Arch.*, v. 14, p. 56–67, 1873.

[12] PARSONS, C. A. *The Steam Turbine*. Cambridge: University Press, 1991.

[13] GILMORE, F. R. The growth or collapse of a spherical bubble in a viscous compressible liquid. *Office of Naval Research*, California Institute of Technology, 1952.

[14] MIKSIS, M. J.; VADEN-BROECK, J. M.; KELLER, J. B. Rising bubbles. *J. Fluid Mechanics*, v. 123, p. 31–41, 1982.

[15] MASON, T. J.; LORIMER, J. P. *Sonochemistry: theory, applications and uses of ultrasound in chemistry*. Chichester, UK: Ellis Horword, 1988.

[16] DOKTYCZ, S. J.; SUSLICK, K. S. Interparticle collisions driven by ultrasound. *Science*, v. 247, p. 1067–1069, 1990.

[17] KAILATH, T. *Perspective of Combination of Ozone and Ultrasound*. Masschelein: John Wiley and Sons, 1982.

[18] OHL, C. et al. Surface cleaning from laser-induced cavitation bubbles. *Applied Physics Letters*, v. 89, 2006.

[19] CHANG, R. et al. Bubble contrast echocardiography in detecting pulmonary arteriovenous shunting in children with univentricular heart after cavopulmonary anastomosis. *J. of the American College of Cardiology*, v. 33, n. 7, p. 2052–2058, 1999.

[20] LINDNER, J. R. *Nature Rev. Drug Discovery*, p. 527–533.

[21] LARINA, I. V.; EVERS, B. M.; ESENALIEV, R. B. Optimal drug and gene delivery in cancer cells by ultrasound-induced cavitation. *Anticancer Res.*, v. 25, p. 149âĂŞ156, 2005.

[22] CHEN, S. et al. Efficient gene delivery to pancreatic islets with ultrasonic microbubble destruction technology. *Proceedings of the Natural Academy of Sciences of the United States of America*, v. 22, p. 103, 2006.

[23] WINER, N.; SOWERS, J. R. Epidemiology of diabetes. *J. Clin. Pharmacol.*, v. 44, p. 397–405, 2004.

[24] SUSLICK, K. S. *Rising bubbles*. NY: VHC, 1988.

[25] MASON, T. J.; LORIMER, J. P. *Sonochemistry: theory, applications and uses of ultrasound in chemistry*. Chichester, UK: Ellis Horword, 1988.

[26] LEIGHTON, T. G. The acoustic bubble. *J. Fluid Mechanics*, v. 272, p. 407–408, 1994.

[27] HYNYNEN, K. et al. Noninvasive mr imaging-guided focal opening of the blood-brain barrier in rabbits. *Radiology*, v. 220, p. 640–646, 2001.

[28] FRENZEL, H.; SCHULTES, H. Luminescenz im ultraschallbeschickten wasser. *Phys. Chem.*, v. 27B, p. 427, 1934.

[29] LANDAU, L. D.; LIFSHITZ, E. M. *Course of Theoretical Physics 6 - Fluid Mechanics*. USSR: Institute of Physical Problems/U.S.S.R, Academy of Sciences, 1987.

[30] LOHSE, D.; SCHMITZ, B.; VERSLUIS, M. Snapping shrimp make flashing bubbles. *Nature - Brief Communications*, v. 413, p. 477–478, 2001.

[31] CRUM, L. A. Synchronous picosecond sonoluminescence. *Phys. Today*, v. 47, n. 22, 1994a.

[32] PUTTERMAN, S. J. Sonoluminescence: Sound into light. *Scientific American*, v. 272, n. 2, p. 46–51, 1994a.

[33] GONTIJO, R. G.; CUNHA, F. R. Dynamic numerical simulations of magnetically interacting suspensions in creeping flow. *Powder Technology*, v. 279, p. 146–165, 2015.

[34] MENDELEV, V. S.; IVANOV, A. O. Ferrofluid aggregation in chains under the influence of a magnetic field. *Physical Review E*, v. 70, 2004.

[35] CUNHA, F. R.; ABADE, G. C. *Instability of a magnetic fluid*. 2007. URL: (*https* : *//www.youtube.com/watch?v* = 9*GOXoCVG*6*q*4).

[36] CUNHA, F. R. et al. Modelling and direct simulation of velocity fluctuations and particle-velocity correlations in sedimentation. *J. Fluids Engineering - ASME*, v. 124, 2002.

[37] CUNHA, F. R. *Fundamentals of Magnetic Fluid Hydrodynamics, in Turbulence*. (v. 8). Poli-USP, São Paulo: EPTT, ISBN: 978-85-85769-49-9, 2012. (p. 257-339).

[38] DUTZ, S.; HERGT, R. Magnetic nanoparticle heating and heat transfer on a microscale: Basic principles, realities and physical limitations of hyperthermia for tumour therapy. *Int J Hyperthermia*, v. 28, n. 8, p. 790–800, 2013.

[39] ROSENSWEIG, R. E. *Ferrohydrodynamics*. Cambridge: Cambridge University Press, 1985.

[40] ALBERNAZ, D. L.; CUNHA, F. R. Bubble dynamics in a maxwell fluid with extensional viscosity. *Mechanics Research Communications*, v. 38, n. 3, p. 255, 2011.

[41] ALBERNAZ D. L., C. F. R. Unsteady motion of a spherical bubble in a complex fluid: Mathematical modelling and simulation. *Applied Mathematical Modelling*, v. 37, 2013.

[42] CUNHA, F. R.; ALBERNAZ, D. L. Oscillatory motion of a spherical bubble in a non-newtonian fluid. *J. of Non-Newtonian Fluid Mechanics*, v. 191, p. 35–44, 2013.

[43] RATULOWSKI, J.; CHANG, H. C. Marangoni effects of trace impurities on the motion of long gas bubbles in capillaries. *J. of Fluid Mechanics*, v. 210, p. 303–328, 1990.

[44] YOUNG, T. An essay on the cohesion of fluids. *Philos. Trans. R. Soc.*, v. 95, p. 65, 1805.

[45] LAPLACE, P. *Méchanique Céleste*. Paris: Courcier, 1806.

[46] POZRIKIDIS, C. *Boundary Integral and Singularity Methods for Linearized Viscous Flow*. UK: Cambridge University Press, 1992.

[47] FOGLER, H. S.; GODDARD, J. D. Collapse of cavities in viscoelastic fluids. *Phys. Fluids*, v. 13, n. 5, p. 1135–1141, 1970.

[48] MALVAR, S. Dinâmica de bolhas em meio magnético: formulação, modelagem e controle. *Unívesidade de Brasília*, 2014.

[49] PRESS, W. H. *Numerical Recipes*. UK: Cambridge University Press, 1992.

[50] BESANT, W. H. *Hydrostatics and Hydrodynamics*. UK: Cambridge University Press, 1859.

[51] RAYLEIGH, L. On the pressure developed in a liquid during the collapse of a spherical cavity. *Phil. Mag.*, 1917.

[52] CASH, J. R.; KARP, A. H. A variable order runge-kutta method for initial value problems with rapidly varying right-hand sides. *Transactions on Mathematical Software*, v. 16, p. 201–222, 1990.

[53] SHLIOMIS, M. I. Magnetic fluids. *Sov. Phys. Usp.*, v. 17, n. 2, p. 153, 1974.

[54] SHLIOMIS, M. I.; MOROZOV, K. I. Negative viscosity of ferrofluids under an alternating magnetic field. *Phys. Fluids*, v. 6, n. 8, p. 2855–2861, 1994.

[55] BACRI, J.-C. et al. Negative-viscosity effect in a magnetic fluid. *Phys. Rev. Lett.*, v. 75, p. 2128, 1995.

[56] ZEUNER, A.; RICHTER, R.; REHBELG, I. Negative viscosity in a dispersion of magnetite. *Abstracts of the 8th International Conference on Magnetic Fluids*, Timisoara, Romania, p. 72–73, 1998.

[57] YAMANE, R. et al. Oscillation of a diamagnetic liquid bubble suspended by magnetic force. *J. of Magnetism and Magnetic Materials*, v. 252, n. 1-3, p. 268–270, 2002.

[58] PARLITZ, U. et al. Biffurcation structure of bubble oscillators. *Institut fÃijr Angewandte Physik, Technische Hochschule Darmstadt*, 2013.

[59] BEHNIA, S.; MOBADERSANI, F.; YAHYAVI M., R. A. Chaotic behavior of gas bubble in non-newtonian fluid: a numerical study. *Nonlinear Dynamics*, v. 74, p. 559, 2013.

[60] SIU, S. W. K. Lyapunov exponents toolbox. *City University of Hong Kong*, 1998.

[61] MALVAR, S.; GONTIJO, R. G.; CUNHA, F. R. Vibrational modes on the non-linear motion of an oscillating bubble in a newtonian fluid using neural networks. *DINAME 2015 - Proceedings of the XVII International Symposium on Dynamic Problems of Mechanics (Natal, Brazil)*, 2015.

[62] MOLLER, M. F. A scaled conjugate gradient algorithm for fast supervised learning. *Neural Networks*, v. 6, n. 4, p. 525–533, 1993.

[63] YOSHIMURA, N. Application of magnetic action for sterilization of food. *Shokukin Kihatsu*, v. 24, n. 3, p. 46–48, 1989.

[64] MOORE, R. L. Biological effects of magnetic fields. studies with microorganisms. *Can. J. Microbiol*, v. 25, p. 1145–1151, 1979.

[65] HUND, A. *Frequency Modulation*. University of California: McGraw-Hill Book Company, 1942.

[66] LAUTERBORN, W.; CRAMER, L. Subharmonic route to chaos observed in acoustics. *Physical Review Letters*, v. 47, n. 20, p. 1445–1448, 1991.

[67] LAUTERBORN, W.; KOCH, A. Holographic observation of period-doubled and chaotic oscillations in acoustic cavitation. *Phys. Rev. A*, v. 47, n. 20, p. 1445–1448, 1991.

[68] HOLT, R. G. et al. Chaotic sonoluminescence. *Phys. Rev. Lett.*, v. 72, p. 1376–1379, 1994.

[69] PARLITZ, U. et al. Holographic observation of period-doubled and chaotic oscillations in acoustic cavitation. *Acoust. Soc. Am.*, v. 88, p. 1061–1077, 1990.

[70] AKHATOV, I. S.; KONOVALOVA, J. Regular and chaotic dynamics of a spherical bubble. *Appl. Math. Mech*, v. 69, p. 575–584, 2005.

[71] GALKA, A. *Topics in Nonlinear Time Series Analysis: With Implications for EEG Analysis*. Singapore: World Scientific Publishing, 2000.

[72] SINAI, G. Y. Dynamical systems with elastic reflections. ergodic properties of dispersing billiards. *Uspekhi Mat. Nauk*, v. 25, n. 2(152), p. 141–192, 1970.

[73] KANG, K. H.; KANG, I. S.; LEE, C. M. Effects of a uniform magnetic field on a growing or collapsing bubble in a weakly viscous conducting fluid. *Physics of Fluids*, v. 14, n. 1, 1970.

[74] FELDERHOF, B. U.; KROH, H. J. Hydrodynamics of magnetic and dielectric fluids in interaction with the electromagnetic field. *J. Chem. Phys.*, v. 110, p. 7403, 1999.

[75] CUNHA, F. R.; SOBRAL, Y. D. Characterization of the physical parameters in a process of magnetic separation and pressure-driven flow of a magnetic fluid. *Physica A*, v. 343, p. 36–564, 2004.

[76] VARADAN, V. K.; CHEN, L.; JINING, X. *Physical Background for the Biomedical Applications of Functional Magnetic Nanomaterials*. UK: John Wiley and Sons, Ltd, 2008.

[77] WANG, Z.; HOLM, C.; MULLER, H. W. A molecular dynamics study on the equilibrium magnetization properties and structure of ferrofluids. *Max Planck-Institut fur Polymerforschung*, 2008.

[78] TAYLOR, T. D.; ACRIVOS, A. Numerical simulation of bubble rising in viscous liquid. *J. of Computational Physics*, v. 222, p. 769–795, 2006.

[79] MOORE, D. W. he rise of a gas bubble in viscous liquid. *Fluid Mech*, v. 6, p. 113–130, 1959.

[80] TAYLOR, T. D.; ACRIVOS, A. On the deformation and drag of a falling viscous drop at low reynolds number. *J. Fluid Mech.*, v. 18, p. 466–476, 1964.

[81] TAYLOR, G. I.; DAVIES, R. M. The rate of rise of large volumes of gas in water in underwater explosions research. *Office of Naval Research*, v. 2, 1944.

[82] KURTOGLU, I.; LIN, C. L. Lattice boltzmann study of bubble dynamics. *Numer Heat Transfer*, 2006.

[83] AMAYA-BOWER, L.; LE, T. Single bubble rising dynamics for moderate reynolds number using lattice boltzmann method. *Computers and Fluids*, v. 39, p. 1191–1207, 2010.

[84] CLIFT, R.; GRACE, J. R.; WEBER, M. *Bubbles, drops, and particles*. New York: Academic Press, 1978.

[85] MAGNAUDET, J.; EAMES, I. The motion of high-reynolds-number bubbles in inhomogeneous flows. *Annu. Rev. Fluid Mech.*, v. 32, p. 659, 2000.

[86] DUINEVELD, P. C. The rise velocity and shape of bubbles in pure water at high reynolds number. *J. Fluid Mech.*, v. 292, p. 325, 1995.

[87] CLEGG, A. G.; MCGAIN, M. *Permanent Magnets in Theory and Practice*. London: Pentech Press, 1977.

[88] CROSS, M. M. Rheology of non-newtonian fluids: a new flow equation for pseudoplastic systems. *J. Colloid Sci.*, v. 20, p. 417–437, 1965.

[89] GENNES, P. G. D. Reptation of a polymer chain in the presence of fixed obstacles. *J. of Chemical Physics (AIP)*, v. 55, n. 2, p. 572–571, 1971.

[90] BERRY, G. C.; FOX, T. G. The viscosity of polymers and their concentrated solutions. *Advances in Polymer Science/Fortschritte der Hochpolymeren-Forschung*, v. 292, p. 325–332, 1968.

[91] NA, N. P. et al. Free instrument for measurements of motion. *Revista Brasileira de Ensino de Física*, v. 35, n. 3, p. 1–5, 2013.

[92] TAYLOR, G. I. The viscosity of fluid containing small drops of another fluid. *Proc. R. Soc. A.*, v. 138, p. 41–48, 1932.

[93] LEE, J. C.; HODGSON, T. D. Film flow and coalescence. *Chem. Eng Sci*, v. 23, p. 1375–1397.

[94] MURDOCH, P. G.; LENG, D. E. The mathematical formulation of hydrodynamic film thinning and its application to colliding drops suspended in a second liquid. *Chem. Eng Sci.*, v. 26, p. 1881–1892, 1971.

[95] TRAYKOV, T. T.; IVANOV, I. B. Hydrodynamics of thin liquid films: effect of surfactants on the velocity of thinning of emulsion films. *Int. J. Multiphase Flow*, v. 3, p. 471–483.

[96] IVANOV, I. B.; TRAYKOV, T. T. Hydrodynamics of thin liquid films: rate of thinning of emulsion films from pure liquids. *Int. J. Multiphase Flow*, v. 2, p. 397–410, 1976.

[97] JONES, A. F.; WILSON, S. D. R. The film drainage problem in droplet coalescence. *J. Fluid Mech*, v. 87, p. 263–288, 1978.

[98] SHERLE, G. F.; LENG, D. E. An experimental study of factors which promote coalescence of two colliding drops suspended in water. *Chem. Engng Sci.*, v. 26, p. 1867–1879, 1971.

[99] D., K. R.; LOCKETT, M. J. The influence of approach velocity on bubble coalescence. *Chem. Engng Sci.*, v. 29, p. 2363–2373, 1974.

[100] VIJAYAN, S.; PONTER, A. B.; JEFFREYS, G. V. *Chem. Engng J.*, p. 145–154.

[101] THOMAS, R. Bubble coalescence in turbulent flows. *International J. of Multiphase Flow*, v. 7, n. 6, p. 709–717, 1981.

[102] CUNHA, F. R. et al. Modeling and direct simulation of velocity fluctuations and particle-velocity correlations in sedimentation. *J. of Fluids Engineering*, v. 124, p. 957–968, 2002.

[103] GONTIJO, R. G. *Micromecânica e Microhidrodinâmica de Suspensões Magnéticas*. Tese (Doutorado) — UnB - Brasília, 2013.

[104] J., B. C. W. Ewald sum of the rotne-prager tensor. *J. Chem. Phys.*, v. 853, p. 1581–1582, 1986.

[105] EWALD, P. P. Die berechnung optisher und elektrostatischer gitterpotentiale. *Ann. Phys. Lpz.*, v. 64, p. 253, 1921.

[106] ROTNE, J.; PRAGER, S. Variational treatment of hydrodynamic interaction in polymers. *J. Chem. Phys.*, v. 5011, p. 4831–4837, 1969.

[107] ABADE, G. C.; CUNHA, F. R. Computer simulation of particle aggregates during sedimentation. *Comput. Methods Appl. Mech. Engrg.*, v. 196, p. 4597–4612, 2007.

[108] GONTIJO, R. G.; CUNHA, F. R. Experimental investigation on thermo-magnetic convection inside cavities. *J. Nanosci. Nanotechnol.*, v. 12, p. 9198–9207, 2012.

APPENDIX 1 - Formulation of the Magnetic Rayleigh-Plesset Equation

This appendix aims to describe the algebra behind the magnetic formulation proposed. In chapter 2, Cauchy's equation for non-Newtonian fluid was given by 2.12. In the case of a bubble immersed in a magnetic fluid, that same condition is used:

$$\rho\left(\frac{\partial u}{\partial t}+u.\nabla u\right)=-\nabla p+\nabla\sigma^{N}+\nabla\sigma^{mag}, \tag{1}$$

where $\boldsymbol{\sigma^N}$ represents the Newtonian contribution of the stress tensor, while $\boldsymbol{\sigma}$ is used to denote the non-Newtonian effects of the fluid. To the unidimensional movement (radial) proposed in the formulation, the velocity field consists in $\boldsymbol{u}=u_{rr}\hat{e}$. Thus, in spherical coordinates we have:

$$\rho\left(\frac{\partial u}{\partial t}+u\frac{\partial u}{\partial r}\right)=-\frac{\partial p}{\partial r}+\frac{1}{r^2}\frac{\partial}{\partial r}(r^2\sigma_{rr}^{N})-\frac{(\sigma_{\theta\theta}^{N}+\sigma_{\varphi\varphi}^{N})}{r}+\frac{1}{r^2}\frac{\partial}{\partial r}(r^2\sigma_{rr})-\frac{(\sigma_{\theta\theta}^{N}+\sigma_{\varphi\varphi}^{N})}{r}. \tag{2}$$

After some algebraic manipulation:

$$\rho\left(\frac{\partial u}{\partial t}+u\frac{\partial u}{\partial r}\right)=-\frac{\partial p}{\partial r}+\frac{\partial\sigma_{rr}^{N}}{\partial r}+\frac{\partial 3\sigma_{rr}^{N}}{\partial r}+\frac{1}{r^2}\left(r^2\frac{\partial\sigma_{rr}}{\partial r}+2r\sigma_{rr}\right)-\frac{\sigma_{\theta\theta}}{r}. \tag{3}$$

In the Newtonian formulation, however, $\boldsymbol{\sigma}$ trace is null. This afirmation is still valir but only for the Newtonian part of the tensor.

$$\rho\left(\frac{\partial u}{\partial t}+u\frac{\partial u}{\partial r}\right)=-\frac{\partial p}{\partial r}+\frac{\partial\sigma_{rr}^{N}}{\partial r}+\frac{\partial 3\sigma_{rr}^{N}}{\partial r}+\frac{\sigma_{rr}}{\partial r}+\frac{2\sigma_{rr}}{r}+\frac{\sigma_{\theta\theta}}{r}. \tag{4}$$

In order to continue the formulation, it is necessary to calculate the non-Newtonian integral obtained previously.

$$\frac{1}{\rho}\int_{R}^{\infty}\frac{\partial\sigma_{rr}}{\partial r}dr+\frac{1}{\rho}\int_{R}^{\infty}\left(\frac{2\sigma_{rr}}{r}-\frac{\sigma_{\theta\theta}}{r}\right)dr. \tag{5}$$

Knowing that the force related to the interaction between two dipoles is:

$$\boldsymbol{F}=\mu_0\boldsymbol{H}(\boldsymbol{\nabla}\cdot\boldsymbol{H}), \tag{6}$$

we may define which one is the related stress tensor:

$$\boldsymbol{T}=\mu_0\boldsymbol{H}\boldsymbol{H}-\frac{1}{2}\mu_0H^2\boldsymbol{I}. \tag{7}$$

Knowing that $\boldsymbol{B}=\mu_0(\boldsymbol{H}+\boldsymbol{M})$ and that, in the superparamagnetic case, $\boldsymbol{B}=\mu_0(1+\chi)\boldsymbol{H}$, it is possible to define, in that case, considering only the radial and polar components:

$$\sigma_{\theta\theta}^{mag} = -\frac{\mu_0}{2}(H_r^2 + H_\theta^2) + \mu_0(1+\chi)H_\theta^2, \tag{8}$$

$$\sigma_{rr}^{mag} = -\frac{\mu_0}{2}(H_r^2 + H_\theta^2) + \mu_0(1+\chi)H_r^2. \tag{9}$$

Since the formulation considers only the radial movement, there are no parameters to define the values of θ that should be used. For that reason, we may calculate the mean value in order to considerate the medium effects of de colatitude of the applied field.

$$\frac{1}{2\pi}\int_0^{2\pi} cos^2\theta d\theta = \frac{1}{2\pi}\int_0^{2\pi}\left(\frac{1+cos2\theta}{2}\right)d\theta = \frac{1}{2\pi}\left(\frac{\theta}{2} + \frac{sen2\theta}{4}\right)|_0^{2\pi} = \frac{1}{2}. \tag{10}$$

the same is done for $sin\theta$:

$$\frac{1}{2\pi}\int_0^{2\pi} sin^2\theta d\theta = \frac{1}{2\pi}\int_0^{2\pi}\left(\frac{1-cos2\theta}{2}\right)d\theta = \frac{1}{2\pi}\left(\frac{\theta}{2} - \frac{sen2\theta}{4}\right)|_0^{2\pi} = \frac{1}{2}. \tag{11}$$

At this time, the three terms of non-Newtonian integral will be divided and resolved separately. Thus, we have:

$$\text{Fator 1 - } \frac{\sigma_r r}{\rho}|_R^\infty, \tag{12}$$

$$\text{Fator 2 - } \frac{1}{\rho}\int_R^\infty \frac{2\sigma_{rr}}{r}dr, \tag{13}$$

$$\text{Fator 3 - } \frac{1}{\rho}\int_R^\infty \frac{\sigma_{\theta\theta}}{r}dr, \tag{14}$$

• **First Term**

$$\frac{1}{\rho}\Big\{ -\frac{\mu_0}{2}\left[\frac{C^2}{2} - \frac{4DC}{2r^3} + \frac{4D^2}{2r^6} + \frac{C^2}{2} + \frac{2DC}{2r^3} + \frac{D^2}{2r^6}\right] + \mu_0(1+\chi)\left[\frac{C^2}{2} - \frac{4DC}{2r^3} + \frac{4D^2}{2r^6}\right]\Big\}. \tag{15}$$

after some algebric manipulation, nullifying the terms available, we have:

$$\frac{1}{\rho}\Big\{ -\frac{\mu_0}{2}\left[C^2 - \frac{DC}{r^3} + \frac{5D^2}{2r^6}\right] + \mu_0(1+\chi)\left[\frac{C^2}{2} - \frac{4DC}{2r^3} + \frac{4D^2}{2r^6}\right]\Big\}. \tag{16}$$

Isolating the term as a function of μ_0 e $\mu_0\chi$:

$$\frac{1}{\rho}\Big\{\mu_0\left[\frac{C^2}{2} - \frac{4DC}{2r^3} + \frac{4D^2}{2r^3} - \frac{C^2}{2} + \frac{DC}{2r^3} - \frac{5D^2}{4r^6}\right] + \mu_0\chi\left[\frac{C^2}{2} - \frac{4DC}{2r^3} + \frac{4D^2}{2r^6}\right]\Big\}. \tag{17}$$

Manipulating the terms in order to get the leanest possible expression and applying the limits of integration from R to ∞, it is possible to obtain:

$$\frac{1}{\rho}\Big\{\mu_0\left[\frac{-3DC}{2r^3}+\frac{3D^2}{4r^6}\right]+\mu_0\chi\left[\frac{C^2}{2}-\frac{4DC}{2r^3}+\frac{4D^2}{2r^6}\right]\Big\}|_R^\infty. \tag{18}$$

In this case, when $r\to\infty$, the terms cancel. Thus, the resulting equation reduces to

$$\frac{1}{\rho}\Big\{\mu_0\left[\frac{-3DC}{2R^3}-\frac{3D^2}{4R^6}\right]+\mu_0\chi\left[\frac{4DC}{2R^3}-\frac{4D^2}{2R^6}\right]\Big\}. \tag{19}$$

• **Second Term**

$$\frac{1}{\rho}\int_R^\infty\frac{2}{r}\Big\{\mu_0\left[-\frac{3DC}{2r^3}+\frac{3D^2}{4r^6}\right]+\mu_0\chi\left(\frac{C^2}{2}-\frac{4DC}{2r^3}+\frac{4D^2}{2r^6}\right)\Big\}dr. \tag{20}$$

integrating from R to ∞:

$$\frac{1}{\rho}\int_R^\infty\Big\{\mu_0\left(\frac{3DC}{3r^3}-\frac{3D^2}{12r^6}\right)+\mu_0\chi\left(C^2\ln(r)+\frac{4DC}{3r^3}-\frac{4D^2}{6r^6}\right)\Big\}|_R^\infty, \tag{21}$$

substituting the integrating limits and reorganizing the terms, we have:

$$\frac{1}{\rho}\int_R^\infty\Big\{\mu_0\left(-\frac{DC}{R^3}+\frac{D^2}{4R^6}\right)+\mu_0\chi\left(C^2\ln(R_\infty)-C^2\ln(R)-\frac{4DC}{3R^3}+\frac{2D^2}{3R^6}\right)\Big\}. \tag{22}$$

• **Third Term**

$$\frac{1}{\rho}\int_R^\infty\Big\{\mu_0\left[\frac{3DC}{2r^4}-\frac{-3D^2}{4r^7}\right]+\mu_0\chi\left(\frac{C^2}{2r}-\frac{DC}{r^4}+\frac{D^2}{2r^7}\right)\Big\}dr, \tag{23}$$

integrating from R to ∞.

$$\frac{1}{\rho}\Big\{\mu_0\left[-\frac{3DC}{6r^3}+\frac{3D^2}{24r^6}\right]+\mu_0\chi\left(\frac{C^2}{2}\ln(R_\infty)-\frac{DC}{3r^3}-\frac{D^2}{12r^6}\right)\Big\}|_R^\infty. \tag{24}$$

reorganizing the terms of the equation, we have:

$$\frac{1}{\rho}\Big\{\mu_0\left[\frac{DC}{2R^3}-\frac{D^2}{8R^6}\right]+\mu_0\chi\left(\frac{C^2}{2}\ln(R_\infty)-\frac{C^2}{2}\ln(R)+\frac{DC}{3R^3}+\frac{D^2}{12R^6}\right)\Big\}. \tag{25}$$

Organizing and combining the three terms, we obtain:

$$\frac{1}{\rho}\left(\sigma_{rr}+\int_R^\infty\frac{2\sigma_{rr}}{r}dr-\int_R^\infty\frac{2\sigma_{\theta\theta}}{r}dr\right), \tag{26}$$

then

$$\frac{1}{\rho}\Big\{\left[\mu\left(\frac{3DC}{2R^3}-\frac{3D^2}{4R^6}\right)+\mu_0\chi\left(\frac{4DC}{2R^3}-\frac{4D^2}{2R^6}\right)\right]$$
$$+\left[\mu_0\left(\frac{D^2}{4R^6}-\frac{DC}{R^3}\right)+\mu_0\chi\left(C^2\ln(R_\infty)-C^2\ln(R)-\frac{4DC}{3R^3}+\frac{2D^2}{3R^6}\right)\right]$$
$$-\left[\mu_0\left(\frac{DC}{2R^3}-\frac{D^2}{8R^6}\right)+\mu_0\chi\left(\frac{C^2}{2}\ln(R_\infty)-\frac{C^2}{2}\ln(R)+\frac{DC}{3R^3}+\frac{D^2}{12R^6}\right)\right]\Big\}. \tag{27}$$

Separating the terms in commom:

$$\frac{1}{\rho}\Big\{\Big[\mu\Big(\frac{3DC}{2R^3}-\frac{3D^2}{4R^6}+\frac{D^2}{4R^6}-\frac{DC}{R^3}-\frac{DC}{2R^3}+\frac{D^2}{8R^6}\Big)+$$
$$+\mu_0\chi\Big(\frac{2DC}{R^3}-\frac{2D^2}{R^6}+C^2\ln(R_\infty)-C^2\ln(R)+$$
$$-\frac{4DC}{3R^3}+\frac{2D^2}{3R^6}-\frac{C^2}{2}\ln(R_\infty)+\frac{C^2}{2}ln(R)-\frac{DC}{3R^3}-\frac{D^2}{12R^6}\Big)\Big]\Big\}, \tag{28}$$

so

$$\frac{1}{\rho}\Big\{\Big[\mu_0\Big(-\frac{3D^2}{8R^6}-\frac{3D^2}{4R^6}+\frac{DC}{6R^3}\Big)+ \tag{29}$$
$$\mu_0\chi\Big(\frac{DC}{3R^3}+\frac{C^2}{2}\ln(R_\infty)-\frac{C^2}{2}\ln(R)-\frac{4D^2}{3R^6}+\frac{2D^2}{12R^3}\Big)\Big]\Big\}. \tag{30}$$

Using the formulationg poposed by Rosensweig, we have:

$$C=-H_0, \tag{31}$$

$$D=\frac{\mu_2-\mu_1}{\mu_2+2\mu_1}R^3H_0, \tag{32}$$

and considering that

$$\frac{\mu_2-\mu_1}{\mu_2+2\mu_1}=\mu_r, \tag{33}$$

we reach, substituting the terms:

$$\frac{1}{\rho}\Big[\mu\Big(\frac{2\mu_r^2H_0^2}{8}-\frac{\mu_rH_0^2}{6}-\frac{3\mu_r^2H_0^2R^3}{4}\Big)+$$
$$+\mu_0\chi\Big(-\frac{4\mu_r^2H_0^2}{3}-\frac{\mu_rH_0^2}{3}-\frac{\mu_r^2H_0^2}{12}+\frac{H_0^2}{2}\ln(R_\infty)-\frac{H_0^2}{2}\ln(R)\Big)\Big]. \tag{34}$$

From equation 2.96 it is possible to follow the process of writting the magnetiv giverning equation in a non-dimensional form. Observing the process for writing the non-Newtonian integral as dimensionless, we divide the equation by U_c^2:

$$\frac{1}{\rho U_c^2}\left[\mu\left(-\frac{3\mu_r^2 H_0^2}{8}\right)+\mu_0\chi\left(-\frac{\mu_r H_0^2}{3}-\frac{17\mu_r^2 H_0^2}{12}+\frac{H_0^2}{2}\ln(R_\infty)-\frac{H_0^2}{2}\ln(R)\right)\right], \tag{35}$$

considering $\mu_r=-\frac{1}{2}$, some simplifications can be made:

$$\frac{1}{\rho U_c^2}\left[\mu\left(-\frac{3H_0^2}{32}\right)+\mu_0\chi\left(-\frac{9H_0^2}{48}+\frac{H_0^2}{2}\ln(R_\infty)-\frac{H_0^2}{2}\ln(R)\right)\right]. \tag{36}$$

Writting the non-dimensional version of R_∞ and R as:

$$\frac{1}{\rho U_c^2}\left[\mu\left(-\frac{3H_0^2}{32}\right)+\mu_0\chi\left(-\frac{9H_0^2}{48}+\frac{H_0^2}{2}\ln(R_\infty^* R_E)-\frac{H_0^2}{2}\ln(R^* R_E)\right)\right], \tag{37}$$

and considering the magnetic Reynolds numer as

$$Re_{mag}=\frac{\rho U_c^2}{\mu_0 H_0^2}, \tag{38}$$

one reaches:

$$\frac{1}{Re_{mag}}\left[\mu\left(-\frac{C_1}{8}\right)+\chi\left(-\frac{C_1}{4}+\frac{1}{2}\ln\left(\frac{R_\infty^*}{R^*}\right)\right)\right]. \tag{39}$$

APPENDIX 2 - Electric Circuit of the Experimental Bench

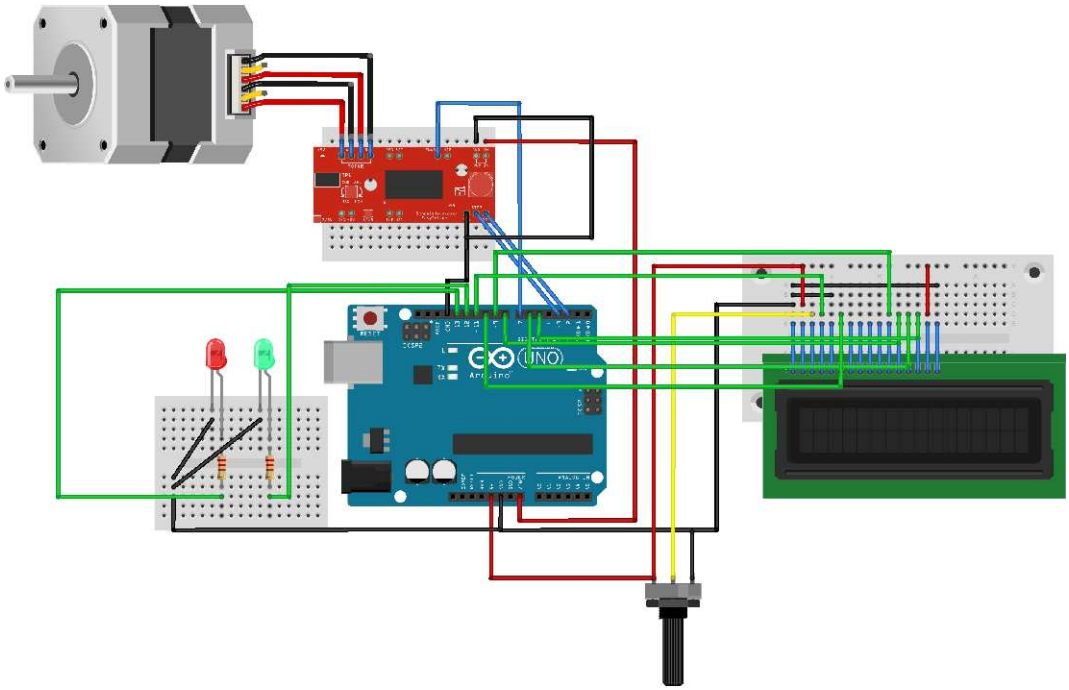

Figure 1: Circuit schematic made with Fritzing

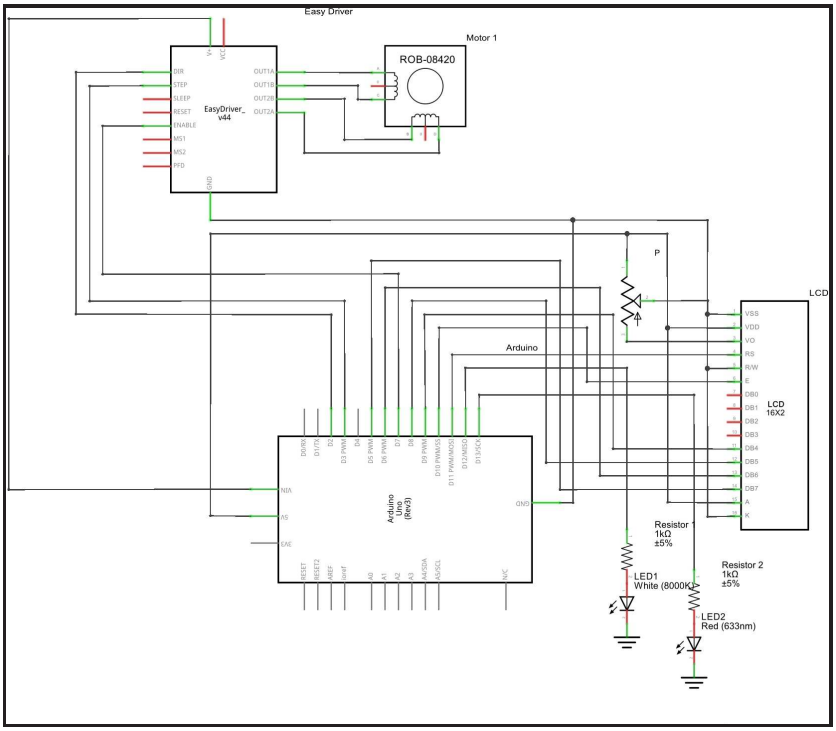

Figure 2: Circuit schematic

APPENDIX 3 - Bubbles and Drops Shapes

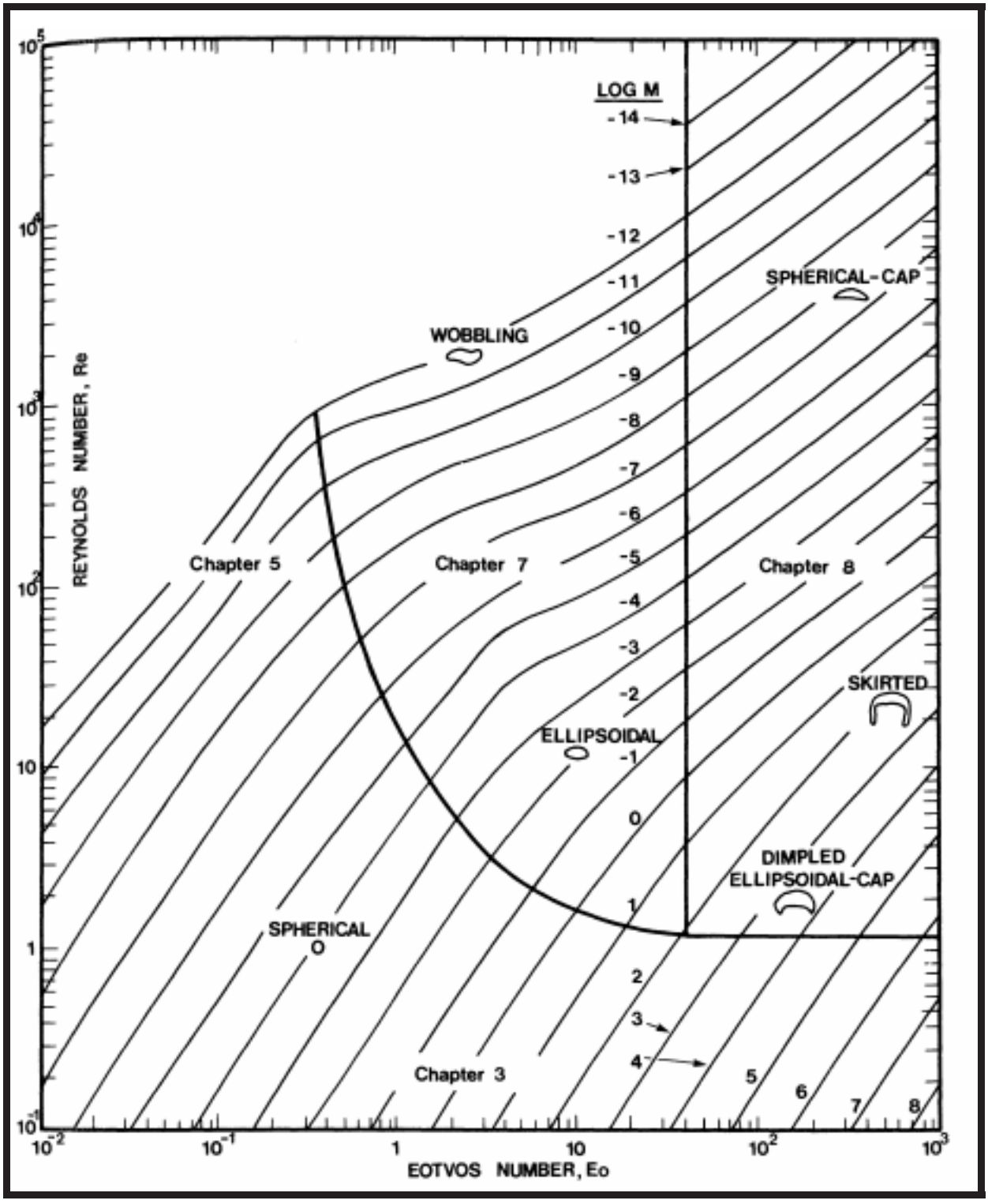

Figure 3: Shape regimes for bubbles and drops in unhindered gravitational motion through liquids proposed by Clift [84].

Submitted Paper # 1

This paper was produced and submitted during the Masters period. Neural networks and dynamic system approaches are used to identify the vibrational patterns of a bubble immersed in a Newtonian fluid.

Identification of Nonlinear Patterns of an Oscillating Bubble using Neural Networks

S. Malvar, R. G. Gontijo and F. R. Cunha

The main goal of this article is to study the oscillatory motion of an spherical gas bubble immersed in a Newtonian liquid subjected to an harmonic pressure excitation. We use the classical Rayleigh-Plesset equation to study the radial motion of the bubble undergoing a forcing acoustic pressure field. The second order non linear ordinary differential equation that governs the bubble motion is solved through a robust fifth order Runge-Kutta scheme with adaptive time-step. Several interesting patterns are identified. First we develop an asymptotic solution for low amplitudes of excitation pressure to validate our numerical code. Then we develop a bifurcation diagram in order to show how the parameters of the flow modify the vibrational patterns of the bubble. We also train a neural network to identify the vibrational pattern through its FFT data. The combination of neural networks with a bifurcation diagram could be useful for the identification of the flow physical parameters in practical applications. For each pattern we also provide an analysis of the motion of the bubble on the phase-space and interpret physically the system behavior with its FFT. In addition we analyse nonlinear patterns using standard tools of dynamical systems such as Poincaré sections and calculating the Lyapunov exponents of the system. Based on that, we have identified topological transitions in phase plane using for instance the analysis of Poincaré sections and the solution in the frequency spectrum. We have seen that the mechanisms that dominates the dynamics of the oscillating bubble is the competition of the acoustic field excitation with surface tension forces and momentum diffusion through by the action of the surrouding fluid's viscosity. **Bubble dynamics, Nonlinear dynamics, Neural networks, Rayleigh-Plesset**

The classical equation describing the oscillating motion of an spherical bubble subjected to an harmonic acoustic excitation field is known as Rayleigh-Plesset equation [1]. This highly nonlinear ODE can be modified or extended to study several phenomena associated with bubble dynamics. For decades engineers and scientists have productively employed single-degree-of-freedom models to understand and explore the behavior of violently collapsing bubbles [2, 3, 4, 5]. These studies have been applied in many areas such as: sonochemistry, bioengineering, cavitation erosion, underwater explosions and sonoluminescence [6].

The bubble shape can vary from spherical to nearly polyhedral, forming a complex geometrical structure insensitive to details of the liquid composition or the average bubble size [7]. However, when small bubbles undergoind small oscillating amplitudes are considered the assumption that the bubble's shape is always spherical can be used. This assumption is valid even in highly nonlinear situations. A bubble immersed in a non-Newtonian fluid, such as a viscoelastic polymeric solution [8, 9, 10, 11] and even a magnetic fluid [12, 13] may have several degrees of freedom, presenting very nonlinear oscillations.

This nonlinearity may present some difficulties in controlling the bubble oscillation. When used in biomedical applications, such as contrast in ultrassonography [14], it is necessary to understand how the bubble is oscillating. In this case microbubbles are injected into the body and take part in image contrast. The ultrasound pulses are applied with the bubbles' resonance frequency. The bubbles respond to pulses increasing and decreasing their radius, generating echoes in their neighborhoods. The difference between these echoes and those shown by tissues generates a contrast. Furthermore, bubbles may be used to transport drugs [15], another example in which the control of its degrees of freedom may be very important.

Considering the relevance of understanding a bubble oscillating patterns and identify them in order to control its motion, a nonlinear tool such as neural networks can be used. In practical applications, the identification of these parameters can become somewhat difficult due to the nonlinearity of the equation that controls the oscillatory regime of the bubble. However, it is a simple problem of pattern identification. Recent works [16, 17, 18] have analyzed the nonlinear motion of a spherical bubble from a nonlinear dynamical system perspective, but none of them have used neural networks in order to identify some of its nonlinear patterns of motion.

The physical and mathematical theory of neural networks have been developed rapidly during the past 25 years. It is a theory whose diversity and complexity reflects the multifaceted organization of the brain in processes that it sets out to explain and identify [19]. A multilayer neural network can be used in order to identify deffects on metal beams and other dynamic systems [20]. The vibrational parameters of the beam and its response in the frequency domain are used to determine the involvement thereof.

In the last 25 years, multilayer perceptrons (MLPs) have been massively used in the area of pattern recognition [21]. The experimental results have been impressive in some applications where we know in advance that the patterns belong to a small number of classes. In those cases, because of their strong discrimination capabilities, MLPs exhibit excellent performance [22, 23].

Considering the microbubble dynamic parameters, such as the system non-dimensional numbers, several vibration patterns may be identified. Those patterns are classified and rec-

ognized by the neural network in order to predict the bubble's oscillatory motion considering its known parameters and vice versa.

In the present study, we use a sinusoidal excitation with variable amplitude and frequency as the pressure forcing field. The main goal is to identify the non-dimensional parameters and excitations that generate different vibrational modes, characterizing the system. Those vibrational patterns are used as a trainning input in a multilayer backpropagation neural network in order to identify them from the flow system non-dimensional physical parameters. This is a first step towards the understanding of the nonlinear response of the bubble from a dynamical system perspective.

II.1 Mathematical Modeling

II.1.1 Rayleigh-Plesset Equation

The study of the dynamic oscillatory movement of a bubble presented in this work is based on the analysis of its radial motion when immersed in an incompressible fluid subjected to an harmonic excitation pressure field. The main governing equations used in the mathematical modeling of the problem are based on the principles of mass conservation (continuity equation) and linear momentum balance (Newton's second law - equation of motion). An appropriate constitutive model to represent the traction jump (i.e. boundary condition for the stress) on the bubble surface is also used. The velocities are continuous on the surface.

Consider a spherical bubble immersed in a Newtonian incompressible fluid of viscosity μ and density ρ. The inner side of the bubble is composed by a mixture of air and contaminant gases (which develop a polytropic process) and steam. We assume that the bubble develops only radial motions due to its surface tension that resists to other non-radial deformational modes, simplifying our analysis to an unidimensional motion, maintaining its spherical shape. This assumption is valid for small excitation amplitudes or for small bubbles. Therefore, effects like pressure gradients in the liquid or surfactants in the fluid are neglected. Changes in the vapour temperature may modify its density modifying the bubble dynamics [24]. However, for a small equilibrium vapour density the isothermal process is valid [25].

The mass conservation equation for a compressible fluid is given by [26]

$$\frac{\partial \rho}{\partial t} + \nabla \cdot (\rho \boldsymbol{u}) = 0, \tag{40}$$

in which ρ is the constant fluid density (i.e. incompressible liquid), t represents time and $\boldsymbol{u}$ is the Eulerian velocity fied on the liquid side. In this model spherical coordinates are used. The velocity components in the directions θ and ϕ are zero. Thus, the mass conservation equation in spherical coordinates for an incompressible fluid is given by

$$\frac{1}{r}\left[\frac{\partial}{\partial r}(r^2 u_r)\right] = 0 \rightarrow \int \frac{\partial}{\partial r}(r^2 u_r) dr = 0, \tag{41}$$

where r represents the physical distance of the center of the bubble to an arbitrary point inside the liquid phase, u_r is the radial component of the velocity field. Integrating equation (41) from the surface of the bubble of radius $R(t)$ to an arbitrary point in the liquid (distance r) after some algebric manipulation, we have

$$u(r,t) = \frac{R^2}{r^2}\frac{dR}{dt} = \frac{R^2}{r^2}\dot{R}. \tag{42}$$

The equation that expresses the balance of linear momentum is given by [26]

$$\rho\left(\frac{\partial \boldsymbol{u}}{\partial t} + \boldsymbol{u}\cdot\nabla\boldsymbol{u}\right) = \nabla\cdot\boldsymbol{\Sigma}, \tag{43}$$

where $\boldsymbol{\Sigma} = -p\boldsymbol{I} + 2\mu\boldsymbol{D}$ is the stress tensor for a Newtonian incompressible fluid, written in terms of the pressure field p, the identity tensor $\boldsymbol{I}$ and

the rate of strain tensor $\boldsymbol{D} = 1/2(\nabla \boldsymbol{u} + (\nabla \boldsymbol{u})^T)$. Considering the radial component of Navier-Stokes equation in spherical coordinates, equation (43) reduces to

$$\rho \frac{\partial u}{\partial t} + u\frac{\partial u}{\partial r} = \frac{-1}{\rho}\frac{\partial p}{\partial r} + 2\frac{\mu}{\rho}\left[\frac{\partial^2 u}{\partial r^2} + \frac{2}{r}\frac{\partial u}{\partial r} - \frac{2u}{r^2}\right]. \tag{44}$$

integrating the resulting equation in the flow field (the region between the surface of the bubble and the infinite quiescent liquid) after some algebric manipulation, we have

$$2\dot{R}^2 + \ddot{R}R - \frac{\dot{R}^2}{2} = \frac{p_\ell(R) - p_\infty}{\rho}, \tag{45}$$

where p_∞ is the ambient pressure and p_ℓ denotes the pressure on the liquid phase at the bubble surface. As the bubble is considered in the present context a clean curved interface between two immiscible fluids, there is a normal stress discontinuity in the interface due to its surface tension. This jump of normal stresses is given by Young-Laplace equation:

$$\Sigma_{rr,\ell} - \Sigma_{rr,b} = \frac{2\tilde{\sigma}}{R}, \tag{46}$$

where $\tilde{\sigma}$ represents the surface tension coefficient and $\Sigma_{rr,\ell}$ and $\Sigma_{rr,b}$ denote the radial component of the traction $(\hat{n} \cdot \boldsymbol{\sigma})$ at the liquid phase and inside the bubble phase, respectively. The pressure inside the bubble is given by $p_b(t) = p_v + p_g(t)$, where p_v is the liquid vapour pressure and $p_g(t)$ refers to the gas pressure. Therefore, the term $\Sigma_{rr,b} = -p_b(t)$ is then given by

$$\Sigma_{rr,b} = -p_v - \left[(\tilde{p}_\infty - p_v) + \frac{2\tilde{\sigma}}{R_E}\right]\left(\frac{R_E}{R}\right)^{(3n)} \tag{47}$$

where $\tilde{p}_\infty$ represents the static pressure for an equilibrium condition and R_E is the bubble equilibrium radius. The Euleurian velocity field induced by the bubble oscillations is given by equation (42). Hence, $\Sigma_{rr,\ell}$ results in

$$\Sigma_{rr,\ell} = -p_\ell - 4\mu\frac{\dot{R}}{R}. \tag{48}$$

Substituting equations (47) and (48) in (46) we obtain

$$p_\ell = -4\mu\frac{\dot{R}}{R} - \frac{2\tilde{\sigma}}{R} + p_v + \left(\Delta\tilde{p} + \frac{2\tilde{\sigma}}{R_E}\right)\left(\frac{R_E}{R}\right)^{3n}, \tag{49}$$

where $\Delta\tilde{p} = \tilde{p}_\infty - p_v$. The forcing acoustic pressure field imposed on the bubble is taken as being $p_\infty(t) = \tilde{p}_\infty[1 + \varepsilon sin(\omega t)]$, where ε represents the pressure amplitude and ω is the forcing pressure frequency. Now, substituting equation (49) in (45), the Rayleigh-Plesset equation is written as

$$\ddot{R}R + \frac{3}{2}\dot{R}^2 = \frac{\Delta\tilde{p}}{\rho} + \frac{1}{\rho}\left(\Delta\tilde{p} + \frac{2\tilde{\sigma}}{R_E}\right)\left(\frac{R_E}{R}\right)^{3n} - \frac{2\tilde{\sigma}}{R\rho} - \frac{\tilde{p}_\infty}{\rho}\varepsilon sin(\omega t) - \frac{4\mu}{\rho}\frac{\dot{R}}{R}. \tag{50}$$

II.1.2 Non-dimensional Formulation

We shall make use of non-dimensional variables indicated by asterisks, namely

$$R^* = \frac{R}{R_E}, \quad t^* = \frac{t}{t_c}. \tag{51}$$

Typical scales of velocity and time are represented by

$$U_c = \left(\frac{|\Delta\tilde{p}|}{\rho}\right)^{1/2}, \quad t_c = \frac{R_E}{U_c} \tag{52}$$

respectively. The excitation amplitude may also be written as $\varepsilon^* = \varepsilon(\Delta\tilde{p}/\tilde{p}_\infty)$. Using these typical scales we can write the non-dimensional form of Rayleigh-Plesset equation (49) as:

$$\ddot{R}^* R^* + \frac{3}{2}\dot{R^*}^2 = \frac{2}{We}\left[\frac{1}{(R^*)^{3n}} - \frac{1}{R^*}\right] - 1 - \varepsilon * sin(\omega^* t^*) + \frac{1}{R^{*(3n)}} - \frac{4}{Re}\frac{\dot{R}^*}{R^*} \tag{53}$$

Here, $Re = \frac{\rho U_c R_E}{\mu}$ corresponds to the Reynolds number which measures the relative importance between inertial and viscous forces. and $We = \frac{\rho U_c^2 R_E}{\tilde{\sigma}}$ is the Weber number, which denotes the ratio of inertial and surface tension forces.

II.1.3 Neural Networks

The main goal of this work is to show that it is possible to conceive, design and train a Neural Network used for pattern identification purposes in the specific dynamical problem of an oscillating micro bubble immersed in a Newtonian liquid. Multilayer neural networks are usually composed of an input layer, a hidden layer and an output layer. Those layers can be formed by activation functions and different training methods. Based on the network's input and random initial conditions, a transfer function is then used to calculate the output layer [27]. The output y_k of the kth neuron of the Network is given by

$$y_k = \phi\left(\sum_{j=0}^{n} w_{kj}x_j\right) \tag{54}$$

where y_k is the output of the neural network, w_{kj} determines the weights given for each entry, x_j is the number of inputs and ϕ is the transfer function used. In the present work the output of the network y_k is the number of the pattern found by the network, the input x_j is the information used in order to train the network. In the present the work this information is composed by the amplitude and part of the frequency spectrum around the first harmonic. A sketch of the scheme used to train the network is shown in figure (4).

There are several different trainning methods available in the current literature (e.g [28]). In the present work the Levenberg-Marquardt (LM) backpropagation method [29] is explored. The Levenberg-Marquardt method seeks to minimize a nonlinear function. In this case the error in the pattern identification process is defined as

$$\boldsymbol{e}_{\varphi,o} = \boldsymbol{d}_{\varphi,o} - \boldsymbol{n}_{\varphi,o}, \tag{55}$$

where $\boldsymbol{e}_{\varphi,o}$ is the error in identifying a given pattern φ for a given output o of the network, $\boldsymbol{d}_{\varphi,o}$ is the desired value of the pattern φ that the network should identify in the output o and $\boldsymbol{n}_{\varphi,o}$ is the current output that the network provides for a known pattern φ in a current output o. The idea of the Levenberg-Marquardt method is to minimize this error $\boldsymbol{e}_{\varphi,o}$ for different patterns φ in different outputs o of the network. In this sense the network must adjust its weights w_{kj} for each input and each known pattern during the training period in order to maximize its chances of predicting the correct pattern. Basically the Levenberg-Marquardt algorithm uses the Jacobian matrix containing the first derivatives of the Network errors with respect to its weights and biases, given by

$$\boldsymbol{J} = \begin{pmatrix} \frac{\partial e_{1,1}}{\partial w_1} & \frac{\partial e_{1,1}}{\partial w_2} & \cdots & \frac{\partial e_{1,1}}{\partial w_n} \\ \frac{\partial e_{1,2}}{\partial w_1} & \frac{\partial e_{1,2}}{\partial w_2} & \cdots & \frac{\partial e_{1,2}}{\partial w_n} \\ \cdots & \cdots & \cdots & \cdots \\ \frac{\partial e_{1,o}}{\partial w_1} & \frac{\partial e_{1,o}}{\partial w_2} & \cdots & \frac{\partial e_{1,o}}{\partial w_n} \\ \cdots & \cdots & \cdots & \cdots \\ \frac{\partial e_{p,1}}{\partial w_1} & \frac{\partial e_{p,1}}{\partial w_2} & \cdots & \frac{\partial e_{p,1}}{\partial w_n} \\ \\ \cdots & \cdots & \cdots & \cdots \\ \frac{\partial e_{p,o}}{\partial w_1} & \frac{\partial e_{p,o}}{\partial w_2} & \cdots & \frac{\partial e_{p,o}}{\partial w_n} \end{pmatrix}, \tag{56}$$

where n is the number of weights used for each neuron of the network. The minimization of the error in the identification of each pattern is done through the following equation

$$\boldsymbol{w}_{k+1} = \boldsymbol{w}_k - \left(\boldsymbol{J}_k^T\boldsymbol{J}_k + \alpha\boldsymbol{I}\right)^{-1}\boldsymbol{J}_k\boldsymbol{e}_k, \tag{57}$$

where α is called the *combination coefficient*. Depending on the value of α the LM algorithm switches between the steepest descent and the Gauss-Newton algorithms during the training process. The use of the Jacobian matrix is simpler to compute in comparison with the Hessian matrix in minimization methods such as the Newton algorithm. In this direction the Levenberg-Marquardt algorithm is characterized by a fast convergence rate in comparison to other algorithms used to minimize nonlinear functions.

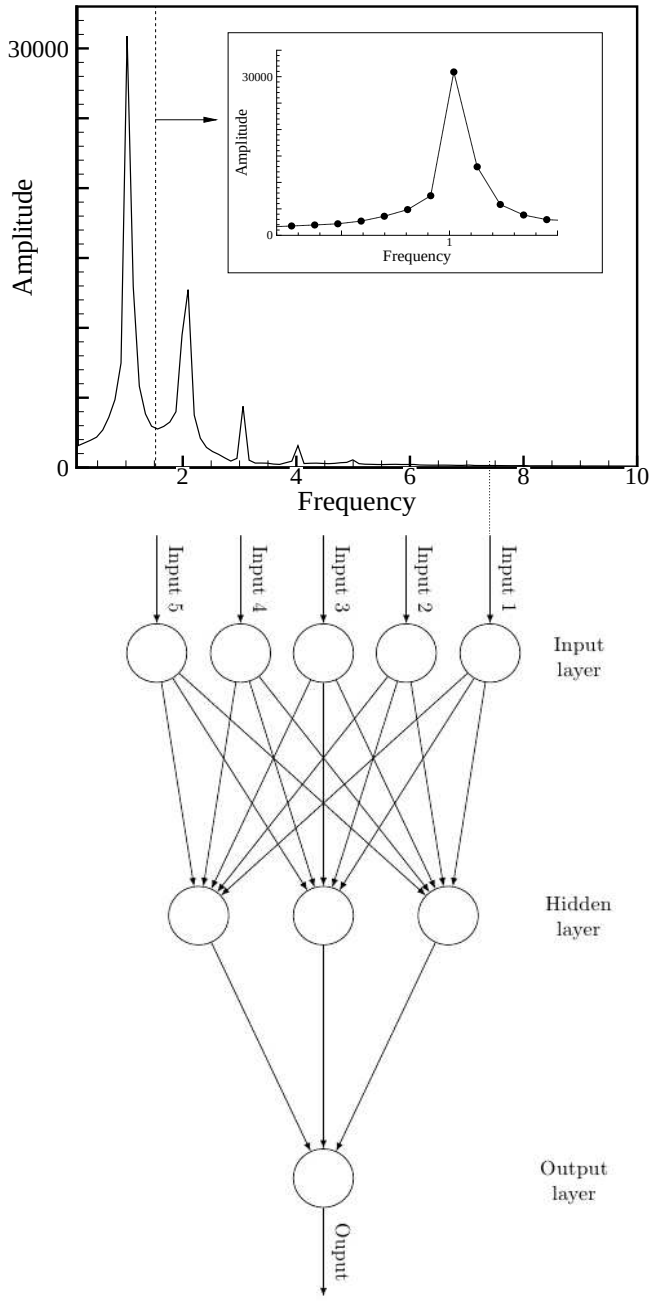

Figure 4: Schematic of a typical Neural Network explored in the present work.

The nonlinearity in the bubble oscillatory motion may generate not only pure harmonics, but also some spectral spreading. This can be identified in the frequency spectrum of the signal $R(t)$. The amplitude of the first harmonic and its spreading can be used to diagnose the nonlinearity degree and the involved vibrational modes in the coupled motion of the bubble and the surrounding liquid. We will show that this dynamic system has a spectra with broad bands, similar to chaotic systems rather than isolated peaks. In this context a training set of 23 differ-

ent simulations containing 7 identified patterns is inserted into the neural network. The validation group also possesses the same amount of information, but in this case, the neural network should identify the pattern from the frequency signature. Seven tests are conducted with different initial random conditions of the neural network weights. Each test improves the weights and the identification becomes more effective, displaying a very good percentage of correct answers in the sample. More details on the implementation, training and performance of the Neural Network will be given in subsequent sections.

II.2 Numerical Methodology

Due to the nonlinearity of the governing differential equation we do not have an analytic solution for arbitrary input parameters. In this sense we must recur to the use of a numerical algorithm to integrate the governing equation of the bubble-liquid dynamic system. In this work we use a Runge-Kutta scheme (RKS). Our RKS algorithm uses the advanced predictor-corrector algorithm, which uses weighted averages of a function f calculated at the extremes and at intermediate points of several time intervals $[t_j, t_j + 1]$ [30].

The nonlinearity of our dynamic system requires a careful calibration of the numerical time-step. For the most unstable regions where the radius of the bubble presents a rapid variation in time, the time step must be very small. On the other hand, when the bubble oscillating movement is harmonic, the computational cost may be unnecessarily increased by using small time steps. In order to solve this numerical issue an adaptive time scheme is incorporated to the dynamic simulations. Here we use the adaptive time step method scheme first proposed by Fehlberg [27] who uses the difference between two R predictions. The first prediction of R using a fifth order scheme and the second prediction of R by means of a fourth order scheme. In this way we have a good prediction of the truncation error by dynamically adjusting the numerical time step. The formula written in terms of k_n constants for each time step is given by [32] :

$$\tilde{y}_{n+1} = y_n + \frac{2825}{27648}k_1 + \frac{18575}{48384}k_3 + \frac{13525}{55296}k_4 + \frac{277}{14336}k_5 + \frac{1}{4}k_6. \quad (58)$$

The recurrence formula of a fourth order RKS is given by

$$y_{n+1} = y_n + \frac{37}{378}k_1 + \frac{250}{621}k_3 + \frac{125}{594}k_4 + \frac{512}{1771}k_6, \quad (59)$$

with the associated error given by

$$\Delta_e = \tilde{y}_{n+1} - y_{n+1}. \quad (60)$$

In bubble dynamics studies it is useful to establish a minimum radius R_{min} associated with a collapse criteria to stop the simulation. In order to evaluate the minimum radius at the eminence of the collapse an asymptotic theory [33] is used as a criteria to stop our simulations. In this asymptotic theory the most adverse flow condition is considered, that is $Re \to \infty$ and a constant ambient pressure $p_\infty(t) = \tilde{p}$ that compresses the bubble. Under this condition we can solve Rayleigh-Plesset equation using the integrating factor method. The asymptotic expression for R_{min} results in

$$R_{min} = R_0 e^{-(R_0)^2\left[\frac{1+R_0\frac{We}{3}}{We+2}\right]}, \quad (61)$$

where R_{min} is the minimum radius, R_0 is the initial radius and We is the Weber number.

It should be instructive to know that the collapse in the present context is defined as an abrupt release of pressure that occurs outside the spectrum of continuum mechanics time scales. This sudden expansion occurs after significant rapid shape deformations. During these

extremely small time intervals the bubble cannot be considered as an isotropic sphere. It is important to say that we are not focused in exploring bubble collapse in the present work. Instead of this, we are interest to explore nonlinear patterns associated to the nonlinear motion of a bubble that leads to bifurcations in the unstable vibrational modes.

II.2.1 Numerical tools

In this work we have used a series of numerical tools. The code that computes the motion of the bubble was written in Fortran95 for Linux platforms. For the post-processing of the numerical results, the Softwares *Matlab* and *Tecplot* have been used. The full analysis of the neural network is done by the neural networks toolbox of Matlab, which is based on the FFT responses acquired by a *Scilab* computational script. The neural network is based on the Levenberg-Marquardt method. We also used the gradient descent method, which allows us to recalculate the delta function based on the weights updated using the decrease of the error and determining the minimum value of the error function [34]. The training method used, trainoss (i.e. one step secant backpropagation), is a more efficient version of the Levenberg-Marquardt algorithm and has allowed calculations requiring less computational cost with better accuracy. For computing the Lyapunov exponents of the system we have also used a Matlab Lyapunov Exponents Toolbox (Matlab LET code [35]).

II.2.2 Code validation

In order to validate our numerical code, an asymptotic solution for $\varepsilon \ll 1$ is proposed. For this end, a regular asymptotic expansion method is proposed [25]. Specifically, a regular disturbance parametric method was used. In order to develop the asymptotic solution for the nonlinear governing equation 53 in the limit $\varepsilon \ll 1$, a convenient change of variable is proposed so that $R = (1 + r)$. The disturbances r around an equilibrium radius $R = 1$ are assumed to have the form $r(t) = \varepsilon y_1(t) + \varepsilon^2 y_2(t) + \mathscr{O}(\varepsilon^3)$, here we truncate the regular expansion for terms $\mathscr{O}(\varepsilon^3)$. After this expansion we obtain the following system of two linear differential equations $\mathscr{O}(\varepsilon)$ and $\mathscr{O}(\varepsilon^2)$ governing the quasi-nonlinear dynamic system

$$\ddot{y}_1(t) + \gamma \dot{y}_1(t) + \kappa y_1(t) = -sen(\omega t). \qquad (62)$$

and

$$\ddot{y}_2(t) + y_1(t)\ddot{y}_1(t) + \frac{3}{2}\dot{y}_1(t)^2 - \alpha y_2(t) - \beta y_1(t)^2 - \gamma(y_1(t)\dot{y}_1(t) - \dot{y}_2(t)) + \lambda y_2(t) - \eta y_1(t)^2 = 0. \qquad (63)$$

Note that equations (62) and (63) are both second order ordinary differential equations. The constants that appear in (62) and (63) are given by

$$\alpha = \frac{2}{We}(1 - 3n), \quad \lambda = 3n \qquad (64)$$

$$\beta = \frac{2}{We}\left[\frac{9}{2}n^2 + \left(\frac{3}{2}\right)n - 1\right] \qquad (65)$$

$$\eta = \left[\frac{9}{2}n^2 + \left(\frac{3}{2}\right)n\right], \quad \kappa = \lambda - \alpha \qquad (66)$$

Figure (35) shows a comparison between $\mathscr{O}(\varepsilon)$ and $\mathscr{O}(\varepsilon^2)$ asymptotic solutions with the numerical solution (RKS). It is seen that in the limit $\epsilon \to 0$ the asymptotic solutions are exact solutions of the problem.

Essentially figure (35) indicates that for small values of ε a perfect agreement exists between asymptotic solutions and the numerical silution (RKS). The insert of figure (35) shows the behavior of each solution for the interval $0 \leq \varepsilon \leq 0.2$. The error between the $\mathscr{O}(\varepsilon^2)$ and the numerical solution exceeds 1% for $\varepsilon \approx 1$. In addition, the results presented in figure (35) serve as a validation of the proposed algorithm.

Therefore, in the next sections we to use the developed code in order to explore other regimes that cannot be captured by our asymptotic solution

II.3 Results

In this section we present different vibrational patterns of the nonlinear bubble motion that have been organized in seven possible patterns observed within the range of parameters $Re = [0, 100]$, $\varepsilon = [0, 1]$ for constant values of $We = 6$, $n = 1$ and $\omega = 1$. In the present context, we do not intend to characterize all possible vibrational modes of the nonlinear bubble oscillatory motion. Our goal is the conception, design and training of a neural network in order to be applied as a tool for identifying patterns and nonlinear responses in the specific flow problem of an oscillating bubble in a Newtonian fluid. This step is quite necessary to extend the approach for investigating bubbles in complex fluids such as non-Newtonian fluid and magnetic suspensions. For this end we propose the classification of different vibrational modes into seven identified patterns based on the time response of the system, on the frequency spectrum and on the phase plane diagram. Each pattern is examined and discussed in details. A bifurcation diagram is also presented as a function of the parameters Re and ε. A bifurcation diagram in these dynamical system analysis is useful in order to identify the oscillating pattern for a given pair of Re and ε. The concept of Poincaré sections and Lyapunov exponent commonly used for analyzing nonlinear responses of dynamical systems is also applied to the investigated bubble system. Actually with these tools, we investigate if a chaotic characteristic is presented in the bubble nonlinear motion. Next, a neural network is designed and trained based on informations regarding the first harmonic on the frequency response of the bubble motion.

II.3.1 Different patterns of response

Four of the seven identified patterns are shown in figure (16). Based on the distortions of the bubble response on the phase diagrams, the vibrational modes of the bubble system are identified in seven different ways. 1) periodic with mild distortion in the lower peak; 2) periodic with moderate distortion in the lower peak; 3) periodic with mild distortion; 4) periodic with moderate distortion; 5) without harmonic distortion; 6) non-harmonic and non-periodic; 7) non-harmonic and non-periodic type 2. Here we have proposed that the concept of distortion should be based on a pattern deformation coefficient. So we define this coefficient as the ratio between the two coexisting peaks shown in figure (7). This ratio determines the degree of distortion in the time response. While values bellow a unit correspond to a slight distortion, a null value means that the answer is harmonic and values greater than the unit represent a moderate signal distortion by our definition. The simulations all assume a polytropic coefficient $n = 1$, a forcing pressure frequency $\omega = 1$ as a Weber number constant, $We = 6$.

Figure 16 indicates that under the simulated conditions if $Re < 5$ the bubble response corresponds always to the harmonic pattern 1 regardless of the pressure forcing amplitude. Is is

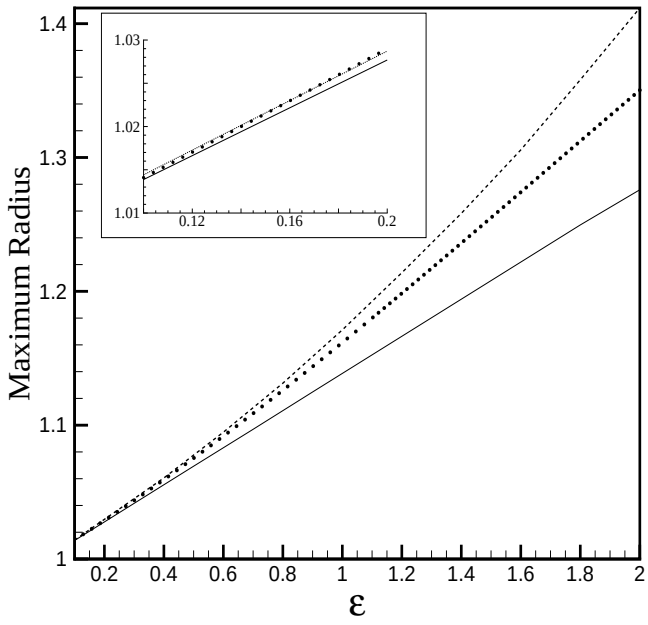

Figure 5: Comparison between the asymptotic solutions $\mathscr{O}(\varepsilon)$ (filled line), $\mathscr{O}(\varepsilon^2)$ (dashed line) and the numerical RKS (filled black circles) for the maximum bubble radius during its oscillatory motion as a function of the forcing pressure amplitude ε.

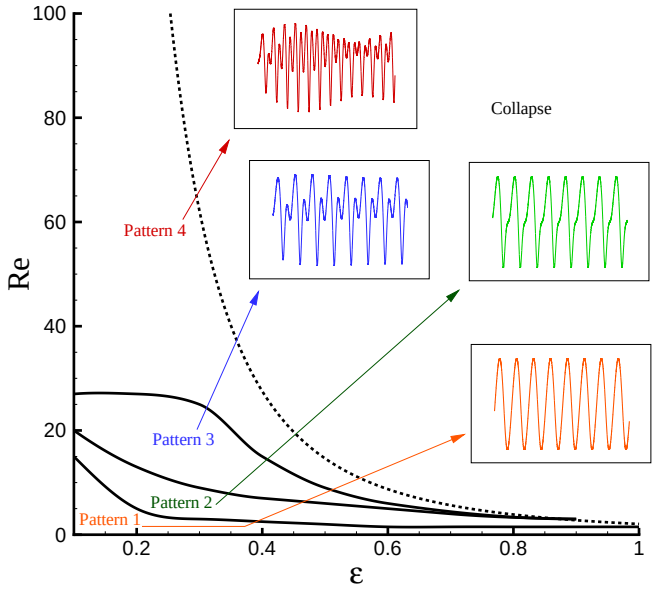

Figure 6: Bifurcation diagram. Parameter Re as a function of the pressure forcing amplitude ε, for We=6.

also interesting to note that with $\varepsilon \sim 1$ all patterns tends to an harmonic configuration at low Re. So, we identify a critical Reynolds number for which the bubble motion seems to be always harmonic even for $\varepsilon \sim 1$.

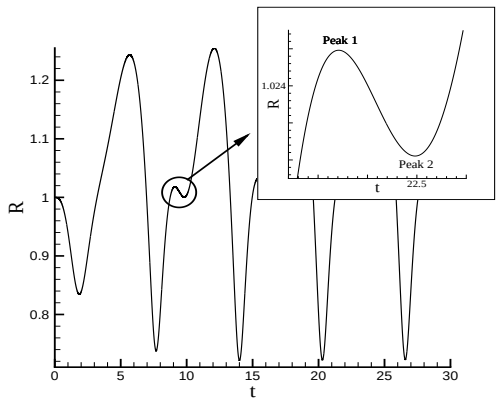

Figure 7: Identification of a typical time series (R versus t) of the bubble response.

Now, the stability of the bubble motion is analyzed by examining the phase plane (where g represents $\dot{R}$), frequency and time responses of the seven identified patterns.

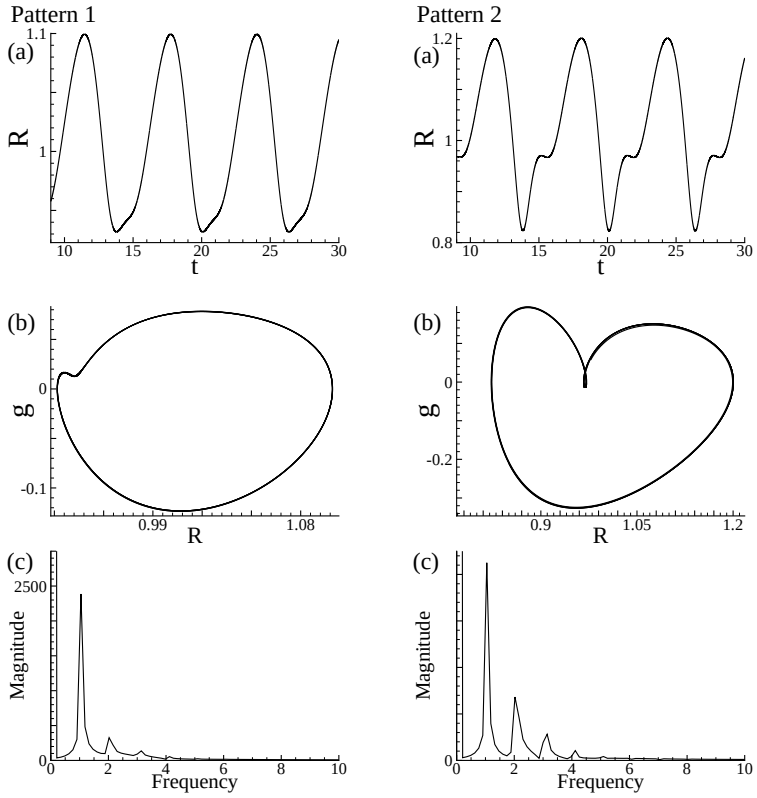

Figure 8: Left: pattern 1 characterized by a time series of R(t) (a), (b) phase plane and (c) Power spectrum given by FFT of the output. Right: pattern 2 characterized by a time series of R(t) (a), (b) phase plane and (c) Power spectrum given by FFT of the output.

Figure (17) shows that the phase space for pattern 1 approaches to a stable, periodic and harmonic response. In this case, the bubble response is represented by a figure similar to a cir-

cle in the phase diagram, despite a slight distortion in the second quadrant as a direct consequence of the velocity variations on the lower peak for smaller radius. The limit cycle, is also seen as a closed orbit, representing in the phase space a periodic trajectory with a finite and well defined period. In this case, we have an attracting limit cycle. The bubble response on the frequency domain shows that most part of the energy is located in frequencies around $\omega = 1$. This implies a signal (or time series) pretty close to a harmonic response. A second harmonic is presented due to the small deformation in the lower peak of the time response signal.

In pattern 2, the shape anisotropy of the phase diagram is more significant due to higher distortions. A suddeng change in speed not only increases the amplitude of the frequency response in the Fourier space, but produces a third harmonic to the system.

On the other hand, the phase diagram distortion is not enough to produce an inner limit cycle. In pattern 2, shown in figure (17), the distortion on the phase space suggests the deviation from the harmonic response. This deviation is associated with a higher contribution of inertial forces on the liquid. As shown in figure (16) for a given value of ε, say $\varepsilon = 0.1$, the transition from pattern 1 to pattern 2 occurs for $Re = 10$, so for $Re < 10$ the bubble response is represented by pattern 1, while for $Re > 10$ the bubble responds according to pattern 2.

The presence of a slight distortion on the time response (pattern 2) allows us to infer about the existence of different harmonics with different energetic levels. Pattern 2 is characterized by different states with nonlinear characteristics but still having one period. In contrast pattern 3 is seen clearly to have a time-series with double-periods that represents an unstable motion of the bubble in comparison to the harmonic one of pattern 1. At higher Reynolds number even for $\varepsilon \sim 0.1$ we can seen a quite nonlinear response of the bubble motion tending to present a continuous spectrum of vibrational degrees of freedom or periods. So, the bubble develops a quite strong unstable motion immersed in the Newtonian liquid. We can see similar speed changes on patterns 3 and 4, figure (18).

However, the change in position of pattern 4 is much more expressive, also increasing the amplitude of the fourth harmonic. In particular, the moderate distortion provides a new limit cycle, smaller than the main one. Thus, it is observed that the common generated distortion transforms the stable cycle and attenuates abrupt velocity variations of the bubble surface. In other words we can say that large accelerations of the bubble surface induce internal extra cycles with different periods. The size of the main limit cycle is proportional to acceleration?s variations.

The third pattern, shown in figure (18), does not present a distortion over the valley in the time response. The phase space becomes more symmetric, showing that the velocity changes of patterns 3 and 4 are quite similar. However, there is an expressive change in position in pattern 4, which increases the amplitude of the fourth harmonic.

Patterns 5 and 6 are shown in figure (19). It is noted that these patterns are harmonic without distortion and non-harmonic and non-periodic, respectively. Pattern 5 has a tendency of stability in the phase space and only two harmonics in the frequency response. The first harmonic contains almost all the energy of the

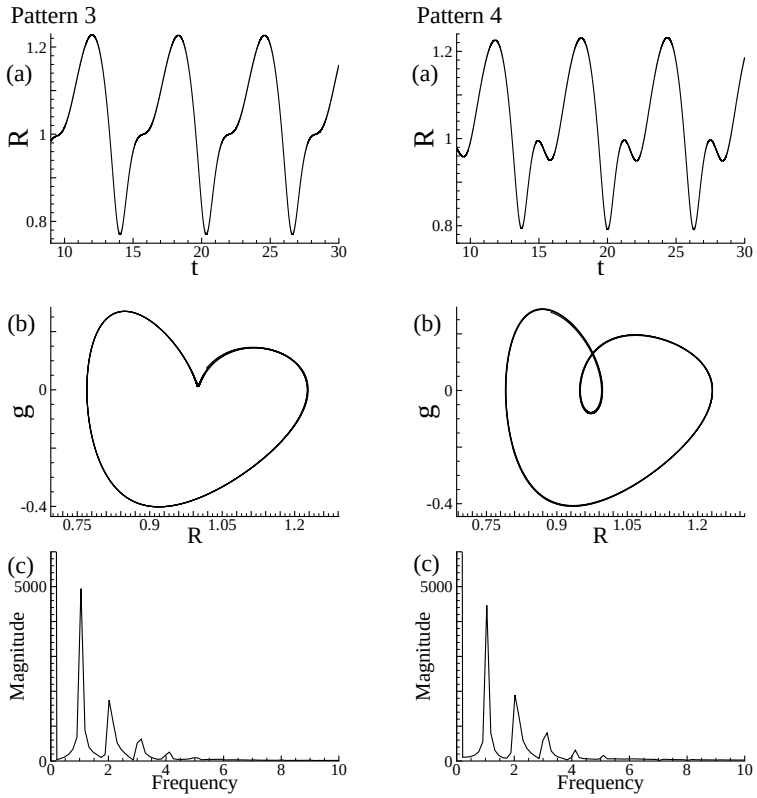

Figure 9: Left: pattern 3 characterized by a time series of R(t) (a), (b) phase plane and (c) Power spectrum given by FFT of the output. Right: pattern 4 characterized by a time series of R(t) (a), (b) phase plane and (c) Power spectrum given by FFT of the output.

system. On the other hand, pattern 6 shows a damping effect on the bubble time response and a continuos decrease in its energetic level in the phase diagram. We speculate that this energy loss is associated with an energy exchange between the bubble and the surrounding liquid. During this bubble-liquid interaction the viscosity of the liquid works as a damper decreasing the overall energy of the oscillating bubble. In the time response, we note that in each oscillation, the distortion parameter changes, inducing different vibrational responses.

Finally, pattern 7 shown in figure (23) has low distortion of the peak and a weak aperiodicity. This anisotropic behavior in the shape of the phase diagram is observed, which may be interpreted as a superposition of several degrees of freedom or energy levels. This system is highly nonlinear, showing a different frequency spectrum and phase space according to the variation of the non-dimensional parameters. This indicates that in the studies of dynamics systems stability, controlling the physical parameters of the problem is as important as the oscillation amplitude or even the type of external forcing. Viscous and restoring forces in relation to inertia forces are much important on the dynamics of the system than its forcing field.

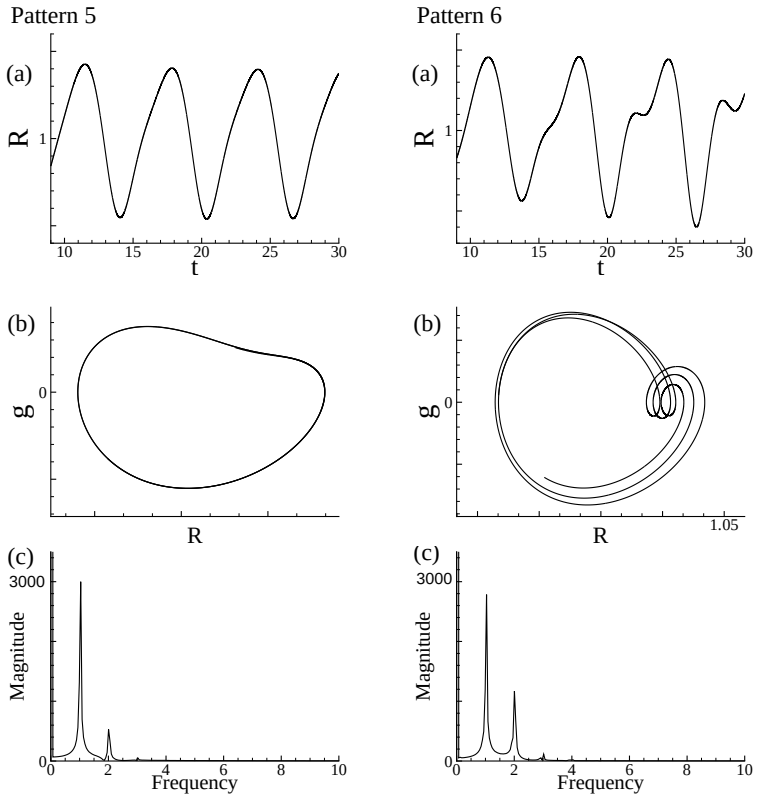

Figure 10: Left: pattern 5 characterized by a time series of R(t) (a), (b) phase plane and (c) Power spectrum given by FFT of the output. Right: pattern 6 characterized by a time series of R(t) (a), (b) phase plane and (c) Power spectrum given by FFT of the output.

II.3.2 Poincaré sections and Lyapunov exponents

Another interesting approach used to explore the behavior of our nonlinear system is the Poincaré section of the phase plane. For instance. the construction of the Poincaré map (section) is extremely useful in order to convert the study of the flow in the vicinity of a closed orbit. Roughly speaking, the Poincaré map corresponds to the process of periodically strobing a phase portrait. In particular we can see from figure (24) that different parameters can lead to an attractor if the collapse criteria is turned off. However, the results indicate that even a bubble describing nonlinear oscillations its motion will not bifurcate for a chaotic motion if it is immersed in a linear liquid. This type of response is seen even under a high Re and We numbers condition. We might argue, however, that for a chaotic configuration to appear the bubble should develops oscillations with a period in the same time scale of a complex nonlinear liquid such as a viscoelastic and magnetic fluid (see [12], [11]). In another words the motion of the bubble should be coupled with the mechanism of structure relaxation (e.g. macromolecules and chains present on these liquids). As the relaxation time of a Newtonian linear liquid is zero compared with any period of the bubble oscillation, the effect of the liquid is related with dissipation and inertia. These mechanisms are not sufficient to produce a chaotic route. Theses findings have currently motivated us to examine in full details the bubble dynamics in a magnetic anisotropic suspension [13]. Actually, in

practical application the bubble would collapse before its motion displays a chaotic motion. In order to produce the attractor shown in figure (24) the collapse criteria suggested in [10] based on a asymptotic critical radius of collapse was turned off in this specific simulation.

Now, we continue examining the nonlinear response of the bubble dynamics through the concept of Lyapunov exponents of this system. This study allows to observe the sensitive of the bubble system to initial conditions and also the divergence and convergence rates of nearby trajectories in the phase space. In other words the Lyapunov exponents (LE) herein called λ are a measure of the exponential separation (e^{λ}) of the neighboring trajectories over all points of a trajectory around an attractor. For stable cycles $\lambda < 0$ and neighboring trajectories converge, whereas $\lambda > 0$ corresponds to a chaotic attractor. In terms of the Kolmogorov entropy (entropic metric) the LE may be interpreted as a measure of the disorder in the bubble motion response due to the acoustic forcing pressure and its nonlinear interaction with the surrounding liquid. The Lyapunov exponents are also considered to be a dynamic measure of the complexity of delays and may be used for the characterization of chaos and bifurcations. These are standard consequences of a dynamical system with a high degree of nonlinearity and instabilities as can be seen in the unsteady oscillatory motion of a bubble in a complex liquid. LE are found in the present work by numerical computations. It can only be evaluated analytically in some simple cases. Most of them without practical importance in the scenery of nonlinear dynamic systems.

We shall now explore the behavior of Lyapunov exponents for an equivalent autonomous system representing the nonlinear motion of the bubble. Since we are considering the radial motion of a non deformable bubble in a three dimensional quiescent liquid in the absence of any rotational motion, we have a dynamical system with three translational degrees of freedom. In this sense we can use equation (53) in order to express the primary system as being an autonomous system. In this particular case, in which the bubble is immersed in a Newtonian liquid, Rayleigh-Plesset equation can be just written as an equivalent autonomous system as

$$\begin{cases} \frac{dx}{dt} = y \\ \frac{dy}{dt} = \frac{1}{x}\left[-\frac{3}{2}y^2 + \frac{2}{We}\left(\frac{1}{x^3} - \frac{1}{x}\right)\right] \\ -\frac{1}{x} - \frac{\varepsilon sin(\omega z)}{x} + \frac{1}{x^4} - \frac{4}{Re}\frac{y}{x^2} \\ \frac{dz}{dt} = 1 \end{cases} \tag{67}$$

The Jacobian of the system of nonlinear ordinary differential equations given in (67) is expressed by equation (68). Considering different values of Re, We, ε and the initial conditions it is possible to test whether the bubble presents a chaotic behavior. For this purpose, we have used the Matlab Lyapunov Exponents Toolbox [35]. The output can present different behaviors which are characterized as periodic cycles or stable equilibrium, nonlinear chaos and pure random processes. In the Jacobian approach, the Jacobians are usually found by locally linear mapping in the neighborhoods near the reference trajectory to neighborhoods at a subse-

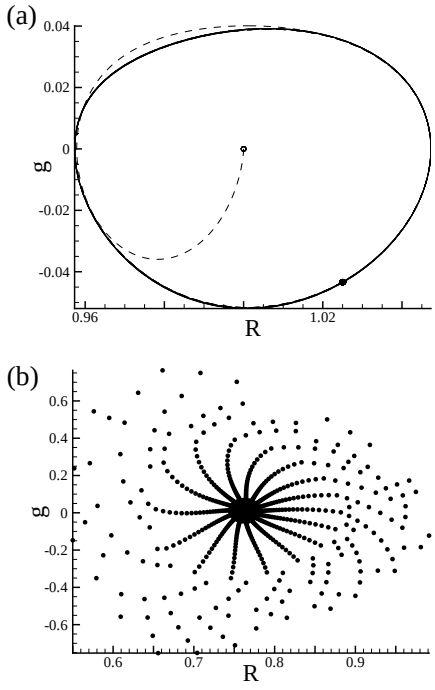

Figure 12: Poincaré section for different patterns. (a) the phase plane and the Poincaré section of an harmonic pattern with low Reynolds and Weber numbers. The transient response is represented by the dashed line. (b) a nonlinear pattern obtained with high Reynolds number and excitation amplitude when the collapse criteria is turned off. Those different parameters leads to an attractor.

quent time [37]. Along with the Lyapunov exponents, the Lyapunov dimension is also given for each time step. This dimension, also known as Kaplan-York dimension can be defined as the fractal dimension in which a cluster of initial conditions will neither expand nor contract as it evolves in time [29]. The rate of expansion is the sum of the Lyapunov exponents, and this sum will necessarily be negative for an attractor, for example.

$$\begin{bmatrix} 0 & 1 & 0 \\ \left(1.5\frac{y^2}{x^2} - 4\frac{(2/We)}{x^5} + 2\frac{(2/We)}{x^3} + \frac{1}{x^2} + \frac{\varepsilon sin(\omega t)}{x^2} - \frac{4}{x^5} + 2(4/Re)\frac{y}{x^3}\right) & \left(-3\frac{y}{x} - \frac{(4/Re)}{x^2}\right) & \varepsilon\omega cos(\omega t) \\ 0 & 0 & 0 \end{bmatrix} \tag{68}$$

Figure (25) shows that even though the bubble response in a Newtonian fluid is highly nonlinear, the formal requirements for reaching chaotic configurations of the bubble oscillations are not satisfied. Actually all Lyapunov exponents are negatives and the Lyapunov dimensions of both systems are null. The Lyapunov dimension is zero when the system is a first order one-dimensional system, such as it occurs in the logistic map or all the Lyapunov exponents are negative (or zero). All the tests were conducted with no collapse criteria. Under this condition, we can argue that none of the combination of parameters physically accepted would lead to a chaotic motion.

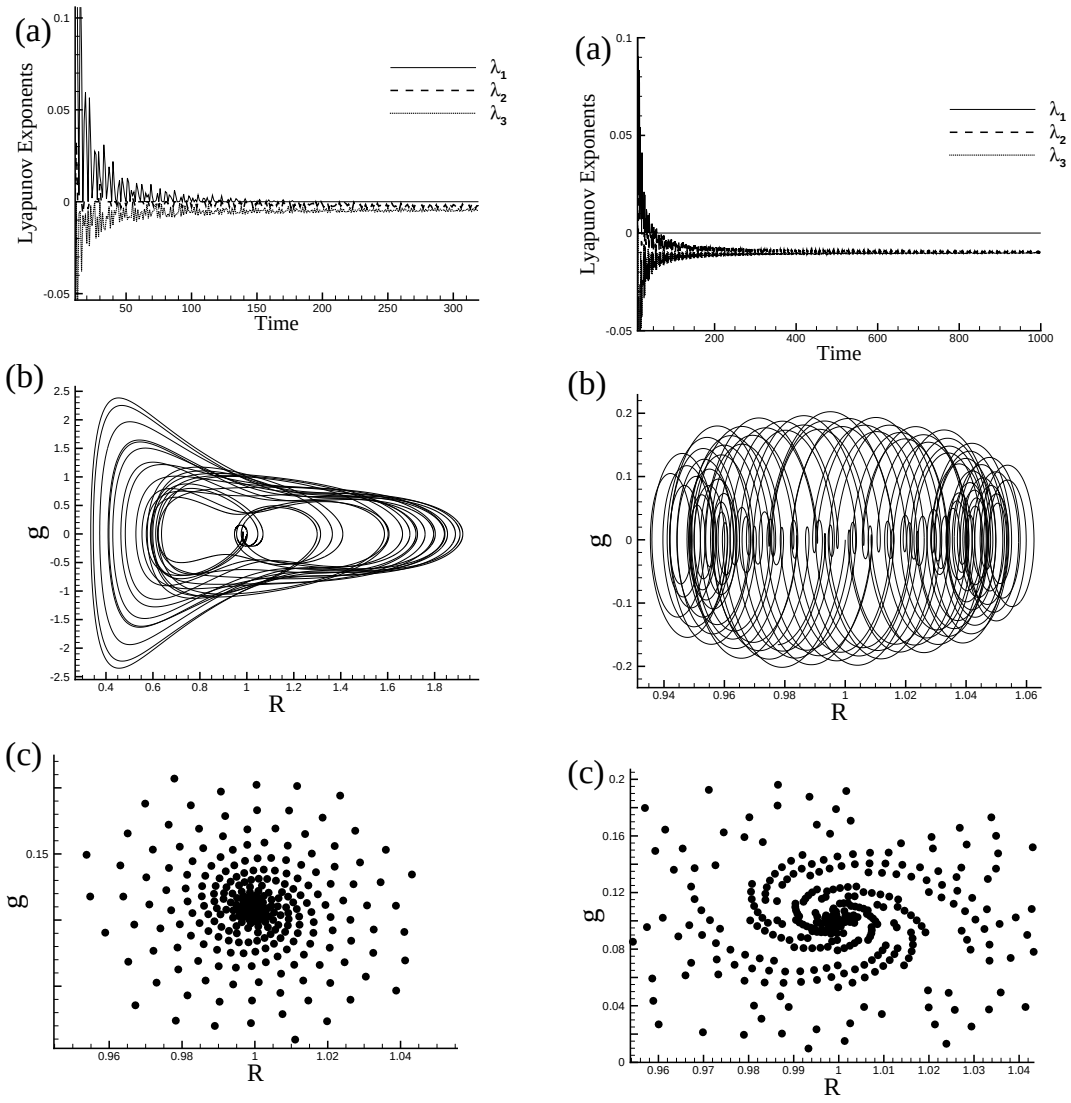

Figure 13: Left: (a) Lyapunov exponents for the bubble dynamic system, (b) phase space and (c) Poincaré section for $Re = 150$, $We = 2$, $\varepsilon = 0.8$ and $\omega = 8$. Right:(a) Lyapunov exponents for the bubble dynamic system, (b) phase space and (c) Poincaré section for $Re = 200$, $We = 200$, $\varepsilon = 1.5$ and $\omega = 15$.

II.3.3 Neural Network Training data from the Bubble Dynamical System

In this part of our dynamic analysis a neural network is designed for identifying the vibrational patterns of the nonlinear motion of the bubble through its FFT response. Previously, we know that the bubble motion is stable. The set of parameter ranges for these tests are $Re = [0, 100]$, $\varepsilon = [0, 1]$ under a condition of constant $\omega = 1$, $n = 1$ and $We = 6$. More precisely the input data on the network consists on the frequency f spectrum ranging from $0.2 \leq f \leq 1.5$. This band in the frequency spectrum includes informations regarding the amplitude of the first harmonic together with the spectral spreading behavior on its vicinities.

The trained network uses a set of 36 input matrices called *Patterns*. Each one with 15 different pairs of information concerning a set of points that accounts for the spectral spreading around frequencies in the interval $0.2 \leq f \leq 1.5$. The system uses 1000 epochs with a linear transfer function on the first layer of the network and a logarithmic transfer function on the second layer. The first layer is built with 30 neurons and the second with a single neuron. Each training set has an output, called *target*, referring to its vibrational pattern. The validation set is not used for training. In this sense we test the performance of the network by providing an input with information never seen before during its training. In order to validate the performance of the network and its ability in identifying the vibrational patterns of the bubble nonlinear dynamic we have carried out seven tests. In each test the network uses a different set of weights in its initial condition. For a given input data containing 15 points of the FFT signal in the interval $0.2 \leq f \leq 1.5$, the output of the network is a real number. This real number corresponds to the pattern the network is supposed to identify. Figure (14) shows the plots of the network performance for identifying the particular patterns

Figure (14 a) shows the output for seven different tests for a given input containing all the possible patterns. The symbols denote the output of the network for different tests. The continuous line would be the expected answer of the network. Since the network uses different initial conditions its output changes for each test. In order to demonstrate the ability of the network in identifying the patterns we might perform an ensemble average over all validation tests. The result of this ensemble average is presented in figure (14b). It is seen that the resulting network is able to identify the correct pattern for all the defined patterns within the range of the physical parameters explored in this work. This result indicates that the network has the ability of reading a new set of data that it had never seen before and predict what pattern is responsible for that specific data. The tests point out that using a simple statistical analysis by considering an ensemble average of 7 tests the confidence of the network ability for recognizing the vibrational patterns is of 100%.

Identifying the pattern supports us for understanding the nonlinear bubble motion and the influence of the physical parameters on the vibrational modes of the oscillating bubble. Using the collapse diagram available from our previou work [30], we can identify the full range of Reynolds and Weber numbers that leads to the bubble collapse. As a promising application the control of a cavitating bubble by monitoring the bubble collapse time could be done by using neural networks.

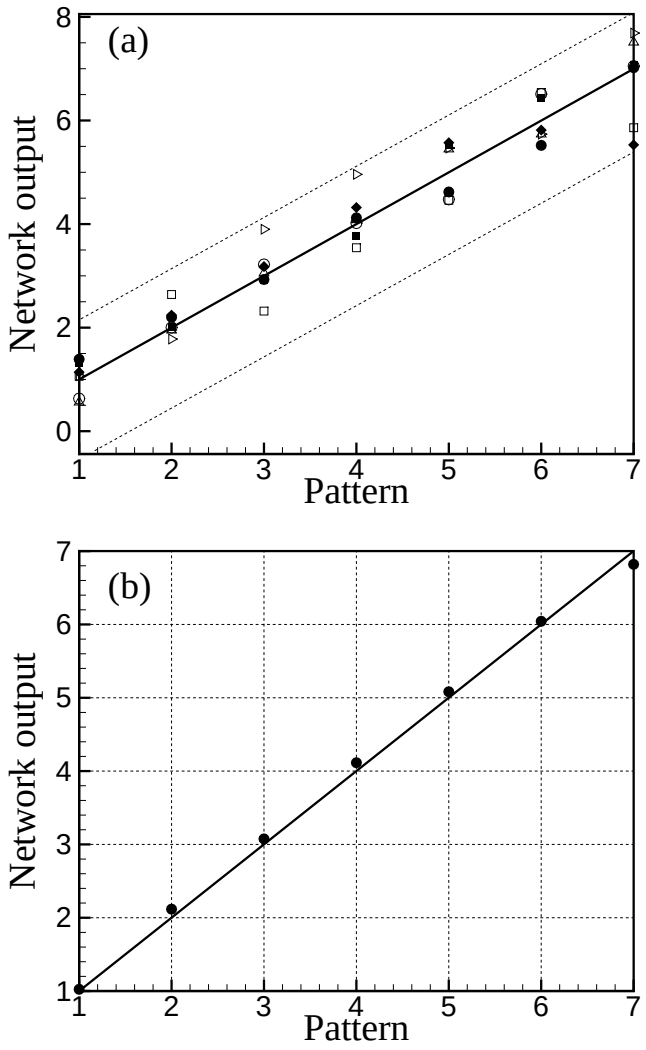

Figure 14: (a) Network output as a function of the patterns considering seven tests with different initial weights for each neuron, the full circles represent the Network output for a given test. (b) average values of the Network output for seven different tests, denoted by the filled black circles. In both plots the full line represents the desired output for each pattern.

II.4 Conclusions

The dynamic behavior of a single gas bubble immersed in a Newtonian liquid in the presence of an acoustic pressure forcing was successfully observed and identified with a neural network. The bubble motion dynamics was governed by the classical Rayleigh-Plesset equation with both Reynolds and Weber number being the non-dimensional physical parameter of the bubble dynamics explored here. In pratical applicatios involving cavitating bubbles the identification of these paramaters and their dynamic control in nonlinear bubble oscillatory motion is a quite important feature for understanding and controlling the instability and cavitation in such a nonlinear system. The proposed model has considered a one dimensional flow in the radial direction due to the spherical shape of the bubble, the sinusoidal excitation in the same di-

rection allowed visualization of the anisotropic effect on the stability thereof.

The numerical simulations performed in this work were quite important for identifying several anisotropic shape in the phase diagram and different modes in the frequency response of the nonlinear bubble oscillatory motion. These different vibrational modes shows us the richness of the dynamical behavior of the bubble-liquid dynamic system explored here. Surprisingly, even having identified several modes of vibration for the analysis of the bubble dynamics in a Newtonian fluid, a chaotic configuration was never reached. We argue that a chaotic situation related to a strange attractor could evolve if the bubble is immersed in a complex fluid like a viscoelastic liquid or a magnetic suspension. In this case a drastic change in the bubble oscillations would be possible if a period of oscillation the bubble surface is influenced by the particle relaxation time of theses complex liquids.

We have observed, however attractors resulting from the nonlinear motion in the phase plane in the absence of bubble collapse. This analysis was performed by both the Lyapunov exponents as well as by the Poincaréé section approach. Regardless the nonlinearities on the movement of the bubble, the Lyapunov exponents were always negative under all conditions simulated. In addition, the existence of a fractal dimension was not identified, resulting in a null value. The lack of a purely chaotic behavior contributes to the stability of the neural network.

From our knowledge this work seems to be a first step towards understanding and controlling the nonlinear response of bubbles in oscillatory motions from a dynamical system point of view. We have identified topological transitions in phase plane using for instance the analysis of Poincaré sections and the solution in the Fourier space.

The training of a neural network is a slow processing analysis, in particular because it requires the use of different random weights in its initial conditions. On the other hand, its apllication is rapid and simple once it is trained in order to perform a specific task. The current literature recommends that the number of epochs, neurons and training algorithm is an important factor for the choice of the network weights [28]. After determining the network paramaters, the vibrational patterns were identified and related as a function of the relevant non-dimensional physical parameters governing the bubble motion dynamics. This study has successfully shown a rate of 100% guesses of the network in identifying the vibrational pattern of the bubble response system by using numerical which did not belong to the training set.

When identifying the history of bubble patterns and oscillations, the present analysis can be used to predict the collapse time and also to control the set of dynamic parameters that could avoid it. The presence of microbubbles enormously enhances delivery of genetic material, proteins and smaller chemical agents. Delivery of genetic material is greatly enhanced by ultrasound in the presence of microbubbles [38]. In this particular case, after characterizing the vibrational pattern of the bubble nonlinear oscillations new investigations and studies could be performed in order to extract the full details of the bubble dynamic response. Moreover, determining which vibrational pattern one desires, the ultrasound may be adjusted likewise. In this context, using neural networks to identify cavitational vibrational modes seems to be a quite effective process. Generalization in a two-layer neural network with multiple outputs In future works, we plan to use the approach of Poincaré sections for all identified patterns as an input information in order to test its influence on the ability of the network identification. In addi-

tion, we have been already using currently the same approach presented here for examining [13] bubble dynamic systems immersed in a complex surrounding liquid.

BIBLIOGRAPHIC REFERENCES

[1] Rayleigh, L., 1917, *On the Pressure Develop in a Liquid During the Collapse of a Spherical Cavity*, Phil. Magazine, series 6, Vol 34, 94-98.

[2] Leighton, T. G., 1994, *The Acoustic Bubble*, Academic, New York.20, 638-645.

[3] Young, F. R., 1989, *Cavitation*, Mc-Graw-Hill, London, Chap. 2.

[4] Young, F. R., 2005, *Sonoluminescente*, CRC, Boca Raton, Chap. 5.

[5] Brenner, P. M., Hilgenfeldt, S., and Lohse, D., 2002, *Single-bubble sonoluminescence*, Rev. Mod. Phys. 74, 425?483.

[6] Geers, T. L., Lagumbay, R. S., and Valisyev, O. V., 2012, *Acoustic-wave effects in violent bubble collapse*, Journal of Applied Physics 112, 054910.

[7] Gopal, A. D., Durian, D. J., 1995, *Nonlinear Bubble Dynamics in a Slowly Driven Foam*, Physical Review Letters, Vol 75, 13.

[8] Street, J. R., 1968, *The rheology of phase growth in elastic liquids*, Trans. Soc. Rheol., 12, 103.

[9] Fogler, H. S., Goddard, J. D., 1969, *On the Stability and Collapse of Spherical Cavities in Viscoelastic Fluids*, paper number 63A presented at the 62nd. Ann. Meeting A. I. Ch. E., Washington, D.C.

[10] Albernaz, D. L., Cunha, F. R., 2013, *Unsteady Motion of a Spherical Bubble in a Complex Fluid: Mathematical Modelling and Simulation*, Applied Mathematical Modelling, Vol 37, 8972-8984.

[11] Cunha, F. R., Albernaz, D. L., 2013, *Oscillatory motion of a spherical bubble in a non-Newtonian fluid*, Journal of Non-Newtonian Fluid Mechanics, Vol 191, 35-44.

[12] Cunha, F. R., Sousa, A. J., Morais, P. C., 2002, *The Dynamic Behavior of a Collapsing Bubble in a Magnetic Fluid*, Journal of Magnetism and Magnetic Materials, Vol 252, 271-275.

[13] Malvar, S, Gontijo, R. G. and Cunha, F.R., 2015, *On the Nonlinear Motion of an Oscillating Bubble Immersed in a Magnetic Fluid*, In preparation.

[14] Chang, R., Alejos, J. C., Atkinson, D., Jesen, R., Drant, S., Galindo, A., Laks, H., 1999, *Bubble contrast echocardiography in detecting pulmonary arteriovenous shunting in children*

with univentricular heart after cavopulmonary anastomosis, Journal of the American College of Cardiology, Vol 33, Issue 7, 2052-2058.

[15] Marmottant, P., Hilgenfeldt, S., 2004, *A bubble-driven microfluidic transport element for bioengineering*, J. American Chemical Society, Vol 101, Issue 26.

[16] Sorokin, V.S., Blekhman, I.I. and Vasilkov, V.B., 2012, *Motion of a gas bubble in fluid under vibration*, Nonlinear Dyn (2012) 67:147?158.

[17] Schembri, F., Sapuppo, F. and Bucolo, M., 2012, *Experimental classification of nonlinear dynamics in microfluidic bubble's flow*, Nonlinear Dyn (2012) 67:2807?2819

[18] Behnia, S., Mobadersani, F., Yahyavi, M. and Rezavand, A., 2013, *Chaotic behavior of gas bubble in non-Newtonian fluid: a numerical study*, Nonlinear Dyn (2013) 74:559?570.

[19] Grossberg, S., 1988, *Nonlinear Neural Networks: Principles, Mechanicsms, and Architectures*, Neural Networks, Vol 1, 17-61.

[20] Genovese, M., Bauchpiess, A., Brito, J. L. V. de, Doz, G. N., 2001, *Damage Detection Using an Hibrid Formulation Between Changes in Curvature Mode Shapes and Neural Networks*, CILAMCE - 22th. Iberian Latin-American Congress on Computational methods in Engineering, Campinas. XXII CILAMCE, 1-10.

[21] Gori, M., Scarselli, F., 1998, *Are Multilayer Perceptrons Adequate for Pattern Recognition and Verification?*, IEEE Transations on Pattersn Analysis and Machine Intelligence, Vol 20, 11.

[22] Waibel, A., Hanazawa, T., Hinton, G., Shikano, K., Lang, K., 1989, *Phoneme Recognition Using Time-Delay Neural Networks*, IEEE Trans. Acoustics, Speech, and Signal Processing, vol. 37, 3, 328-339.

[23] le Cun, Y., Boser, B., Denker, J., Henderson, D., Howard, R., Hubbard, W., Jackel, L.,1989 *Backpropagation Applied to Handwritten Zip Code Recognition*, Neural Computation, Vol 1, 541-551. Generalization in a two-layer neural network with multiple outputs

[24] Soh, W. K., Karimi, A. A., 1996, *On the calculation of heat transfer in a pulsating bubble*, App. Math. Modell.

[25] Brujan, E. A., 1999, *A first-order model for bubble dynamics in a compressible viscoelastic liquid*, J. Non-Newtonian Fluid Mech., 84, 83-103.

[26] Batchelor G. K., 1967, *An introduction to fluid dynamics*, Cambridge University Press.

[27] Kang, K., Oh, J-H., Kwon. C., Park, Y., 1996, *Generalization in a two-layer neural network with multiple outputs*, Physical Review E, 54/2.

[28] Sanaga, S., Jain, A., 2006, *A comparative analysis of training methods for artificial neural network rainfall?runoff models*, Applied Soft Computing, Vol 6/3, 295-306

[29] Chlouverakis, K. E., Sprott, J. C., 2005, *A comparison of correlation and Lyapunov dimensions*, Physica D, 156-164.

[30] Malvar, S., Gontijo, R. G., Cunha, F. R., 2014 *Vibrational modes on the nonlinear motion of an oscillating bubble in a Newtonian Fluid using Neural Networks*, DINAME - 17th. International Symposium on Dynamic Problems of Mechanics, Natal - RN - Brazil.

[31] Press, W. H., Teukolsky, S. A., Vetterling, layerW. T., Flannery, B. P., 1992, *Numerical recipes in C: The art of scientific computing*, Cambridge: Cambridge Univ. Press, second edition.

[32] Cash, J. R., Karp, A. H., 1990, *A variable order Runge?Kutta method for initial value problems with rapidly varying right-hand sides.*, ACM Trans. Math. Softw. 16, 201-222.

[33] Albernaz, D. L., Cunha, F. R., 2011,*Bubble dynamics in a Maxwell fluid with extensional viscosity*, Mechanics Research Communications, Vol 38/3, 255.

[34] Kazemi, P., Renka, R. J., 2012, *A Levenberg?Marquardt method based on Sobolev gradients*, Nonlinear Analysis: Theory, Methods and Applications, 75/16, 6170-6179.

[35] Siu, S., 1998, *Lyapunov Exponents Toolbox (LET)*

[36] Hinch E.J., 1991, *Pertubation methods*, Cambridge University Press, Cambridge.

[37] Ataei, M., Khaki-Sedigh, A., Lohmann, B., Lucas, C., 2003, *Estimating the Lyapunov exponents of chaotic time series: A model based method*, European Control Conf (ECC), Cambridge, UK.

[38] Pitt, W. G., Husseini, G. A., Staples, B. J., 2004, *Ultrasonic Drug Delivery ? A General Review*, Expert Opin Drug Deliv, 37?56.

Submitted Paper # 2

This paper was produced and submitted during the Masters period. The dynamic behavior of a magnetoheological fluid in the presence of a magnetic field and undergoing an unsteady oscillatory shear is studied. For that, the authors used the same approaches used in this dissertation in order to compute dynamical parameters.

A Microstrucutural Study of a Magnetorheological Fluid from the Perspective of a Nonlinear Dynamical System

R. G. Gontijo, S. Malvar and F. R. Cunha

This paper focus on the dynamic behavior of a magnetorheological fluid undergoing an unsteady oscillatory shear under the presence of an applied magnetic field. The problem is studied from a nonlinear mechanical system perspective using tools such as: analysis in the phase space, frequency response and neural networks for parameters identification. For this purpose several numerical simulations are performed to compute the motion of N magnetic rigid spheres suspendend in a Newtonian carrier liquid. The particles are neutrally buoyant and interact both hydrodynamically and magnetically throughout the process of dynamic simulation. We apply an external magnetic field together with an oscillatory shear. These two deterministics mechanisms compete with which other to align the particles in a preferential direction. The nonlinearities are introduced into the system due to particle-particle interaction. The intensity of the non-deterministic mechanisms is regulated by two physical parameters that appear in the present formulation. The numerical simulations are based on a sophisticated technique of Ewald sums that compute convergent hydrodynamic and magnetic interactions. A numerical research code developed by the authors is used for this purpose. The code is both accurate and computationally efficient. The present work intends to show that several tools, otherwise thought to be mostly applied to the dynamics of nonlinear systems, can be used to explore the physical behavior of wet suspensions in fluid mechanics. Moreover several details of the micromechanics of these complex materials are captured and physically interpreted through the use of the proposed tools.

Magnetorheological fluid, nonlinear dynamics, Ewald sums, hydrodynamic interactions, dipolar matter.

III.5 Introduction

A ferrofluid is defined as a stable colloidal magnetic suspension of nanometric particles immersed in a carrier liquid [1]. The addition of small magnetic particles inside a carrier liquid (usually oil or water based) leads to new possibilities regarding the fluid response due to the application of an external field. In the absence of a magnetic field, a ferrofluid behaves as a Newtonian liquid, but when an external field is applied the fluid magnetizes itself and, as a consequence, several rheological properties are altered [2]. The discover of ferrofluids in the 1960s opened the doors for several interesting applications. At first, ferrofluids were mostly used in applications where the focus was to control its motion due to the application of an external field. As years of research went by we now understand that ferrofluids can be used in a great wide of otherwise unthinkable applications. We can mention for example the use of ferrofluids to increase the efficiency of heat transfer devices [4, 4], magnetic pumping [5] and drag reduction due to the magnetoviscous effect [6]. Just recently [7] have shown that the interaction between magnetic particles and the application of an external field can help to stabilize a fluidized bed.

Another interesting class of magnetic suspensions are the so called Magnetorheological Suspensions (M.R.S), or magnetorheological fluids. This type of fluid is a noncolloidal liquid-solid suspension made through the addition of micro-sized magnetic particles in a Newtonian carrier liquid. The primary difference between a M.R.S and a ferrofluid is the particle sensibility to thermal fluctuations induced by the liquid molecules [2, 8]. In recent years some interesting studies have been done regarding the use of M.R.S in practical applications or simply exploring the physics of this complex material. [9] made an interesting experimental study on the dynamics of droplets of M.R.S impacting on a flat surface under the presence of an applied field, in this study they used M.R.S drops of 2.08 mm containing micro-sized particles. Recent studies have tried to link nonlinear dynamic tools, such as neural networks and fuzzy logic to control the behavior of M.R.S in different applications [10, 11, 12].

One interesting fact about ferrofluids and M.R.S is that they tend to form self-organized patterns depending on the applied field and geometry where those fluids are confined. Since the 1980s we can observe interesting pattern formation in magnetic fluids [13, 14, 15]. For instance [16] used a 3D finite element method to identify hexagonal ferrofluid pattern formation under the presence of an applied field. Other authors have used theoretical approaches in order to understand the theory of pattern formation [17, 18]. A recent experimental study shows the fingering formation of an imiscible ferrofluid drop immersed in water and subjected to a radial magnetic field [19].

Another great research field regarding ferrofluids and M.R.S is the rheology of these complex class of fluids. In order to study the rheological behavior of a complex fluid, we must apply a simple rheological flow and observe how it resists to the attempt of shearing it. The interesting feature of magnetic fluids is that its macroscopic rheological response is intricately related to its microstructural behavior. A great amount of experimental works have been done in recent years in order to understand the rheological re-

sponse of ferrofluids [20, 21, 22, 23]. Another possible way to study the rheology of magnetic fluids is through numerical simulations [24] in a microstrucural scale.

Even though magnetic fluids present several interesting patterns under the presence of an applied field and a rich rheology due to dipolar interactions in the micro or nano scale, these two features have not been explored jointly. This works seeks to perform a numerical study using an oscillatory shear rate as a rheological flow to understand the microstructural dynamics of M.R.S under the presence of an applied field. Dipolar [25, 26] and hydrodynamic [27, 28, 30, 31] interactions between all the particles within the suspension space are also considered. We use nonlinear dynamic system tools to explore the unsteady behavior of the suspension magnetization under different conditions of the problem physical parameters. We intend to show that due to its intrinsic microstructure nonlinearity, mainly under the action of strong magnetic interactions, the output of the fluid system when excited in an harmonic way may be highly nonlinear. Several different features are explored and interpreted from a physical perspective. A neural network is also trained to identify the problem physical parameters based on the FFT response of the excited complex fluid and its energetic dispersion on the phase plane. Several nonlinear dynamical system tools, such as phase space analysis, FFT and neural networks are used in this work to capture the physics of this complex material.

III.6 Formulation of the problem

In this problem, we consider a suspension of N spherical magnetic particles with radius a suspended in a Newtonian liquid with viscosity η and density ρ_f. The density of the particles ρ_p is the same as the liquid density ($\rho_p = \rho_f$) so the suspension is assumed to be neutrally buoyant. An external magnetic field $\boldsymbol{H}$ is suddenly applied in the suspension space. The field is applied in the same direction but with opposite sense to the gravitational acceleration vector $\boldsymbol{g} = g\hat{\boldsymbol{g}}$. The particles are initially distributed in an ordered manner. Their magnetic dipole moments $\boldsymbol{d} = d\hat{\boldsymbol{d}}$ are set to be initially aligned transversely to gravity, so $\hat{\boldsymbol{d}}\cdot\hat{\boldsymbol{g}} = 0$. An unsteady oscillatory shear is applied at the same moment as the magnetic field. The upper boundary of our calculation domain is set to move with velocity $\dot{\gamma} \times h$, where h denotes the separation between the upper and lower boundaries of our domain. The applied shear rate $\dot{\gamma}$ is a function of time, given by $\dot{\gamma}(t) = \dot{\gamma_0}\sin(\omega t)$, where $\dot{\gamma_0}$ is the amplitude of the applied shear, ω denotes its frequency and t is the time. A simple sketch of our problem is shown in figure (15).

The dimensionless expression to compute the velocity of an arbitrary i^{th} particle in the suspension space is based on the linearity of Stokes equations (valid for $Re_p \ll 1$, where Re_p is the particle Reynolds number of the flow induced by the motion of the spheres). This expression is given by

$$\boldsymbol{u}_i = \dot{\gamma_d} z_i \hat{\boldsymbol{e}}_{\boldsymbol{x}} + \boldsymbol{M}^s_{i,i}\cdot\boldsymbol{f}_i + \sum_{j\neq i, j=1}^{N} \boldsymbol{M}^p_{i,j}\cdot\boldsymbol{f}_j, \quad (69)$$

where $\dot{\gamma_d}$ is the dimensionless shear rate, in this case $\dot{\gamma_d} = \dot{\gamma}a/U_s$, being a the particle radius and U_s the Stokes velocity of an isolated particle, z_i denotes the dimensionless height of particle i with respect to the lower boundary of the

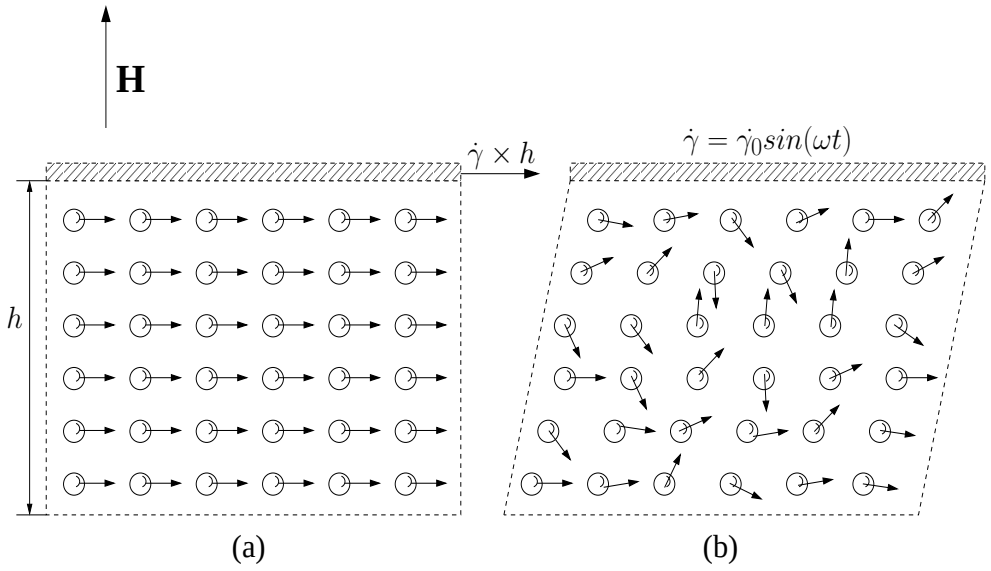

Figure 15: A sketch of our problem. An ordered distribution of monodisperse magnetic particles firstly aligned in the transveral direction to the applied field (a). Application of an oscillatory shear in the suspension space together with an applied field. Particle hydrodynamic and dipole-dipole magnetic interactions are also considered. The interactions between the particles and with the applied magnetic field and shear may lead to a highly nonlinear distribution of the particles dipole moments and positions as represented in figure (b).

calculation domain, $\hat{\boldsymbol{e}}_{\boldsymbol{x}}$ is the direction of the imposed shear (in the $\hat{\boldsymbol{e}}_{\boldsymbol{z}}$ plane), $\boldsymbol{M}^s_{i,i}$ is the self mobility matrix that relates linearly the velocity of one particle with its own force field, $\boldsymbol{f}_i$ and $\boldsymbol{f}_j$ represent the forces acting on particles i and j respectively and $\boldsymbol{M}^p_{i,j}$ is the pair mobility matrix, which conects the disturbances induced on the motion of an arbitrary i particle due to the presence of the neighbouring j particles. The forces acting on an arbitrary i particle are given by

$$\boldsymbol{f}_i = \boldsymbol{f}^r_i + \boldsymbol{f}^c_i + \boldsymbol{f}^m_i, \tag{70}$$

where $\boldsymbol{f}^r_i$ is a repulsive force for near particles given by a variance of the screened Coulomb potential, $\boldsymbol{f}^c_i$ is a contact Hertz force for overlaped particles and $\boldsymbol{f}^m_i$ represents the magnetic forces due to dipole-dipole interaction acting on the particles. More details can be found in [32]. We may also account a force $\boldsymbol{f}^{mf}_i$ for the field-dipole interaction. This force is proportional to $\boldsymbol{f}^{mf}_i \sim \nabla \boldsymbol{H}$, where $\boldsymbol{H}$ is the applied field. In this work we consider that the suspension is confined in an infinitesimal continuum volume, so field gradients are neglegible within this volume. A consequence of this assumption is that the particles will not suffer any magnetic force due to the influence of an external field, but will be subjected to magnetic field torques and will interact magnetically with all the particles of the suspension.

The dimensionless versions of the mobility matrices are given by [33] as a consequence of the application of the [34] summation technique to the [35] mobility tensor:

$$\boldsymbol{M}^s_{i,i} = \left(1 - 6\xi\pi^{-1/2} + \frac{40}{3}\xi^3\pi^{-1/2}\right)\boldsymbol{I}. \tag{71}$$

and

$$\boldsymbol{M}^{ij}(\boldsymbol{r}^{'}) = \sum_{\boldsymbol{x}\in\mathscr{L}} \boldsymbol{M}^{1}(\boldsymbol{r}^{'}+\boldsymbol{x}) + \frac{1}{V}\sum_{\boldsymbol{k}\in\hat{\mathscr{L}},\boldsymbol{k}\neq 0} \boldsymbol{M}^{2}(\boldsymbol{k})\cos(\boldsymbol{k}\cdot\boldsymbol{r}^{'}). \tag{72}$$

where the mobilities $\boldsymbol{M}^1$ and $\boldsymbol{M}^2$ are given by

$$\begin{aligned}\boldsymbol{M}^{1}(\boldsymbol{r}) = \frac{3}{4}\left\{\left(\frac{1}{r}+\frac{2}{3r^3}\right)\operatorname{erf}(\xi r) + \left(\frac{16}{3}\xi^7 r^4 + 4\xi^3 r^2 - \frac{80}{3}\xi^5 r^2 - 6\xi + \frac{56}{3}\xi^3 + \frac{4}{3}\xi r^2\right)\frac{1}{\sqrt{\pi}}\exp(-\xi^2 r^2)\right\}\boldsymbol{I}\\ +\frac{3}{4}\left\{\left(\frac{1}{r}-\frac{2}{r^3}\right)\operatorname{erfc}(\xi r) + \left(-\frac{16}{7}\xi^7 r^4 - 4\xi^3 r^2 + \frac{64}{3}\xi^5 r^2 + 2\xi - \frac{8}{3}\xi^3 - 4\xi - 4\xi\frac{1}{r^2}\right)\frac{1}{\sqrt{\pi}}\exp(\xi^2 r^2)\right\}\hat{\boldsymbol{r}}\hat{\boldsymbol{r}}\end{aligned} \tag{73}$$

$$\boldsymbol{M}^{2}(\boldsymbol{k}) = \left(\boldsymbol{I}-\hat{\boldsymbol{k}}\hat{\boldsymbol{k}}\right)\left(1-\frac{1}{3}k^2\right)\left(1+\frac{1}{4\xi^2}k^2+\frac{1}{8\xi^4}k^4\right)\frac{6\pi}{k^2}\exp\left(\frac{-k^2}{4\xi^2}\right), \tag{74}$$

where r is the distance between two arbitrary particles, $\hat{\boldsymbol{k}} = \boldsymbol{k}/k$ represents the direction of a wave number vector (will be discussed later) and $\xi = \pi^{1/2}V^{-1/3}$ is a parameter set to accelerate the convergence of the sum. It is important to notice that the distance r and the parameter ξ expressed in equations (73 - 74) must be used in their dimensionless versions. The forces $\boldsymbol{f}_i^r, \boldsymbol{f}_i^c, \boldsymbol{f}_i^m$ necessary to calculate each particle velocity as expressed in (69) are given in their dimensionless versions as

$$\boldsymbol{f}_i^r = \Lambda\,|\boldsymbol{u}_i|\,e^{\left(-\frac{\epsilon_{ij}}{\mathscr{Y}}\right)}\hat{\boldsymbol{e}}_r, \quad \boldsymbol{f}_i^c = P_c\epsilon_{ij}^{3/2}\hat{\boldsymbol{e}}_r, \tag{75}$$

where Λ and $\mathscr{Y}$ are calibration constants of the model, $|\boldsymbol{u}_i|$ is the magnitude of particle i velocity, ϵ_{ij} represents the distance between the surfaces of two close particles i and j, $\hat{\boldsymbol{e}}_r$ is the direction of repulsion (opposite to the motion of the spheres), P_c is the contact parameter for overlaped particles, this parameter was considered to be $P_c = 100$ in all simulations performed in this work. The magnetic force is taken as the gradient of the potential energy interaction ψ_{ij} between two magnetic dipoles, given by

$$\psi_{ij} = \sum_{i\neq j}\frac{\varphi_m}{r_{ij}^3}\left[\boldsymbol{d_i}\cdot\boldsymbol{d_j} - 3\left(\boldsymbol{d_i}\cdot\hat{\boldsymbol{r}}_{\boldsymbol{ij}}\right)\left(\boldsymbol{d_j}\cdot\hat{\boldsymbol{r}}_{\boldsymbol{ij}}\right)\right], \tag{76}$$

and

$$\boldsymbol{f_i}^m = \sum_{i\neq j}\frac{\varphi_m}{r_{ij}^4}\left[\left(\boldsymbol{d}_i\cdot\boldsymbol{d}_j\right)\hat{\boldsymbol{r}}_{ij} + \left(\boldsymbol{d}_i\cdot\hat{\boldsymbol{r}}_{ij}\right)\boldsymbol{d}_j + \left(\boldsymbol{d}_j\cdot\hat{\boldsymbol{r}}_{ij}\right)\boldsymbol{d}_i - 5\left(\boldsymbol{d}_i\cdot\hat{\boldsymbol{r}}_{ij}\right)\left(\boldsymbol{d}_j\cdot\hat{\boldsymbol{r}}_{ij}\right)\hat{\boldsymbol{r}}_{ij}\right],$$

here $\varphi_m = \mu_0 m_d^2/8\pi^2\eta a^5 U_s$ measures the intensity of dipole-dipole interactions, μ_0 is the magnetic permeability of free space and m_d is the magnitude of the particle dipole moment. In this context φ_m is the physical parameter that measures the intensity of particle-particle magnetic interactions. In Brownian magnetic dispersions a parameter $\lambda = \mu_0 m_d^2/(4\pi k_B T d^3)$ is generally used, here k_B represents the Boltzmann constant, T is the absolute temperature of the fluid and d is the particle diameter. Since we are working with non-Brownian magnetic suspensions, the influence of the carrier liquid thermal fluctuations will not affect the behavior of the immersed particles, hence the use of φ_m is more appropriate than λ. For the rotational motion of the particles we assume that the particle may be subjected to a small effect of rotational inertia, this effect seems to be important in order to describe the behavior of magnetic suspensions as observed by [36]. The governing equation used to compute the angular velocity of the

magnetic particles is given by

$$St_r \frac{d\boldsymbol{\omega}_i}{dt} = -\boldsymbol{\omega}_i + \boldsymbol{T}^i_m, \tag{77}$$

where $St_r = J_s U_s/(8\pi\mu a^4)$ is the rotational Stokes number of the particles, being J_s the polar inertia moment of the particle. The rotational Stokes number measures the relative importance of a rotational relaxation time scale with respect to a typical time that the fluid molecules take to diffuse angular momentum. In addition, $\boldsymbol{\omega}_i$ is the angular velocity of a particle i and $\boldsymbol{T}^i_m$ represents the magnetic torques to which the particles are subjected. Equation (77) considers that the rotational motion of the particles is governed by inertia, viscous drag and magnetic torques. The magnetic torques are computed by the following expression

$$\begin{aligned}\boldsymbol{T_m}^i = \psi_m \left(\boldsymbol{d}_i \times \hat{\boldsymbol{h}}\right) - \varphi_m \Big\{ \sum_{\boldsymbol{x}\in\mathscr{L}} \Big[(\boldsymbol{d}_i \times \boldsymbol{d}_j)\, \mathscr{B}(r_{ij}) - (\boldsymbol{d}_i \times \hat{\boldsymbol{r}}_{\boldsymbol{ij}})\, (\boldsymbol{d}_j \cdot \hat{\boldsymbol{r}}_{ij})\, \mathscr{C}(r_{ij}) \Big] \\ + \frac{1}{L^3} \sum_{\boldsymbol{k}\in\hat{\mathscr{L}}, \boldsymbol{k}\neq 0} 4\pi \left(\boldsymbol{d}_i \times \hat{k}\right) \left(\boldsymbol{d}_j \cdot \hat{k}\right) \exp\left[-\left(\frac{\pi k}{\xi}\right)^2 \right] \cos\left(2\pi \hat{k} \cdot \hat{\boldsymbol{r}}_{ij}\right) \Big\},\end{aligned}$$

where $\psi_m = \mu_0 m_d H_0/6\pi\eta a^2 U_s$ is a physical parameter that measures the relative importance of the torques exerted by an applied magnetic field with respect to the viscous torques that the particles are subjected. The functions $\mathscr{B}(r_{ij})$ and $\mathscr{C}(r_{ij})$ that appear in expression (78) are given by

$$\mathscr{B}(r_{ij}) = \left[erfc\,(\xi r_{ij}) + \left(\frac{2\xi r_{ij}}{\sqrt{\pi}}\right) e^{\left(-\xi^2 r_{ij}^2\right)} \right] r_{ij}^{-3}. \tag{78}$$

and

$$\mathscr{C}(r_{ij}) = \left(\frac{2\xi r_{ij}}{r_{ij}^4 \sqrt{\pi}}\right) \left(3 + 2\xi^2 r_{ij}^2\right) e^{\left(-\xi^2 r_{ij}^2\right)} + \frac{3erfc\,(\xi r_{ij})}{r_{ij}^4}, \tag{79}$$

where $erfc$ is the complementary error function, defined as

$$erfc(x) = 1 - \frac{2}{\sqrt{\pi}} \int_0^x e^{-t^2} dt. \tag{80}$$

Note that the summation used to compute magnetic torques is taken in the analogous manner as the one used to compute hydrodynamic interactions. In both we must build a periodic structure to compute thoses sums in the physical and reciprocal spaces. This is a consequence of the use of the [34] summation technique. This procedure is necessary to accurately compute long range interactions in particulate systems with slow decays. Due to the fast nature decay of magnetic forces ($1/r^4$) we can compute them in a non periodic and consequently cheaper way.

III.7 Numerical methodology

We have developed a non commercial research code written in Fortran for Linux Platforms. This code calculates the translational and rotational velocities of a set of N magnetic particles suspended in a viscous Newtonian fluid. In order to calculate these velocities the code is structured in several sequential steps. First we must create a periodic structure with several boxes, called lattices. These lattices are spreaded through the physical and reciprocal spaces. Figure (16a) illustrates a 2D

view of a set of 125 lattices distributed through space. Note that in this view only 25 of those 125 lattices are seen, since the other lattices are distributed through the other plane. The central lattice is the real lattice where the particles are properly located. All the surrounding lattices are simply an imaginay representation of the behavior presented by the particles in the real lattice. The construction of these imaginary lattices is a requirement of the [34] summation technique and aims the emulation of an infinite suspension to accelerate the convergence rate of long range sums that compute hydrodynamic and magnetic torque interactions.

The procedure of creating the imaginary lattices is done in two parts, one for the real space lattices and other for the reciprocal space lattices. For the real space lattices the vector $\boldsymbol{x}^R$ is added to the position of each particle in the central cell, this vector is defined as

$$\boldsymbol{x}^R = \sum_{i=1}^{3} \gamma_i l_i \hat{e}_i, \qquad \gamma_i \in \mathbb{Z} \tag{81}$$

here $\gamma_1, \gamma_2, \gamma_3$ are integers that in the present simulations vary from $[-2, +2]$ and l_1, l_2, l_3 are the lengths of each edge of the central cell. The vectors denoted by $\gamma_i \hat{e}_i$ are called lattice vectors. These possible combinations lead to a total of $5^3 = 125$ lattices. Note that when $\gamma_1 = \gamma_2 = \gamma_3 = 0$ we are exactly on the central cell. Each combination of values for the γ_i coefficients denotes a different lattice. For the reciprocal space sum we must add to the position of each particle the vector $\boldsymbol{x}^k$ defined as

$$\boldsymbol{x}^k = \sum_{i=1}^{3} \frac{2\pi\beta_i}{l_i} \hat{e}_i, \qquad \beta_i \in \mathbb{Z} \tag{82}$$

where $\beta_1, \beta_2, \beta_3$ are integers varying in the range of [-2,+2]. This procedure is responsible for creating the reciprocal lattices for several possible wavelengths.

After generating the initial condition in the real and imaginary lattices a table with ten thousand values of the scalar functions required to compute $\boldsymbol{M}^1(\boldsymbol{r})$, $\boldsymbol{M}^2(\boldsymbol{k})$, $\mathscr{B}(r_{ij})$ and $\mathscr{C}(r_{ij})$ is built. Since these functions depend on the distance between two arbitrary particles and on different wave numbers, they may be previously calculated and storaged in several tables. These tables consider all the possible range of distances and wavenumbers used through the simulation, based on the number of particles and the suspension volume fraction $\phi = Nv_p/V$, where v_p is the volume of a particle and V is the suspension volume. When a value needs to be calculated it is taken from the table by interpolating the output of these functions using the closests numbers storaged. This idea was proposed in the works of [30, 37] and aims to decrease the simulation computational cost. Since we run dynamic simulations, the calculation of expensive mathematical functions in several loops through the time evolution scheme may substantially increase the computational cost.

After creating the periodic structure illustrated in figure (16a) and mouting the tables with the numerical values of the required scalar functions, the simulation process begins. The first step is to calculate the velocity of each particle through equation (69). Two important remarks must be made. Each particle in the real lattice interacts with all the other particles, but the particles in the imaginary lattices only interact with the ones in the real lattice. When the shear is applied all the lattices must be sheared with the imposed shear rate, as illustrated in figure (16b). After calculating the particles ve-

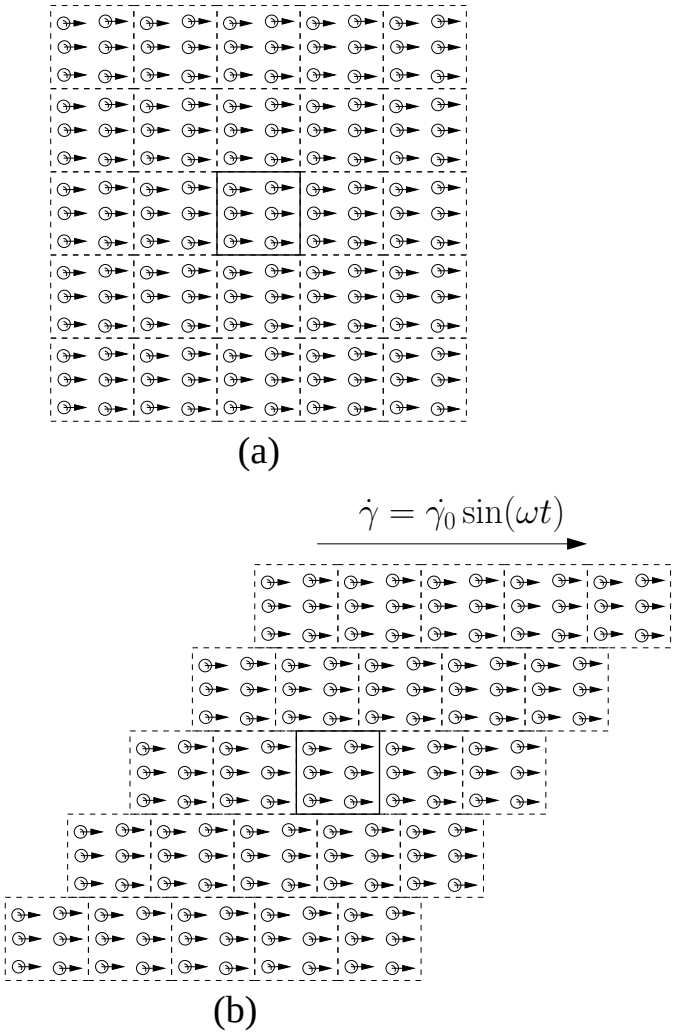

Figure 16: Generation of an initial ordered condition (a) in several lattices and its consequence deformation due to the imposed shear (b).

locities, their angular velocities are calculated through equation (77). The next step is the calculation of the particles new positions and dipole moments. In this work, we consider that the dipole moments of the particles are fixed and turn with them. The simulation evolves in time by recalculating the linear and angular velocities of the particles in subsequent moments. In each time step the suspension configuration is updated by their new positions and dipole moments distribution. Figure (17) shows the initial configuration for the simulations done in this work.

In this work all simulations have the same initial configuration with $6 \times 6 \times 6 = 216$ particles in the central cell distributed in an orderly way. The particles dipole moments are initially set to be aligned transversely to gravity. The separation between the particles on the X, Y, Z axes is the same and vary as a function of the volume fraction of particles ϕ.

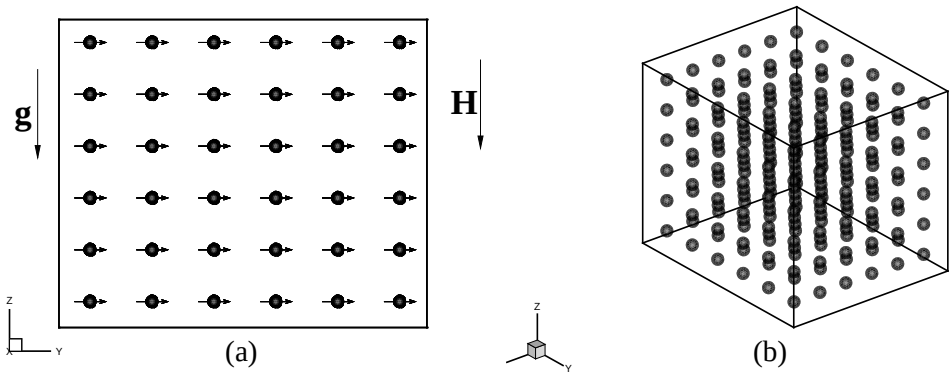

Figure 17: These figures show the initial condition used in all the simulations of this work. In figure (a) a side view of the initial configuration is shown, while in figure (b) we have a three dimentional view.

III.8 Code validation

Before proceding to the *results and discussions* section it would be instructive to show an example of the capabilities of our code in order to predict magnetic suspensions transport properties. This sections intends to show an example of code validation. More details about it can be found on [2, 32]. Figure (18) shows two plots. In (18a) the mean sedimentation velocity of an ordered suspension of nonmagnetic spheres with hydrodynamic interactions is shown. Figure (18b) shows the behavior of the equilibrium magnetization of a ferrofluid as a function of the volume fraction of particles.

In figure (18) we define $U = \overline{U}/U_s$, where U_s is the Stokes velocity of an isolated particle and

$$\overline{U} = \frac{1}{N}\sum_{i=1}^{N} U_i, \tag{83}$$

represents the mean sedimentation velocity of the suspension, U_i is the sedimentation velocity of an aribitrary i particle, moreover M^* is the dimensionless suspension magnetization, here

$$M^* = \frac{M_0}{M_d}, \tag{84}$$

where M_0 is the equilibrium, or steady state, magnetization and M_d denotes the magnetization of the particles.

Figure (18) shows a very good agreement between our numerical outputs and the theoretical approaches used for code validation purposes. For the case of nonmagnetic spheres a perfect agreement between the numerically predicted sedimentation velocity and the theoretical solutions of [38, 39] is observed. For the magnetization it is observed that for values of $\phi < 12\%$ the numerical and asymptotic solutions present a perfect match. When the volume fraction of particles increases above 12% the numerical solution overestimates the $\mathcal{O}(\phi^3)$ asymptotic solution proposed by [40]. The explanation for this divergence lies on the fact that the asymptotic solution only considers magnetic interactions for up to three particles. For diluted suspensions the physics is indeed dominated by interactions of two or three particles. However, for denser ferrofluid the probability of finding small clusters with more than three close particles increases. In this sense the numerical solution is more reliable for predicting the magnetization of dense

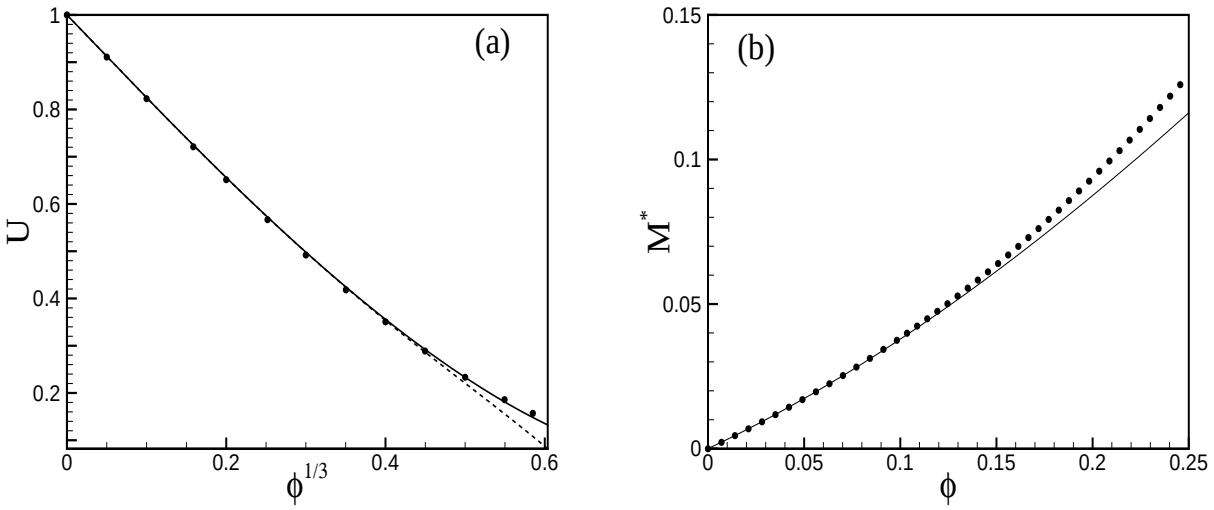

Figure 18: Figure (a) illustrates the behavior of the suspension mean sedimentation velocity as a function of $\phi^{1/3}$ for an ordered distribution of hydrodynamically interacting spheres. The continous line represents the [38] theoretical solution, the dashed line denotes the asymptotic expression of [39] and the filled black circles represent numerical values obtained with the present code. In figure (b) we show the behavior of the equilibrium magnetization as a function of ϕ. The continous line represents the $\mathscr{O}(\phi^3)$ solution of [40] while the black circles denote the numerical solution obtained with the present code.

ferrofluids since it considers all particle-particle magnetic and hydrodynamic interactions [32].

III.9 Results and discussions

First a non-interacting suspension ($\varphi_m = 0$ and no hydrodynamic interactions) under the presence of an applied magnetic field ($\psi_m = 1$) and an oscillatory shear with $\omega = 1$ for $\phi = 5\%$ is considered. For all the simulations in this work the dimensionless applied shear rate intensity is set to be $\dot{\gamma_0} = 1$. For the picture shown in figure (19) there are two deterministic mechanisms competing for ruling the microstructural dynamics: the external magnetic field and the imposed shear.

It is possible to observe at figure (19a) that a non interacting suspension responds with an harmonic signal to the imposition of a sinuisodal oscillatory shear. Nevertheless it is interesting to notice at figure (19b) that the initial transient, induced by the attempt of the applied field to align the particles in its direction, produces a rapid variation of the suspension magnetization. For the combined physical parameters we observe that the suspension magnetization goes from zero to its saturation value in less than 1 t_s, being t_s the Stokes time (the time in which a particle with radius a takes to sediment its own radius with velocity U_s). This initial transient is clearly observed in the phase space diagram shown in figure (19c), labeled as letter A. One interesting feature seen in figure (19c) is a moderate distortion on the phase space at the end of the initial transient, labeled as letter C. This distortion may be atributed by the interac-

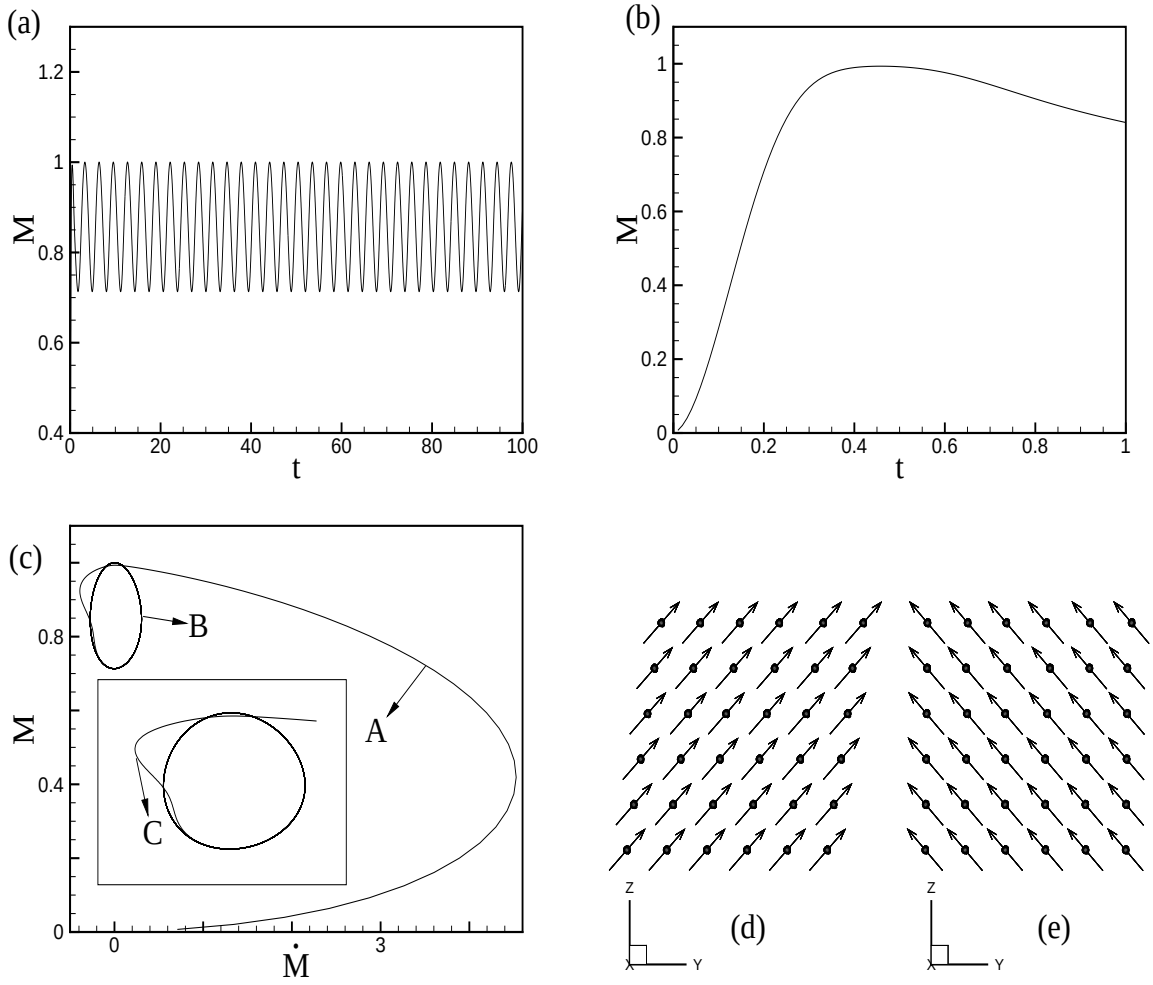

Figure 19: Figure (a) shows the unsteady response of the suspension magnetization as a function of time after the initial transient (b). Figure (c) illustrates the phase diagram of the signal shown in (a) and (b). In (d) we have the suspension microstructure after 8 t_s while in (e) we show the microstrucutre for 11 t_s. Here t_s is the Stokes time, defined as $t_s = a/U_s$.

tion between the applied field and the imposed shear. We may speculate from figures (19b) and (19c) that for the time interval defined as $0.3 < t_s < 0.8$ the shear is out of phase with respect to the applied field. While the field is still trying to align the particles in its direction, the shear is attempting to dishevel them. When the suspension magnetization finally reaches its saturation value at $t_s = 0.45$ the particles oscillate around an axis parallel to the direction of the applied field. This harmonic oscillation produces a perfect limit cycle with one energetic level shown in figure (19c) and labeled as letter B.

In figure (20) an interacting suspension ($\varphi_m = 0.4$ with magnetic and hydrodynamic interactions) under the presence of an applied magnetic field ($\psi_m = 1$) and an oscillatory shear with $\omega = 1$ for $\phi = 1\%$ is simulated.

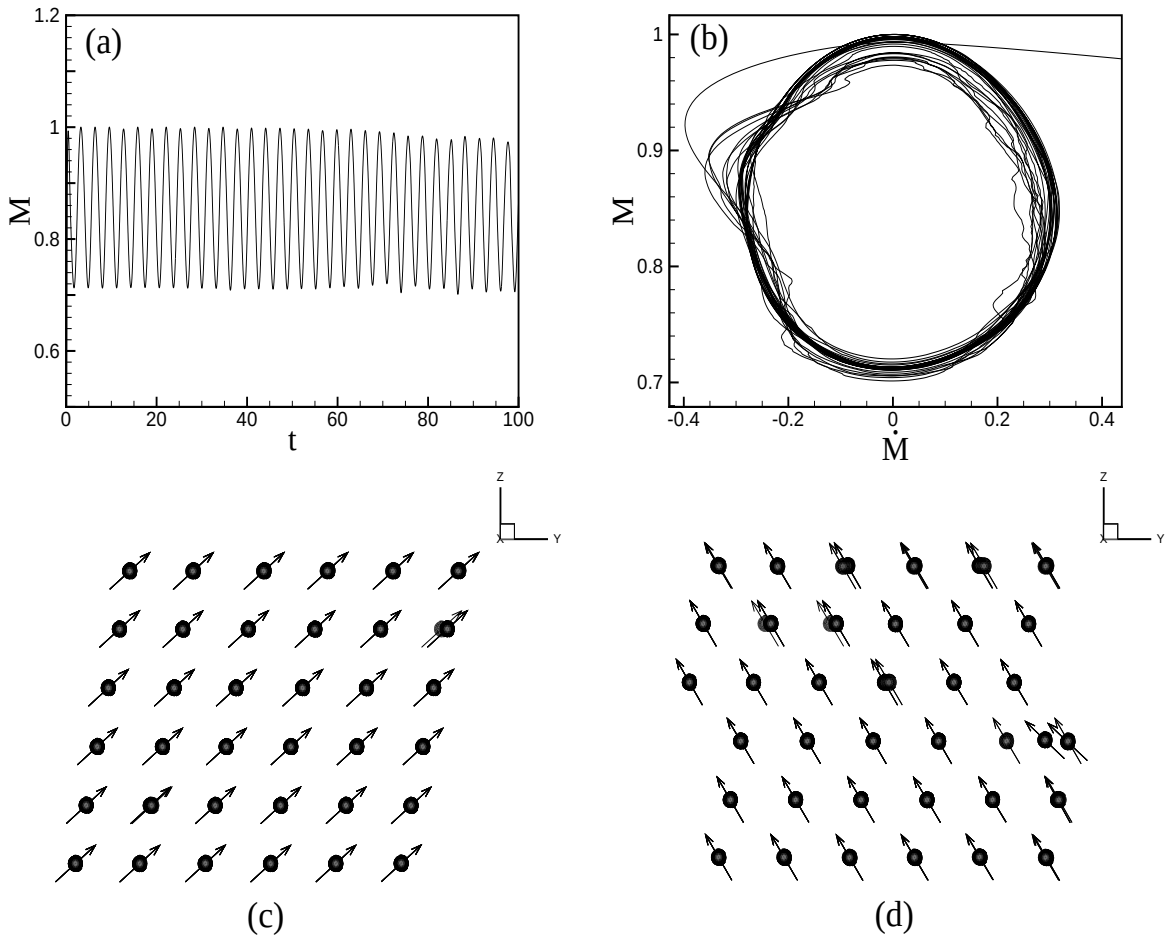

Figure 20: Figure (a) shows the unsteady response of the suspension magnetization as a function of time after the initial transient. Figure (b) illustrates the phase diagram of the signal shown in (a). In (c) we have the suspension microstructure after 8 t_s while in (d) we show the microstrucutre for 12 t_s. Here t_s is the Stokes time, defined as $t_s = a/U_s$.

For the picture shown in figure (20) besides the two deterministic mechanisms competing for ruling the microstructural dynamics (external magnetic field and the imposed shear) a moderate influence of particle-particle hydrodynamic and magnetic interactions is also present. These interactions lead to a systematic energy loss on the suspension space as it may be noticed on the phase diagram shown in (20b). When the time response signal is observed, in figure (20a), it is not clear the overall effect of particle interaction on the suspension unsteady magnetization, however the energy loss associated with particle interaction is evident on the phase space. We may interpret that while the applied field and the imposed shear compete with each other by exchanging energy with the particles, this energy is dissipated through two mechanisms: dipole-dipole and hydrodynamic interactions. Instead of observing perfect aligned particles in preferential directions we now see that some of the particles are misaligned with respect to axis z (parallel to the direction of the applied field). This phenomenon is noticed in figures (20c) and

(20d). Although some nonlinearities are introduced into the system due to particle interaction, for a very dilute suspension ($\phi = 1\%, \varphi_m = 0.4$) the response is similar to a damped mass-spring system. We may then ask what would happen to a magnetic suspension under these conditions, undergoing strong magnetic interaction effects. It would be interesting to analyze if the system could present a chaotic behavior for more concentrated suspensions.

In order to see whether the system may present a chaotic behavior, a simulation was perfomed for the following parameters: $\psi_m = 1$, $\omega = 1$ for $\phi = 1\%$ and $\varphi_m = 1$. The results are presented in figure (21).

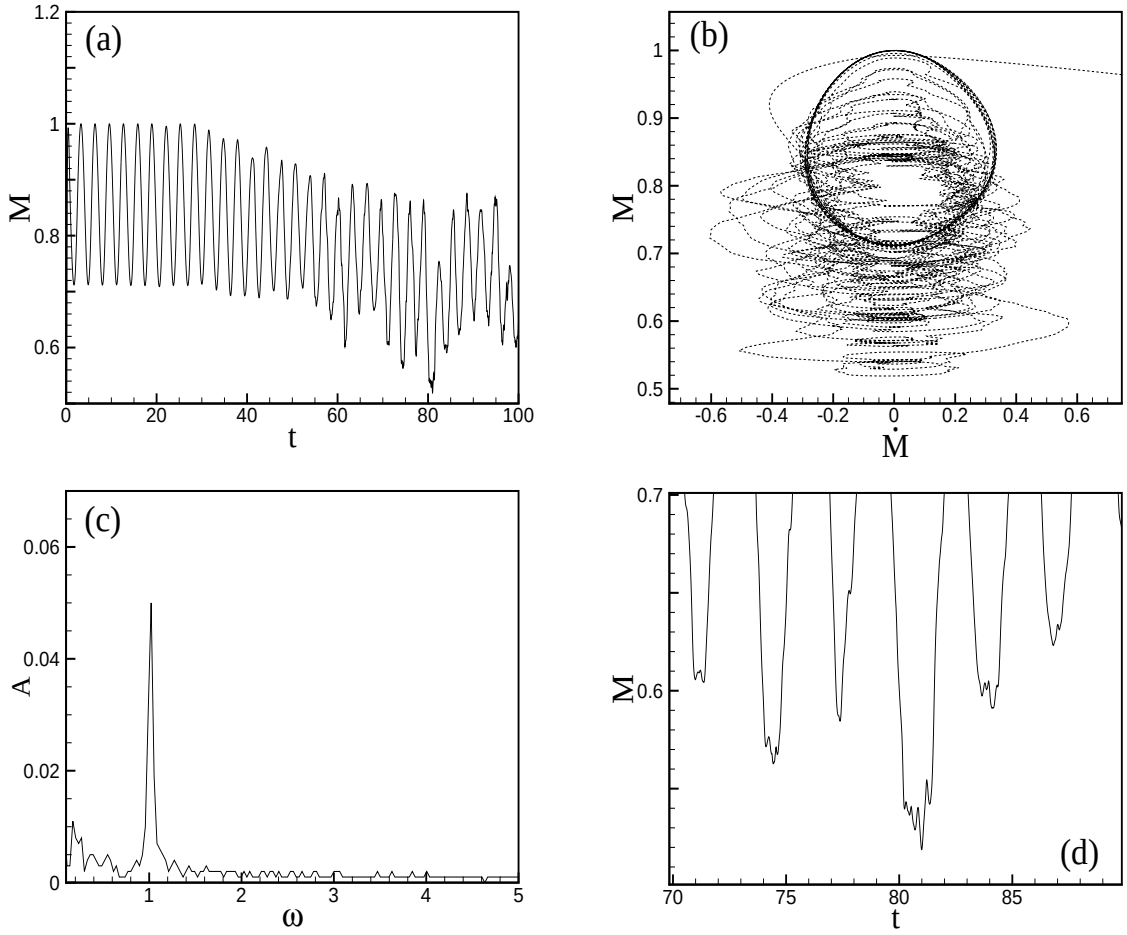

Figure 21: Figure (a) shows the unsteady response of the suspension magnetization as a function of time after the initial transient. Figure (b) illustrates the phase diagram of the signal shown in (a). In figure (c) we illustrate the FFT of the signal (a). In (d) we show a detail of rapid magnetization fluctuations. These rapid fluctuations are responsible for inducing several higher frenquencies and low energy peaks in the frequency spectrum.

It is possible to see that the time response signal presents a damping effect, but also some energy spreading in other frequencies. Observing the phase diagram it is possible to notice

the mentioned *energy loss* due to the damping caused by particle interaction, but also an energy spreading in different possible states. A complementary information regarding the system frequency response is the FFT of the signal shown in (21a), this result is presented in figure (21c). It is possible to observe that most of the energy is concentrated in the excitation frequency ($\omega = 1$). It is also observed for higher frequencies several low energy peaks. When the size of the signal shown in (21a) is enlarged for a time interval that goes from $70 < t_s < 90$ we observe several rapid magnetization fluctuations induced by particle interactions. We may then speculate that part of the energy imposed by the shear in the attempt of misaligning the particles from their preferential orientation (i.e. the magnetic field direction) is lost due to dipole-dipole magnetic interactions. Particle-particle interaction ends up spending part of this energy inducing the observed low energy and high frequency magnetization fluctuations. It is interesting to notice that the system takes a very long time to present this nonlinear behavior induced by dipole-dipole and hydrodynamic interactions. This seems to be a typical chaotic behavior in the sense of sudden bifurcations in the oscillatory motion of the particles dipoles. After 30 t_s a systematic energy decay is seen in figure (21a). This time interval is 30 times longer than a typical time scale associated with the excitation frequency. This behavior indicates that the microstructure is slowly altered by the imposed shear and dipole-dipole particle interaction. At first small microstructure alterations are present. These alterations evolve through time and induce an increasing nonlinear feature on the system. Once the system starts its trajectory to a more nonlinear behavior it presents a constantly increase in this tendency.

It is important to notice that all the analysis done so far are focused more on dipole-dipole interaction rather than on hydrodynamic interactions. Since we have considered a very dilute suspension ($\phi = 1\%$) and varied the intensity of magnetic interactions, we focused on the influence of magnetic interactions. In order to avail how these dipole-dipole interactions steal part of the energy concentrated on the excitation frequency we show figure (22). In this picture we still consider a very dilute suspension ($\phi = 1\%$), but intend to explore the effect of more intense magnetic interactions ($\varphi_m > 1$) on the frequency response. A substantial reduction on the amplitude of the excitation frequency is noticed for this case. This reduction is around 45% and is followed by an increase in the amplitude of other frequencies, especially in lower frequencies. In both cases we have a deterministic frequency peak at zero related to the constant applied field. Since the focus of this work is the nonlinear dynamics induced by many-body interactions it is not worthy to discuss further details about this deterministic peak.

We have mentioned that the system presents a long time memory even in the presence of considerable magnetic interactions. This so called memory is related to the time it takes to leave its harmonic behavior and start to present a nonlinear feature due to magnetic interactions. In order to measure this correlation time we define the normalized self correlation function of particle velocity fluctuations $R(t)$. This function in a more general case is a second rank tensor $\mathscr{R}(t)$ defined as

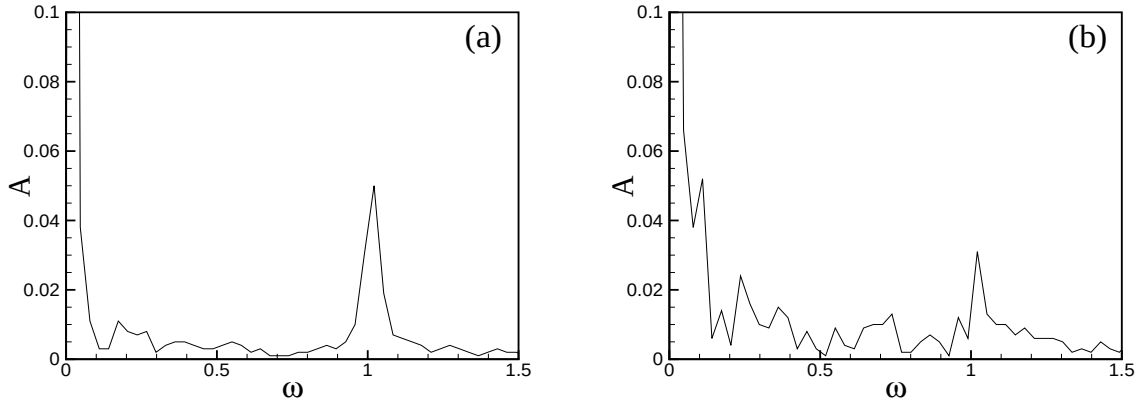

Figure 22: Figure (a) shows the FFT response for $\varphi_m = 1$ and figure (b) for $\varphi_m = 4$.

$$\mathscr{R}(t) = \frac{\langle \boldsymbol{u'}(\tau)\boldsymbol{u'}(t+\tau)\rangle}{\langle \boldsymbol{u'}(\tau)\boldsymbol{u'}(\tau)\rangle} = \begin{pmatrix} \frac{\langle u'_x(\tau)u'_x(t+\tau)\rangle}{\langle {u'_x}^2(\tau)\rangle} & \frac{\langle u'_x(\tau)u'_y(t+\tau)\rangle}{\langle u'_x(\tau)u'_y(\tau)\rangle} & \frac{\langle u'_x(\tau)u'_z(t+\tau)\rangle}{\langle u'_x(\tau)u'_z(\tau)\rangle} \\ \frac{\langle u'_y(\tau)u'_x(t+\tau)\rangle}{\langle u'_y(\tau)u'_x(\tau)\rangle} & \frac{\langle u'_y(\tau)u'_y(t+\tau)\rangle}{\langle {u'_y}^2(\tau)\rangle} & \frac{\langle u'_y(\tau)u'_z(t+\tau)\rangle}{\langle u'_y(\tau)u'_z(\tau)\rangle} \\ \frac{\langle u'_z(\tau)u'_x(t+\tau)\rangle}{\langle u'_z(\tau)u'_x(\tau)\rangle} & \frac{\langle u'_z(\tau)u'_y(t+\tau)\rangle}{\langle u'_z(\tau)u'_y(\tau)\rangle} & \frac{\langle u'_z(\tau)u'_z(t+\tau)\rangle}{\langle {u'_z}^2(\tau)\rangle} \end{pmatrix}, \tag{85}$$

here τ denotes a time interval that for statistical purposes goes from $0 \leq \tau \leq t$, $< \ >$ denotes an ensemble average. In this context, since we define the same intitial configuration for all of our simulations and have no random fluctuations induced by Brownian motion, our average is taken over one realization, $\boldsymbol{u'}(t)$ is the system velocity fluctuation for a given time instant t, defined as

$$\boldsymbol{u'}(t) = \frac{1}{N_{rea}} \frac{1}{N} \sum_{j=1}^{N_{rea}} \sum_{i=1}^{N} \left(\boldsymbol{u}_i^j - \boldsymbol{U}_j \right), \tag{86}$$

where N_{rea} represents the number of different numerical experiments (realizations), N is the number of particles in each realization, $\boldsymbol{u}_i^j$ is the velocity of an arbitrary particle i in a realization j and $\boldsymbol{U}_j$ is the suspension average velocity for a given j realization in a given time t, defined as

$$\boldsymbol{U}_j = \frac{1}{N} \sum_{i=1}^{N} \boldsymbol{u}_i^j. \tag{87}$$

Note that the second rank tensor $\mathscr{R}(t)$ is related to particle velocity fluctuations in the particle scale. We can use this tensor to measure a particle pressure or a particle viscosity in the context of magnetorheological suspensions. These macroscopic properties are related to an equivalent Reynolds stress in the same way that the fluid pressure and viscosity are related to velocity fluctuations in the molecular scale and the turbulent viscosity is defined based on the flow velocity fluctuations in a microscopic, but not molecular scale. In this work we are interested in computing the correlation time of the magnetization signal extracted from numerical simulations. By taking only the component of the tensor $\mathscr{R}(t)$ in the direction of the shear, here called $R_{||}(t)$, we plot figure (23).

We notice that for a non interacting suspension the time response signal of $R_{||}(t)$ oscillates in the interval $[-1, 1]$ through time. This oscillation indicates that the signal never decor-

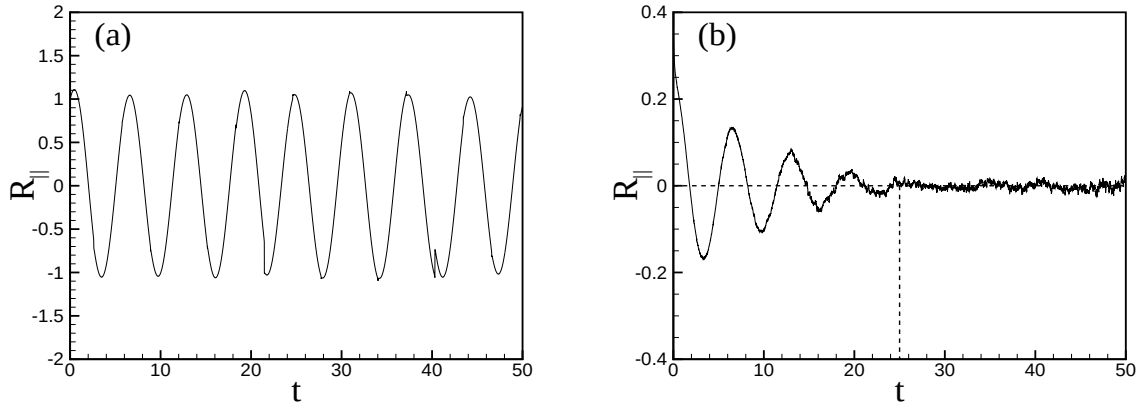

Figure 23: Figure (a) shows the normalized self correlation function of particle velocity fluctuations in the direction of the shear for $\varphi_m = 0$ while figure (b) considers $\varphi_m = 4$.

relates and reaches a stable value around zero after a certain time (correlation time). In figure (b) we observe that velocity fluctuations induced by dipole-dipole interactions are responsible for taking the deterministic influence of the imposed field and oscillatory shear. Therefore conducting the system to a nonlinear regime that is no longer correlated to its initial behavior. After 25 t_s we may say that for this combination of physical parameters the unsteady behavior of the magnetorheological suspension is no longer related to its initial configuration.

From the analysis done so far it is possible to highlight that any attempt of providing a systematic parameter recognition study using for example neural networks will demand the understand of the best variables for this purpose. We have explored the influence of dipole-dipole interactions on the overall behavior of the suspension for very dilute magnetorheological suspensions. In order to understand how hydrodynamic interactions may alter the suspension microstructure and consequently its overal behavior we must vary the volume fraction of particles ϕ.

Figure (24) shows the phase space plot for different values of ϕ accounting for just a small contribution of magnetic effects with $\varphi_m = 0.1$. It is possible to observe that the overall behavior of the suspension unsteady magnetization response for $\varphi_m \ll 1$ is a clear tendency of a damped oscillator. When we increase the intensity of hydrodynamic interactions the energy imposed by the deterministic oscillatory shear is spreaded due to other mechanisms such as particle interactions. By consequence the suspension response is a decrease in its magnetization with time.

Even though we have observed an alteration in the suspension oscillatory motion due to the presence of hydrodynamic interactions, we have noted that dipole-dipole interactions overcomes any hydrodynamic interaction effects with respect to the system overall nonlinearity. Figure (25) shows the magnetization time response for several values of ϕ but considering $\varphi_m = 1$. We observe a clear damping tendency, as we have seen for $\varphi_m \ll 1$, but in this case when $\varphi_m \sim 1$ we also observe that this damping effect is more intense with ϕ. We can also see that when the mangetic interaction parameter is higher the system reponds with several rapid magnetization

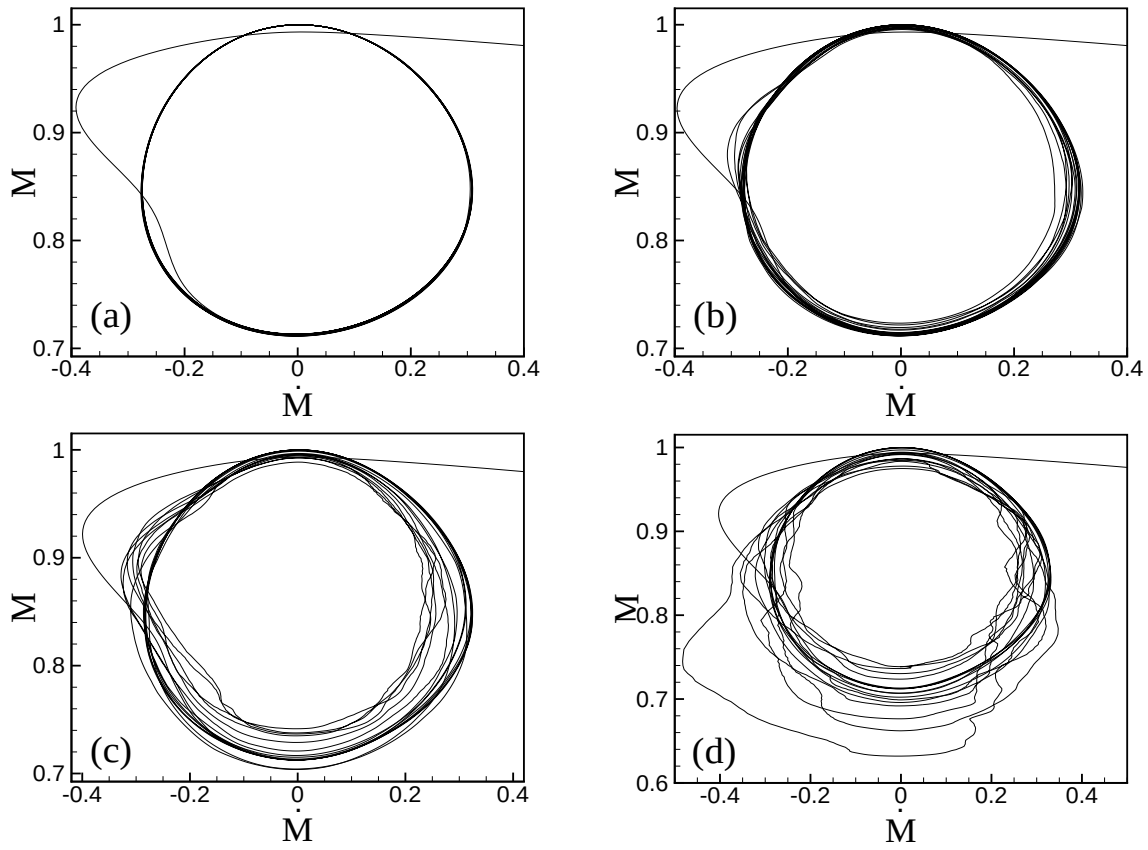

Figure 24: Phase space plot for $\varphi_m = 0.1$ and: (a) $\phi = 1\%$, (b) $\phi = 4\%$, (c) $\phi = 7\%$ and (d) $\phi = 10\%$.

fluctuations leading to a hihgly nonlinear signal. This information is confirmed in figure (26) that shows the phase space plots for the same cases.

In figure (26), we see that the nonlinearities introduced into the system by dipole-dipole interactions lead the system to several other possible energetic states. In this sense we observe a considerable energy spreding in the phase plot. It is worthy to notice that a rectangular region with area ζ is marked in figure (26). This parameter ζ may be defined as $\zeta = |M_{max} - M_{min}| \times |\dot{M}_{max} - \dot{M}_{min}|$. Here M_{max} and M_{min} represent the maximum and minimum value of the suspension magnetization after the initial transient and $\dot{M}_{max}$ and $\dot{M}_{min}$ denote the maximum and minimum value of the magnetization derivative also after the initial transient period. The definition of the area ζ is an attempt to measure the intensity of this energetic spreding associated with the identified rapid fluctuations in the time response signal due to particle interactions. When the frequency spectrum of the cases explored in figures (25) and (26) is analyzed it is observed a systematic decay on the amplitude of the first harmonic (associated with the oscillatory shear). This result is shown in figure (27).

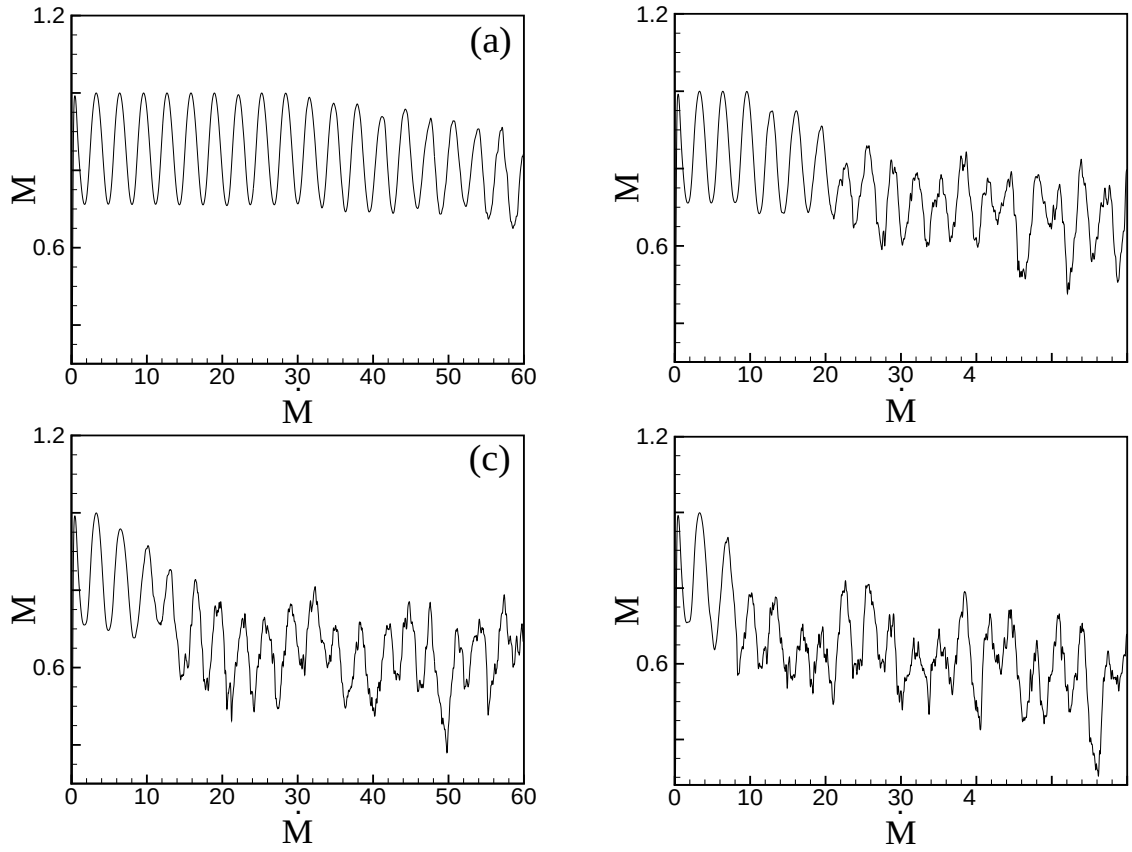

Figure 25: Time response plot for $\varphi_m = 1$ and: (a) $\phi = 1\%$, (b) $\phi = 2\%$, (c) $\phi = 3\%$ and (d) $\phi = 4\%$.

The combination of figures (25), (26) and (27) leads us to the following physical interpretation of the suspension behavior. First the particles are aligned within a 90 degree angle with respect to the applied field at $t_s = 0$. At this moment the shear and the external field are applied and the particles that start to rotate in the direction of the applied field due to a magnetic torque $\boldsymbol{T_m} = \mu_0 \boldsymbol{d} \times \boldsymbol{H}$, here μ_0 is the magnetic permeability of the free space. Since $\boldsymbol{d} \perp \boldsymbol{H}$ this magnetic torque is maximum in the beginning of the simulation. The consequence is a fast alignment in the direction of the field. At the same time we have the undergoing oscillatory shear trying to misalign the particles and rotate them in the same direction of the fluid vorticity induced by the shear. In order to explain the competition between the applied magnetic field and the imposed shear we may define a magnetic time scale t_m and a typical flow scale t_f based on the frequency of the oscillatory shear.

These time scales can be defined as

$$t_m = \left(\frac{\rho_s d_m}{\mu_0 H_0^2}\right)^{1/2} \qquad \text{and} \qquad t_f = \frac{1}{\omega}, \tag{88}$$

where ρ_s is the density of the magnetic particles, d_m is the particle magnetic diameter (excluding the surfactant thickness), H_0 is a typical intensity of the applied field and ω is the shear frequency. If we divide t_m by t_f we have

$$\mathscr{F} = \frac{t_m}{t_f} = \frac{\omega \mathscr{A}}{H_0}, \qquad \text{with} \qquad \mathscr{A} = \sqrt{\frac{\rho_s d_m}{\mu_0}} \tag{89}$$

where $\mathscr{F}$ is a normalized magnetic time scale

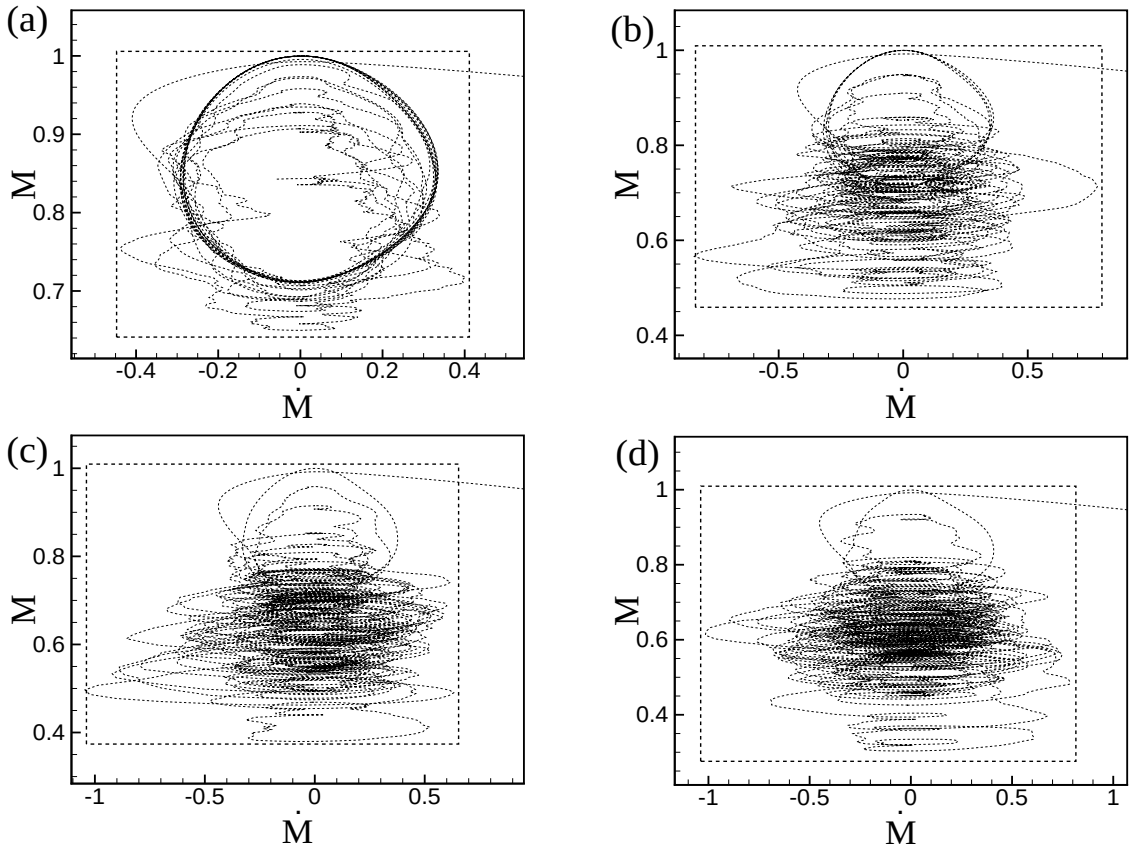

Figure 26: Phase space plot for $\varphi_m = 1$ and: (a) $\phi = 1\%$, (b) $\phi = 2\%$, (c) $\phi = 3\%$ and (d) $\phi = 4\%$.

(equivalent to magnetic Strouhal number). If we perform a numerical simulation for $\mathscr{F} \neq 1$ the tendency of particle aligment due to the applied field will be out of phase with the attempt of the undergoing shear of misaligning these particles. After an initial operational transient the particles will tend to oscillate around an axis $z \parallel \boldsymbol{H}$ and this behavior will be harmonic for $\varphi_m \ll 1$ or $\phi \ll 1$. After some scale analysis, we can also express the normalized magnetic time scale $\mathscr{F}$ as a combination of other parameters. These parameters are the normalized frequency of the flow St (equivalent to a hydrodynamic Strouhal number), the magnetic parameters φ_m and ψ_m and the particle Reynolds number Re_p as

$$\mathscr{F} = \frac{St}{\psi_m} \times \sqrt{\varphi_m \times Re_p}, \tag{90}$$

here $St = \omega a/U_s$ and $Re_p = \rho_s U_s a/\eta$. Note that in this work we assume $Re_p \ll 1$ and consider the Creeping flow regime, but the term $\sqrt{\varphi_m \times Re_p}$ is not necessary $\ll 1$. Since the square root increases the magnitude of its attribute when the combination $\varphi_\times Re_p < 1$. The important conclusion of this scale analysis is that the relation between the two deterministic time scales of the problem (t_m and t_f) is associated with the physical parameters of the problem. For example, if the intensity of the applied field is increased ($\psi_m \uparrow$) maintaining all the other parameters constant, we observe a decrease in the magnetic time scale. This decrease indicates that the particles will respond to the action of the field in a shorter time. The same thought may be applied to understand how the applied shear rate changes the nonlinear response of the suspension. When $\omega \ll 1$, by equa-

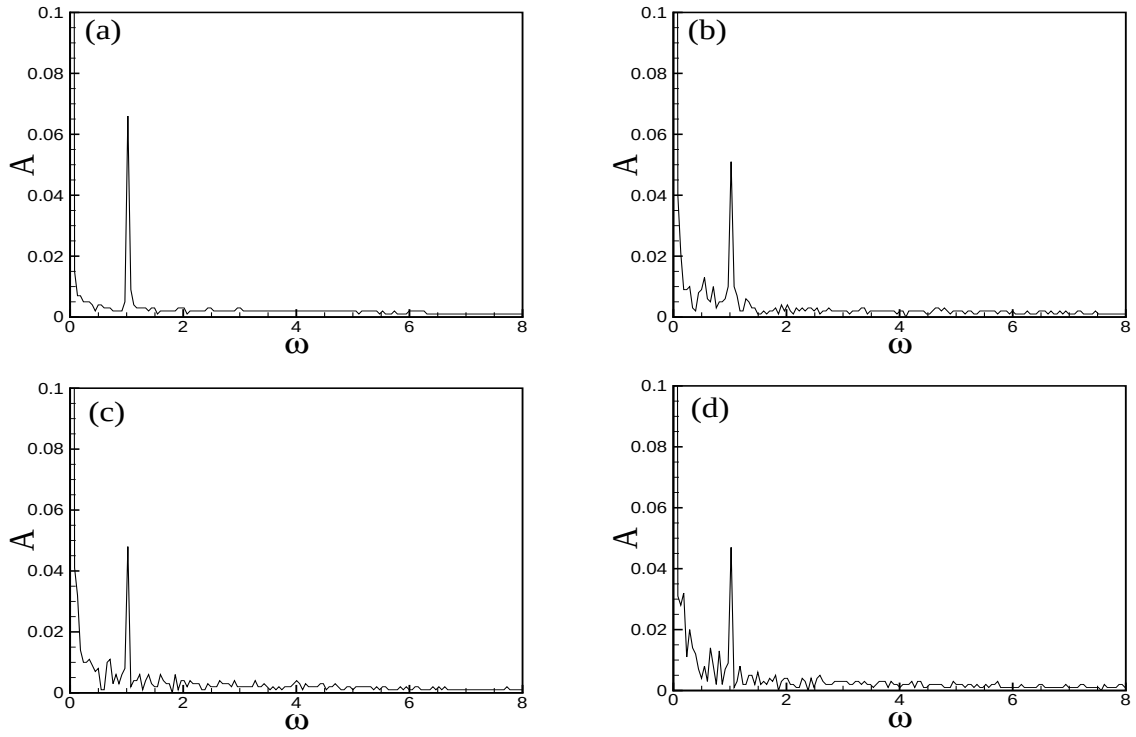

Figure 27: Frequency response for $\varphi_m = 1$ and: (a) $\phi = 1\%$, (b) $\phi = 2\%$, (c) $\phi = 3\%$ and (d) $\phi = 4\%$.

tion (89) we have $t_f \ll 1$. In this asymptotic limit $t_f \ll t_m$ and so the particles take a very long time to perceive any magnetic effect. In this situation they are moved simply by the undergoing shear. As we have presented in this work, the most interesting behavior is obtained when both scales are of the same order and so we have a coupled problem where both mechanisms are able to interact and produce a rich suspension response.

This discussion is valid for the deterministic mechanisms of applied field and shear. However if we increase the intensity of particle interaction effects the tendency is that the energy injected into the system by the deterministic mechanisms of applied field and external shear will be transferred to other vibrational modes and the system will present extra degrees of freedom in its oscillatory motion. These extra degrees of freedom will be responsible for a decrease in the energy of the first harmonic at frequencies $\omega = \omega_0$, where ω_0 is the frenquency of the imposed oscillatory shear and for a spreading in the energetic levels seen in the phase plot. In this work, we are dealing with a hihgly nonlinear phenomenon and one of our goals is to investigate the possibility of using nonlinear control tools such as Neural Networks to identify the physical parameters ϕ and φ_m (related to particle interaction) that produce different vibrational modes. For this purpose it would be interesting to define a physical variable that would allow us to obtain a well behaved function even for hihgly nonlinear cases and at the same time could summarize in a single pair of information several aspects of the nonlinear system we are dealing with. With this goal in mind we present figure (28).

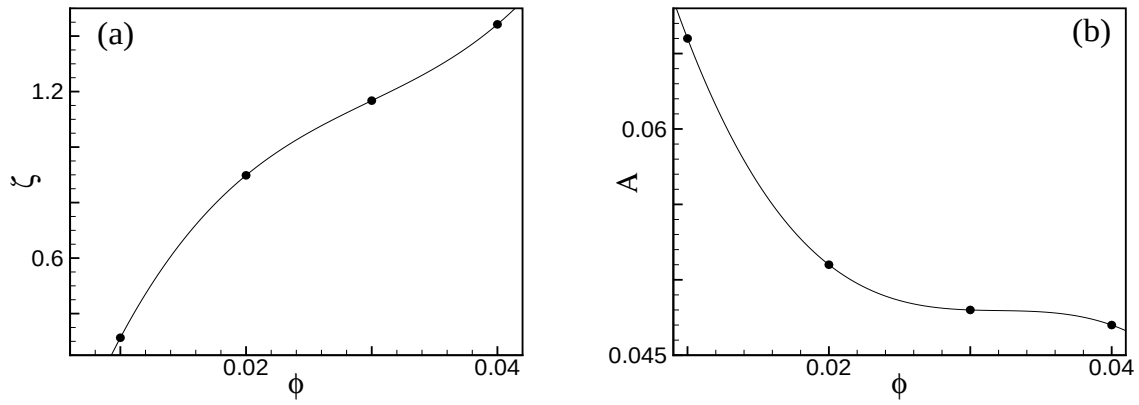

Figure 28: Area ζ as a function of ϕ and the amplitude A of the system harmonic at $\omega = 1$ also as a function of ϕ.

In figure (28) we note that both ζ and A are well behaved, smooth, monotonic functions of ϕ even though they are associated with the hihgly nonlinear behavior shown in figures (25), (26) and (27). It is instructive to show figure (29). This figure shows the suspension microstructure for a condition of $\phi = 4\%$, $\varphi_m = \psi_m = 1$ after 13 Stokes time of simulation in (a) while in (b) we have the trajectory of a typical test particle immersed in the middle of the suspension. It is possible to observe that both magnetic and hydrodynamic interactions have led the suspension to a completely different configuration when compared to its initial ordered distribution. It is also clear that each particle may have an extremely complicated kinematic due to particle interactions. These nonlinear behaviors are responsible for the nonlinearities observed in figures (25), (26) and (27).

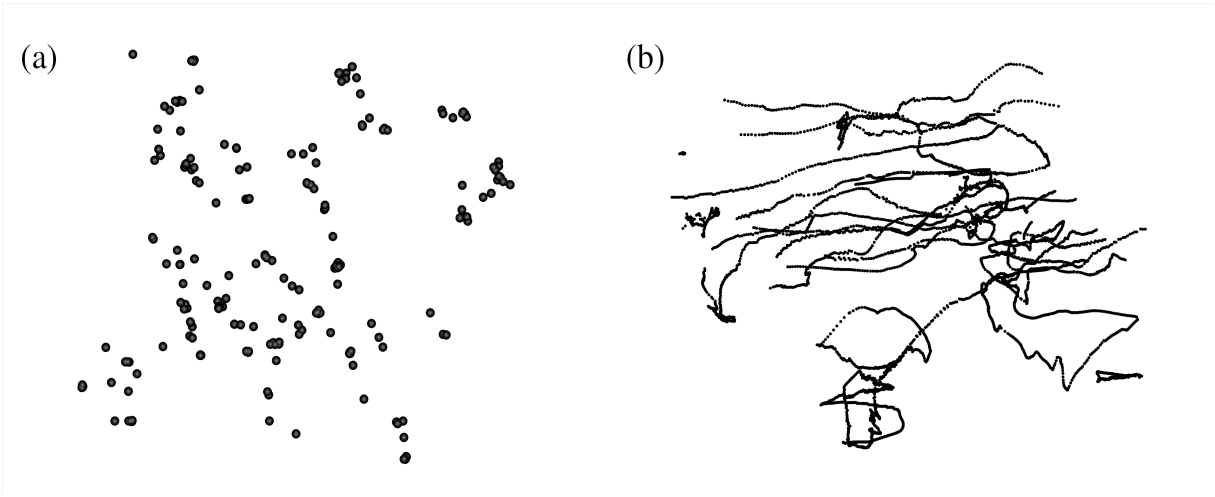

Figure 29: Figure (a) shows the microstructure for $\phi = 4\%$, $\varphi_m = \psi_m = 1$ for $t_s = 13$. Figure (b) shows the trajectory of a typical test particle in the periodic dynamical simulation.

The fact that both ζ and A present a smooth behavior even being associated with the nonlinearities shown in figures (25), (26), (27), (28) and (29) leads us to speculate if ζ or A would work as good parameters to train a beural betwork capable of recognizing the flow parameters ϕ and φ_m only by a pair of values of ζ or A. If so, it would be interesting to avail how the network would respond to the attempt of identifying these patterns.

III.9.1 Neural networks

A Neural Network was trained in order to avail its learning capabilities in identifying the combination of the physical parameters ϕ and φ_m that lead to the responses observed in previous sections. For this purpose the Neural Network uses the values of ζ and A obtained for several simulations varying ϕ and φ_m in the range of $0.5\% < \phi < 3.0\%$ and $1 < \varphi_m < 2$. More precisely 36 long time simulations were perfomed considering several combinations of ϕ and φ_m within the mentioned range. However from these 36, six were removed (one for each ϕ) to be part of the test group (validation set). The 30 files from the trainning set were linked to two targets: the concentration and the magnetic parameter. These simulations were used to train a Neural Network with the goal of identifying the combination of parameters φ_m and ϕ that could lead to the nonlinear behavior explored in previous sections.

The network was trainned with 100 neurons in the hidden layer and two neurons in the output layer for 300 epochs. The basic conjugate gradient backpropagation algorithm was used to adjusts the weights in the steepest descent direction (negative of the gradient). This is the direction in which the nonlinear function, here defined by the error (difference between target and output), decreases most rapidly. Even though the Scaled Conjugate Gradient needs more storage than other second order algorithms, its convergence is more rapid. This algorithm is based upon a class of optimization techniques well known in numerical analysis as the Conjugate Gradient Methods [41]. From an optimization point of view learning in a neural network is equivalent to minimizing a global error function, which is a multivariate function that depends on the weights in the network. This perspective gives some advantages in the development of effective learning algorithms since the problem of minimizing a function is well known in other fields of science, such as conventional numerical analysis [42]. In the first layer of the Network a logarithmic transfer function was used, while in the output layer a linear function was adopted. Under this configuration, ten tests were conducted in order to see if the neural network was able to identify the correct values of ϕ. The first result regarding the performance of the Network is shown in figure (30).

Figure (30) shows the ability of the Network in predicting the volume fraction of particles used in the simulations that could lead to the combination of ζ and A used as in input for the Network. It is possible to note a small deviation between the continous line (correct value) and the dashed line (Network output). In this sense we may say that the Network has learned how to identify the correct value of ϕ with good precision. Physically we may speculate that the influence of hydrodynamic interactions between the particles leads to nonlinearities identifiable by the Network. Here ϕ is the hydrodynamic parameter since it measures the influence of hydrodynamic interactions between the suspended particles.

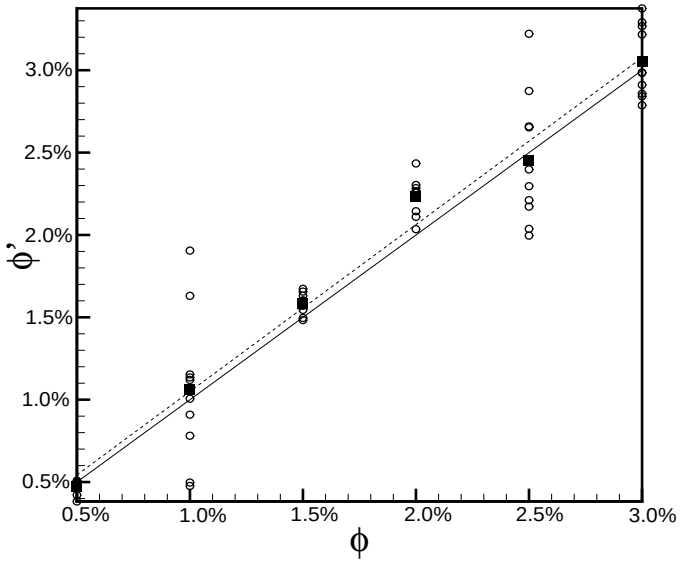

Figure 30: Predicted volume fraction $\phi^{'}$ by the Network as a function of the input value of ϕ used in the simulations. The continous line represent the expected prediction. The blank symbols represent the Network responses for several tests. The filled symbols denote the average output of the Network. The dashed line represents a linear fit obtained by the average responses of the Network.

To check how the Network identifies the magnetic parameter φ_m we show figure (31). In this picture the dashed horizontal lines represent constant values of ϕ for which different simulations varying φ_m were perfomed. The circles filled in black represent values of φ_m considered under six different simulations (for six different values of ϕ). The blank circles represent the Network output in φ_m for several tests with different initial weights. The circles filled in gray are the average response of the Network considering all the tests. From figure (31) it is clear that the network is not capable to identify the value of φ_m for small volume fraction of particles. This statement is equivalent to say that it can't capture the influence of magnetic effects in very dilute suspensions. For volume fractions above 2.0% the distance between the black and gray circles decreases. This behavior indicates that the network ability in predicting the correct value of φ_m and hence in understanding the influence of magnetic effects increases with ϕ.

We may say that despite of the nonlinearities in the time response signal observed in this manuscript, the use of A and ζ seems to be a good choice to train a Neural network capable of identifying the physical parameters used in the simulations. Moreover, it is clear that the network failure in predicting the intensity of φ_m for very dilute suspensions ($\phi < 2\%$) is a consequence of the low influence of magnetic effects in these limits of ϕ.

III.10 Concluding remarks

In this work we have developed a nonlinear dynamic system analysis to treat the microstru-

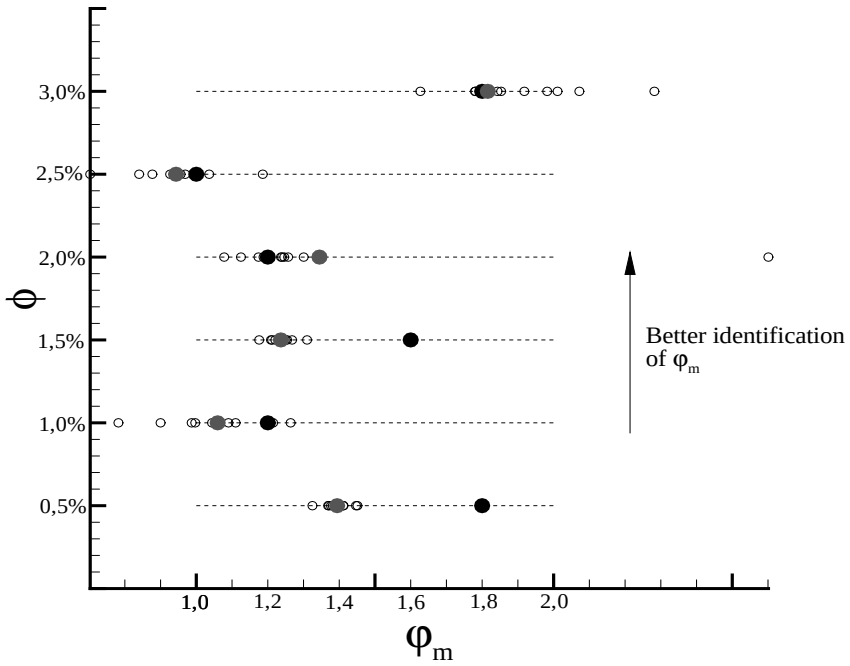

Figure 31: Predicted value of φ_m for several values of ϕ. The dashed lines represent constant values of ϕ for which several values of φ_m were tested. The blank symbols denote the Networks predictions of φ_m for a given condition of this parameter considering different tests with different initial weights. The filled black circles represent the used (correct) value of φ_m in the simulation while the circles filled in gray denote the average value of φ_m predicted by the Network.

cural response of a magnetorheological suspension. For this purpose we have developed a numerical research code written in Fortran for Linux Platforms that compute the motion of N neutrally buoyant rigid spherical particles suspended in a viscous fluid. These particles are made of magnetic material and are subjected to long range interactions through their individual dipole moments. We decided to apply simultaneously an external magnetic field and an oscillatory shear. Since the particles are suspendend in a viscous fluid their individual displacements induce a flow field in their neighborhoods which induce a secondary motion on other particles in a process known as hydrodynamic interaction. The combination of an applied steady state magnetic field with a time varying hydrodynamic field forces the system (here defined as a magnetorheological suspension) to respond to the action of these deterministic mechanisms. Since the particles interact and are free to translate and rotate we end up with a system that presents several degrees of freedom.

To investigate the microstructural behavior of this many-body problem we decided to use classical tools of nonlinear dynamic system analysis, such as its response on the frequency spectrum and phase plane. We were able to use these tools in order to understand how the coupling between the mechanisms of magnetic and hydrodynamic interaction governs the micromechanics of these complex materials. For instance, a clear increase on the nonlinear response of the unsteady magnetization was observed as we increased ϕ and φ_m. We have identified that

while the volume fraction of particles is responsible for computing mostly the influence of hydrodynamic interactions, the magnetic parameter φ_m computes how long range magnetic interactions alter the microstructural dynamics of the system. Even though the increase ϕ for a given value of φ_m also increases the magnetic response, for very diluted suspensions ($\phi < 2\%$) we may observe the influence of long range hydrodynamic interactions. The reason for this behavior may lie on the fact that while hydrodynamic interactions are proportional to $1/r$ (being r the distance of arbitrary particles), interparticle magnetic forces and torques are proportional to $1/r^4$ and $1/r^3$ respectively. The slow decay nature of hydrodynamic interaction is then responsible for a higher influence of ϕ in the microstructural response of a very dilute magnetorheological suspension.

We have also identified that the influence of these non deterministic mechanisms (hydrodynamic and magnetic interactions) leads to rapid angular velocity fluctuations on near interacting particles. This phenomenon was observed as an energetic spreading of the suspension magnetization on the phase plane. These flucutations are concentrated just below the saturation magnetization. Despite of a highly nonlinear response we were able to define two important parameters A and ζ that behave smoothly with respect to the problem main physical parameters ϕ and φ_m. In our definition A is the amplitude of the first harmonic in the frequency spectrum response of the unsteady magnetization. ζ was defined as the area in the phase plane $M \times \dot{M}$ that concentrates the energetic spreading of the system response after an initial deterministic transient. We have then used A and ζ to train a neural network to identify the values of ϕ and φ_m used in our simulations. The idea was to see if we could concentrate in a single pair of data the overall behavior of our nonlinear system and see wheter a neural network was capable to learn how particle interactions are somehow responsible for generating the observed responses. We observed that the Network was extremely efficient in identifying the volume fraction of particles ϕ. In this sense we may conclude that regardless of the volume fraction of particles the choice of a single pair of date A and ζ seems to be enough for the Network to identify the influence of hydrodynamic interactions. For very dilute suspensions $\phi < 2\%$ the Network fails in the identification of φ_m. We speculate that this result is a direct consequence of the slow decay nature of hydrodynamic interactions that overwhelms the influence of magnetic effects for very dilute magnetorheological suspensions.

An important application of this work would be the use of neural networks to characterize the properties of a magnetic fluid through its response to an applied field and shear rate. Since the macrorheology of a complex fluid is directly linked to its microstructural dynamics, we could use an observable output of this complex material to infer its volume fraction of particles. The highlight of the present work is that we can use several tools of classic nonlinear system analysis to understand in greater depth the rich and intricated micromechanics of magnetorheological suspensions.

BIBLIOGRAPHIC REFERENCES

[1] Rosensweig, R. E., 1985, *Ferrohydrodynamics*, Dover Publications Inc., New York.

[2] Gontijo, R.G., 2013, *Micromechanics and Microhydrodynamics of Magnetic Suspensions*, PhD. Thesis, University of Brasília, Brazil, 262 p.

[3] Gontijo, R.G. e Cunha, F.R., 2012, *Experimental Investigation on Thermo-Magnetic Convection Inside Cavities*, J. Nanosci. Nanotechnol., Vol 12, pp. 9198–9207.

[4] Sheikholeslami, M. and Ganji, D. D., 2014 *Ferrohydrodynamic and magnetohydrodynamic effects on ferrofluid flow and convective heat transfer*, Energy 75 (2014) 400-410.

[5] Zahn, M. and Greer, D. R., 1995, *Ferrohydrodynamic pumping in spatially uniform sinusoidally time-varying magnetic fields*, J. Magn. Magn. Mater., Vol. 149, 165-173.

[6] Shiliomis, M. I. and Morozov, K. I., 1994, *Negative Viscosity of Ferrofluid under Alternating Magnetic Fluid*, Phys. Fluids, 6, 2855-2861.

[7] Cunha, F.R., Sobral, Y.D., Gontijo, R. G., 2013, *Stabilization of concentration waves in fluidized beds of magnetic particles*, Powder Technology, vol.241, pp. 219–229.

[8] Einstein, A., 1956, *Investigations on the theory of the Brownian Movement*, Dover Publications, New York.

[9] Sudo, S., Funaoka, M. and Nishiyama, H., 2002, *Impact of Droplets of Magneto-Rheological Suspension under Applied Magnetic Fields*, Journal of Inteligent Material Systems and Strcutures, Vol.13, DOI: 10.1106/104538902029184

[10] Dong, XM., Yu, M., Liao, CR. and Chen, WM., 2009, *Comparative research on semi-active control strategies for magneto-rheological suspension*, Nonlinear Dyn (2010) 59: 433?453, DOI 10.1007/s11071-009-9550-8

[11] Dong, XM., Yu, M., Zushu, L., Liao, CR. and Chen, WM., 2009, *Neural network compensation of semi-active control for magneto-rheological suspension with time delay uncertainty*, Smart Mater. Struct. 18 (2009) 015014 (14pp), DOI:10.1088/0964-1726/18/1/015014

[12] Dong, XM. and Yu, M., 2014, *Genetic algorithm based fuzzy logic control for a magneto-rheological suspension*, Journal of Vibration and Control, Vol. 20(9) 1343?1355, DOI: 10.1177/1077546312472703

[13] Weiss, R. D., Schifter, J., Borduz, L. and Raj, K., 1985, *Ferrofluid studies of recorded data and defect identification in small high?performance rigid discs*, Journal of Applied Physics 57, 4274 (1985); DOI: 10.1063/1.334583

[14] Parekh, K, Patel, R., Upadhyay, R.V. an Mehta, R.V., 2005, *Field-induced diffraction patterns in a magneto-rheological suspension*, Journal of Magnetism and Magnetic Materials 289 (2005) 311?313, DOI: 10.1016/j.jmmm.2004.11.088

[15] Fallah, M. A. and Abiri, H., 2013, *Electromagnetic Fields Induced by the Motion of Di-Hull Bodies in a Conducting Fluid*, IEEE TRANSACTIONS ON MAGNETICS, VOL. 49, NO. 10, OCTOBER 2013, DOI: 10.1109/TMAG.2013.2260345

[16] Cao, Y. and Ding, Z.J., 2013 *Formation of hexagonal pattern of ferrofluid in magnetic field*, Journal of Magnetism and Magnetic Materials 355 (2014) 93?99, DOI: http://dx.doi.org/10.1016/j.jmmm.2013.11.042

[17] Richardi, J. and Pileni, M.P., 2004, *Towards efficient methods for the study of pattern formation in ferrofluid films*, Eur. Phys. J. E 13, 99?106 (2004), DOI: 10.1140/epje/e2004-00044-1

[18] Richardi, J. and Pileni, M.P., 2004, *Nonlinear theory of pattern formation in ferrofluid films at high field strengths*, PHYSICAL REVIEW E 69, 016304 (2004), DOI: 10.1103/PhysRevE.69.016304

[19] Chen, CY,. Wu, WL. and Miranda, J.A., 2010, *Magnetically induced spreading and pattern selection in thin ferrofluid drops*, PHYSICAL REVIEW E 82, 056321(2010), DOI: 10.1103/PhysRevE.82.056321

[20] Vicente, J., Vereda, F. and Segovia-Gutiérrez, J. P., 2010, *Effect of particle shape in magnetorheology*, J. Rheol. 54?(6), 1337-1362, DOI: 10.1122/1.3479045

[21] Pinho, M., Brouard, B., Génevaux, J.M., Dauchez, N., Volkova, O., Mézière, H. and Collas, P., 2011, *Investigation into ferrofluid magnetoviscous effects under an oscillating shear flow*, Journal of Magnetism and Magnetic Materials 323 (2011) 2386?2390, DOI:10.1016/j.jmmm.2011.05.002

[22] See, H., 2003, *Transient response of a magneto-rheological suspension after a double-step shear strain*, Colloid Polym Sci (2003) 281: 788?793, DOI: 10.1007/s00396-002-0844-3

[23] Felicia, L.J. and Philip, J., 2014, *Probing of Field-Induced Structures and Their Dynamics in Ferrofluids Using Oscillatory Rheology*, Langmuir 2014, 30, 12171?12179, DOI: dx.doi.org/10.1021/la502878v

[24] Soto-Aquino, D., Rosso, D. and Rinaldi, C., 2011, *Oscillatory shear response of dilute ferrofluids: Predictions from rotational Brownian dynamics simulations and ferrohydrodynamics modeling*, PHYSICAL REVIEW E 84, 056306 (2011), DOI: 10.1103/PhysRevE.84.056306

[25] McWhirter, J. L. and Patey, G.N., 2002, *Nonequilibrium molecular dynamics simulations of a simple dipolar fluid under shear flow*, Journal of Chemical Physics, Vol. 117, No. 6, pp. 2747-2761.

[26] Wang, Z., Holm, C. and Müller, H. W., 2003, *Boundary condition effects in the simulation study of equilibrium properties of magnetic dipolar fluids*, J. Chem. Phys, Vol. 119, p. 379.

[27] Batchelor, G. K., 1972, *Sedimentation in a Dilute Dispersion of Spheres*, J. Fluid Mech., 52, pp. 245-268.

[28] Brady, J. F. and Durlofsky, L. J., 1988, *The Sedimentation Rate of Disordered Suspensions*, Phys. Fluids, 31(4), pp. 717-727.

[29] Richardson, J. F. e Zaki, W. N., 1954, *Sedimentation and Fluidization: I*, Trans. Inst. Chem. Eng., 3235, pp. 35-52.

[30] Cunha, F. R., Abade, G. C., Souza, A. J. and Hinch E. J., 2002, *Modeling and Direct Simulation of Velocity Fluctuations and Particle-Velocity Correlations in Sedimentation*, Journals of Fluids Engineering, Vol. 124, pp-957-968.

[31] Kim, S. and Karrila, S. J., 2005, *Microhydrodinamics - Principles and Selected Applications*, 2005, Dover Edition, ISBN-13: 978-0486442198.

[32] Gontijo, R. G. and Cunha, F. R., 2015, *Dynamic numerical simulations of magnetically interacting suspensions in creeping flow*, Powder Technology, 279, July 2015, Pages 146?165

[33] Beenakker, C. W. J., 1986, *Ewald Sum of the Rotne-Prager Tensor*, J. Chem. Phys., 853, pp. 1581-1582.

[34] Ewald, P. P. 1921, *Die Berechnung Optisher und Elektrostatischer Gitterpotentiale*, Ann. Phys. Lpz., Vol. 64, p. 253.

[35] Rotne, J. and Prager, S., 1969, *Variational Treatment of Hydrodynamic Interaction in Polymers*, J. Chem. Phys., 5011, pp. 4831-4837.

[36] Cunha, F. R., Gontijo, R. G. and Sobral Y. D., 2013, *Symmetry breaking of particle trajectories due to magnetic interactions in a dilute suspension*, Journals of Magnetism and Magnetic Materials, Vol. 326, pp-240-250.

[37] Abade, G.C. and Cunha, F.R., 2007, *Computer simulation of particle aggregates during sedimentation*, Comput. Methods Appl. Mech. Engrg. 196 (2007) 4597–4612.

[38] Sangani, A. S. and Acrivos, A., 1982, *Slow Flow Through a Periodic Array of Spheres*, Int. J. Multiphase Flow, 84, pp. 343-360.

[39] Hasimoto, H., 1959, *On the Periodic Fundamental Solutions of the Stokes Equations and Their Applications to Viscous Flow Past a Cubic Array of Spheres*, J. Fluid Mech., Vol. 5, pp. 317-328.

[40] Ivanov, A. O. e Kuznetsova, O. B., 2001, *Magnetic properties of dense ferrofluids: An influence of interparticle correlations*, Physical Review E, Vol. 64, 041405.

[41] Moller, M. F., 1993, *A scaled conjugate gradient algorithm for fast supervised learning*, Neural Networks, **6**(4), 525-533.

[42] Watrous, R. L., 1987, *Learning Algorithms for Connectionist Networks: Applied Gradient Methods of Nonlinear Optimization*, Proc. IEEE 1st International Conference on Neural Networks, Vol. 2, pp. 619-628.

Submitted Paper # 3

This paper was produced and submitted during the Masters period. This work focus on a theoretical investigation of the shape of a magnetic liquid-liquid interface formed between two vertical flat plates. An oscillating magnetic field is applied. The shape and equilibrium height are analysed with tools such as wavelet transforms.

The influence of a magnetic field on the mechanical behavior of a fluid interface

R. G. Gontijo, S. Malvar, Y. D. Sobral and F. R. Cunha

This work focus on a theoretical investigation of the shape and equilibrium height of a magnetic liquid-liquid interface formed between two vertical flat plates in response to vertical magnetic fields. The formulation is based on an extension of the so called Young-Laplace equation for an incompressible magnetic fluid infor a two-dimensional free interface. A first order dependence of the fluid's susceptibility with respect to the magnetic field is considered. The formulation results in a hydrodynamic-magnetic coupled problem governed by a nonlinear second order differential equation that describes the liquid-liquid meniscus shape. According to this formulation, five relevant physical parameters are revealed in this fluid static problem. The standard gravitational Bond number, the contact angle and three new parameters related to magnetic effects in the present study: the magnetic Bond number, the magnetic susceptibility and its derivative with respect to the field. The nonlinear governing equation is integrated numerically using a fourth order Runge-Kutta method with a Newton-Raphson scheme, in order to accelerate the convergence of the solution. The influence of the relevant parameters on the rise and shape of the liquid-liquid interface is examined. The interface shape response in the presence of a magnetic field varying with characteristic wavenumbers is also explored. The numerical results are compared with asymptotic predictions also derived here for small values of the magnetic Bond number and constant susceptibility. A very good agreement is observed. Furthermore, all the parameters are varied in order to understand how the scales influence the meniscus shape. Finally, is

shown how the magnetic field can control the format of the meniscus. **Meniscus, free surface, magnetic fluid, non-linear response, asymptotic solution**

IV.11 Introduction

Recently the study of magnetic fluids has gained increasing importance in the global research landscape due to its many possible application fields. These fluids can be used in a great number of industrial processes, biomedical applications, optimization of heat transfer rates [1, 2, 3, 4] and so on. Recent advances in magnetic fluid flows are described in the current literature [5, 6]. Theoretical works and optical experimental measurements of ferrofluid free surfaces for tangential and perpendicular magnetic fields developed in recent years have been considered of special importance [7, 8, 9, 10, 11]. Some studies have shown the possibility of displacing magnetic fluids inside porous media by the combination of capillary and magnetic pressures [8, 12]. The possibility of using a magnetic fluid for promoting a more effective capillary displacement is promising for applications of oil industries. Oil reservoirs constitute a porous medium where capillary pressure plays an important role on the dynamics of fluid displacement inside small porous containing immiscible fluids.

Bragard and Lebon [12] investigated the capillary rise of a non-magnetic fluid in a porous media and developed a scaling law that establishes a relationship between the microstructure of the porous medium and the height that a fluid rises by capillary pressure, here called the free surface equilibrium height. The first experimental evidence on the possibility of pumping a magnetic fluid due to an external applied magnetic field was shown by [13]. In their pioneer work the authors studied the effect of magnetic pumping at high oscillating magnetic fields finding a negative viscosity, which depends on the orientation of the applied field. A first attempt of developing a study for capillary rise of magnetic fluids by the effect of magnetic pressure in a porous medium was done by [14]. These authors examined the equilibrium height of a magnetic fluid column inside a cylindrical capillary in the presence of an external uniform magnetic field. They found that due to the fluid meniscus deformation,the surface pressure drop in the fluid decreases in the longitudinal and transverse direction of the field with respect to the capillary axis.

Just to mention, some works [11, 15, 16] have done numerical simulations and measurements of ferrofluid meniscus shape around a vertical cylindrical wire carrying electric current and observed the influence of the viscosity, the contact angle and the surface tension on the shape of the meniscus. Possible instabilities formed on a ferrofluid free surface due to the presence of external applied magnetic fields have been also investigated [7, 17, 18].

Boudouvis et al. [19] were the first to examine the deformation of a free surface of a ferrofluid by numerical simulation using a Galerkin method and carrying out some experimental observations. Their main focus was to investigate the effect of the contact angle on the deformation of the ferrofluid's free surface pool and to observe the deformation of a captive ferrofluid drop at different magnetic field strengths. A related problem using the Young-Laplace equation coupled to Maxwell equations in order to investigate stability of polarized droplets between two faces of charged parallel

plates in the presence of a magnetic field or electric field has been examined by Wohlhuter and Barasan [20].

The present theoretical work aims to study the behavior of the shape and the equilibrium height of a ferrofluid meniscus in the presence of a vertical magnetic field against the direction of gravity. The meniscus shape is investigated for different combinations of the magnetic parameters: magnetic Bond number, susceptibility and its derivative with respect to the field. We consider both uniform and non-uniform fields as the magnetic field depends on the wavenumbers in the longitudinal direction. In addition, we present an asymptotical expression for the ferrofluid meniscus shape under conditions of small values of the magnetic Bond number and for constant magnetic susceptibility. Magnetic fluid rise with contact angles higher than $\pi/2$ by combining the values of the magnetic Bond number and the magnetic susceptibility is also examined. One of the motivations for this work is to investigate possibilities of capillary rise of a magnetic fluid by controlling the identified magnetic physical parameters of the system even at conditions of null meniscus curvatures.

The highlights of this article are: the proposed formulation for describing the shape and predict the equilibrium height of a magnetic fluid, the identification and influence of the problem's physical parameters, the proposition of several theoretical solutions in different asymptotic regimes, the validation of those solutions by a numerical research code and finally a physical interpretation of the results obtained here.

IV.12 Formulation of the problem

The problem to be examined here considers a magnetic fluid between two parallel flat plates as illustrated in figure (32). In the lower side of the interface we have a magnetic fluid, called in this formulation Fluid 1 and in the upper side of the interface we have a non magnetic fluid, called Fluid 2.

The spacing between the plates is $2b$. The magnetic fluid has density ρ_1, dynamic viscosity η_1 and magnetic susceptibility χ_1. The non-magnetic fluid has properties ρ_2, η_2 and $\chi_2 = 0$. A meniscus between fluid 1 and fluid 2 is formed. The surface tension is denoted by γ. The shape of the meniscus is described by the curve $y - f(x) = 0$. Here d denotes the vertical distance from the origin of the coordinate system xy to the bottom of the container. In in this problem d is also called the meniscus equilibrium rise. The mean curvature of the function $y = f(x)$ is denoted by C_k and α represents the contact angle between the magnetic liquid and the plate's solid walls.

IV.12.1 General governing equations

Maxwell's equations are considered in the magnetostatic limit and the hydrodynamics of an inviscid fluid (governed by Euler's equation). Therefore, we have the following governing equations of the problem:

$$\nabla \times \boldsymbol{H} = \mathbf{0}, \tag{91}$$

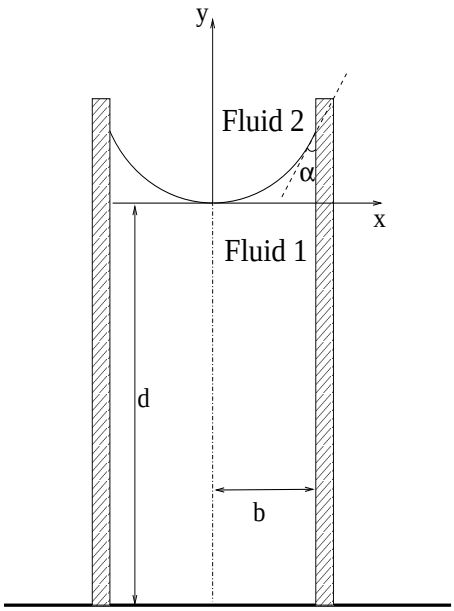

Figure 32: A sketch of the problem used in the mathematical formulation.

$$\boldsymbol{B} = \mu_0 \left(\boldsymbol{M} + \boldsymbol{H} \right), \tag{92}$$

$$\nabla \cdot \boldsymbol{B} = 0, \tag{93}$$

$$\rho \frac{D\boldsymbol{u}}{Dt} = \nabla \cdot \boldsymbol{\sigma} + \rho \boldsymbol{g}. \tag{94}$$

Here ∇ denotes the gradient vector operator, $\boldsymbol{H}$ is the applied magnetic field, $\boldsymbol{B}$ represents the magnetic induction vector field, $\boldsymbol{M}$ is the medium magnetization field, μ_0 is the magnetic permeability of the free space, $\boldsymbol{u}$ would represent the fluid's velocity field (in this case $\boldsymbol{u} = \boldsymbol{0}$), $\boldsymbol{\sigma}$ is the fluid's stress tensor, ρ is the density of the fluid and $\boldsymbol{g}$ denotes the gravity acceleration vector field.

IV.12.2 A discussion on the constitutive equation for a magnetic fluid

Even assuming in this article that the magnetization vector is always parallel to the applied field (i.e. symmetric fluid), it would be instructive to give a brief discussion on the constitutive equation for the magnetic stresses. Additionally, there are some controversies in the current literature about what would be the more appropriate constitutive equation to describe the behavior of a magnetic fluid [7, 21, 22, 23, 24].

A well-known constitutive equation for describing the stress tensor of a magnetic fluid in the absence of shear stresses is given by [1]

$$\boldsymbol{\sigma} = \boldsymbol{\sigma}_h + \boldsymbol{\sigma}_m = -p_h \boldsymbol{I} - (p_m \boldsymbol{I} - \boldsymbol{B}\boldsymbol{H}). \tag{95}$$

The tensor $\boldsymbol{\sigma}_h$ denotes the hydrodynamic contribution represented by $p_h \boldsymbol{I}$ for the particular case of an inviscid or static fluid. The second rank tensor $\boldsymbol{\sigma}_m$ is the magnetic contribution of the total stresses. Here, $\boldsymbol{H}$ represents an external magnetic field, $\boldsymbol{B}$ is the magnetic induction field, $\boldsymbol{u}$ is the Eulerian velocity field of the fluid, $\boldsymbol{\sigma}$ is the fluid stress tensor, $\boldsymbol{g}$ denotes the gravity acceleration

vector field, p_h denotes the hydrodynamic pressure and $p_m = \mu_0(\boldsymbol{H}\cdot\boldsymbol{H})/2$ is called the magnetic pressure.

Now, when we replace (95) in (94) we obtain the modified Euler equation for a ferrofluid

$$\rho\frac{D\boldsymbol{u}}{Dt} = -\nabla p_h + \mu_0\boldsymbol{M}\cdot\nabla\boldsymbol{H} + \rho\boldsymbol{g}. \tag{96}$$

The only magnetic contribution in equation (96) is the magnetic force per unit of volume $\boldsymbol{f}_M = \mu_0\boldsymbol{M}\cdot\nabla\boldsymbol{H}$. We argue that the constitutive equation (96) seems to be not suitable in a more general case of non symmetric fluids, when the presence of magnetic torque should give the extra contribution $\boldsymbol{f}_M = \mu_0\nabla\times(\boldsymbol{M}\times\boldsymbol{H})/2$. More intriguing is to see that while the divergent of the symmetrical part of the stress tensor in equation (95) results in a magnetic force per unit of volume $\boldsymbol{f}_M = \mu_0\boldsymbol{M}\cdot\nabla\boldsymbol{H} + \mu_0\nabla\times(\boldsymbol{M}\times\boldsymbol{H})/2$, the divergent of the non-symmetrical part gives $-\mu_0\nabla\times(\boldsymbol{M}\times\boldsymbol{H})/2$. So, the terms associated with magnetic torques will be always canceled. This indicates that it is not possible with the constitutive model given by equation (95) to study the flow of a non-symmetrical fluid in the presence of a field gradient.

In contrast, when considering the constitutive equation based on a generalization of the Maxwell stress tensor for a magnetic medium using the dyadic $\boldsymbol{HB}$,

$$\boldsymbol{\sigma} = -\left(p_h + p_m\right)\boldsymbol{I} + \boldsymbol{HB}, \tag{97}$$

and replacing equation (97) into equation (94), we obtain

$$\rho\frac{D\boldsymbol{u}}{Dt} = -\nabla p_h + \mu_0\boldsymbol{M}\cdot\nabla\boldsymbol{H} + \frac{1}{2}\mu_0\nabla\times(\boldsymbol{M}\times\boldsymbol{H}) + \rho\boldsymbol{g}. \tag{98}$$

Now, the divergent of equation (97) results separately in two different contributions relevant to the problem of describing an arbitrary ferrofluid. The first one, $\mu_0\boldsymbol{M}\cdot\nabla\boldsymbol{H}$, represents magnetic surface forces due to field gradients and, in a more general case, it is ncessary for describing both symmetric and non-symmetric fluids in the presence of a field gradient. This contribution however is null for fluids undergoing an applied uniform field. This situation

occurs in rheological investigations which usually consider the application of an uniform field in a simple shear flow for measuring a rotational viscosity, resulting from magnetic torques. In this case, the second magnetic term on the RHS of equation (98), $\mu_0\nabla\times(\boldsymbol{M}\times\boldsymbol{H})/2$ is not null even for an uniform field distribution, and it accounts for the magnetoviscous effects. This proposal seems to be a formidable task because the divergent of the symmetric part of the magnetic tensor $-p_m + (\boldsymbol{HB}+\boldsymbol{BH})/2$ gives only the magnetic force per unit of volume $\mu_0\boldsymbol{M}\cdot\nabla\boldsymbol{H}$, whereas the divergent of the non-symmetrical contribution leads to the force per unit of volume $\mu_0\nabla\times(\boldsymbol{M}\times\boldsymbol{H})/2$, associated with magnetic torques which arise in non-symmetric fluids. Thus, a typically non-symmetric ferrofluid in the presence of an uniform field should be described simply by:

$$\boldsymbol{\sigma}_m = \frac{1}{2}\mu_0\left(\boldsymbol{HM} - \boldsymbol{MH}\right). \tag{99}$$

Equation (99) has been also proposed in a heuristic way by [23, 24].

In the present work we use the standard superparamagnetic assumption, i.e. $\boldsymbol{M} = \chi(H)\boldsymbol{H}$, where χ is the fluid susceptibility. In this case, the stress contribution can be described by using the symmetric part of $\boldsymbol{HB}$, as first proposed by [22]:

$$\boldsymbol{\sigma}_m = -p_m\boldsymbol{I} + \frac{1}{2}\mu_0\left(\boldsymbol{HM} + \boldsymbol{MH}\right). \tag{100}$$

Under this condition equation (98) can be simplified to equation (96). So, in the case of symmetrical fluids the constitutive equations (95), (97), (100) lead to the same description of the fluid, producing the same magnetic effect since the contribution $\mu_0\nabla \times (\boldsymbol{M} \times \boldsymbol{H})/2$ is always null. This justifies why in this work we can just use the standard equation (95) for describing a symmetric magnetic fluid.

IV.12.3 Condition of fluid at rest

For an equilibrium condition the fluid between the rigid plates is in rest, so $\boldsymbol{u} = \boldsymbol{0}$. In addition, we consider the superparamagnetic condition, expressed by $\boldsymbol{M} = \chi(H)\boldsymbol{H}$, where $\chi(H)$ is the magnetic susceptibility which in a more general case may depends on the magnitude $H =\mid \boldsymbol{H} \mid$. Under these conditions, equation (96) reduces to

$$\nabla p_h = \mu_0\chi(H)\nabla\left(\frac{H^2}{2}\right) + \rho\boldsymbol{g}, \tag{101}$$

In this work we just consider a first correction of the χ filed dependence so that a Taylor series around H_0 truncated at $\mathscr{O}(\Delta H)$ can be applied:

$$\chi(H) = \chi(H_0) + \beta_0\Delta H + O(\Delta H^2), \tag{102}$$

where $\Delta H = H - H_0$ and $\beta_0 = (d\chi/dH)_{H_0}$. Here χ_0 represents $\chi(H_0)$.

Making a scalar product of equation (101) by $d\boldsymbol{x}$ and integrating, we obtain

$$p_h = \rho\boldsymbol{g}\cdot\boldsymbol{x} + \frac{\mu_0\chi_0 H^2}{2} + \mu_0\beta_0\left(\frac{H^3}{3} - \frac{H_0H^2}{2}\right) + A, \tag{103}$$

where A is an integration constant.

IV.12.4 Two immiscible fluids

Let's consider the system showed in figure (32) filled with two immiscible fluids where the liquid 1 is a magnetic

and fluid 2 is not magnetic. Now, applying equation (103) for each side of the interface we obtain

$$p_h^1 = \rho_1\boldsymbol{g}\cdot\boldsymbol{x} + \frac{\mu_0\chi_0 H_1^2}{2} + \mu_0\beta_0\left(\frac{H_1^3}{3} - \frac{H_0H_1^2}{2}\right) + A_1, \tag{104}$$

$$p_h^2 = \rho_2 \boldsymbol{g} \cdot \boldsymbol{x} + A_2, \tag{105}$$

for convenience the terms p_h^1 and p_h^2 will be simply called p_1 and p_2, respectively. Thus the pressure jump at the interface between the fluids is given by

$$\begin{aligned} p_2 - p_1 = {} & (\rho_2 - \rho_1)\, \boldsymbol{g} \cdot \boldsymbol{x} \\ & -\mu_0 \left[\tfrac{\chi_0 H_1^2}{2} + \beta_0 \left(\tfrac{H_1^3}{3} - \tfrac{H_0 H_1^2}{2} \right) \right] + (A_2 - A_1)\,. \end{aligned} \tag{106}$$

In order to calculate the term $(A_2 - A_1)$ the boundary condition at $y = -d$ where pressures $p_2 = p_1 = p_0$ and $H_1 = 0$ is applied. In this case it is considered that the external magnetic field is applied in the meniscus region and that it decays far away from the surface, where it is null. Note that $\boldsymbol{g} \cdot \boldsymbol{x} = -gy$, where g is the magnitude of the vector $\boldsymbol{g}$. We find

$$(A_2 - A_1) = (\rho_1 - \rho_2)\, gd.$$

Hence equation (106) becomes

$$\begin{aligned} p_2 - p_1 = {} & (\rho_1 - \rho_2)\, g\, (y + d) \\ & -\mu_0 \left[\tfrac{\chi_0 H_1^2}{2} + \beta_0 \left(\tfrac{H_1^3}{3} - \tfrac{H_0 H_1^2}{2} \right) \right]. \end{aligned} \tag{107}$$

IV.12.5 Jump of traction on the interface

Now let's examine the jump of normal tractions on the interface between those two fluids given by the so called Young-Laplace equation:

$$\left[\boldsymbol{f}^{(n)} \right] = \boldsymbol{f}_1^{(n)} - \boldsymbol{f}_2^{(n)} = 2 C_k \gamma \hat{\boldsymbol{n}}, \tag{108}$$

where the symbol [ ] denotes the jump of a certain property on the interface, $\boldsymbol{f}$ is the traction, given by $\boldsymbol{f} = \hat{\boldsymbol{n}} \cdot \boldsymbol{\sigma}$, n denotes the normal component of the traction $\boldsymbol{f}$, C_k represents the mean curvature of the surface and γ is the surface tension of the meniscus. In the a general case, fluids 1 and 2 can be considered two immiscible incompressible ferrofluids. The stress tensor in both sides of the interface are written respectively as

$$\boldsymbol{\sigma}_1 = -p_1 \boldsymbol{I} - \frac{\mu_0 H_1^2}{2} \boldsymbol{I} + \boldsymbol{B}_1 \boldsymbol{H}_1, \tag{109}$$

$$\boldsymbol{\sigma}_2 = -p_2 \boldsymbol{I} - \frac{\mu_0 H_2^2}{2} \boldsymbol{I} + \boldsymbol{B}_2 \boldsymbol{H}_2. \tag{110}$$

Now calculating the traction due to fluid 1 and fluid 2 and using the jump of normal stresses on the interface, equation (108) results in

$$2 C_k \gamma \hat{\boldsymbol{n}} = (p_2 - p_1)\, \hat{\boldsymbol{n}} + \frac{\mu_0}{2} \left(H_2^2 - H_1^2 \right) \hat{\boldsymbol{n}} - \left(B_{2n} \boldsymbol{H}_2 - B_{1n} \boldsymbol{H}_1 \right), \tag{111}$$

where B_{1n} and B_{2n} denote the normal components of vector $\boldsymbol{B}$ on fluids 1 and 2, respectively. The magnetic boundary conditions given in [1] are $B_{1n} = B_{2n}$ and $H_{1t} = H_{2t}$, which means that the normal components of $\boldsymbol{B}$ and the tangential component of $\boldsymbol{H}$ are continuous across the interface.

Applying the magnetic boundary conditions and after some algebraic manipulations we obtain

$$2C_k\gamma = (p_2 - p_1) + \frac{\mu_0}{2}\left(H_{2n}^2 - H_{1n}^2\right) - B_n\left(H_{2n} - H_{1n}\right). \tag{112}$$

Since $\boldsymbol{B} = \mu_0(\boldsymbol{M} + \boldsymbol{H})$ and also considering the fluid 1 a magnetic liquid and fluid 2 a non-magnetic fluid (so the magnetization in 2 is null), we obtain

$$H_{1n} = \frac{B_n}{\mu_0} - M_{1n} \tag{113}$$

and

$$H_{2n} = \frac{B_n}{\mu_0}. \tag{114}$$

Replacing (113) and (114) in (112) we obtain

$$p_2 - p_1 = 2C_k\gamma + \frac{\mu_0}{2}\left[\chi_0^2 H_{1n}^2 + \beta_0^2\left(H_{1n}^2 - 2H_{1n}H_0\right)H_{1n}^2\right]. \tag{115}$$

Now substituting equation (115) into equation (107) we have

$$2C_k\gamma = \Bigg[\Delta\rho g\left(y + d\right) - \frac{\mu_0\chi_0}{2}\left(H_1^2 + \chi_0 H_{1n}^2\right) - \mu_0\beta_0\left(\frac{H_1^3}{3} - \frac{H_0 H_1^2}{2}\right)\Bigg], \tag{116}$$

The average curvature of an arbitrary curve $y = f(x)$ is given by

$$C_k = \frac{y''}{2\left(1 + y'^2\right)^{3/2}}, \tag{117}$$

where $y' = dy/dx$. Using equation (117) into equation (116) finally results

$$y'' = \left(1 + y'^2\right)^{3/2}\Bigg[\frac{\Delta\rho g}{\gamma} - \frac{\mu_0\chi_0}{2\gamma}\left(H_1^2 + \chi_0 H_{1n}^2\right) - \frac{\mu_0\beta_0}{\gamma}\left(\frac{H_1^3}{3} - \frac{H_0 H_1^2}{2}\right)\Bigg]. \tag{118}$$

In the present work, equation (118) represents a modified Young-Laplace equation with non-constant curvature in the presence of magnetic effects.

IV.12.6 Dimensionless governing equation

It is important to write equation (118) in terms of dimensionless quantities. For this purpose, we consider a typical length scale of the problem as being the gap between the plates. According to

figure (32) the size b is the characteristic length scale. For making magnetic quantities dimensionless the reference H_0 is used. Here H_0 represents a typical applied field. Therefore equation (118) written in terms of dimensionless quantities is given by

$$Y'' = \left(1+Y'^2\right)^{3/2}\Big[Bo\,(Y+D) - Bo_m\chi_0\left(\tilde{H}_1^2 + \chi_0\tilde{H}_{1n}^2\right) - 2Bo_m\beta_0^*\left(\frac{\tilde{H}_1^3}{3} - \frac{\tilde{H}_1^2}{2}\right)\Big], \tag{119}$$

where $Y = y/b$ and $D = d/b$. Also, $\tilde{H} = H/H_0$, Bo and Bo_m are two important physical parameters of the problem called the Bond number and the magnetic Bond number defined respectively as

$$Bo = \frac{\Delta\rho g b}{\gamma/b} \tag{120}$$

and

$$Bo_m = \frac{\mu_0 H_0^2}{2\gamma/b}. \tag{121}$$

The Bond number can be interpreted as the relation between the hydrostatic pressure and the interfacial tension, whereas the magnetic Bond number represents the ratio between magnetic pressure and interfacial tension.

The following boundary conditions of the problem are considered

$$Y(-1) = -\cot\alpha, \quad \text{and} \quad Y'(1) = \cot\alpha \tag{122}$$

The solution of the ordinary nonlinear differential equation of second order $Y'' = F(X, \tilde{H}_1, \alpha, Bo, Bo_m, \chi, \beta_0^*)$ (i.e. equation (118)) with the boundary conditions (122), gives the shape of the meniscus formed on the interface between two immiscible fluids under action of a perpendicular magnetic field. Here fluid 1 is taken as the magnetic liquid.

IV.13 Theoretical Solutions

Analytical formulae are useful for validating numerical results. In this section, we develop and review several possible analytical solutions for a ferrofluid meniscus rising under actions of capillary and magnetic pressure. For all analytical solutions we use the assumption $Y'^2 \ll 1$ so that the meniscus mean curvature is reduced to

$$C_k = \frac{Y''}{2}. \tag{123}$$

IV.13.1 Geometric solution for the meniscus shape under constant curvature

A specific geometric solution of the meniscus shape is obtained for a constant curvature $C_k = \cos\alpha/2$, according to the sketch illustrated in figure (33).

When equation (123) is integrated with boundary conditions $Y(0) = 0$ and $Y'(1) = \cot\alpha$, yields

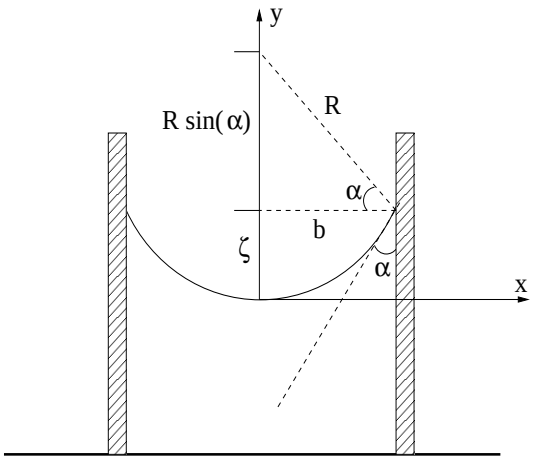

Figure 33: A sketch of the free surface's geometrical parameters.

$$Y(X) = X\left(\cot\alpha - \cos\alpha\right) + X^2\frac{\cos\alpha}{2}. \tag{124}$$

Note that in this case the solution is symmetric with respect to the Y axis and that the boundary condition $Y'(-1) = -\cot\alpha$ is automatically satisfied due to the problem's symmetry. Moreover, the condition $Y(0) = 0$ is only a geometrical restriction associated with the definition of the origin of the problem's coordinate system and it does not represent an extra boundary condition. The model is well posed.

The first derivative of equation (124) can be used to find a geometric constraint in terms of contact angle for the application of analytic solutions based on equation (123).

$$L(\alpha) = (X-1)\cos\alpha + \cot\alpha \ll 1 \tag{125}$$

Equation (125) and its derivative points out that the minimum value of $L(\alpha)$ occurs for $\alpha = \pi/2$ in all X. However, at $X = 1$ that implies $L(\alpha) = \cot\alpha$ the value of this functions is maximum. So, if $\cot\alpha \ll 1$ the constraint (123) is satisfied at any X of the meniscus shape.

IV.13.2 Meniscus shape for a non magnetic fluid for $\cot(\alpha) \ll 1$ and non-constant curvature

Another analytic solution is obtained by direct integration of (119), in the limit of $Y'^2 \to 0$ and $\chi_0 = 0$ under the same boundary conditions $Y(-1) = -\cot\alpha$ and $Y'(1) = \cot\alpha$. We have

$$Y(X) = -D + \frac{\cot(\alpha)\cosh\left(\sqrt{Bo}X\right)\operatorname{csch}\left(\sqrt{Bo}\right)}{\sqrt{Bo}} \tag{126}$$

Equation (126) gives the meniscus shape under condition of non-magnetic fluid (i.e, $\chi_0 = 0$) with contact angles satisfying the constraint $\cot(\alpha) \ll 1$, that is $\alpha \sim \pi/2$.

IV.13.3 Prediction of D for a non-magnetic fluid meniscus with constant curvature

Again, consider the sketch of the meniscus shown in figure (33). We have that $\zeta = R(1-\sin\alpha)$ and $\cos\alpha = b/R$. For a meniscus with a constant mean curvature we assume that Y'' is constant so that the dimensionless mean curvature C_k is given simply by

$$C_k = \frac{Y''}{2} = \frac{1}{2R} = \frac{\cos\alpha}{2}. \tag{127}$$

The necessary and sufficient condition for assuming a constant meniscus curvature occurs when $\zeta << d$, where $d = bD$ is the dimensional equilibrium rise of the meniscus. In dimensionless terms we can write that

$$1 - \sin\alpha << D\cos\alpha, \tag{128}$$

Now, the dimensionless governing equation (119) under condition of constant curvature condition is given by

$$2C_k = Bo\,(Y + D) - Bo_m\chi_0\left(\tilde{H}_1^2 + \chi_0\tilde{H}_{1n}^2\right) \\ -2Bo_m\beta_0^*\left(\tfrac{\tilde{H}_1^3}{3} - \tfrac{\tilde{H}_1^2}{2}\right), \tag{129}$$

Evaluating equation (129) at the origin for a non-magnetic fluid ($\chi_0 = 0$) we find that the capillary rise

D_c for the condition of constant curvature is given by

$$D_c = \frac{\cos\alpha}{Bo}. \tag{130}$$

The sign of the capillary rise in equation (130) is determined by the value of the contact angle α When $\alpha < \pi/2$ the meniscus rises, when $\alpha > \pi/2$ the meniscus submerges, and when $\alpha = \pi/2$ the meniscus remains flat at the level of the free surface outside the plates.

Substituting equation (130) into (128) yields

$$Bo << 1 + \sin\alpha, \tag{131}$$

that is the condition for the constant mean curvature approach to be applied.

IV.13.4 Prediction of D for a non-magnetic fluid meniscus for $\cot(\alpha) \ll 1$ and non-constant curvature

Equation (126) provides the shape of a non-magnetic fluid meniscus in the limiting case of $\cot(\alpha) \ll 1$. As seen by equation (125), this is the necessary condition for the assumption that $Y'^2 \ll 1$. Using the geometrical condition that $Y(0) = 0$, we obtain an analytical expression for the equilibrium displacement D_0, given by

$$D_0 = \sqrt{Bo}D_c \times \left[\frac{\operatorname{csch}\left(\sqrt{Bo}\right)}{\sin(\alpha)}\right] \tag{132}$$

IV.13.4.1 Prediction of D for a ferrofluid for $\cot(\alpha) \ll 1$ and constant curvature

Now, applying equation (129) evaluated at the origin for the case of a ferrofluid undergoing a vertical magnetic field $\tilde{\boldsymbol{H}}_{\mathbf{1}}(X,Y) = (1+Y/D)G(X)\hat{e_y}$, yields

$$D = D_c + \frac{Bo_m}{B_0}\left[\chi_0(1+\chi_0) - \frac{1}{3}\beta_0^*\right]. \tag{133}$$

Equation (133) states that a magnetic fluid in the small gap between two parallel plates can rise against gravity

by magnetic pressure even if the effect produced by capillary pressure D_c is null, that occurs for $\alpha = \pi/2$ and the condition for $Bo >> 1$. In this case, there is a new contribution from the magnetic action corresponding to the second term on the right hand side of equation (133) that can produce the fluid meniscus elevation inside a small porous. This behavior can be better seen in figure (34).

It is possible to observe that even though different combinations of Bo_m and χ_0 may produce $D > 0$ and $D < 0$, the shape of the free surface practically does not change for different pairs of these parameters. The shapes ilustrated in the details of figure (34) were obtained with numerical simulations using the methodology presented in the next section. In the next sections it will show the application of a variable magnetic field like $sin(kX)$, where k is a wave number, may drastically change the meniscus shape of a magnetic fluid.

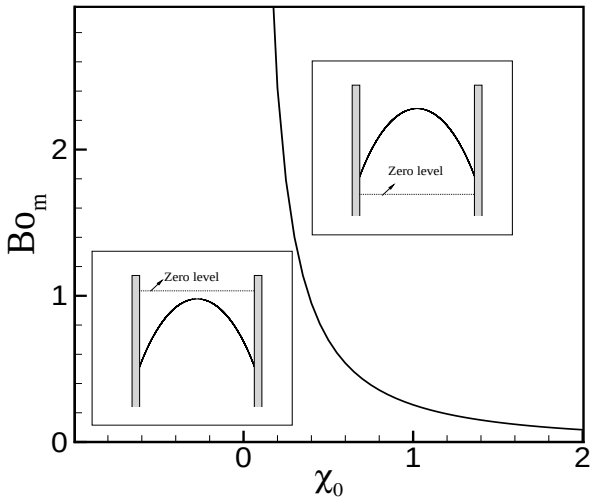

Figure 34: Combination of Bo_m and χ_0 in which a magnetic fluid in the small gap between two parallel plates can rise against gravity for contact angles higher than $\pi/2$. This curve was plotted using the constant curvature theory, equation (133). In this case we consider $\beta = 0.1$ and $Bo = 0.1$.

IV.13.5 An asymptotic solution for a ferrofluid meniscus shape : $Bo_m \ll 1$, $\chi_0 \sim 1$, $\cot(\alpha) \ll 1$ and non-constant curvature

Consider a ferrofluid meniscus where $Bo_m \ll 1$, but not necessary null and $\cot(\alpha) \ll 1$, so Y'^2 is small as required by equation (125). In this case the governing equation of the problem is given by

$$Y'' = Bo\,(Y+D) - Bo_m\chi_0\left(\tilde{H}_1^2 + \chi_0\tilde{H}_{1n}^2\right) \\ -2Bo_m\beta_0^*\left(\tfrac{\tilde{H}_1^3}{3} - \tfrac{\tilde{H}_1^2}{2}\right), \tag{134}$$

for a magnetic field like

$$\boldsymbol{H_1}(X,Y) = (1+Y/D)\hat{e_y}, \tag{135}$$

we have that

$$Y'' = Bo\,(Y+D) - Bo_m\Big[\chi_0\,(1+\chi_0)\left(1+\frac{2Y}{D}+\frac{Y^2}{D^2}\right) + \\ \tfrac{\beta_0^*}{3}\left(-1+\tfrac{3Y^2}{D^2}+\tfrac{2Y^3}{D^3}\right)\Big]. \tag{136}$$

Equation (136) does not have an analytical solution, but it is possible to seek an asymptotic solution for small values of the magnetic Bond number. For this purpose consider a regular asymptotic expansion, [25, 26], given by

$$Y(X) = Y_0(X) + Bo_mY_1(X) + Bo_m^2Y_2(X) + ... \tag{137}$$

and

$$D = D_0 + Bo_mD_1 + Bo_m^2D_2 + ..., \tag{138}$$

where $Y_0(X)$ is the leading order term for the non-perturbated equation, $Y_1(X)$ represents the first correction of the magnetic effect, $Y_2(X)$ is the second correction, and so on. Thus, we have D_0 as the equilibrium rise for the case of a non magnetic fluid, D_1 is the first correction of magnetic effects on the equilibrium rise D, and so on. Applying the regular asymptotic expansion, equation (137) at the governing equation (136), we find that

$$Y_0'' = Bo\,(Y_0+D_0), \tag{139}$$

$$Y_1'' + \frac{3Y_0''D_1}{D_0} = Bo\left[Y_1 + 4D_1 + \left(\frac{3Y_0D_1}{D_0}\right)\right] - \mathscr{F}, \tag{140}$$

$$\frac{3}{D_0}\left(Y_0''D_2 + \frac{Y_0''D_1^2}{D_0} + Y_1''D_1\right) + Y_2'' = Bo\Bigg[Y_2 + 4D_2 + 6\frac{D_1^2}{D_0} \\ + \frac{3}{D_0}\left(Y_0D_2 + Y_0D_1^2Y_1D_1\right)\Bigg] \\ - \frac{\chi_0\,(1+\chi_0)}{D_0}\left(3D_1 + \frac{Y_0D_1}{D_0} + 2Y_1 + \frac{Y_0^2D_1}{D_0^2} + \frac{2Y_0Y_1}{D_0}\right) \\ - \frac{\beta_0^*}{3D_0}\left(-3D_1 + \frac{3Y_0^2D_1}{D_0^2} + \frac{6Y_0Y_1}{D_0} + 6\frac{Y_0^2Y_1}{D_0^2}\right), \tag{141}$$

where $\mathscr{F}$ is given by

$$\mathscr{F} = \chi_0 \left(1 + \chi_0\right) \left[1 + \frac{2Y_0}{D_0} + \frac{Y_0^2}{D_0^2}\right] + \frac{\beta_0^*}{3} \left[-1 + \frac{3Y_0^2}{D_0^2} + \frac{2Y_0^3}{D_0^3}\right], \tag{142}$$

equation (139) represents the leading order solution of the non magnetic problem and was already presented in equation (126). The equation that governs the behavior of the $\mathscr{O}(Bo_m)$ correction is given by (140), while equation (141) is the governing equation for the $\mathscr{O}(Bo_m^2)$ correction.

The boundary conditions used for these asymptotic solutions are $Y_0^{'}(-1) = -\cot(\alpha)$, $Y_0^{'}(1) = \cot(\alpha)$, $Y_1^{'}(-1) = Y_1^{'}(1) = 0$ and $Y_2^{'}(-1) = Y_2^{'}(1) = 0$. The leading order solution is given by

$$Y_0(X) = \frac{\cot(\alpha)\cosh\left(\sqrt{Bo}X\right)\operatorname{csch}\left(\sqrt{Bo}\right)}{\sqrt{Bo}} - D_0. \tag{143}$$

Details of the analytical solution of differential equation (140) are presented in the appendix of this article. In contrast the correction $\mathscr{O}(Bo^2)$, that was solved using the software Mathematica presents a too tedious calculation for the details to be given in this work. So, we have omitted this calculations by convenience. The comparision of the asymptotic solutions with numerical results will be presented in the next section. The values of D_0, D_1 and D_2 are obtained by applying the geometrical conditions given respectively by: $Y_0(0) = 0$, $Y_1(0) = 0$ and $Y_2(0) = 0$. As pointed out before, this procedure is tedious and generates huge expressions for D_1 and D_2. All the manipulations done related to these asymptotic theories were made by using the Wolfram Mathematica 7 for Linux.

IV.14 Numerical solution

In order to validate our theories and to extend the solution of the problem to more complicated cases where we don't have a theoretical solution, we developed a researh code written in Fortran called MENIS-2D. This code computes the equilibrium height D of a ferrofluid and the free surface shape $Y = F(X, \tilde{H}_1, \alpha, Bo, Bo_m, \chi, \beta_0^*)$ of a two-dimensional ferrofluid meniscus between two vertical plates as the sketch shown in figure (32). The system of 2 ordinary differential equations

$$\frac{dY_k}{dt} = G_k(X, \tilde{H}_1, \alpha, Bo, Bo_m, \chi, \beta_0^*), \quad \text{where} \quad k = 1, 2, \tag{144}$$

resulting from the second order nonlinear differential equation (118) and boundary conditions (122) was integrated numerically using a fourth-order Runge-Kutta scheme. The method requires four G_k evaluations at each step of the numerical integration. The problem was transformed in an Initial Valor Problem (IVP) using an iterative scheme and a Newton-Rhapson method to accelerate the convergence of the solution [27]. The solution was advanced according to the following algorithm

$$
\left[\begin{array}{ll}
\texttt{1.} & \text{Set } Bo, \alpha, Bo_m, \chi_0, \beta_0^*, \text{ and } \Delta X; \\
\texttt{2.} & \text{Set Boundary conditions ;} \\
\texttt{3.} & \text{Set initial value for} D; \\
\texttt{4.} & \text{Compute } \; G_k(X, \tilde{H}_1, \alpha, Bo, Bo_m, \chi_0, \beta_0^*); \\
\texttt{5.} & \dfrac{dU}{dX} \to G \text{ and } \dfrac{dY}{dX} \to U; \\
\texttt{6.} & F_c(D) \to Y'(1) - \cot(\alpha); \\
\texttt{7.} & J_c[Y(0)] \to Y(0) - 0; \\
\texttt{8.} & \texttt{If } |F_c(D)| < tol \texttt{ then} \to \textbf{ END} \\
\texttt{9.} & \texttt{If } |J_c[Y(0)]| < tol \texttt{ then} \to \textbf{ END} \\
\texttt{10.} & F_c(D + \Delta D) \to Y'(1) - 1; \\
\texttt{11.} & J_c[Y(0) + \Delta Y(0)] \to Y(0) - 0; \\
\texttt{12.} & D \to D - \dfrac{Fc(D)}{Fc(D + \Delta D) - F_c(D)} \Delta D \\
\texttt{13.} & Y(0) \to Y(0) - \dfrac{Jc[Y(0)]}{Jc[Y(0) + \Delta Y(0)] - J_c[Y(0)]} \Delta Y(0) \\
\texttt{14.} & \texttt{Back to step 4.}
\end{array}\right. \tag{145}
$$

The algorithm (145) makes a picture of the whole numerical integration scheme.

The dimentionless space step ΔX was sufficiently small to ensure an error in the numerical integration less than 10^{-3}. A typical value of the space step was $b \times 10^{-4}$. An initial guess for the equilibrium height D is required in order to initialize the iterative scheme of the transformed IVP. The maximum number of iterations needed for each space step integration is around 20.

The integration starts at $X = -1$ with boundary condition $Y'(-1) = -\cot(\alpha)$ and with arbitrary values of D and $Y(-1)$. After each integration step the boundary condition $Y'(1) = \cot(\alpha)$ and the geometrical restriction $Y(0) = 0$ are verified. If these conditions are not satisfied, a Newton-Rhapson scheme is used in order to updated a new rise D that must satisfy

$$Y'(1) - \cot(\alpha) = 0 \tag{146}$$

and a new value of $Y(-1)$ that must satisfy

$$Y(0) = 0. \tag{147}$$

The procedure is repeated until both conditions given by equations (146) and (147) are satisfied within a tolerance of 10^{-6}. In this way the initial guess of the equilibrium rise D and the position $Y(-1)$ are carefully controlled in order to ensure the convergence of the method. The external magnetic field in the direction of gravity was considered as being a function of x and y; $H(x, y) = h_1(x)h_2(y)$. For instance, an uniform field on the gravity direction is imposed with $h_1(x) = 1$ and $h_2(y) = H_0\hat{e_y}$. Here H_0 denotes a constant value of a reference applied field. In addition, an uniform field gradient is imposed with $h_1(x) = 1$ and $h_2(y) = Ho(1 + y/d)\hat{e_y}$. In a more general form we propose $h_1(x) = [1 + \varepsilon \sin(kx)]$ $h_2(y) = Ho(1 + y/d)\hat{e_y}$, that depends on the wavenumbers $k = 2\pi n/b$ where n=0, 1, 2,.... This proposition is done in order to test the response of this nonlinearsystem when we apply an harmonic periodic input.

IV.14.1 Validation and preliminary results

One test of the full numerical integration scheme was to reproduce the exact solution obtained under conditions of non-constant curvature, small Bo_m and arbitraty values of the parameter β_0^*, as shown in figure (35). We can see that within the range of Bo_m in which the asymptotic solution is valid ($Bo_m \ll 1$), the numerical solution presents a very good agreement with the exact solution. The agreement between the $\mathscr{O}(Bo_m)$ solution and the numerical values is very good with Bo_m ranging in the interval [0,0.15]. After this point, the $\mathscr{O}(Bo_m^2)$ solution starts to agree much better than solution $\mathscr{O}(Bo_m)$ correction. The agreement between the numerical and $\mathscr{O}(Bo_m^2)$ solutions works very well for Bo_m up to 0.3.

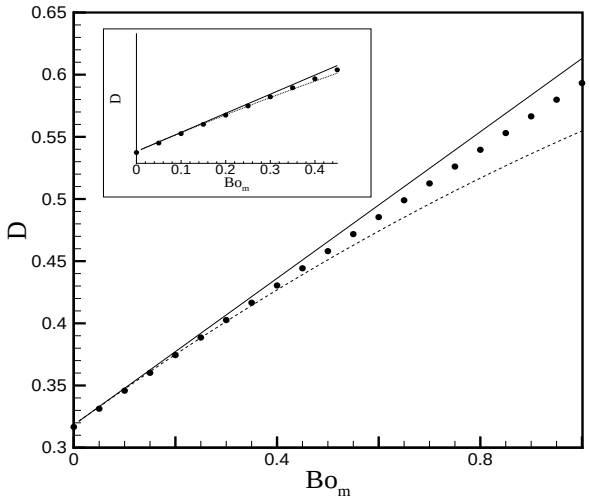

Figure 35: Equilibrium height versus the magnetic Bond number. The black circles represent numerical results, the solid line denotes the exact solution for small values of the magnetic Bond number given by the $\mathscr{O}(Bo_m)$ asymptotic theory, while the dashed line denotes the $\mathscr{O}(Bo_m^2)$ solution. For this plot: $Bo = 0.3$, $\chi_0 = 0.1$, $\beta_0^* = 0.1$ and $\alpha = \pi/2 - \frac{1}{10}$.

Another important test for the numerical solution and also to check the theoretical solution for constant curvature, eq. (133), is a comparison of the equilibrium rise for several values of the magnetic Bond number under condition of constant curvatures. This result is shown in figure (36).

It is possible to observe a great agreement between the numerical solution and the theory of constant curvature, specially for higher magnetic Bond number values. Under light and conditions of the result showed in figure (36), for small values of Bo_m, capillary pressure is more important than magnetic pressure against hydrostatic pressure. So, as the capillary pressure is proportional to the mean curvature a model with a constant curvature will show some discrepancies at small Bo_m. On the other hand for moderate value of $Bo_m \sim 0.5$ magnetic pressure dominates capillary pressure against gravity and variations of curvatures becomes unimportant. Figure (36) also suggests that for $Bo_m \geq 0.5$, the magnetic effect on the shape makes curvature variations unimportant on the equilibrum rise. In this range of parameters the effect of a magnetic field tends to jump the meniscus shape from a non-constant curvature curve to a condition of constant curvature.

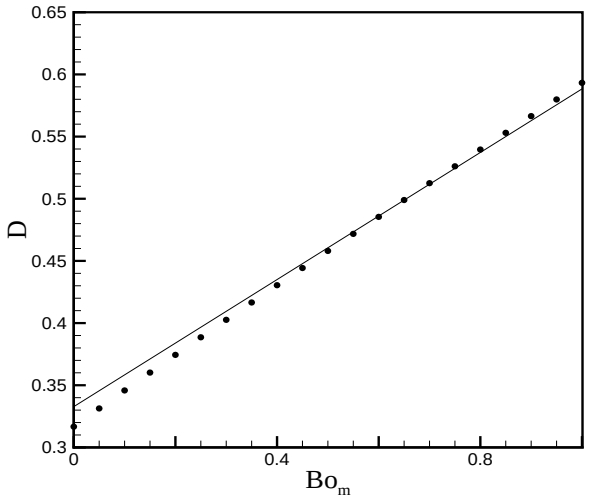

Figure 36: Equilibrium height as a funtion of the magnetic Bond number. The black circles represent numerical values, the solid line denotes the theoretical solution for the constant curvature condition. For this plot: $Bo = 0.3$, $\chi_0 = 0.1$, $\beta_0^* = 0.1$ and $\alpha = \pi/2 - 0.1$.

IV.15 Results and discussions

In the previous section of this work, some of our theories were compared with the numerical results in order to test them. In this section we present numerical results that cannot be explored or examined using the analytical solutions developed here. Such as the influence of the wave number k and the parameter ε used to impose an harmonic field, on the shape of the meniscus and on its equilibrium rise D.

IV.15.1 Meniscus shape

Figure (38) shows four configurations of the meniscus shape for different values of the harmonic field wave number.

The parameter n is related to the wavenumber $k = 2\pi n/b$. It is important to notice that the variations of n allow us to examine different length scales of the problem. The wavenumber may also be related to the spatial frequency, given by $\xi = \frac{k}{2\pi}$. In other words, a characterization of a structure's periodicity across any position in space.

Figure (38) shows that increasing the wavenumber results in different meniscus shapes of the magnetic meniscus free surface, including asymetrical ones. It also indicates that the asymmety degree between the left and right side of the curve, that could be defined by $Y(-1)-Y(1)$, decreases with the increase of the wavenumber. We argue that in the limiting case of $n \to \infty$ the shape tends to the case of a magnetic problem with a non-harmonic field, as indicated by figure (37).

In the limiting case of $n \to \infty$ the corresponding wavelenghts go to zero, meaning that the harmonic contribution of the applied field tends to a constant behavior equivalent to the imposition

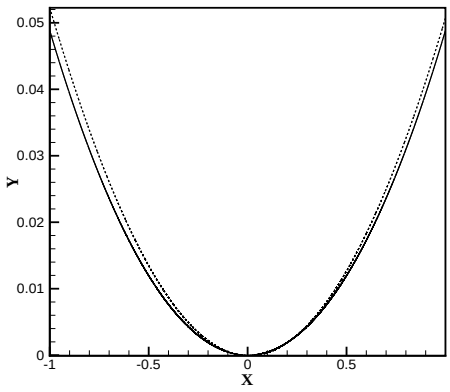

Figure 37: Meniscus shape for $n = 100$. The solid line represents $Bo_m = 0$ while the dashed line considers $Bo_m = 1.5$. For this plot: $Bo = 0.3$, $\chi_0 = 0.1$, $\beta_0^* = 0.1$, $\alpha = \pi/2 - \frac{1}{10}$, $\varepsilon = 1$.

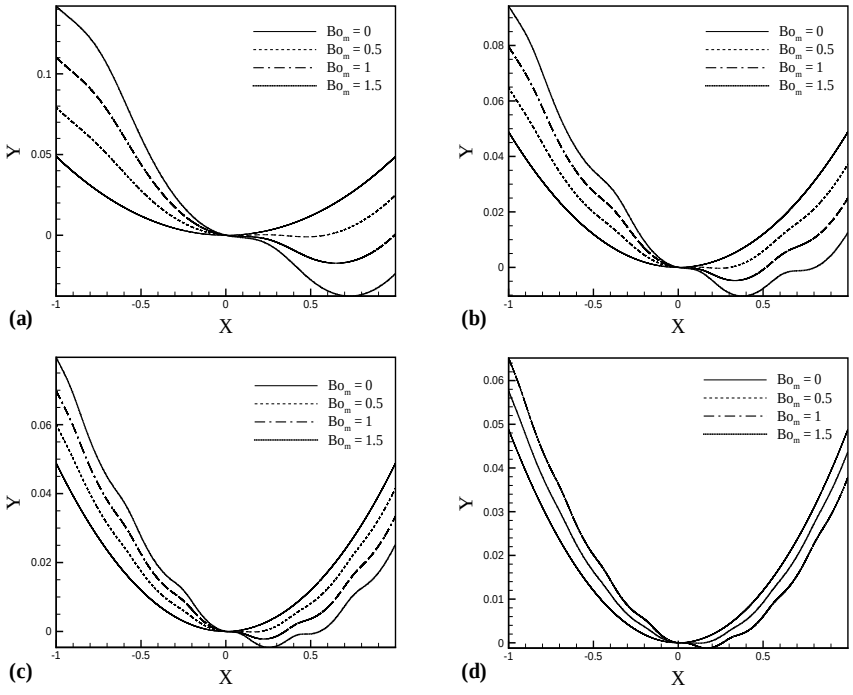

Figure 38: Meniscus shape for different values of n. Figure (a) stands for $n = 1$, (b) for $n = 2$, (c) for $n = 3$ and (d) for $n = 4$. For this plot: $Bo = 0.3$, $\chi_0 = 0.1$, $\beta_0^* = 0.1$, $\alpha = \pi/2 - \frac{1}{10}$, $\varepsilon = 1$ and magnetic Bond numbers varying from 0 to 1.5.

of a non-harmonic mangetic field in the vertical direction. Note that when the wavenumber is increased, the wavelenth becomes smaller. Consequently, there are more waves in a shorter distance b. It would be similar to increase the frequency of an external excitation. In the frequency case, it generates a time scales' decoupling and thus the system will not respond to the excitation. In this work, specifically, a space scale can be assumed. When the wave number increases, the system

does not respond to this excitation, producing a more symmetrical and less nonlinear response. Furthermore, the system has an entropy increase.

Another interesting finding in this problem are the bifurcations of the meniscus shape in the presence of a magnetic field. Figure (39) shows the shape of the meniscus and the equivalent FFT plots in the inserts of the graphics for the case of a non-magnetic fluid ($Bo_m = 0$) and for a small value of the magnetic bond number ($Bo_m = 0.2$). In this figure A represents the FFT amplitude.

For figure (39) it is observed that for higher values of the harmonic magnetic field, the non linearity is strongly influenced by just small variations of the magnetic parameters of the system. This strong dependence on small pertubations of a physical parameter is a typical characteristic of problems governed by nonlinear differential equations. It is also interesting to notice that other shape configurations start to appear when magnetic pressure tends to dominate capillary pressure on the liquid-interface, indicating a more nonlinear and complex behavior of the meniscus shape. We note that the excitation wavenumber is present as the first harmonic. It means that even being very non-linear, the meniscus still has a frequency signature. In both cases, most of the energy is concentrated in the first harmonic, in which $k/\pi = 2$. We noted that when there is an applied magnetic field, the second, third and fourth harmonics are concentrated in the same wavenumber: $k/\pi = 4$, $k/\pi = 6$ and $k/\pi = 8$, respectively. Nevertheless, when the magnetic field is applied, those harmonics steal energy from the first one, providing a more non-linear response to the meniscus. In addition, many other harmonics can be seen at $k/\pi = 10$ and $k/\pi = 12$, for example.

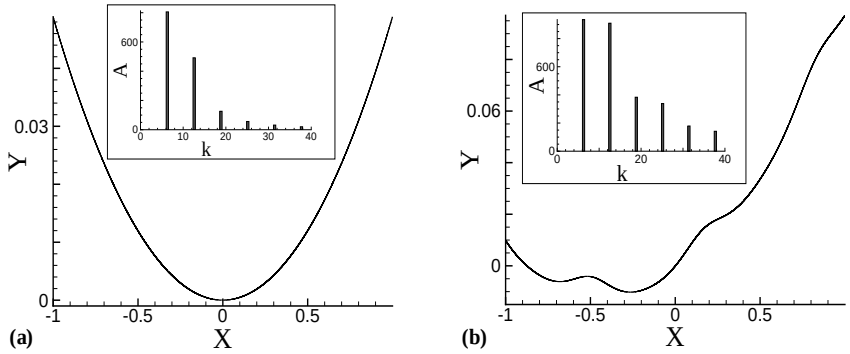

Figure 39: Meniscus shape for a non magnetic case $Bo_m = 0$ (a) and $Bo_m = 0.2$ (b). For this plot: $\varepsilon = 3$, $Bo = 0.3$, $\chi_0 = 0.1$, $\beta_0^* = 0.1$, $\alpha = \pi/2 - \frac{1}{10}$, $k/\pi = 2$.

On Figure (41), for example, only the magnetic effects are analyzed. We can see from the frequency (or wavenumber) spectrum that the increase of the Magnetic Bond number is associated with a spectrum spreading. In other words, more energy is lost to other harmonics, what causes the translation of the meniscus symmetry. For $Bo_m = 0,5$ there is a small loss of energy in the peak shown by the dotted line in the insert (a). Nevertheless, since the amplitude of excitation is small, the magnetic effects are not very prominent.

FFT is a very interesting tool, but has some disadvantages. The biggest disadvantage of a Fourier expansion however is that it has only frequency resolution (or wavenumber) and no time

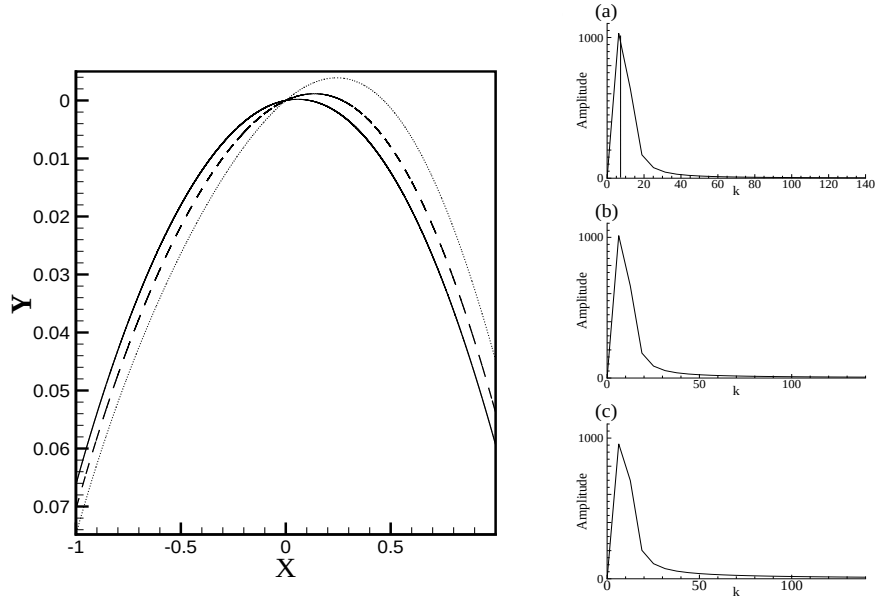

Figure 40: Meniscus shape for three different cases. The solid line represents $Bo_m = 0.1$, the dashed one features $Bo_m = 0.25$ and the dotted one represents $Bo_m = 0.5$. (a) Shows the FFT for $Bo_m = 0.1$, (b) represents $Bo_m = 0.25$ and (c) $Bo_m = 0.5$. For this plot: $\varepsilon = 0.5$, $\chi_0 = 0.1$, $\beta_0^* = 0$, $\alpha = \pi/2 + \frac{1}{8}$, $k/\pi = 2$.

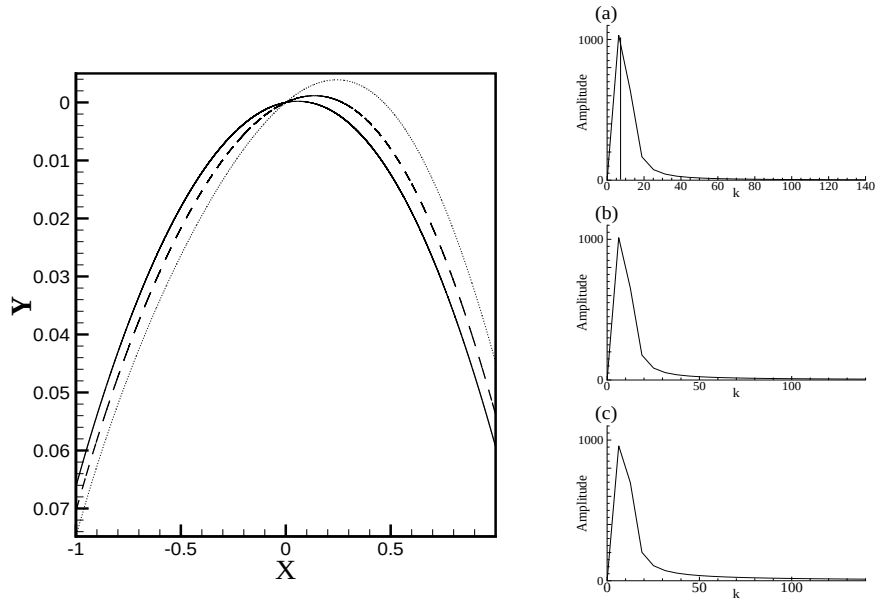

Figure 41: Meniscus shape for three different cases. The solid line represents $Bo_m = 0.1$, the dashed one features $Bo_m = 0.25$ and the dotted one represents $Bo_m = 0.5$. (a) Shows the FFT for $Bo_m = 0.1$, (b) represents $Bo_m = 0.25$ and (c) $Bo_m = 0.5$. For this plot: $\varepsilon = 0.5$, $\chi_0 = 0.1$, $\beta_0^* = 0$, $\alpha = \pi/2 + \frac{1}{8}$, $k/\pi = 2$.

resolution (or space). The wavelet transform or wavelet analysis is probably the most recent solution to overcome the shortcomings of the Fourier transform. Since the introduction of wavelets as a

signal processing tool in the late 1980âĂŹs, considerable attention has focused on this application [29, 30]. For instance, one can apply a rectangular (so-called Haar-basis) window function [31], to âĂİzoom-inâĂİ on the singularity of a signal. On Figure (42) it is possible to see two different combination of parameters that lead to nonlinear responses. In this figure, the wavelet transforms using Haar-basis are shown with the FFT transforms. The FFT does not show many relevant information in addition to the energy loss in the spectral signature harmonic. Note that this signature is in different positions, as shown by the dotted lines, due the excitation's wavenumber. Haar basis best represents functions that consist of sharp peaks and discontinuities. In the upper case (a), the clearer parts of the wavelet transform correspond to bigger coeficients. In this case, The coefficients become larger in the vicinity of a singularity and in this case, a null derivative. The larger scales represent low frequencies or large wavelengths. In this case, a low wavenumber.

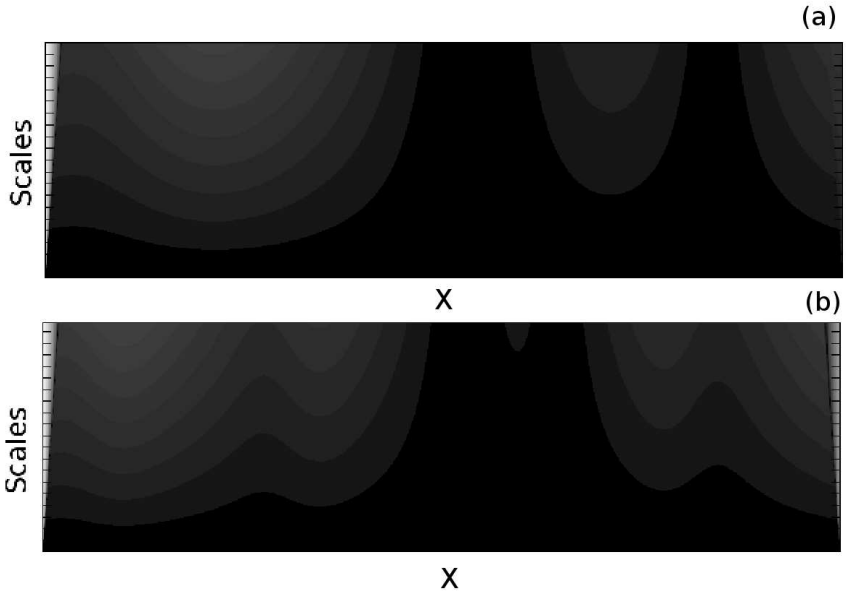

Figure 42: Meniscus Haar wavelet transform. (a)$k/\pi = 2$, $Bo_m = 1.4$, $\chi_0 = 0.1$, $\beta_0^* = 0$, $\varepsilon = 1.0$ and $\alpha = \frac{\pi}{2} - \frac{1}{10}$ (b) $k/\pi = 4$, $Bo_m = 1$, $\chi_0 = 0.1$, $\beta_0^* = 0.2$, $\varepsilon = 0.7$ and $\alpha = \frac{\pi}{2} - \frac{1}{10}$

Once the system is excited with a low wavenumber, the coefficients are higher in larger scales and not present the the smaller ones. As the scale decreases, there is less energy on the harmonics, since the wavenumbers are bigger, which can be confirmed through the FFT. Furthermore, in this case, it is possible to determine that the right side of the meniscus presents a non imposed boundary condition $Y \approx 0$. This can be observed because the signals tend to have higher coefficient values at the edges, due to the high derivatives and the boundary conditions. In this case, this does not occur, demonstrating the proximity to the null value or to what could be considered a resting value for a situation without capillary forces. The comparison between the wavelet transform and the physical shape of the meniscus and wavenumber spectrum response can be seen in figure (43).

In the case bellow (b), the excitation has a larger k, which can be observed by the coefficients on the wavelet transform. It is noted that the coefficients are large even in smaller scales when compared with the case presented in (a). In addition, the singularities appear almost together and can be seen as an inflection. In this case, it is possible to determine that the shape of the meniscus

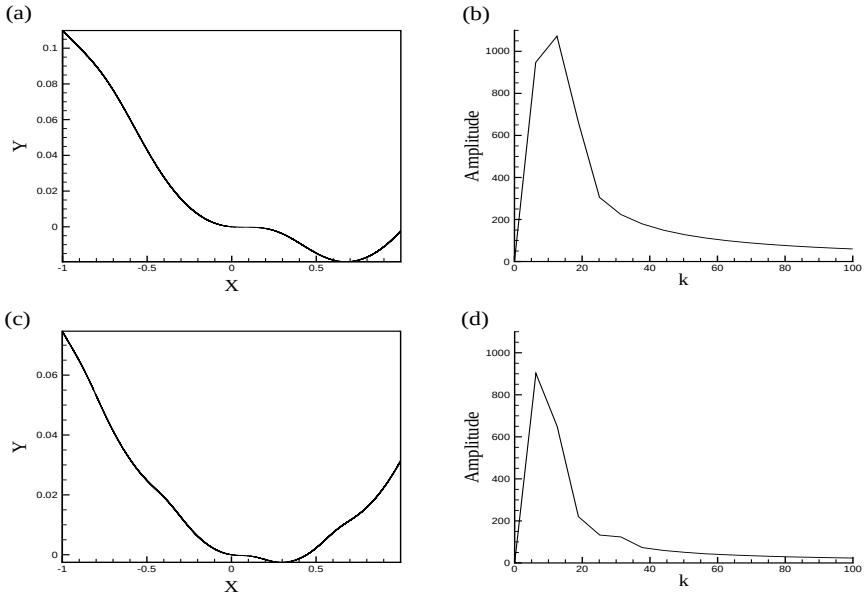

Figure 43: Source of meniscus shape used to compute the wavelet transform. (a) Meniscus shape for $k/\pi = 2$, $Bo_m = 1.4$, $\chi_0 = 0.1$, $\beta_0^* = 0$, $\varepsilon = 1.0$ and $\alpha = \frac{\pi}{2} - \frac{1}{10}$. (b) Correspondent FFT. (c) $k/\pi = 4$, $Bo_m = 1$, $\chi_0 = 0.1$, $\beta_0^* = 0.2$, $\varepsilon = 0.7$ and $\alpha = \frac{\pi}{2} - \frac{1}{10}$. (d) Correspondent FFT.

approaches a paraboloid.

Figure (44) shows the amplitude of the first harmonic in the wavenumber spectrum as a function of the Bo_m. it is possible to see that, the increase of the magnetic field, transfers energy into the system, which now has harmonics with higher amplitudes. In this respect, the signal carries more power. The way this amplitude increases as a function of the magnetic Bond can be described by a second-degree polynomial.

To sum up, it is possible to see in Figure (45) many different patterns formed by the meniscus shape. In general, the modification of the system's control parameters, such as magnetic Bond number, oscillation amplitude and wavenumber, can modify the anisotropy in the meniscus' shape. Furthermore, high magnetic fields at low values of oscillation can generate highly non-linear results. The ability to control the shape of the meniscus opens doors for the study of traction jump and even modifications on the capillary forces. The applications are diverse both in oil and bioengineering industry.

IV.15.2 Equilibrium rise of the meniscus

In this section we examine the dependence of the equilibrium rise of the meniscus on the contact angle α. A comparison between equation 133 and numerical results is presented in the plot of figure (46). We can see that when the $\alpha \to \pi/2$ both solutions provide the same result. As the values of α start to differ significantly from $\pi/2$, because the curvature can not be defined by the second derivative of the shape and it can not be assumed constant. For $\alpha = 0$, the error is about 15%.

The plot in figure (46) is also pointing out the range of application of the theory given by

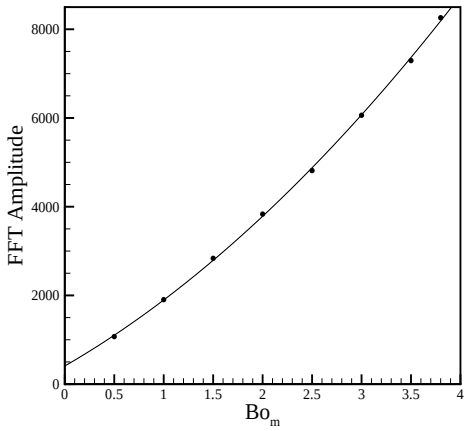

Figure 44: Comparison between the amplitude of the first harmonic in the wavenumber spectrum and the Magnetic Bond number. The dotted curve can be approximated as second order polynomial given by $A = 408.38 + 1288.59Bo_m + 199.65Bo_m^2$. For this plot: $\varepsilon = 1$, $\chi_0 = 0.1$, $\beta_0^* = 0$, $\alpha = \pi/2 - \frac{1}{8}$, $k/\pi = 1$.

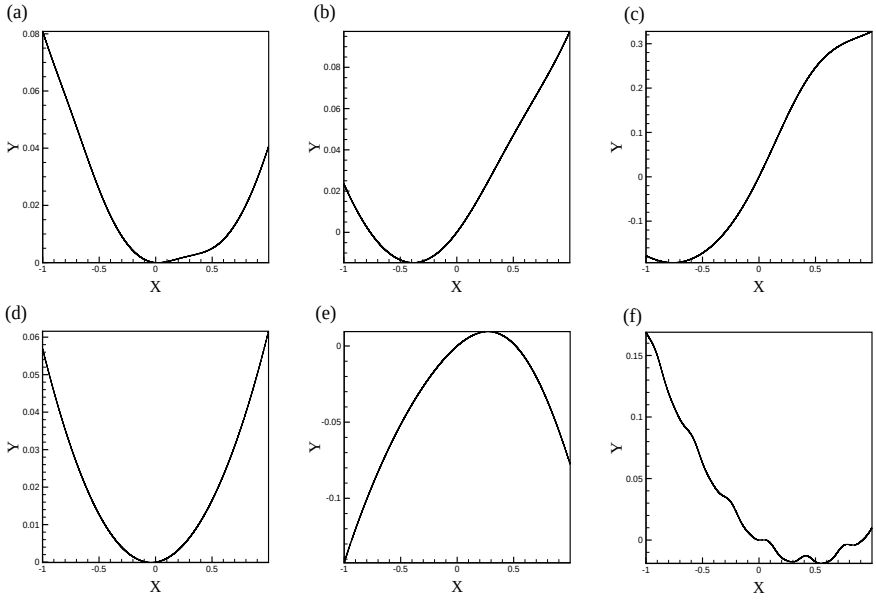

Figure 45: Comparison between the meniscus patterns formed by different controlling parameters. (a) $\varepsilon = 1$, $\chi_0 = 0.1$, $\beta_0^* = 0$, $\alpha = \pi/2 - \frac{1}{8}$, $k/\pi = 2$, $Bo_m = 1.5$. (b) $\varepsilon = 1$, $\chi_0 = 0.1$, $\beta_0^* = 0$, $\alpha = \pi/2 - \frac{1}{8}$, $k/\pi = 1$, $Bo_m = 1.5$. (c) $\varepsilon = 3$, $\chi_0 = 0.1$, $\beta_0^* = 0$, $\alpha = \pi/2 - \frac{1}{8}$, $k/\pi = 1$, $Bo_m = 1.3$. (d) $\varepsilon = 0.3$, $\chi_0 = 0.1$, $\beta_0^* = 0.1$, $\alpha = \pi/2 - \frac{1}{5}$, $k/\pi = 1$, $Bo_m = 0.1$. (e) $\varepsilon = 1$, $\chi_0 = 0.1$, $\beta_0^* = 0$, $\alpha = \pi/2 + \frac{1}{4}$, $k/\pi = 1$, $Bo_m = 0.5$. (f) $\varepsilon = 3$, $\chi_0 = 0.1$, $\beta_0^* = 0$, $\alpha = \pi/2 - \frac{1}{6}$, $k/\pi = 6$, $Bo_m = 2$.

equation (133). It should be said that that all analytical solutions consider the restriction that $Y'^2 \ll 1$, that requires $\alpha - \pi/2 \ll 1$. In addition figure (46) shows the importance of the numerical solution for exploring other regimes within the full range of contact angles.

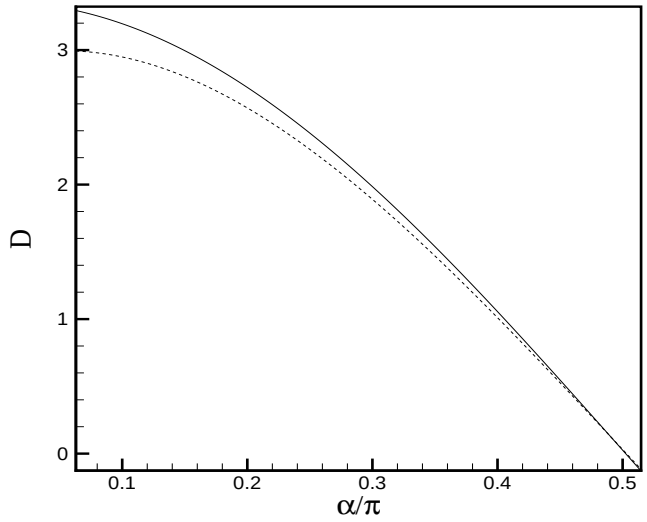

Figure 46: Equilibrium rise D as a function of the contact angle α. The solid line represents the theory with constant curvature and magnetic effects, equation (133), while the dashed line is the numerical solution. For this plot: $\varepsilon = 0$, $Bo = 0.3$, $\chi_0 = 0.1$, $\beta_0^* = 0.1$, $Bo_m = 0.1$.

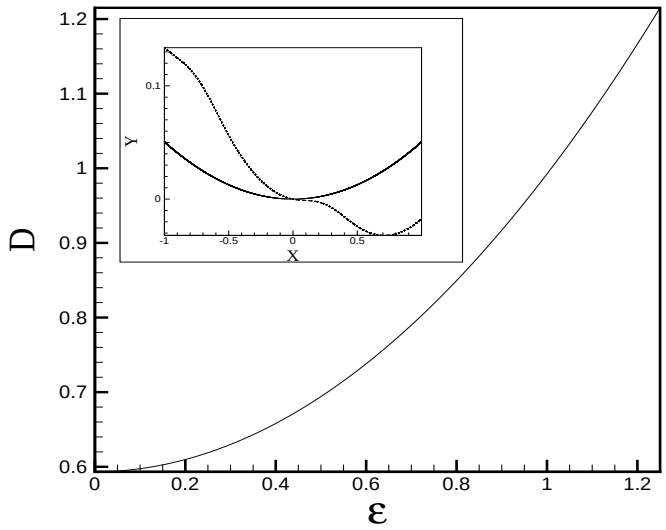

Figure 47: Equilibrium rise D as a function of ε. In the insert the solid line represents $\varepsilon = 0$ while the dashed line denotes $\varepsilon = 1.25$. For this plot: $n = 1$, $Bo = 0.3$, $\chi_0 = 0.1$, $\beta_0^* = 0.1$, $Bo_m = 1.0$. The solid line is well fitted by the relation: $D = c_0 + c_1\varepsilon + c_2\varepsilon^2 + c_3\varepsilon^3$, where $c_0 = 0.593, c_1 = 0.003, c_2 = 0.398$ and $c_3 = -0.003$.

An interesting result is the behavior of D when varying the amplitude of the harmonic contribution of the field. This result is particulary important because there is no theory to predict how the nonlinearities on the meniscus shape may change the equilibrium rise in which a magnetic interface can be displaced in a capillary under the influence of a magnetic pressure. Figure (47) shows the plot of D as a function of ε.

We can see that D is a rapid varying function of the amplitude ε of the magnetic field. It is observed that the variation of D with ε is $\mathscr{O}(\varepsilon^3)$ as showed by the best fit. This indicates that displacements of magnetic liquid interfaces against gravity may have much higher equilibrium rise by monitoring the amplitude of an external magnetic field, in contrast with the displacement produced by capillary pressure.

From this results we can see that while D is proportional to Bo_m and χ_0^2 it goes like $\mathscr{O}(\varepsilon^3)$. In general, the results indicates that as the nonlinearities related to magnetic effect on the polar fluid free surface increase, the equilibrum rise of the magnetic meniscus may increase even in the absence of capillary pressure.

IV.15.3 A brief discussion on the boundary conditions of the problem

The formulation of the problem requires some assumptions related to the boundary condition used in order to provide the shape of the meniscus. We must choose a physically consistent boundary condition in order to properly model the problem. One important discussion is the appropriate choice of the boundary condition used in the problem. In this section we show two options and discuss the differences between them. We define here the following options:

$$\text{B.C.1:} Y^{'}(0) = 0 \quad \text{and} \quad Y^{'}(1) = cot(\alpha), \quad 0 \leq X \leq 1 \tag{148}$$

and

$$\text{B.C.2:} Y^{'}(-1) = -cot(\alpha) \text{ and } Y^{'}(1) = cot(\alpha), \;\; -1 \leq X \leq 1 \tag{149}$$

Boundary condition 1 requires the imposition of vertical symmetry in order to provide the full shape of the meniscus. Figure (48) shows the difference between the meniscus shape considering boundary conditions 1 and 2 for several magnetic Bond numbers.

We can see from figure (48) that the assumption of vertical symmetry leads to an unrealistic behavior of the free surface. Indeed we do not know the derivatives values in the center of the meniscus. The only real boundary conditions that we know for sure from the physics of the problem are the values of the derivatives in the walls, since they depend exclusively on the contact angle, that is a property from the fluid and the wall material. It is interesting to notice in the insert of figure (48.b) that as we increase the magnetic Bond number the derivatives in the center of the meniscus increase in magnitude. For the non magnetic case, $Bo_m = 0$ both boundary conditions provide the same result, since we obtain a symmetrical profile. We argue that the deviation of the symmetry condition in the magnetic free surface shape is a measurement of the intensity of the magnetic effects.

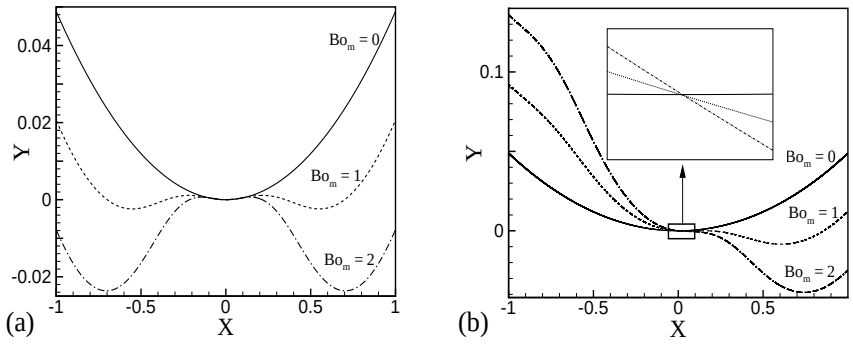

Figure 48: Meniscus shape considering symmetrical boundary conditions (a) and non-symetrical boundary conditions (b). For this plot: $n = 1$, $Bo = 0.3$, $\chi_0 = 0.1$, $\beta_0^* = 0.1$, $\varepsilon = 1.0$ and $\alpha = \frac{\pi}{2} - 0.1$.

IV.16 Conclusions

In this work we have presented a theoretical and numerical analysis on the behavior of two important variables regarding the behavior of a magnetic fluid freesurface. The shape of the surface and the equilibrium rise were explored. The numerical code developed to solve the nonlinear modified Young-Laplace differential equation has been validated against several theories, including non-magnetic cases for constant and non-constant curvature, magnetic problem for constant curvature and an asymptotic theory valid of small magnetic effects and non-constant curvature.

We showed that even for the condition of an interface with no curvature it is possible to lift a magnetic fluid due to magnetic pressure effects. Additionally, it was shown that variations of the magnetic liquid susceptibility with respect to the applied field decrease the effect of magnetic pressure on the magnetic interface for contact angle higher than $\pi/2$. Another interesting finding of this work regards the non-linearities on the free surface shape with respect to the wavelength and the intensity of the applied field. It was also shown that for the case of $\varepsilon \neq 0$, which cannot be solve by and analytical expression, a small variation of the magnetic Bond number may produce a significant change in the shape of the free surface, leading to additional shape configurations.

Finally, we found out that the increase of the dimensionless amplitude ε leads to a nonlinear behavior of the equilibrium rise of the magnetic liquid. This magnetic effect has been described by a $\mathscr{O}(\varepsilon^3)$ shape dependence.

IV.17 Appendix

The $\mathscr{O}(Bo_m)$ asymptotic solution is given by

$$
\begin{aligned}
Y_1(X) = -\frac{\operatorname{csch}^4\left(\sqrt{Bo}\right)}{96Bo^{5/2}D_0^3}\Big\{ & 12\sqrt{Bo}D_0\left[3Bo^2D_0^2D_1 + 2(\xi-\beta_0^*)\cot^2(\alpha)\right] \\
& - 24\sqrt{Bo}D_0\left[2Bo^2D_0^2D_1 + (\xi-\beta_0^*)\cot^2(\alpha)\right]\cosh\left(2\sqrt{Bo}\right) \\
& + 12Bo^{5/2}D_0^3D_1\cosh\left(4\sqrt{Bo}\right) + \cot^2(\alpha)\Big[8(-\xi+\beta_0^*)\sqrt{Bo}D_0\cosh(\alpha_4) \\
& + 4\sqrt{Bo}\left\{2\xi D_0 - \beta_0^*\left[2D_0 + 3\cot(\alpha)(1+X)\right]\right\}\cosh(\alpha_3) \\
& + 4\sqrt{Bo}D_0\cosh(2\alpha_3)\left[\xi-\beta_0^*\right] - 8\xi\sqrt{Bo}D_0\cosh\left(2\sqrt{Bo}X\right) \\
& + 8\beta_0^*\sqrt{Bo}D_0\cosh\left(2\sqrt{Bo}X\right) + 8\sqrt{Bo}D_0\cosh(\alpha_1)\left[\xi-\beta_0^*\right] \\
& - 12\beta_0^*\sqrt{Bo}\cot(\alpha)\cosh(\alpha_1)\left[1-X\right] + 4\xi\sqrt{Bo}D_0\cosh(2\alpha_1) \\
& - 4\beta_0^*\sqrt{Bo}D_0\cosh(2\alpha_1) - 8\sqrt{Bo}D_0\cosh(\alpha_2)\left[\xi-\beta_0^*\right] \\
& + \beta_0^*\cot(\alpha)\sinh\left[\sqrt{Bo}(1-3X)\right] + 3\beta_0^*\cot(\alpha)\left[\sinh(\alpha_4) - \sinh(\alpha_2)\right] \\
& - 12\beta_0^*\cot(\alpha)\left[\sinh(\alpha_1) - \sinh(\alpha_3)\right] + \beta_0^*\cot(\alpha)\sinh(\alpha_5)\Big]\Big\}
\end{aligned}
$$

with

$$
\begin{aligned}
&\alpha_1 = \sqrt{Bo}(1+X) && \alpha_2 = \sqrt{Bo}(3+X) && \alpha_3 = \sqrt{Bo}(-1+X) \\
&\alpha_4 = \sqrt{Bo}(-3+X) && \alpha_5 = \sqrt{Bo}(1+3X) && \xi = \chi_0\left(1+\chi_0\right)
\end{aligned}
$$

BIBLIOGRAPHIC REFERENCES

[1] Rosensweig R.E., 1985, *Ferrohydrodynamics*, New York: Cambridge University Press, 1985: republished by New York: Dover Publications, 1997.

[2] Odenbach S., (Ed.), 2009, *Colloidal Magnetic Fluids: Basics, Development and Application of Ferrofluids*, Lect. Notes Phys. 763, Springer, Berlin Heidelberg.

[3] Cunha F. R., Couto H. L. G. and Marcelino N. B., 2007, *A study on magnetic convection in a narrow retangular cavity*, Magnetohydrodynamics, Vol **43**, No 4, pp 421-428.

[4] Gontijo, R.G. e Cunha, F.R., 2012, *Experimental Investigation on Thermo-Magnetic Convection Inside Cavities*, J. Nanosci.Nanotechnol., Vol 12, pp. 9198-9207.

[5] Rinaldi C., Chaves A., Elborai S., He X., Zahn, M., 2005, *Magnetic fluid rheology and flows*, Current Opinion in Colloid and Interface Science, Vol **10**, pp 141-157.

[6] Gontijo R. G., 2013, *Micromechanics and hydrodynamics of magnetic suspensions*, Ph.D Thesis, University of Brasilia - Brazil, 227 pages (in Portuguese).

[7] Rosensweig R.E., Elborai S., Lee S.-H. Lee and Zahn M., 2005, *Theory and measurements of ferrofluid meniscus shape in applied uniform horizontal and vertical magnetic fields*, Journal of Magnetism and Magnetic Materials 289, 192?195.

[8] Bashtovoi V., Bossis G., Kuzhir P. and Reks A., 2005, *Magnetic field effect on capillary rise of magnetic fluids*, Journal of Magnetism and Magnetic Materials, Vol **289**, pp 376-378.

[9] Rosenthal, A. D., Rinaldi, C., Franklin, T., and Zahn, M., 2004, *Torque Measurements in Spin-Up Flow of Ferrofluids*,J. Fluids Eng. 126(2), 198-205 (May 03, 2004) (8 pages), doi:10.1115/1.1669030

[10] Chaves, A., Gutman, F. and Rinaldi, C., 2006, *Torque and Bulk Flow of Ferrofluid in an Annular Gap Subjected to a Rotating Magnetic Field*,J. Fluids Eng. 129(4), 412-422 (Nov 29, 2006) (11 pages) doi:10.1115/1.2567918

[11] Eissmann P-B, Lange, A. and Odenbach, S., 2011, *Meniscus of a magnetic fluid in the field of a current-carrying wire: two dimensional numerical simulations*, Magnetohydrodynamics, Vol **47**, Issue 2, pp. 149-157.

[12] Bragard J. and Lebon G., 1994, *Capillary ascension in porous media: a scaling law*, Transport in Porous Media, Vol **16**, pp 253-261.

[13] Bacri J.-C., Perzunski R., Shliomis M. I. and Burde G. I., 1995, *"Negative-viscosity" effect in a magnetic fluid*,Physical Review Letters, Vol **75**, No 11, pp 2128-2131.

[14] Bashtovoi V., Kuzhir P. and Reks A., 2002, *Capillary ascension of magnetic fluids*, Journal of Magnetism and Magnetic Materials, Vol **252**, pp 265-267.

[15] John T., Rannacher D., and Engel A., 2007, *Influence of surface tension on the conical meniscus of a magnetic fluid in the field of a current-carrying wire*, Journal of Magnetism and Magnetic Materials, Vol **309**, No 4, pp 31-35.

[16] John T., May K. and Stannarius R. , 2011, *Meniscus of a ferrofluid around a vertical cylindrical wire carrying electric current*, Physical Review E, Vol **83**, Issue 5.

[17] Bashtovoi V., Lavrovab O.A., Polevikovb V.K., Tobiskac L.,2002, *Computer modeling of the instability of a horizontal magnetic-fluid layer in a uniform magnetic field*, Journal of Magnetism and Magnetic Materials, Vol **252**, pp 299-301.

[18] Polevikova, V.,and Tobiskab L., 2005, *Instability of magnetic fluid in a narrow gap between plates*, Journal of Magnetism and Magnetic Materials, Vol **289**, pp 379-381.

[19] Boudouvis, A.G, Puchalla, J. L. and Scriven, L.E., 1988, *Interaction of Capillary Wetting and Fringing Magnetic Field in Ferrofluid Systems*, Journal of Colloid Interface Science, Vol **124**, pp 677-687.

[20] Wohlhuter, F. K. and Basaran, O. A., 1993, *Effects of physical properties and geometry on shapes and stability of polarizable drops in external fields*, Journal of Magnetism and Magnetic Materials, Vol **122**, pp 259-263.

[21] Jansons, K.M., *Determination of the constitutive equations for a magnetic fluid*, Journal of Fluid Mechanics, Vol **137**, 187-216.

[22] Ferderhof, B.U, 2000, *Magnetoviscosity and relaxation in ferrofluids*, Phys Rev E., Vol **62**, 3848-3854.

[23] Shliomis, M.I., 2001a, *Comment on magnetoviscosity and relaxation in ferrofluids*, Phys Rev E., Vol **64**, 063501.

[24] Shliomis, M.I., 2001b, *Ferrohydrodynamics: Testing a third magnetization equation*, Phys Rev E., Vol **64**, 063501.

[25] Hinch E.J., 1991, *Pertubation methods*, Cambridge University Press, Cambridge.

[26] Albernaz D.L., and Cunha, F.R, 2013, *Unsteady Motion of a Spherical Bubble in a Complex Fluid: Mathematical Modelling and Simulation*, Applied Mathematical Modeling, Vol 37, 8972-8984.

[27] Press W.H., Teukolsky S. A., Vetterling W.T., Flannery B.P., 1992, *Numerical recipes in Fortran 77*, 1, Cambridge University Press, Cambridge.

[28] Abramowitz M., and Stegun I.A., 1962, *Handbook of mathematical functions*, Applied Mathematics Series - 55, NBS, Washington.

[29] Lewis, A. and Knowles, G., 1992, *Image compression using the 2-D wavelet transform*, IEEE Trans. Image Processing, Vol 1, 224-250. 55, NBS, Washington.

[30] Shapiro, J. M., 1993, *Embedded image coding using zerotrees of wavelet coefficient*, IEEE Trans. Signal Processing, Vol 41, 3445âĂŞ3463

[31] Poularikas, A. D., 2000, *The Transforms and Applications Handbook*, CRC Press, 2 ed.